Faculty of Mathematics, Computer Science and Natural Sciences | RWTH AACHEN UNIVERSITY

Understanding Circular Dichroic Angle-Resolved Photoemission from Quantum Materials

Von der Fakultät für Mathematik, Informatik und Naturwissenschaften der RWTH Aachen University zur Erlangung des akademischen Grades einer Doktorin der Naturwissenschaften genehmigte Dissertation

vorgelegt von

Honey Boban
Master of Science

aus
Kerala, India

Berichter:
Prof. Dr. Markus Morgenstern
PD. Dr. Lukasz Plucinski

Tag der mündlichen Prüfung: 22.01.2025

Declaration of Authorship

I, Honey Boban, declare that this thesis and the work presented in it are my own and have been generated by me as the result of my own original research.

I do solemnly swear that:

1. This work was done wholly or mainly while in candidature for the doctoral degree at this faculty and university.
2. Where any part of this thesis has previously been submitted for a degree or any other qualification at this university or any other institution, this has been clearly stated.
3. Where I have consulted the published work of others or myself, this is always clearly attributed.
4. Where I have quoted from the work of others or myself, the source is always given. This thesis is entirely my own work, with the exception of such quotations.
5. I have acknowledged all major sources of assistance.
6. Where the thesis is based on work done by myself jointly with others, I have made clear exactly what was done by others and what I have contributed myself.
7. Parts of this work have been published before as [1]

15.04.2025

Honey Boban

Abstract

The physics of two-dimensional (2D) material has become a rapidly expanding field of research due to their unique electrical, optical, and mechanical properties, as well as their wide range of potential applications. The electronic band structure of these materials strongly influences their quantum transport properties, which is critical for next-generation quantum devices based on phenomena such as the quantum Hall effect, spin Hall effect, and orbital Hall effect. Consequently, a detailed characterization of the band structure, particularly focusing on the orbital angular momentum (OAM) and spin angular momentum (SAM), is essential for realizing the practical applications of 2D materials. Circular dichroic angle-resolved photoemission spectroscopy (CD-ARPES) is a widely used technique for investigating the OAM of bands, as it has been thought to be able to probe the OAM of the band structure.

This thesis provides an in-depth analysis of various contributions to the CD-ARPES spectra, including the photoionization process, experimental geometry, inter-atomic interference, and multiple scattering. These factors are explored in the context of two technologically relevant 2D materials, graphene and WSe_2, both of which exhibit unique electronic and optical properties that are of interest for quantum and electronic applications.

In addition, the thesis provides a detailed characterization of the electronic band structure of 2D magnetic materials, specifically $Cr_2Ge_2Te_6$ and Fe_3GeTe_2. Recognizing the importance of magnetic domain structure in determining the overall magnetic properties, this work also presents a thickness-dependent study of the magnetic domain structure in Fe_3GeTe_2, shedding light on how reduced dimensions influence the magnetic behavior at the nanoscale.

Contents

1 Introduction

The isolation of monolayer graphene in 2004 [2, 3] sparked a growing interest in the physics of 2D materials, driven by their remarkable properties, including tunable electrical and optical characteristics [4–6], the exhibition of novel quantum phenomena [7], and a wide range of applications [8]. Subsequently, monolayers of transition metal dichalcogenides were synthesized [9], marking the emergence of 2D materials as a highly active area of research. The reduction in size from the 3D to the 2D limit, combined with the ability to tune electrical properties through external perturbations such as electrical gating, magnetic fields, doping, and strain, makes 2D materials highly relevant for next-generation technological applications. Beyond their potential in future devices, 2D materials also offer an excellent platform for studying fundamental physics in lower dimensions.

A significant milestone in 2D material research occurred in 2017 with the discovery of the first 2D magnetic material [10, 11]. Quantum transport phenomena, such as the quantum anomalous Hall effect [12], the spin Hall effect [13, 14], and orbital Hall effect [15], have been observed in these 2D magnetic materials. Magnetism at the 2D limit is crucial for applications in spin-filter magnetic tunnel junctions [16], spin valves [17], spin field-effect transistors [18, 19], and spin-orbit torque devices [20], where the spin degree of freedom of the electron is exploited.

In addition to the spin degree of freedom, the orbital degree of freedom is also being harnessed in a relatively new field of physics known as *orbitronics* [21–24]. Both the spin and orbital degrees of freedom are closely related to the band structure of solids. The characterization of the spin and orbital character of the electronic band structure is crucial for understanding the quantum mechanical properties that govern the performance of materials in quantum transport devices.

Transverse currents in topologically non-trivial materials with intrinsic out-of-plane magnetization are described by the Kubo formula [25], where the anomalous velocity is dependent on the Berry curvature, which is closely linked to the electronic band structure of the material. Berry curvature typically reaches high values at crystal momenta near anti-crossings of bands with different orbital characters. Non-vanishing Berry curvature could be exploited in devices for spin to charge conversion or vise versa [26]. A detailed analysis of orbital character along with the spin texture and the wave function phases over the entire Brillouin zone is required for successful prediction of quantum transport properties, such as anomalous Hall effect, quantum spin Hall effect, and orbital Hall effect in solids.

One of the techniques that has been widely used for measuring the orbital angular momentum (OAM) of bands is circular dichroic-angle resolved photoemission spectroscopy (CD-ARPES). However, the relation between OAM and CD-ARPES is not trivial. A detailed theoretical calculation is required for comparing the initial state OAM to the measured CD-ARPES magnitude. Even with the recent advancements in the theoretical band structure calculations, there are still uncertainties in determining the initial state band characters from the measurements. Atomic-like photoionization patterns, related to the OAM of bands, are not the only contributions in the CD-ARPES maps. Additional contributions due to the photoemission final state scattering effects and experimental geometry, that are not related to the OAM of the bands, make the interpretation of the results complicated. Determining the initial state band characters require disentangling all the factors influencing the measurements.

Different contributions to the CD-ARPES data from graphene and WSe_2, including the photoionization pattern and its dependence on the experimental geometry, effect of interatomic interference and multiple scattering in CD-ARPES maps, and the dominance of these factors at different photon energy regimes are discussed in detail. A proper description of the photoemission process is a fundamental requirement in the analysis of the results.

Spin angular momentum (SAM) is another important factor in predicting the quantum transport properties of the solid. This is especially important for magnetic materials, where the spin degree of freedom can be exploited in practical applications. Due to their potential use in devices such as spintronic systems, magnetic tunnel junctions, and quantum computing technologies, 2D magnetic materials have become a crucial area of research. The changes in the magnetic properties when moving from the 3D to 2D limit is critical for their future technological applications. The magnetic properties of a 2D magnetic material depend on the domain structure, which in turn exhibits a strong dependence on the thickness of sample. The magnetic interactions in 2D magnetic materials could be determined from the temperature-dependent changes in the band structure. Therefore, a characterization of both band structure and real space domain structure is essential for a complete picture of magnetism in 2D magnetic materials.

The electronic band structure of two 2D magnetic materials, Cr_2 Ge_2Te_6 and Fe_3GeTe_2 has been studied. Photon energy-dependent and polarization-dependent measurements were used to study the composition of the band structure. Theoretical calculations have also been performed to explain the experimental findings. In addition to the band structure study, a real space domain structure study was also performed on exfoliated few layer flakes of Fe_3GeTe_2.

The chapters in this thesis are organized as follows:

- **Chapter 2** provides a fundamental theoretical background on electronic band structure, the photoemission process, and theoretical calculations.
- **Chapter 3** describes the primary experimental technique used in this thesis, the

angle-resolved photoemission spectroscopy (ARPES).

- **Chapter 4** discusses the sample preparation techniques used to produce the few-layer microflake samples, with detailed coverage of the mechanical exfoliation and dry transfer methods.
- **Chapter 5** presents the CD-ARPES results from graphene and WSe_2. The Dirac band near the Fermi level of graphene and the spin-orbit-split bands at the K and K' points of WSe_2 are analyzed. Various contributions to the CD maps are discussed, and multiple scattering calculations for graphene and WSe_2 are also presented.
- **Chapter 6** focuses on the electronic band structure study of $Cr_2Ge_2Te_6$. The atomic and orbital contributions to the band structure are studied using a combination of photon energy-dependent and polarization-dependent ARPES measurements. The magnetic interactions that stabilize magnetism in $Cr_2Ge_2Te_6$ are also discussed in detail. Additionally, CD-ARPES measurements from the valence and core levels are examined to illustrate the influence of multiple scattering in $Cr_2Ge_2Te_6$.
- **Chapter 7** explores the electronic band structure and magnetic domain structure of Fe_3GeTe_2. The theory of itinerant magnetism and X-ray magnetic circular dichroism (XMCD) is also discussed in this chapter.
- **Chapter 8** provides the conclusions drawn from the results presented in this thesis. The chapter also discusses the potential applications of these findings and offers an outlook for future research.

2 Theoretical background

2.1 Electrons in a solid

Many properties of a solid, including the electrical, thermal, optical, and mechanical properties, are determined by behaviour of the valence electrons in the solid. Several attempts were made in the 19th century to properly describe the electrons in the solid and to determine the properties. Initially, Drude proposed the free electron theory [27], where the valence electrons were treated classically and were considered as free electrons moving in the background of positively charged immobile ionic cores. This theory was later redefined by Sommerfeld with quantum mechanics by including the Pauli's exclusion principle (see for example Chapter 2 of reference [28]). Later, with the inclusion of the periodic lattice potential, the current electron band structure theory was developed. In this section a brief description of the development and theory of the electronic band structure will be given.

2.1.1 Free electron theory

Drude applied the kinetic theory of gases to metallic solids to derive the electrical and thermal conductivity with the electron velocity determined by $\frac{1}{2}mv^2 = \frac{3}{2}k_BT$. The charge neutrality of the metal is maintained by the positive ions. The basic assumptions in Drude theory of metals are the free electron approximation, independent electron approximation, and relaxation time approximation. In the free electron approximation, the interactions between electrons and ions are neglected except during collisions. The electrons in a solid are assumed to move in straight paths and only interact with the ions upon collision. In the independent electron approximation, the electron-electron interaction is neglected. In the relaxation time approximation, the collisions are assumed to be spontaneous and do not depend on the local environment or the velocity of the electrons at the time of the collision. The time between successive collisions of an electron and an ion is called the relaxation time or mean free time. The thermal equilibrium of the solid is achieved through these collisions.

Even with these assumptions, Drude theory of metal could explain some of the basic properties like electrical and thermal conductivity of metal, however with an overestimation of magnitudes. The overestimation of electrical and thermal conductivity was a result of using a classical electron distribution given by the Maxwell-Boltzmann distribution. In 1925, Pauli's exclusion principle for electrons were formulated stating that no two bound electrons in an atom can occupy the same quantum mechanical state. The classical description of electrons is insufficient, a quantum mechanical treatment of electrons in the

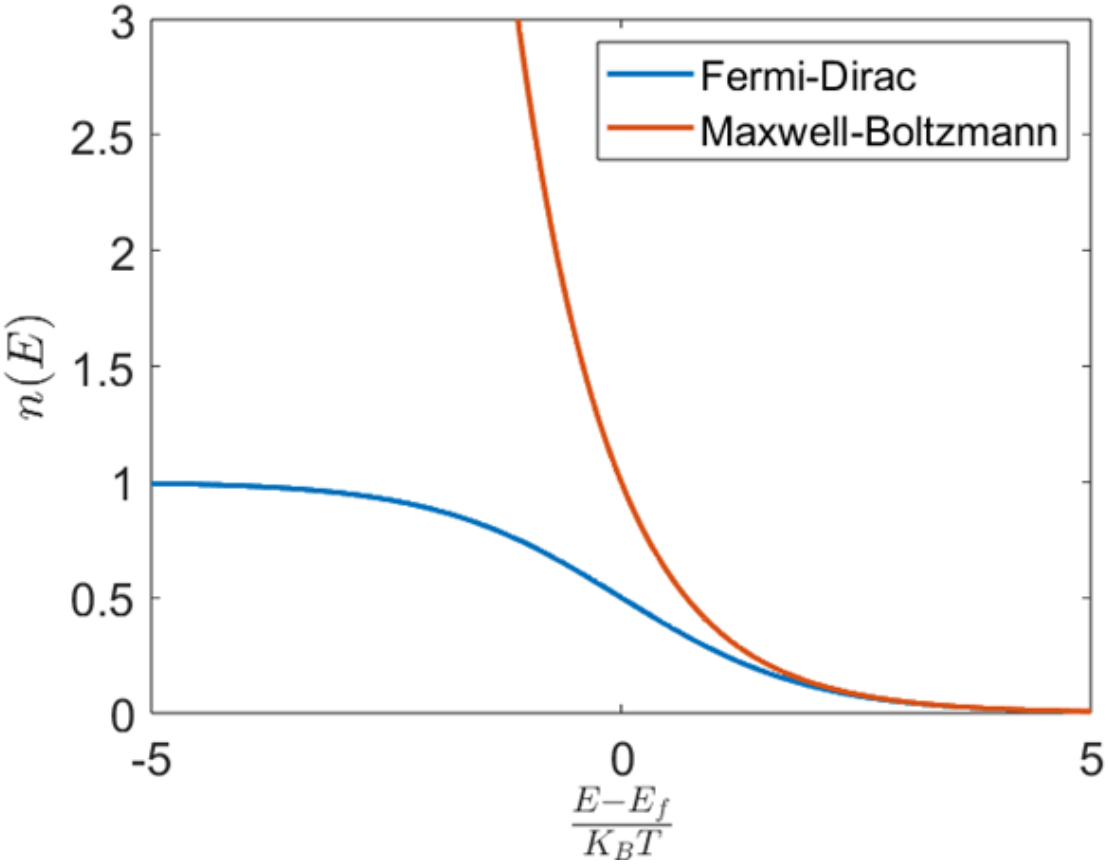

Figure 2.1: Maxwell Boltzmann distribution and Fermi Dirac distribution at room temperature (300 K).

solid is required.

To account for Pauli's exclusion principle, Sommerfeld replaced the Maxwell-Boltzmann distribution with the Fermi-Dirac distribution to describe electrons in a solid. The electron densities predicted by the Maxwell-Boltzmann distribution and the Fermi-Dirac distribution differ at temperatures below 1000 K. This is particularly relevant for determining the properties of solids within this temperature range. Figure 2.1 shows the difference between the Maxwell-Boltzmann distribution and the Fermi-Dirac distribution at room temperature (300 K). The electron distribution in the Sommerfeld theory is given by

$$f(\mathbf{v}) \propto \frac{1}{e^{\frac{\frac{1}{2}mv^2 - k_B T_0}{k_B T}} + 1}, \tag{2.1}$$

where $\mathbf{v}$ is the velocity of the electron, k_B is Boltzmann constant, and T is the temperature. T_0 is determined by the normalization condition, which ensures that the total number of electrons, $n = \int f(\mathbf{v}) d\mathbf{v}$. With the independent electron approximation, where the electrons do not interact with each other, the single electron eigen functions and eigenvalues are obtained by solving the Schrodinger equation, with Born von Karman boundary conditions

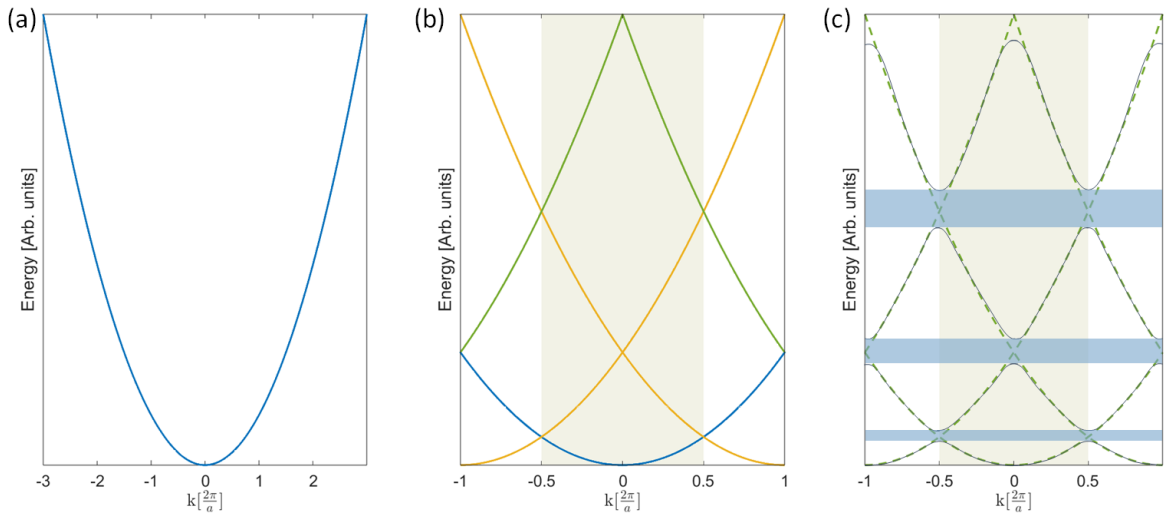

Figure 2.2: Energy eigenvalues of free electrons represented in the (a) extended zone scheme and (b) reduced zone scheme. The shaded region in (b) shows the reduced Brillouin zone. (c) the energy eigenvalues of nearly free electrons in a solid. The forbidden electron states are indicated by the shaded region.

given by

$$\begin{aligned} \psi(x+L,y,z) &= \psi(x,y,z) \\ \psi(x,y+L,z) &= \psi(x,y,z) \\ \psi(x,y,z+L) &= \psi(x,y,z). \end{aligned} \tag{2.2}$$

The eigenfunction is of the form

$$\psi_k(\mathbf{k}) = \frac{1}{\sqrt{V}} e^{i\mathbf{k}\cdot\mathbf{r}}, \tag{2.3}$$

where $k_i = \frac{2\pi n_i}{L}$, n_i = integer for $i = x, y, z$. The energy states are given by

$$E(\mathbf{k}) = \frac{\hbar^2 \mathbf{k}^2}{2m}, \tag{2.4}$$

with momentum $\mathbf{p} = \hbar\mathbf{k}$. The obtained one electron eigen states are then filled with with electrons according to Pauli's exclusion principle. The free electron parabola is shown in Figure 2.2 (a).

Although the Sommerfeld theory addressed many issues related to the overestimation of thermal properties, it still could not accurately determine the Hall coefficient and its dependence on temperature and magnetic field, the temperature dependence of magneto-resistance, and other related phenomena. Additionally, the fundamental distinction between metals, insulators, and semiconductors, as well as the determination of the number of conduction electrons in metals, remained unanswered by the free electron model.

2.1.2 Electrons in a periodic potential

Most of the limitations of the Sommerfeld theory are arising from ignoring the potential of the ionic cores. Distinction between metal, insulator and semiconductor can only be explained by going beyond the free electron approximation. The positively charged ions, which occupy the lattice points, create a periodic potential that affects the behaviour of the valence electrons.

Bloch's theorem is an important theorem in solving the problem of electrons in a periodic potential. In 1929, Felix Bloch showed that the solutions of the Schrodinger equation for an electron in a periodic potential can be expressed as a plane wave modulated by a periodic function [29]. The **Bloch state** is given by

$$\psi_{n\mathbf{k}}(\mathbf{r}) = e^{i\mathbf{k}\cdot\mathbf{r}} u_{n\mathbf{k}}(\mathbf{r}), \tag{2.5}$$

where $u_{n\mathbf{k}}(\mathbf{r}+\mathbf{R}) = u_{n\mathbf{k}}(\mathbf{r})$ for the lattice vector $\mathbf{R}$ [30]. The wave vector $\mathbf{k}$, which is given by $\frac{\mathbf{p}}{\hbar}$ for free electron, is no longer the momentum in the case of electron in a periodic potential. The action of momentum operator on the Bloch wave function gives

$$-i\hbar\frac{d}{d\mathbf{r}}\psi(\mathbf{r}) = -i\hbar\mathbf{k}e^{i\mathbf{k}\cdot\mathbf{r}}u(\mathbf{r}) + (-i\hbar)e^{i\mathbf{k}\cdot\mathbf{r}}\frac{d}{dr}u(\mathbf{r}), \tag{2.6}$$

where the vector $\mathbf{k}$ is called the **crystal momentum**, which contains the information of the translational symmetry of the crystal potential. Another important feature of Bloch wave function is that the wave vector $\mathbf{k}$ can always be restricted to the first Brillouin zone (see Figure 2.2 (b)), and is called reduced zone scheme. Any general $\mathbf{k'}$ not in the first Brillouin zone can be defined as $\mathbf{k'} = \mathbf{k} + \mathbf{G}$, substituting this in the 2.5 we get

$$e^{i\mathbf{k'}\cdot\mathbf{r}}u(\mathbf{r}) = e^{i(\mathbf{k}+\mathbf{G})\cdot\mathbf{r}}u(\mathbf{r}) = e^{i\mathbf{k}\cdot\mathbf{r}}u(\mathbf{r}), \tag{2.7}$$

since $e^{i\mathbf{G}\cdot\mathbf{r}} = 1$ for the reciprocal lattice vector $\mathbf{G}$. The subscript n in Bloch wave function in Equation 2.5 represents the set of solutions of the Schrodinger equation of the form

$$-\frac{\hbar^2}{2m}(-i\hbar\nabla + \mathbf{k})^2 u_{\mathbf{k}}(\mathbf{r}) + U u_{\mathbf{k}}(\mathbf{r}) = E_k u_{\mathbf{k}}(\mathbf{r}), \tag{2.8}$$

with periodic boundary condition, $u_{n\mathbf{k}}(\mathbf{r}+\mathbf{R}) = u_{n\mathbf{k}}(\mathbf{r})$. $U(\mathbf{r})$ is the periodic crystal potential. In a finite volume, the Equation 2.8 can have infinite solutions, which corresponds to discretely spaced eigenvalues counted by n, for a fixed value of $\mathbf{k}$. Similarly, for a particular value of n, the eigen state varies with respect to $\mathbf{k}$, giving the band structure. If the value of $\mathbf{k}$ is not restricted to the first Brillouin zone, the result will be identical bands shifted by the reciprocal lattice vectors because of the periodicity of eigenvalues and eigen functions with respect to $\mathbf{k}$. For a band with index n and wave vector $\mathbf{k}$, the mean velocity can be calculated using the formula:

$$v_n(\mathbf{k}) = \frac{1}{\hbar}\nabla_{\mathbf{k}} E_n(\mathbf{k}). \tag{2.9}$$

This shows that an electron in a band can move indefinitely with the velocity $v_n(\mathbf{k})$ without experiencing any collision with ions, opposite to the Drude model.

To study the characteristics of the electronic band structure of an electron in a periodic potential, the Schrodinger Equation 2.8 can be solved for a general potential U, if U is smaller compared to the kinetic energy of the electron. When the value of U is much smaller compared to the kinetic energy of the electron, the electron can be approximated as a nearly free electron or as an electron in a weak periodic potential, which works reasonably well for most metals. The result can be used to explain the origin of metals, insulators and semiconductors. The conduction electrons are forbidden from approaching the nucleus closely due to Pauli's exclusion principle. Additionally, in the outermost shell where the conduction electrons reside, most of the electric field is screened by the core electrons. The assumption of a weak periodic potential is valid because the potential decays steeply away from the nucleus, resulting in a relatively weak potential for the conduction electrons.

When the periodic potential is zero, the wave function is just a plane wave. One solution for weak periodic potential is to expand the wave function in plane waves with all possible $\mathbf{k}$ that satisfy the boundary conditions of Equation 2.2 and can be written as

$$\psi_k(\mathbf{r}) = \sum_k C_{\mathbf{k}} e^{i\mathbf{k}\cdot\mathbf{r}}. \tag{2.10}$$

The weak periodic potential can be expanded in the reciprocal lattice vectors and can be written as

$$U(\mathbf{r}) = \sum_{\mathbf{G}} U_{\mathbf{G}} e^{i\mathbf{G}\cdot\mathbf{r}}. \tag{2.11}$$

Substituting 2.10 and 2.11 in the Schrodinger equation we get

$$\sum_k -\frac{\hbar^2\mathbf{k}^2}{2m} C_{\mathbf{k}} e^{i\mathbf{k}\cdot\mathbf{r}} + \sum_{\mathbf{G}}\sum_{\mathbf{k}} U_{\mathbf{G}} C_{\mathbf{k}} e^{i(\mathbf{k}+\mathbf{G})\cdot\mathbf{r}} = E \sum_{\mathbf{k}} C_{\mathbf{k}} e^{i\mathbf{k}\cdot\mathbf{r}}, \tag{2.12}$$

which requires same coefficients on each side for each $\mathbf{k}$. This gives

$$\frac{\hbar^2\mathbf{k}^2}{2m} C_{\mathbf{k}} + \sum_{\mathbf{G}} U_{\mathbf{G}} C_{\mathbf{k}-\mathbf{G}} = E C_{\mathbf{k}}, \tag{2.13}$$

and is called the **central Equation** [28].

In the solid, the nearly free electrons travel like waves towards the left or right directions. But at special $\mathbf{k}$ points, like at the Bragg planes (or zone boundaries), the electrons are not travelling waves. At these $\mathbf{k}$ points the wave function is made of equal parts of left and right travelling waves, due to reflection of electrons by the atomic planes, resulting in a standing wave. Therefore the solution is a sum of left and right travelling waves represented by $\pm k$. The approximate solution of the Schrodinger equation can be determined at the zone boundaries by solving the central Equation 2.12 for $\mathbf{k} = \pm\frac{1}{2}\mathbf{G}$. Substituting the two values of $\mathbf{k}$ in 2.12 give two equations:

$$\begin{aligned} \left(\frac{\hbar^2\mathbf{k}^2}{2m} - E\right) C\left(\frac{1}{2}\mathbf{G}\right) + UC\left(-\frac{1}{2}\mathbf{G}\right) &= 0 \\ \left(\frac{\hbar^2\mathbf{k}^2}{2m} - E\right) C\left(-\frac{1}{2}\mathbf{G}\right) + UC\left(\frac{1}{2}\mathbf{G}\right) &= 0, \end{aligned} \tag{2.14}$$

for which the solutions are given by

$$\mathbf{E} = \frac{\hbar^2 \mathbf{k}^2}{2m} \pm U. \tag{2.15}$$

This results in one band having the energy lowered by U and another band having the energy raised by U resulting in a band gap of $2U$ at the Brillouin zone boundary (shown by shaded region in Figure 2.2 (c)). The two wave functions at the zone boundary are

$$\psi_{\pm}(x) = e^{iGx} \pm e^{-iGx}. \tag{2.16}$$

The electron density of ψ_+ is proportional to $cos^2(Gx)$, which results in an accumulation of electrons at the lattice sites whereas the electron density of ψ_- is proportional to $sin^2(Gx)$, which peaks away from the lattice sites. This can be considered as a lower potential energy for ψ_+ and higher potential energy for ψ_- near the lattice points, which gives rise to a band gap near the zone boundary.

Similarly, the central equation can be solved close to the zone boundaries by solving the central Equation 2.12 at **k** and at **k-G**. The solution are given by

$$\mathbf{E}_{\pm} = \mathbf{E}_{\pm} + \frac{\hbar^2(\mathbf{k} - \frac{1}{2}\mathbf{G})^2}{2m} \left(1 \pm \frac{2\hbar^2}{2mU} \left(\frac{1}{2}\mathbf{G}\right)^2\right). \tag{2.17}$$

The solution indicates that the energy of $\mathbf{E}_+$ band decreases near the zone boundary and the energy of $\mathbf{E}_-$ increases, when the sign of U is negative. Here $\mathbf{E}_+$ is the lower band and $\mathbf{E}_-$ is the upper band near the zone boundary.

The one electron eigen states of electrons in weak periodic potential, $\mathbf{E}_n(\mathbf{k})$, where **k** is restricted to the first Brillouin zone, are filled by total number of electrons according to the Pauli's exclusion principle. When there are even number of electrons per primitive cell, there are two possibilities. The topmost occupied band can be fully filled or can be partially filled because of overlapping bands. When the band is fully filled, and if energy difference to the next available band is in the order of k_BT then the solid is a semiconductor. If the difference between the highest occupied band and the lowest unoccupied band is larger than k_BT, then the solid is an insulator. If the band is filled partially, then the solid is a metal. This distinction of metals, insulators and semiconductors is only possible with a non zero band gap. The opening of a band gap near the zone boundary is completely missing in free electron theory, where the energy is a continuous function of **k** and there are no forbidden energies that the electron cannot occupy. The bad gap can only be explained by considering the periodic lattice potential.

2.2 Density functional theory

In this thesis, the electronic band structure of different quantum materials is studied using angle resolved photoemission spectroscopy (ARPES). The experimental spectra

are combined with theoretical initial state band structure calculations to get further information about the character and wave function localization of the observed bands. Density functional theory (DFT) calculations [31, 32] were employed to study the band structure of the solids. A brief description of the fundamental theory of DFT, mainly focusing on Wien2k code [33], will be provided in this chapter.

The entire electronic band structure theory in Section 2.1.2 is explained using one electron wave function. This means one considers a single electron moving in an averaged potential of nuclei and all other electrons. In reality, the electron - electron interactions play an important role in solids. However, accounting for all electronic correlations make calculations nearly impossible even for small systems, as the computational time scales with N^7 as the system size (N) increases [33]. Therefore, several assumptions are made for the calculations.

Including the interactions between nuclei along with electronic correlations will complicate the situation even more. Therefore, the first approximation in DFT is the Born Oppenheimer approximation, in which the motion of nuclei is neglected. The electron when compared to nuclei has low mass and therefore, the electrons move faster than nuclei in solids. Since the time scale of motion of electrons and nuclei are different by many orders of magnitude, the nuclei can be considered as immobile in solid. The positions of the nuclei are determined by relaxing the lattice, which corresponds to finding the configuration with the minimum total energy of the system. The experimental atomic positions are used as the initial starting point for this relaxation process.

The DFT is based on the Hohenberg-Kohn theorems [31, 32] which are formulated for interacting particles in an external perturbation, with one case being the electrons in the field of fixed ions. The Hamiltonian can be written as

$$H = \sum_{i=1}^{N} -\frac{\hbar^2}{2m}\nabla_i^2 + e^2 \sum_i \frac{1}{|\mathbf{r} - \mathbf{r}_i|} - e^2 \sum_j \frac{Z}{|\mathbf{r} - \mathbf{r}_j|} + v_{xc} + v_{ext}(\mathbf{r}). \tag{2.18}$$

The first theorem states that the external perturbation v_{ext} is uniquely represented by the ground state density $\rho_o(\mathbf{r})$, provided the ground state is non degenerate. The second Hohenberg-Kohn theorem is about the total energy of the interacting particle system. The total energy can be represented as $E(\rho(\mathbf{r}))$ and the exact ground state energy corresponds to the ground state electron density, $E(\rho_o(\mathbf{r}))$ [34], that is,

$$E(\rho_o(\mathbf{r})) \leq E(\rho(\mathbf{r})) = T_e(\rho(\mathbf{r})) + v_{ee}(\rho(\mathbf{r})) - v_{Ne}(\rho(\mathbf{r})) + v_{xc}(\rho(\mathbf{r})). \tag{2.19}$$

The kinetic energy T_e, the exchange correlation (v_{xc}), electron - electron (v_{ee}) and electron - nuclei (v_{Ne}) interactions also depend on the density $\rho(\mathbf{r})$.

In 1965, Kohn and Sham applied variational principle by introducing orbitals $\chi_{i,j}(\mathbf{r})$ to minimize the total energy of the system. The electron density is given by

$$\rho(\mathbf{r}) = \sum_{i,j} \rho_{i,j} |\chi_{i,j}(\mathbf{r})|^2, \tag{2.20}$$

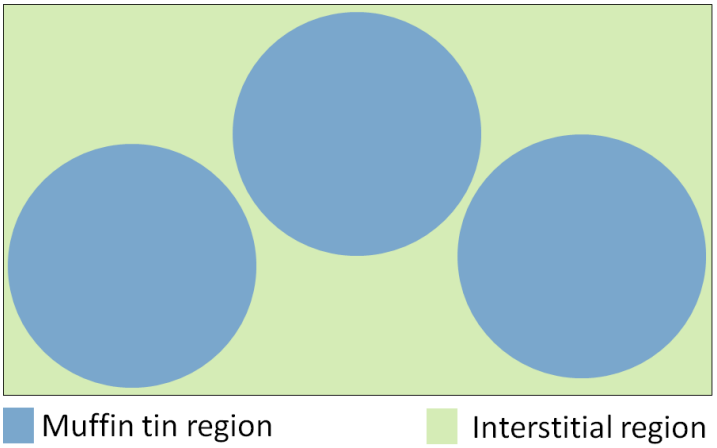

Figure 2.3: Schematic diagram showing the muffin tin region and interstitial regions used for the WIEN2k calculations.

where $\rho_{i,j}$ are the occupation numbers. The variation of the total energy gives set of effective single particle Schrodinger equations,

$$(-\frac{\hbar^2}{2m}\nabla_i^2 + v_{ee} + v_{Ne} + v_{xc})\chi_{i,j}(\mathbf{r}) = E\chi_{i,j}(\mathbf{r}). \tag{2.21}$$

The orbitals $\chi_{i,j}(\mathbf{r})$ depend on the effective single particle potential, where $\chi_{i,j}(\mathbf{r})$ itself depends on the electron density. Therefore, the Kohn-Sham equations must be solved till the self consistency is achieved. The exact form of the exchange correlation potential, v_{xc}, is not known and certain approximations are made to find the potential. Local density approximation (LDA) is one of the approaches to solve the problem, where electrons are treated like in the homogeneous electron gas and the correlation functions depend only on the local electron density. An improved approach is generalized gradient approximation (GGA), where the exchange and correlation potentials also depend on the gradient of the electron density along with the local electron density itself. With GGA, the in-homogeneity of the electrons are included through the gradient of the electron density.

Once the exchange and correlation potentials are determined, an appropriate basis function must be selected. In the Wien2k code [33], which is the one used for most of the theoretical calculations in this thesis, linearized augmented plane wave (LAPW) method is used. In this method, the unit cell is divided into atomic spheres, around the atomic sites, and interstitial sites, as shown in Figure 2.3. Muffin tin approximation is used to define the atomic spheres. In the atomic spheres, where the potential is assumed to be spherically symmetric with non-spherical corrections, the basis set is taken as a linear combination of radial functions times the angular components, given by

$$\phi_{\mathbf{k}_n} = \sum_{l,m}(A_{lm,\mathbf{k}_n}u_l(\mathbf{r},\mathbf{E}_{1,l}) + B_{lm,\mathbf{k}_n}\dot{u}_l(\mathbf{r},\mathbf{E}_{1,l}))Y_{lm}(\hat{\mathbf{r}}) \tag{2.22}$$

where the $u_l(\mathbf{r},\mathbf{E}_{1,l})$ is the radial part of the solution of Schrodinger equation for $E_{1,l}$. The linear combination of the radial part with its derivative linearize the energy dependence of

the radial part. The basis set in interstitial sites is taken as a plane wave (PW) expansion, given by

$$\phi_{\mathbf{k}_n} \propto e^{i\mathbf{k}_n.\mathbf{r}}. \tag{2.23}$$

The coefficients in Equation 2.22 are determined by the boundary conditions at the atomic sphere boundaries. To improve the energy linearization, an additional energy-dependent term, $C_{lm}u_l(\mathbf{r}, \mathbf{E}_{2,l})$, which is independent of $\mathbf{k}_n$ is added to Equation 2.22, called the local orbitals. This term helps to treat both core and valence states in the same energy window. The solutions of Equation 2.21 are expanded in the combined PW and atomic basis set of LAPW as

$$\psi(\mathbf{r}) = \sum_n C_n \phi_{\mathbf{k}_n} \tag{2.24}$$

where the coefficients C_n are determined by variational principle.

In Wien2k, the muffin tin approximation is only used to define the atomic spheres. The potentials are expanded as lattice harmonics and Fourier series in atomic spheres and interstitial sites, respectively. Therefore, the potential does not depend on the shape and is called full potential scheme. The full-potential LAPW method is one of the most efficient techniques for calculating band structures, as it avoids discrepancies and allows for accurate comparison with experimental results.

One of the drawbacks of DFT calculations is that they generally yield incorrect values for band gaps in insulators and semiconductors [35]. When compared to experimental band structures, DFT calculations are considered initial state calculations. As a result, they do not account for the photoexcitation process, meaning that none of the effects related to the excited state or the photoemission process are included. This include the intensity modulation of bands due to the transition matrix elements which depends on the polarization and direction of the light, and effects due to multiple scattering. To explain these photoemission effects on the intensity, an advanced one step model calculations are required, where the photoexcitation, transport and emission processes are included.

2.3 Photoemission spectroscopy

Photoemission spectroscopy is an established technique in solid state physics, which is used to study electronic properties of a wide range of systems from free atoms to bulk solids. In photoemission spectroscopy, the sample is probed using a photon, which can be a discharge lamp, a laser, a synchrotron radiation, or an X-ray source, and electrons emitted by absorbing the photons are measured using a detector. In case of solids, these emitted photo electrons carry information about the initial state of the electronic band structure.

The first observation of photoelectrons was in 1887, when H.Hertz detected electrons emitted from a secondary arc by the absorption of ultra violet radiation [36]. The theoretical explanation of this was given by Einstein in 1905, known as the photoelectric effect [37].

The maximum kinetic energy of the emitted electron is given by

$$E_{kin} = h\nu - \phi_0 \tag{2.25}$$

where $h\nu$ is the energy of the photon and ϕ_0 is a material property related to the surface potential barrier, called the work function. The experimental technique was further developed to use as spectroscopic technique to study the electronic properties of solids.

A quantum mechanical description of the photoemission process is given by time dependent perturbation theory. The Hamiltonian of the electron in the initial state is given by

$$H_0 = \frac{\mathbf{p}^2}{2m_e} + \mathbf{V}_0 \tag{2.26}$$

where p and m_e are the momentum and mass of the electron and V_0 is the potential energy of the electron due to the interaction with other electrons and nucleus. When the system is probed using a photon beam with vector potential $A(\mathbf{r},t)$ and scalar potential $\phi(\mathbf{r},t)$, the Hamiltonian is given by

$$H = \frac{(\mathbf{p} + \frac{e}{c}\mathbf{A})^2}{2m_e} + \mathbf{V}_0 - e\phi(\mathbf{r},t). \tag{2.27}$$

With the conditions $\nabla \cdot \mathbf{A} = 0$ and $\phi(\mathbf{r},t) = 0$ for the electromagnetic radiation and neglecting the $\mathbf{A}^2$ term, because of the assumption of weak radiation, in Equation 2.27, we get

$$H = \frac{\mathbf{p}^2}{2m_e} + \mathbf{V}_0 + \frac{e}{m_e c}\mathbf{A}\cdot\mathbf{p} = H_0 + \mathbf{V}(t), \tag{2.28}$$

where $\mathbf{v}(t) = \frac{e}{m_e c}\mathbf{A}\cdot\mathbf{p}$ represents interaction of the electrons with the radiation and can be treated using the perturbation theory. The vector potential in the perturbation term can be expanded as $A_0\vec{\epsilon}e^{i\vec{k}\cdot\vec{r}-\omega t} + A_0^*\vec{\epsilon}e^{-i\vec{k}\cdot\vec{r}-\omega t}$, where $\vec{\epsilon}$ is the polarization vector of the radiation. This can be solved using the interaction picture in quantum mechanics where both the operator and the wave function depends on the time. The transition probability of emission from the initial state ψ_i to the final state ψ_f is given by

$$W_{if} \propto \frac{2\pi}{\hbar}|\langle\psi_f|e^{i\vec{k}\cdot\vec{r}}\vec{\epsilon}\cdot\vec{p}|\psi_i\rangle|^2\delta(E_f - E_i - \hbar\omega). \tag{2.29}$$

This is called Fermi's golden rule. The delta function in Equation 2.29 ensures energy conservation. The transition probability is usually calculated taking single particle eigen functions and does not take into account the interaction with the rest of the $(N-1)$ electrons in the system, where N is the total number of electrons in the system. But in reality, the photoemission process is a many body problem, the electrons interact with each other and the $(N-1)$ electrons rearrange when the the photo electron is emitted. When the electrons interact, the initial and final states are taken as $\psi_i = \psi_i\phi_i(N-1)$ and $\psi_f = \psi_f\phi_f(N-1)$ where $\phi(N-1)$ is the wave function of $(N-1)$ electrons. The transition probability then becomes

$$W_{if} \propto \frac{2\pi}{\hbar}|\langle\psi_{f,k}|e^{i\vec{k}\cdot\vec{r}}\vec{\epsilon}.\vec{p}|\psi_{i,k}\rangle|^2\sum_s|\langle\phi_{f,s}(N-1)|\phi_{i,k}(N-1)\rangle|^2\delta(E_f + E_s - E_0 - \hbar\omega). \tag{2.30}$$

Here the $\phi_{f,s}(N-1)$ and E_s are the final states and the energies of the $(N-1)$ electrons after the photoemission, and E_0 is the ground state energy of the N electrons. In the sudden approximation or frozen orbital approximation, the overlap integral $\langle\phi_{f,s}(N-1)|\phi_{i,k}(N-1)\rangle$ equals 1, because, in this approximation the $(N-1)$ electrons are unaffected by the emission of the photo electron [38]. The relaxation time for $(N-1)$ electrons are assumed to be longer compared to the photoemission process, and therefore, $\langle\phi_{f,s}(N-1) = \phi_{i,k}(N-1)\rangle$ for $s = k$, and the integral becomes zero for the rest of the terms. The overlap integrals $\langle\phi_{f,s}(N-1)|\phi_{i,k}(N-1)\rangle$ can be non zero for $k \neq s$ for strongly correlated materials, where the many body interaction must be included for proper description. The overlap integral in correlated materials are related to the self energy, which will give rise to many satellites peaks in photoemission along with the main peaks.

For solving the transition probability approximately, the $e^{i\mathbf{k}\cdot\mathbf{r}}$ term in Equation 2.29 can be expanded as

$$e^{i\mathbf{k}\cdot\mathbf{r}} = 1 + i\mathbf{k}\cdot\mathbf{r} - \frac{1}{2}(\mathbf{k}\cdot\mathbf{r})^2 + ... \tag{2.31}$$

Typical photon energies used in photoemission experiments are in the range of 10 to 1000 eV. The wavelength of these photon energies correspond to $\lambda \approx 100$ -1000 Å. The wavelength of the light compared to the inter-atomic distances, which is ≈ 3 Å, is large enough to say that the electromagnetic radiation do not vary much spatially. Therefore, we consider only the first term in the expansion in Equation 2.31, giving the transition probability,

$$W_{if} \propto \frac{2\pi}{\hbar}|\langle\psi_f|\vec{\epsilon}\cdot\vec{p}|\psi_i\rangle|^2\delta(E_f - E_i - \hbar\omega). \tag{2.32}$$

This is called the dipole approximation. This approximation is valid only in the low energy regime where the wavelength of light is large compared to the inter-atomic distances. The Equation 2.32, that represents the velocity form of the matrix element, can be equivalently written in the *length* form using the relation

$$\langle\psi_f|\vec{\epsilon}.\vec{p}|\psi_i\rangle = \frac{m_e}{i\hbar}(\mathbf{E}_f - \mathbf{E}_i)\langle\psi_f|\vec{\epsilon}.\vec{r}|\psi_i\rangle. \tag{2.33}$$

There are several ways to interpret the photoemission process. One common approach is the three-step model, which divides the process into three stages: excitation of the electron, transport of the electron to the surface, and emission of the electron from the surface into the vacuum. Another approach is the one-step model, which provides a more accurate quantum mechanical description of the entire photoemission process.

2.3.1 Three step model

In 1964, Berglund and Spicer first introduced the three step model [39, 40]. As discussed earlier, the three steps in photoemission process are (i) excitation of the electron from the initial state, ψ_i, to the final state, ψ_f, within the solid (the excitation is to the unoccupied

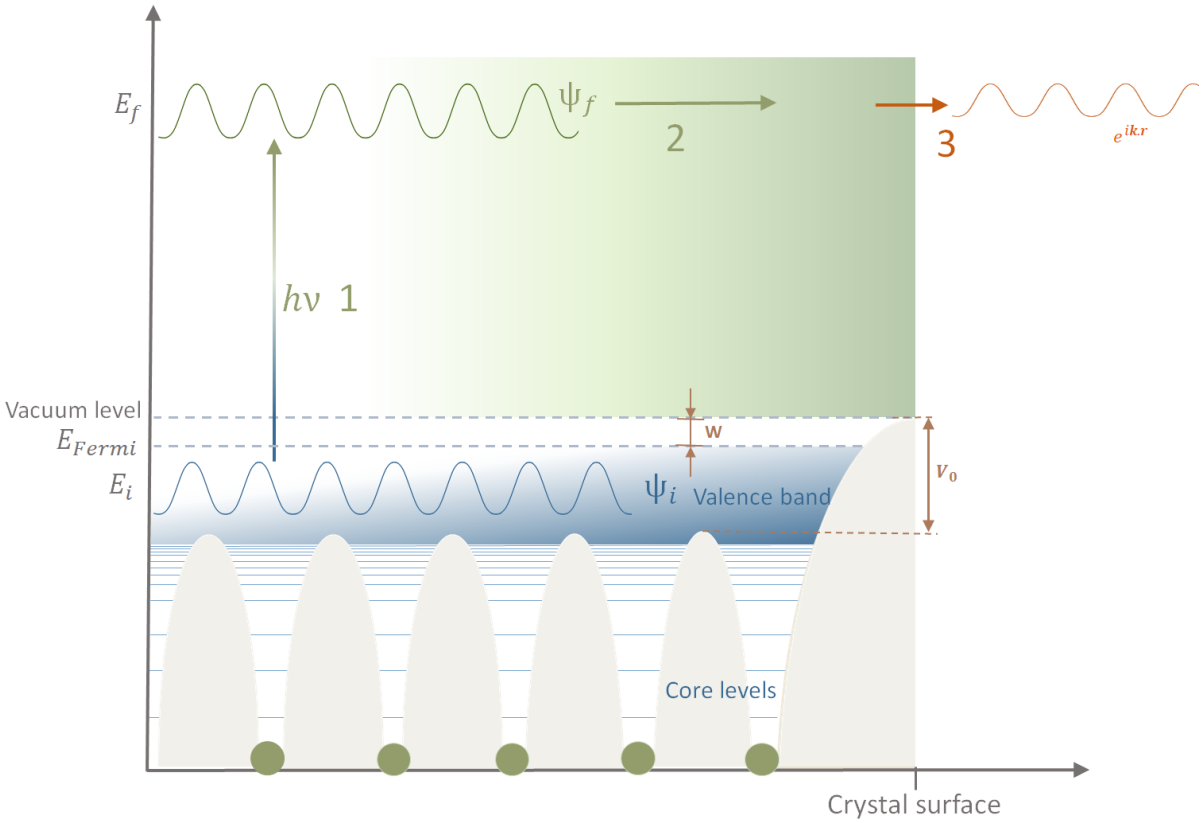

Figure 2.4: Schematic diagram of three step model of photoemission. The excitation form initial state ψ_i to final state ψ_f (which is an unoccupied state within the solid), propagation to the surface and transmission through surface are labelled as 1, 2 and 3 respectively. Fermi level, vacuum level, core level region, valence band region, barrier potential V_0 and work function W are indicated.

state in the solid) by absorbing the photon, (ii) the propagation of the excited electron to the sample surface, and (iii) emission of the electron from the surface into the vacuum, overcoming the surface barrier potential. The three steps are shown in the Figure 2.4. A brief description of the three steps of the photoemission will be given in the following sub-sections.

2.3.1.1 Photoexcitation

The electron in the initial state ψ_i with energy E_i will undergo a photoexcitation by absorbing a photon of energy $h\nu$ to the final state ψ_f, within the solid, with energy E_f such that

$$h\nu = E_f - E_i. \tag{2.34}$$

The transition probability for the transition is given by 2.29. The initial state is a bound state of the atom and can be represented as a linear combination of atomic orbitals (LCAO). The LCAO initial state is a convenient approximation that allows to describe several properties of photoemission spectra. These orbitals can be expressed as a product of a radial part, which depend on the quantum numbers n and l, and spherical harmonics,

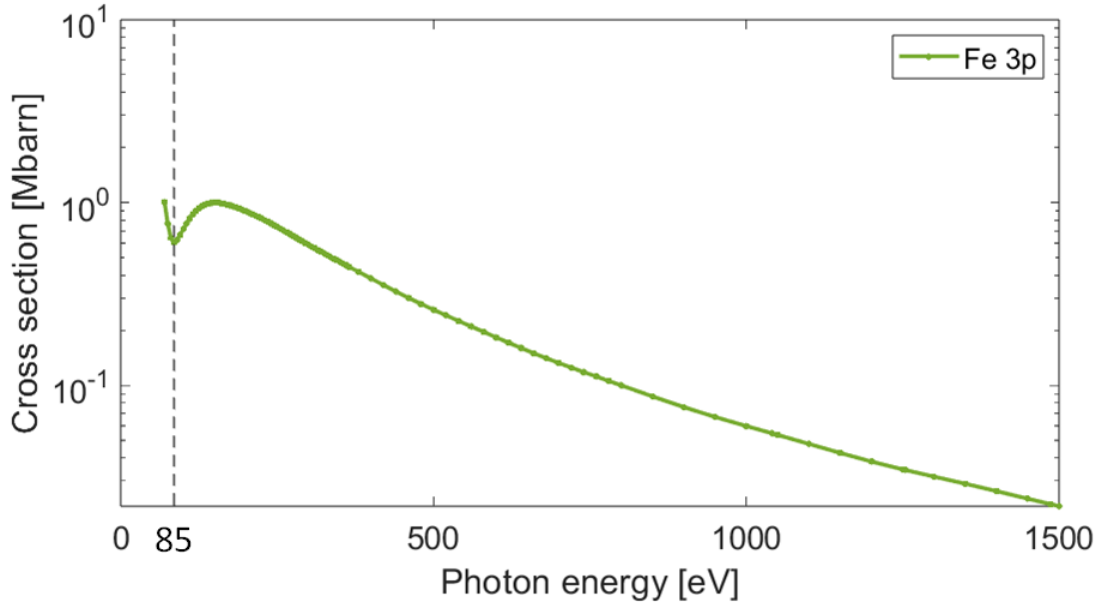

Figure 2.5: Figure shows photo ionization cross section of Fe $3p$ level at photon energies from 10 eV to 1500 eV. Cooper minimum of Fe $3p$ is marked by the vertical dotted line at $h\nu$ = 85 eV.

which depend on the quantum numbers l and m_l. Here n, l and m_l correspond to the principal, azimuthal (or orbital), and magnetic quantum numbers, respectively. The initial state is given by $\psi_i = \sum_{n,l,m_l} C_{n,l,m_l} R_{n,l}(\mathbf{r}) Y_{lm}$ and the transition matrix elements can be written as

$$W_{if} \propto \int \mathbf{R}^*_{n_f,l_f} r \mathbf{R}_{n_i,l_i} r^2 dr \int Y^*_{l_f,m_f} \vec{\epsilon}.\vec{r} Y_{l_i,m_i} d\Omega. \tag{2.35}$$

The radial part of the matrix element satisfies the normalization condition and are given as a function of associated Laguerre polynomial L and orbital radius a,

$$R_{n,l} \propto e^{-r/na} \left(\frac{2r}{na}\right)^l L^{2l+1}_{n-l-1}\left(\frac{2r}{na}\right). \tag{2.36}$$

The radial function has $n-l-1$ nodes [41]. When the wavelength of the photon matches the nodes of the initial state, it results in extremely low photoemission intensity, and these are called Cooper minima. Cooper minima occurs at specific photon energies, corresponding to when the photon wavelength matches the nodes of the initial state orbitals. In solids, these minima are broadened due to the hybridization of orbitals, which results in a wider range of energies where destructive interference can occur, smoothing out the sharpness of the minima observed in isolated atoms. Another effect is the decay of the radial cross section at higher photon energies, where the wavelength is small. The rapid sign change of the photon wave results in a reduced intensity [41]. As an example, the energy dependence of the photo ionization cross section of Fe $3p$ is shown in Figure 2.5. Fe $3p$ has a Cooper minimum at $h\nu$ = 85 eV.

The $\vec{\epsilon} \cdot \vec{r}$ term, in Equation 2.35, can also be represented in the spherical harmonic basis, as the polarization of light can be defined in the spherical harmonic basis with the two

$l+1$	$m+1$	$\sqrt{\frac{(l+m+2)(l+m+1)}{2(2l+3)(2l+1)}}$
	$m-1$	$\sqrt{\frac{(l-m+2)(l-m+1)}{2(2l+3)(2l+1)}}$
$l-1$	$m+1$	$-\sqrt{\frac{(l-m)(l-m-1)}{2(2l-1)(2l+1)}}$
	$m-1$	$-\sqrt{\frac{(l+m)(l+m-1)}{2(2l-1)(2l+1)}}$

Figure 2.6: Angular part of the photoemission matrix element for $C_{\pm}$ light. All the possible transitions allowed by the selection rules are shown.

orthogonal states, which are the right circular polarization (RCP) or C_+ light and the left circular polarization (LCP) or the C_- light. The C_+ and C_- light are defined as

$$\begin{aligned} \epsilon_{C_+} &= \frac{\epsilon_x + i\epsilon_y}{\sqrt{2}} \\ \epsilon_{C_-} &= \frac{\epsilon_x - i\epsilon_y}{\sqrt{2}}. \end{aligned} \tag{2.37}$$

Now, the $\vec{\epsilon} \cdot \vec{r}$ can be written as $\sqrt{\frac{4\pi}{3}}Y_{1,1}$ and $\sqrt{\frac{4\pi}{3}}Y_{1,-1}$ for C_+ and C_- light, respectively, and the linear light is given by $Y_{1,0}$ in the spherical harmonics. This shows that light itself carries an angular momentum with $l = 1$ and with the L_z values of +1,0,-1. By inserting Equation 2.37 in Equation 2.35 and using the Wigner-Eckart theorem, it can be shown that not all transitions that obey the condition Equation 2.34 occur. Light polarization plays an important role in photo excitation process and only certain transitions are quantum mechanically allowed. The allowed transitions are governed by the dipole selection rules, which are $\Delta l = \pm 1$ and $\Delta m = \pm 1/0$ for circularly polarized light (C_+ and C_-) and linearly polarized light, respectively. Therefore, transitions such as $1s \rightarrow 2s$ or $2p \rightarrow 3p$ are not allowed, even if they obey Equation 2.34. These dipole selection rules play an important role in circular dichroic ARPES measurements, which is the main technique used in this thesis. The angular part of the matrix elements corresponding to the allowed transition can be calculated analytically and are given in the table for C_+ and C_- light (see Figure 2.6).

2.3.1.2 Propagation

Once the electrons are emitted according to the dipole selection rules, the next step is the propagation of the electron to the surface. There are two different processes that

can occur during the propagation of the electrons. First is the inelastic scattering, in which the electrons loose their energy and the second is the elastic scattering, in which the energy and momentum of the electron are preserved. Inelastic scattering appears in the photoemission spectra as a broad peak at lower kinetic energy. Electrons in a solid are primarily scattered through electron-electron interactions, electron-phonon interactions, and interactions with defects. In the photon energy range typically used for photoemission measurements, electron-electron interactions are the dominant source of scattering. The electron-electron scattering cross section is given by

$$\frac{d^2\sigma}{d\Omega d\mathbf{E}} = \frac{\hbar^2}{(\pi e a_0)^2}\frac{1}{\mathbf{q}^2} Im\left(\frac{-1}{\epsilon(\mathbf{q},\omega)}\right), \tag{2.38}$$

where the $\mathbf{q}$ and $\mathbf{E}$ are related to the momentum and energy transfer in the scattering process and a_0 is the Bohr radius. From 2.38 we can say that the inelastic scattering is a material property through its relation to the dielectric function, $\epsilon(\mathbf{q},\omega)$.

One of the important parameters for the inelastic scattering is the electron escape depth or mean free path. It is the distance travelled by the electron before it gets scattered. The mean free path for various materials for different kinetic energies are shown in Figure 2.7. The data points approximately align along the so-called universal curve of the electron escape depth, with values being similar across different materials [42]. This is in contrast to Equation 2.38, where the mean free path depends on the dielectric function of the material that enters through the scattering cross section. The mean free path value of different materials are similar because of the kinetic energy that was considered in Figure 2.7. At the kinetic energies considered, the electrons approximately behave like free electrons and mostly the electron densities matter, which is almost the same for different materials.

Another important observation from the universal curve is the actual value of the mean free path. The mean free path is just few Å, which corresponds to one or two atomic layers. This makes photoemission spectroscopy an extremely surface sensitive technique. The sample surface needs to be clean without any contaminants. The accumulation of contaminant layer depends on the material, and can be quantified by the sticking coefficient, which is defined as the ratio between the number of molecules or atoms sticking to the sample surface and the total number of particles hitting the surface. At ambient conditions it only takes few ns to form one monolayer of contaminants, assuming the sticking coefficient equal to 1 [38]. Therefore, a pressure of at least 10^{-10} mbar is required for good quality measurements.

The elastic scattering modulates the intensity of the bands, without any change in the kinetic energy. The elastic scattering plays an important role in the photoemission intensity, and is crucial in the analysis of the CD-ARPES spectra. These elastic scattering is also used in core level photoelectron diffraction for structure determination. Elastic scattering will be discussed in detail in Chapter 5.

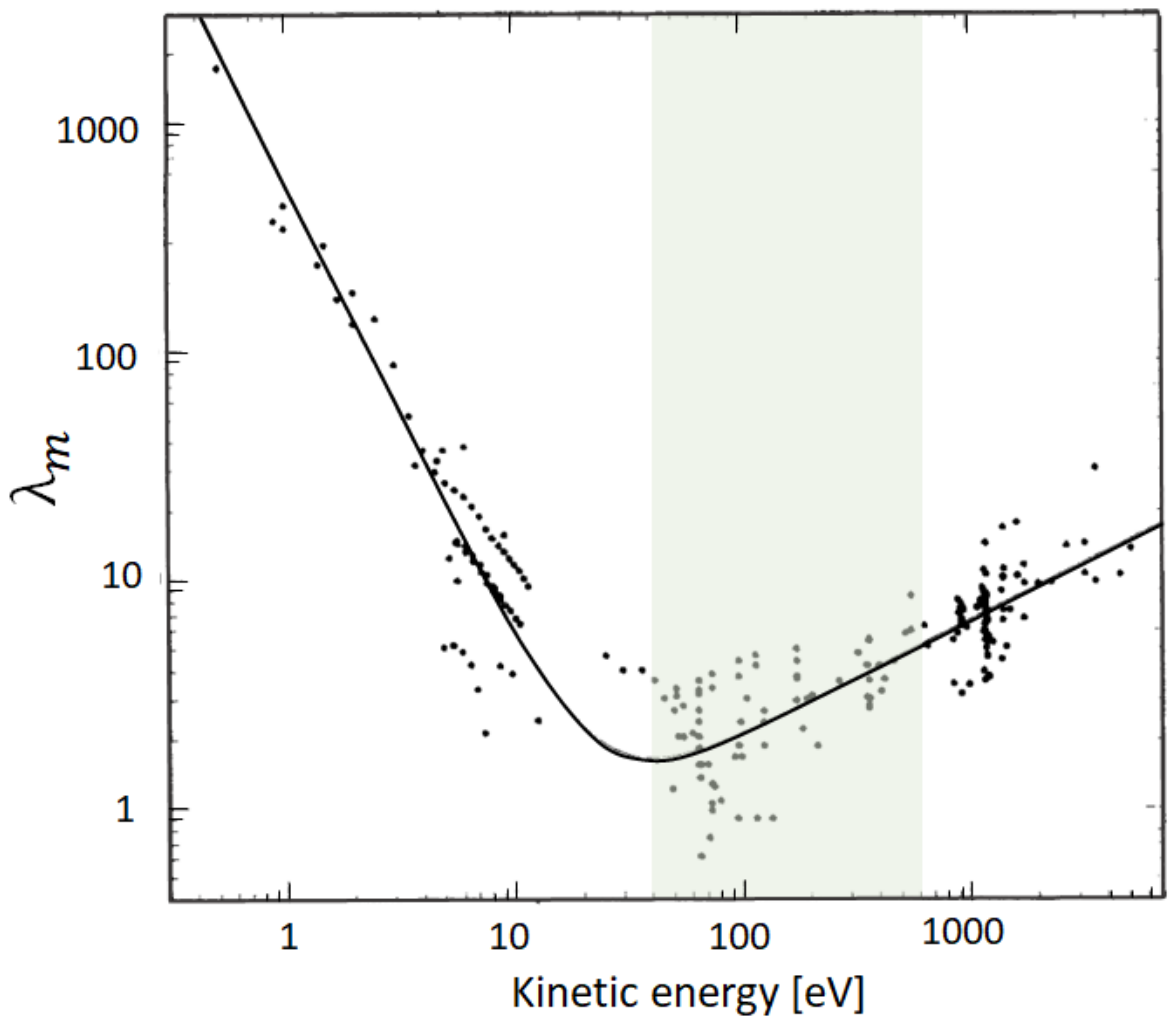

Figure 2.7: The universal curve of inelastic mean free path versus kinetic energy. The kinetic energy range used for the measurements in this thesis is indicated in the shaded region. The mean free path is less 10 Åfor the kinetic energies considered in this thesis. Data taken from [42].

2.3.1.3 Transmission

The final step is emission through the surface into the vacuum. For the electron to come out of the sample, it has to overcome the surface potential barrier, ϕ_0, and due to this inner potential, only electrons with energies greater than the inner potential will come out of the sample. The maximum kinetic energy the electron can have is given by the Equation 2.25. The kinetic energy of the electron is related to the binding energy, E_{bin}, of the electron in the solid and is given by

$$E_{kin} = h\nu - E_{bin} - \phi_0. \tag{2.39}$$

The surface potential is usually considered as a step function and is given by

$$V_0(\mathbf{r}) = \begin{cases} V_0 & \text{if } r_\perp < 0 \\ 0 & \text{if } r_\perp > 0. \end{cases} \tag{2.40}$$

In reality, the potential is a function that varies smoothly near surface as shown in Figure 2.4. The diffraction of the electron results in a larger angle of emission outside the sample compared to the angle inside the sample. This means there is maximum angle θ', which is less than 90°, and electrons emitting with $\theta > \theta'$ will be reflected back into the sample [38]. Therefore we can define a cone called the escape cone (shown in Figure 2.8), which represents all the angles of the electrons that can escape the sample without being back reflected. The momentum of the electron is not conserved because of the barrier potential. The in-plane periodicity ensure the parallel momentum conservation and it is the perpendicular component of the final momentum which suffers reduction due to the potential barrier. The parallel, $\mathbf{k}_{f\parallel}$, and perpendicular, $\mathbf{k}_{f\perp}$, momentum components (shown in Figure 2.8) are given by

$$\begin{aligned} \mathbf{k}_{f\parallel} &= \mathbf{k}_{i\parallel} \\ \mathbf{k}_{f\perp} &= \mathbf{k}_{i\perp} - 2m_e V_0. \end{aligned} \tag{2.41}$$

A typical ARPES experimental geometry is shown in Figure 2.9. The parallel and perpendicular momentum is related to the emission angles θ and ϕ, as labelled in the Figure 2.9. From the geometry, the x, y, z components of the momentum are determined as $\sqrt{2m_eE_{kin}}sin\theta cos\phi$, $\sqrt{2m_eE_{kin}}sin\theta sin\phi$, and $\sqrt{2m_eE_{kin}}cos\theta$, respectively. From the relation $\mathbf{k}_\parallel = \sqrt{p_x^2 + p_y^2}$ and $\mathbf{k}_\perp = \sqrt{p_z^2 + 2m_eV_0}$, the equations for $\mathbf{k}_\parallel$ and $\mathbf{k}_\perp$ are obtained as

$$\begin{aligned} \text{mod } \mathbf{k}_\parallel &= \sqrt{2m_eE_{kin}}sin\theta \\ \text{mod } \mathbf{k}_\perp &= \sqrt{2m_eE_{kin}cos^2\theta + V_0}. \end{aligned} \tag{2.42}$$

The parallel component of the momentum are calculated from the angle of emission and the kinetic energy obtained from the ARPES measurements. The energy versus parallel momentum graphs are obtained from the ARPES, resulting in the band structure of the solid. The precise determination of perpendicular component requires an accurate value of inner potential, V_0.

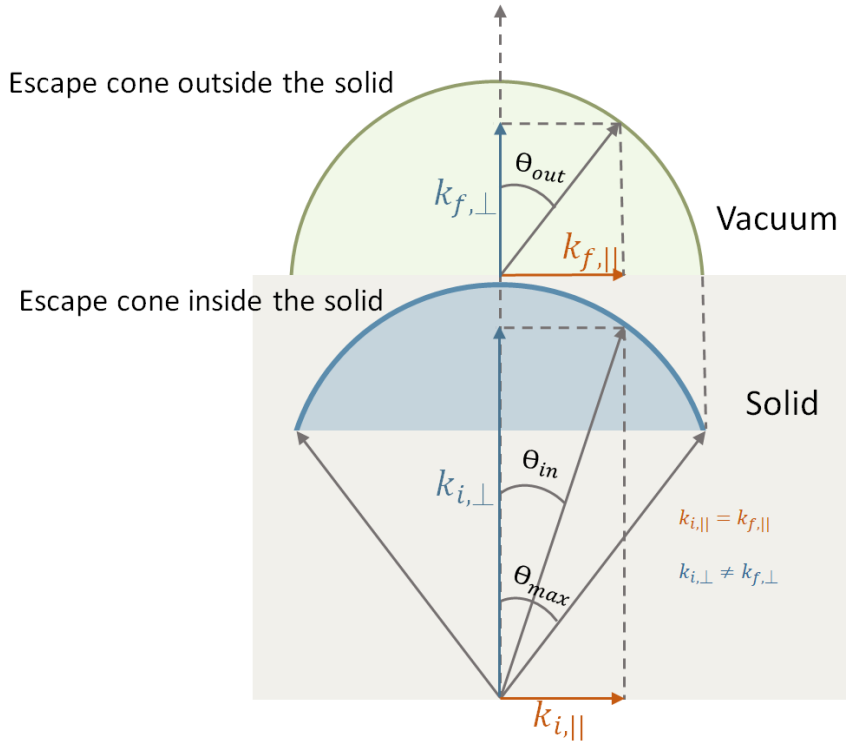

Figure 2.8: (a) shows the schematic diagram of the escape cone inside and outside the solid [38]. The Figure shows the parallel and perpendicular components of the momentum **k**. The diffraction of the electron through sample surface is shown. The parallel momentum is conserved in the process due to the in-plane periodicity.

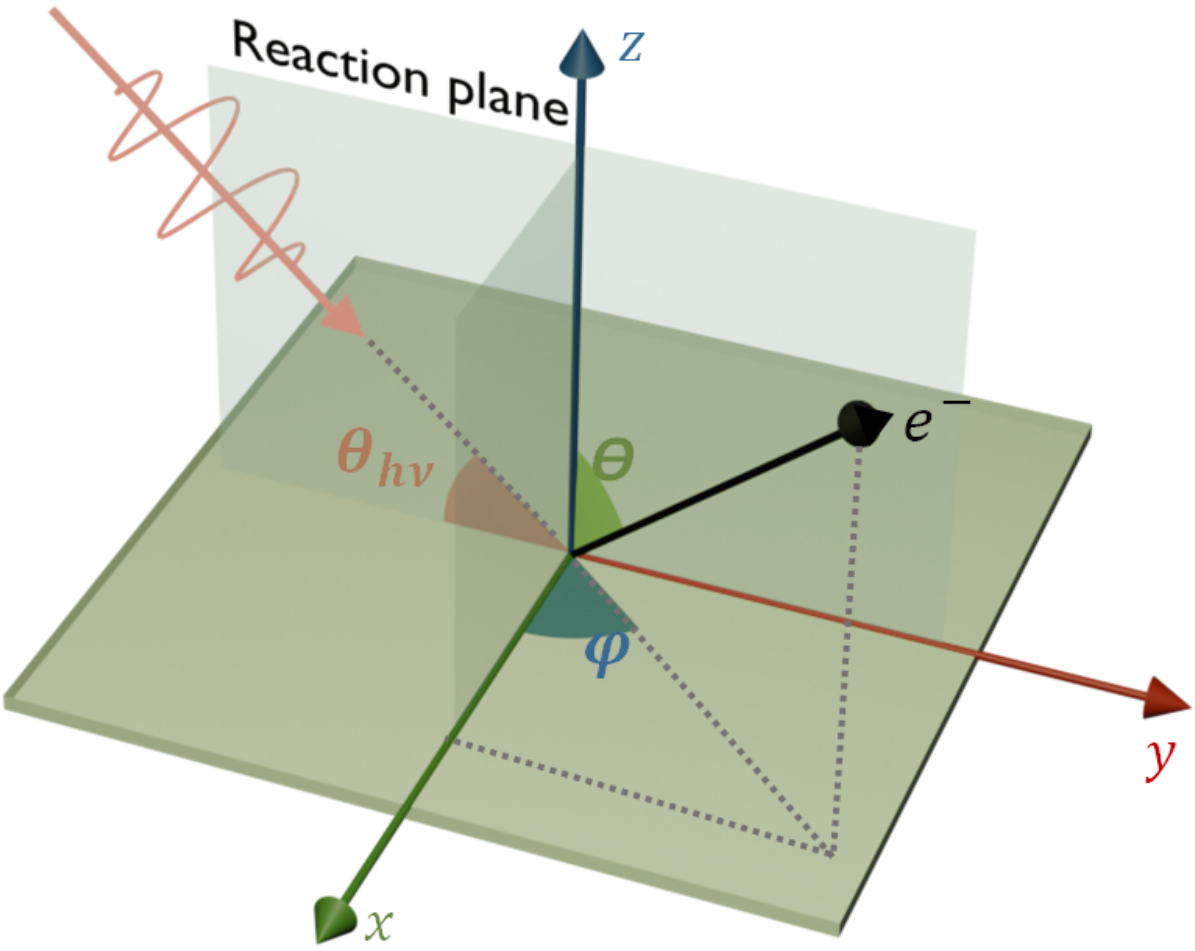

Figure 2.9: Schematic diagram showing the ARPES geometry. The angle of emission (θ and ϕ) are shown.

2.3.2 One step model

Although the three-step model provides a simplified understanding of the photoemission process, it often lacks details and is generally insufficient for comparing with experimental results. The main concept of dividing the process into three steps makes it incoherent, and thereby collapsing the wavefunction in each step, resulting in loss of information from the interference that happen between the different possible channels. As discussed earlier, the multiple scattering that could result from the neighbouring atoms and from the potential barrier is not included in the three step model. Therefore, a more accurate theory is required to understand the experimental spectra.

One step model provides a more realistic description of the photoemission process [43]. Here, the photo excitation, propagation to the surface and transmission through surface are considered coherently. The transition matrix element effects and multiple scattering events will modify the experimental intensity. These are included in the one step model calculations. The multiple scattering in the final state is same as the time reversed low energy electron diffraction (LEED) states. In the LEED measurements the sample is probed with electron beam, and the electron upon entering the sample experiences multiple scattering. When the time is reversed in the LEED measurements, the process is same as the photoemission process.

One step model can be used for a quantitative description of the photoemission spectra. One of the biggest advantages is that the effect of dipole selection rules, which is related to the photoemission intensity through the transition matrix elements, can be studied using this model and is very important for the CD-ARPES studies. The final state of the photoemission process is described using the partial wave expansion to include the effects of scattering and to study the dichroism originating from the multiple scattering. This will be discussed in detail in Chapter 5.

3 Experimental setup

In this chapter, a brief description of the experimental setups, namely a conventional ARPES setup and a momentum microscope, as well as the different light sources used for the measurements will be provided. A brief description of synchrotron radiation, which is produced by accelerating electrons in a storage ring, that was used for all the ARPES measurements, will be provided. Apart from the electronic band structure measurements, magnetic domain structure mapping were performed using photoemission electron microscopy (PEEM) technique. This will be discussed towards the end of the chapter.

3.1 Ultra high vacuum

For photoemission spectroscopy, one of the prerequisite conditions is the ultra high vacuum (UHV). For photon energies in the UV-visible range, the inelastic mean free path of electrons is around 10 Å [42]. This implies that electrons emitted from deeper layers will undergo inelastic scattering, contributing to a background at lower kinetic energies. Only the electrons from the topmost layers that do not undergo inelastic scattering will contribute to the band structure. Therefore, ARPES requires atomically clean sample surfaces, along with periodicity and low defect density, to produce sharp bands. Contamination depends on the material being measured and is determined by its sticking coefficient, which is given by the probability that a molecule is absorbed on the sample after a collision. In ambient conditions, sample surface becomes rapidly contaminated and a monolayer of contaminant is formed on a ns time scale [38]. Another problem is with highly reactive samples, which get oxidized in the air. Most of the magnetic 2D samples belong in this category [44, 45] and it is virtually impossible to measure them without a good vacuum.

The time required for contaminants to form on the sample surface can typically extend to a few hours if the pressure is in the range of 10^{-10} mbar. However, this duration is highly sample-dependent. For example, some surfaces like WSe_2 can remain stable for several days, whereas others like Fe can become contaminated within a few hours even at 10^{-10} mbar. The stability of the sample also depends on the composition of the residual gas in the chamber, for instance, H_2 molecules are always present and cannot be completely removed.

A typical ARPES system consists of a load lock chamber, a preparation chamber, and a main chamber. The load lock chamber is where all the samples are loaded, the preparation chamber is where the samples are cleaved and prepared for the ARPES measurements,

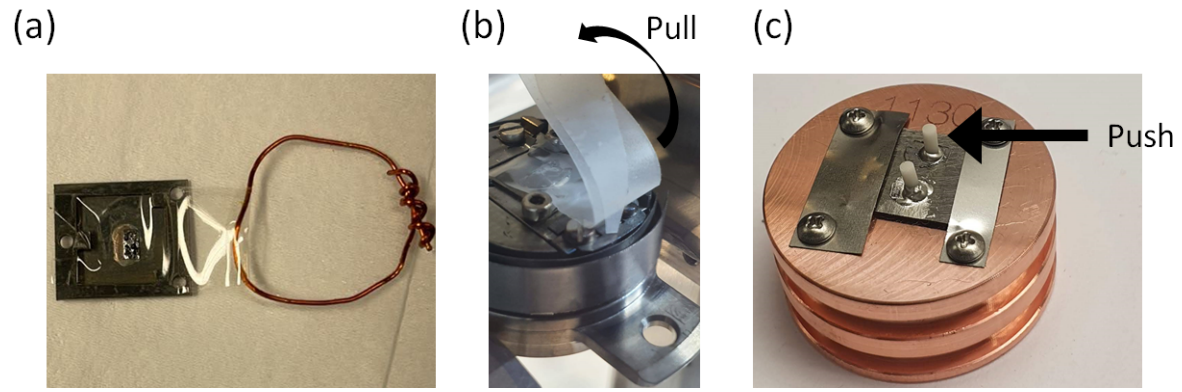

Figure 3.1: Bulk single crystal samples glued on Mo plates using silver epoxy and prepared for cleaving (a) and (b) with scotch tape and (c) with ceramic posts.

and the main chamber is where the photoemission measurements are performed. The load lock, preparation chamber and main chamber are separately pumped using ion pumps and turbo-molecular pumps. Additionally, the turbo-molecular pumps in the preparation and main chamber are pre-pumped to achieve the required pressure. Whenever there is a leak or whenever part of the chamber is vented, the chamber needs to be baked at $\approx 150^{\circ}$ for several days, to remove water and hydrocarbons, adsorbed on the chamber walls. The main chamber is also usually equipped with titanium sublimation pump (TSP) to further pump the adsorbed molecules, such as H_2 molecules which are difficult to pump, that have been attached to the chamber walls. On top of this, everything that is inserted into the vacuum chamber should be handled with gloves to minimize any chance of oil, grease or other particles from entering the chamber.

Samples are loaded into chambers through the load lock, where the pressure is maintained around 10^{-8} mbar. As the load lock chambers are vented frequently for loading the sample, these chambers are designed to be small in volume to reduce the pumping time. When the samples are exposed to air, they require additional cleaning in the ultra high vacuum (UHV) for successful ARPES measurements. The bulk single crystal samples are typically cleaved in the UHV using a scotch tape or ceramic posts (shown in Figure 3.1) to remove the contaminated topmost layer. Cleaving is usually performed in the load lock or in the the preparation chamber in most of the synchrotrons, and will be immediately transferred to the main chamber for ARPES measurements. Thin film samples are either directly transferred from the growth chamber to the ARPES chamber using a vacuum suitcase or are capped with a protective layer, such as Se or Te, which can then be uncapped by annealing or sputtering in the preparation chamber. Similarly, reactive exfoliated flake samples are encapsulated with monolayers of graphene or hBN and are annealed for few hours above 100°C, depending on the material, to get rid of the adsorbed water molecules and hydrocarbons. The sample preparation techniques mentioned above are the main ones used in this thesis; however, many other techniques are also available.

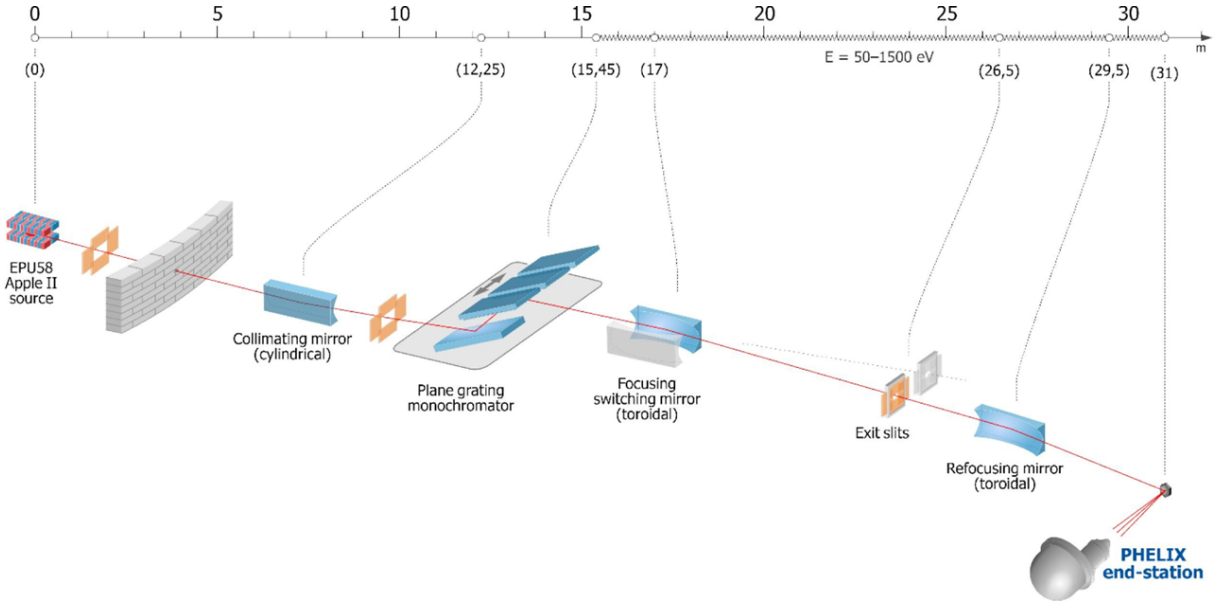

Figure 3.2: Beamline optics at PHELIX endstation at SOLARIS synchrotron. The elliptically polarized undulator, entrance and exit slits, plane grating monochromator and focusing mirrors are shown. Adapted from [46]

3.2 Light sources

Once the sample is prepared, it is transferred from the preparation chamber to the main chamber, where measurements are taken. In the main chamber, the sample is probed with a photon source, which induces the emission of electrons. Since the primary focus of the study in this thesis is to determine the orbital angular momentum character of the bands, switching the polarization and the energy of the photon source is of primary importance. This is possible at selected beamlines at various synchrotron facilities around the world. Depending on the beamline specifications, such as the beam spot size, experimental geometry, and photon energy range available, different beamlines were chosen for measurements on bulk single crystal and 2D heterostructure samples in this thesis.

At synchrotron laboratory, photons are produced by radially accelerating electrons in the synchrotron storage ring. The radiation is produced by bending magnets and undulators [47]. There are various optical components in between the undulator light source and the experimental end station. A schematic diagram of the optics at the PHELIX beamline, SOLARIS, is shown in Figure 3.2. The most commonly used undulator is APPLE II undulator [48]. It is made up of four arrays of magnets, which when moved relative to each other in parallel or anti parallel combinations, produce linear, circular or elliptical polarizations. At the PHELIX beamline at SOLARIS, the beam from the undulator then passes through a slit, which acts as an aperture to remove unwanted radiation. The beam is subsequently collimated using a cylindrical mirror and moves to the monochromator. A monochromator is used to isolate photons of a fixed energy. The main component of monochromator is a diffraction grating. After the monochromator, the beam is focused using different sets of toroidal mirrors before reaching the end station. This results in a

high intensity beam of flux around 10^{12} photons/s. All the optics mentioned above are placed in vacuum and are mechanically stabilized to avoid any vibrations of the beam. At the PHELIX beamline, the mirrors are usually coated with metals such as Pt to improve the reflectivity [46]. Diffraction gratings are also coated with different metals depending on the photon energy range, to improve the reflectivity of the beam.

Exfoliated flake samples, which are usually few microns in size, require focused beam spot. Focusing the beam spot to micrometer size requires special focusing optics, which will produce few μm^2 or even sub-μm^2 sized beam spots. There are three different optics types used for focusing the beam, namely Kirkpatrick–Baez (K-B) optics [49], capillary optics [50] and Fresnel zone plate (FZP) [51] (shown in Figure 3.3). The K-B optics contain two elliptically shaped mirrors, one for the horizontal focusing and the other for the vertical focusing. This will result in a beam spot of size down to few μm. The capillary optics consist of one or many small glass capillaries with reflecting inner surface. The beam will undergo single or multiple internal reflections in the elliptical or cylindrical shaped inner surface of the capillaries [52], respectively, and finally focus on the sample position. Capillary optics can produce sub-micron sized beam spot. FZP consist of a plate with several concentric rings made of opaque and transparent surfaces or of two materials with different refractive indices. The photon beam will undergo diffraction and will constructively interfere at the focal point when the number of rings in the zone plate is large enough. The beam can be focused to few nanometers in this case [53]. In a FZP, the focal point depends on the wavelength of the light used, which helps to prevent unwanted wavelengths from hitting the sample. Although a zone plate can achieve the smallest beamspot possible, enabling precise probing of flake samples, the flux is relatively low, requiring longer probing times to accumulate sufficient data. Another disadvantage of FZP is its limitation when changing photon energy, as it often only supports one or two specific photon energies.

Apart from the synchrotron light sources there are vacuum ultraviolet discharge lamps, that use gases such as He, Xe, Kr, etc., primarily for *lab based* (that is not synchrotron based) ARPES systems [54, 55]. In the discharge chamber with high electric field, the atoms will be ionised forming plasma, where excited electrons while recombining with the atoms emit photons. In modern setups, the photon beam is then focused using a toroidal mirrors or capillary. Another *lab based* light source is based on Ti:Sapphire LASER, which produce light of wavelength ~ 800 nm. This photon beam passes through non linear crystals, like beta barium borate (BBO), which will double the frequency. This process is repeated twice, which will finally result in an energy of $h\nu = 6$ eV (λ=200 nm) [56]. One advantage of Ti:sapphire LASER is that the light is not absorbed by air and does not require vacuum, which makes it easier for alignment. Additionally, LASER produces highly intense photon beams and can be focused to few micron beam spot [57], making measurements on exfoliated flake samples in lab based ARPES setups possible. Similarly, 7 eV LASER photon energy and 11 eV LASER photo energy are also used for ARPES measurements [58, 59]. Apart from the continuous wave LASERs, pulsed LASERs are used for time-resolved ARPES studies [60–62].

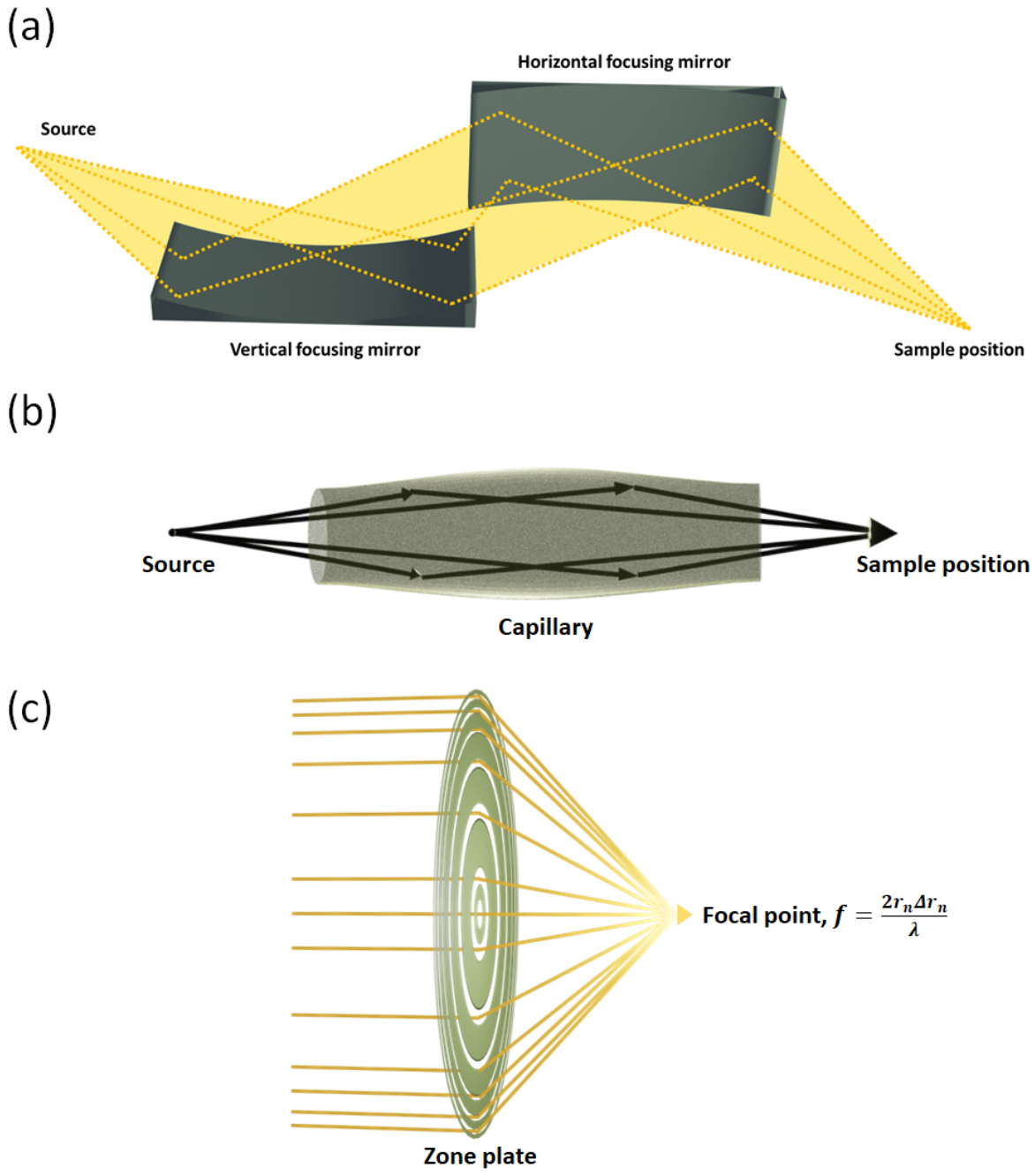

Figure 3.3: (a) K-B optics, (b) capillary optics and (c) Fresnel zone plate

3.3 Analyzer

The core of the ARPES setup is the electron analyzer. The most popular designs are the conventional hemispherical analyzer and the momentum microscope. The results in this thesis include measurements from both of these setups at various synchrotrons.

3.3.1 Conventional hemispherical analyzer

The conventional hemispherical analyzer contains of an electrostatic lens, a capacitor hemispherical analyser, a multichannel plate (MCP) electron detector and CCD camera, to image the electrons (shown in Figure 3.4). The main chamber, where the photoemission

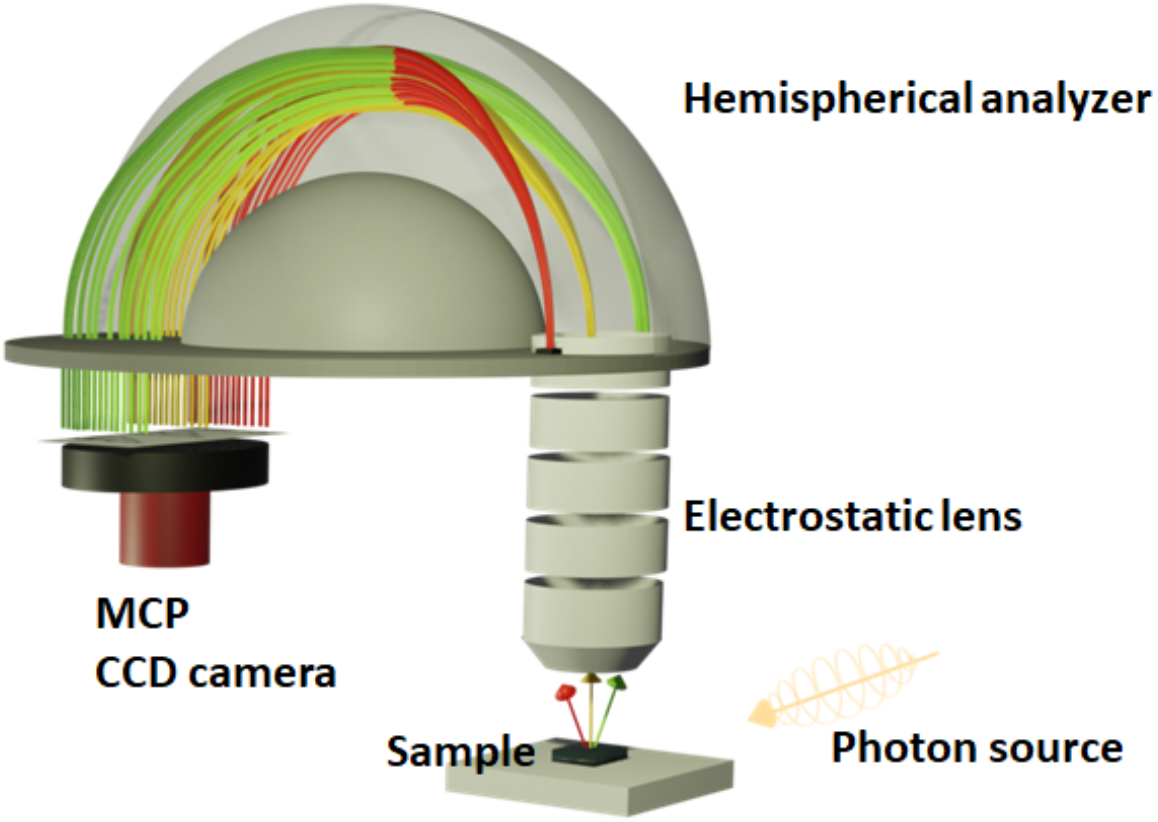

Figure 3.4: Schematic diagram of conventional ARPES setup. The photon incidence, sample position, electrostatic lens, hemispherical analyser, multichannel plate and CCD camera are labelled.

process happen, is usually made out of μ metal or stainless chamber with μ metal shield inside, which is used to shield the emitted electrons from the influence of any magnetic field. The μ metal is a composition of 75% of nickel and 15% of iron along with composites of copper and molybdenum. This material has very high magnetic permeability and therefore reduces the influence of external magnetic field, including the geomagnetic field.

Depending on the lens settings, the emitted electrons are collected by the lens as a spatial or angular image (shown in Figure 3.5). After passing through the electrostatic lens, the electrons reach the analyzer slit of the hemispherical analyzer. The angular acceptance is usually ±15° along the slit direction. In a deflector scan the electrons emitted in the direction perpendicular to the entrance slit is captured by rotating the lens perpendicular to the entrance slit. This will allow to measure the 3D band structure (Energy versus k_x versus k_y). The deflector scan will allow an angular acceptance of ± 15° perpendicular to slit, which demands no rotation of the sample, which if not the case, might move the

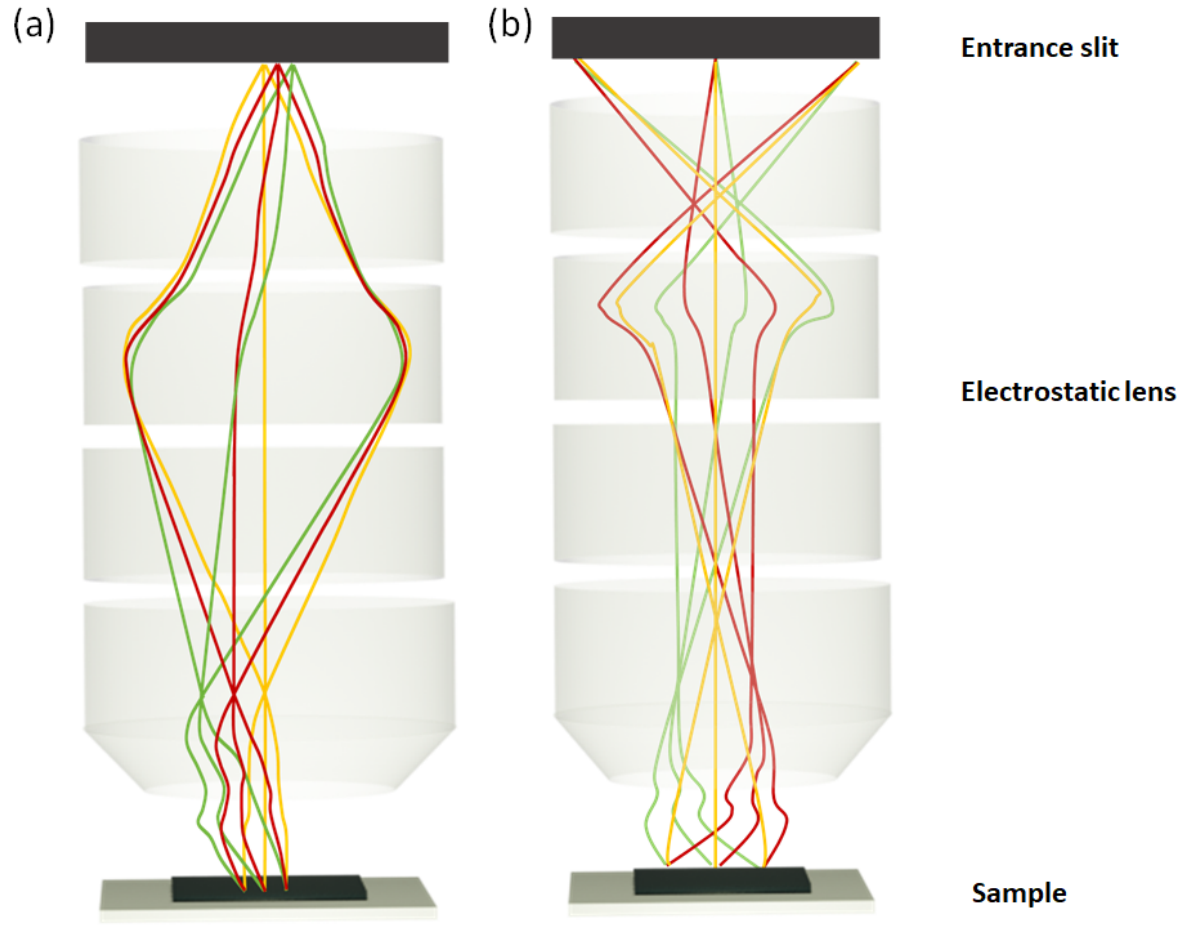

Figure 3.5: Schematic diagram of electron trajectory is an ARPES measurement showing (a) angular mode and (b) spatial mode.

sample spot that is being measured. The electrons are typically retarded down to the pass energy (E_{pass}) between the sample and the entrance slit. The electrons are retarded by applying a voltage between the sample and the entrance slit, corresponding to the E_{pass}. The E_{pass} determine the energy of the electrons that reaches the detector, only electrons within the energy range of 8.7% - 10% of E_{pass} will be transmitted through the hemispherical analyzer, depending on the analyzer used. A constant potential is applied between the inner and outer hemispheres of the analyzer which act like a capacitor. Once the electrons enter the analyzer, the electrons of energy higher than 8.7% - 10% of E_{pass} hit the outer hemisphere of the analyzer and the electrons with energy less than 8.7% - 10% of E_{pass} hit the inner hemisphere (see Figure 3.6). The electrons within the energy range of the E_{pass} are the only electrons that reach the analyzer. In the angular mode settings, an energy versus angular image is formed at the exit slit of the analyzer. These electrons then reach the MCP, where they are multiplied. The electrons from the MCP are accelerated towards the phosphor screen, which emit photons when hit by the electrons. The phosphor screen is photographed by a CCD or CMOS camera. In the angular mode of measurement, the angle of emission is approximately linearly proportional to the position along the slit. While analyzing the angular image, the angle of emission is finally converted

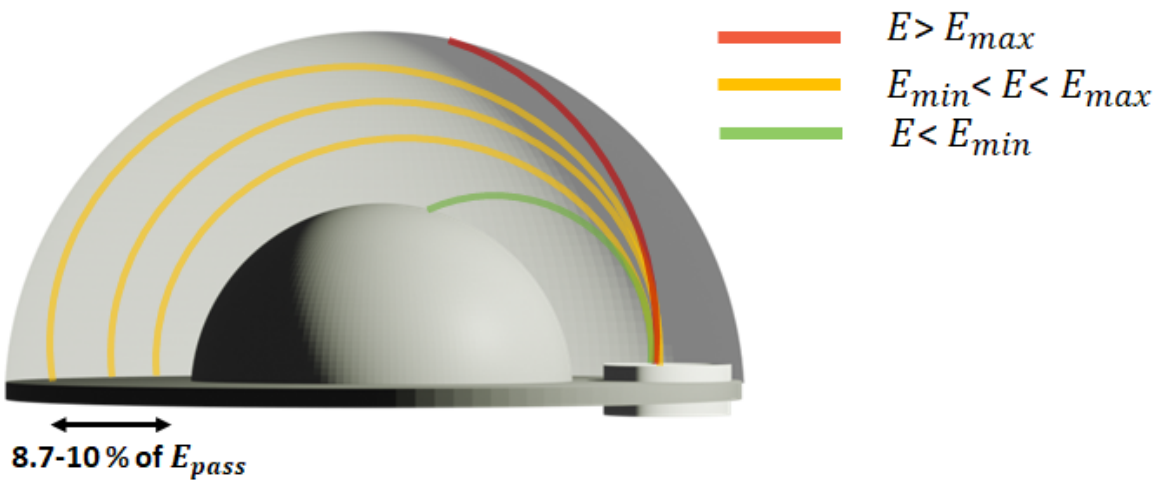

Figure 3.6: Schematic diagram of electron trajectory is an ARPES measurement. Red indicates trajectory of electron with energy greater than 10% of E_{pass}, yellow indicates trajectory of electron with energy within 10 % of E_{pass} and green indicates trajectory of electron with energy less than 10 % of E_{pass}.

to the $k_{||}$ using the relation

$$k_{||} = 0.512\sqrt{E_{kin}}sin\theta. \tag{3.1}$$

By sweeping the voltage between the sample and the analyzer, a wide-range kinetic energy scan can be performed.

Another important factor to be considered is the energy resolution of the analyzer. The spectrometer resolution is given by the relation [63]

$$\Delta E_A = E_{pass}\left(\frac{w_0}{2R_0} + \frac{\alpha^2}{2}\right) \approx \frac{E_{pass}[eV]\cdot w_0[mm]}{R_0[mm]}. \tag{3.2}$$

The resolution depends on the E_{pass}, the slit width (w_0) and on the average radius of the hemisphere ($R_0 = \frac{R_1+R_2}{2}$). α is the angular acceptance of the entrance slit. With low E_{pass} the energy width is small ($\approx 10\%$ of E_{pass}) and therefore the dispersion in energy is large, resulting in high resolution. The slit width is adjusted to maximize the resolution and counts. The energy resolution also depends on other factors such as the band width of photon, thermal broadening, etc., which will also be limiting the total resolution.

3.3.2 Momentum microscope

Momentum microscope is another experimental design for measuring band structure [64]. The key difference between the conventional hemispherical analyzer and momentum microscope is that, in momentum microscope, the the constant energy $k_x - k_y$ cuts are measured and cover entire half momentum space at lower photon energies. The image scale in momentum microscope images are proportional to the $k-$scale. Additionally, the

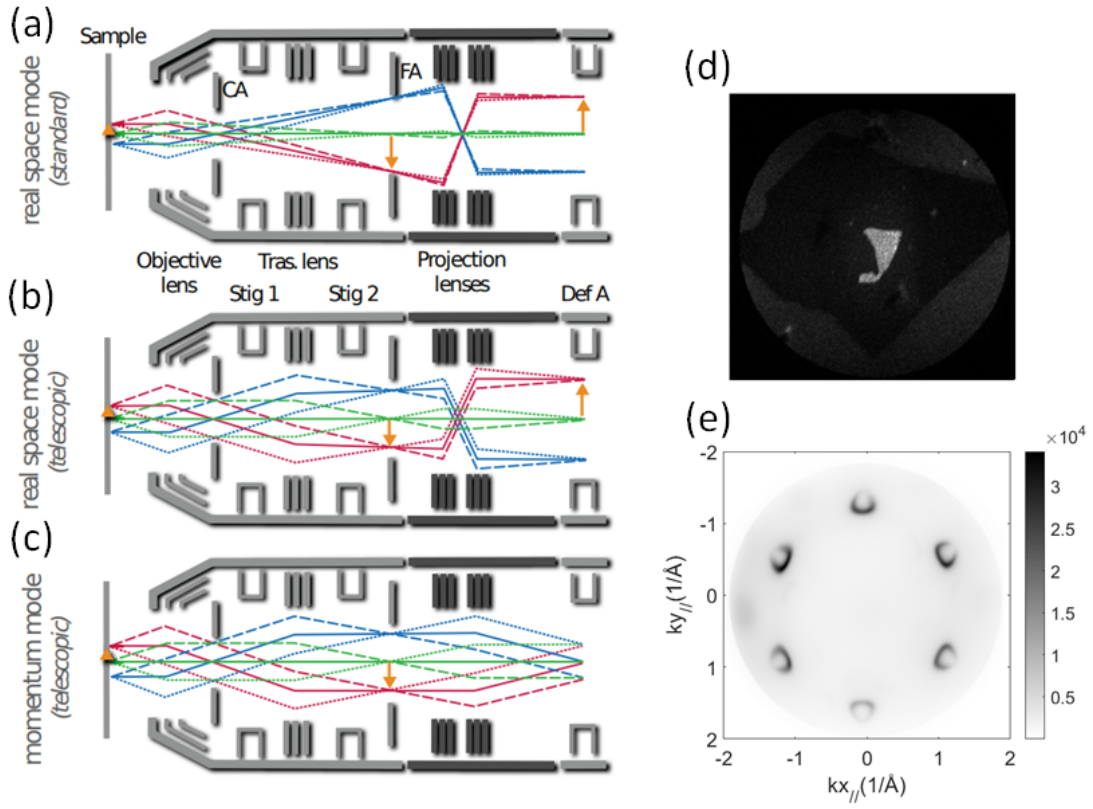

Figure 3.7: (a) Schematic diagram of electron trajectory is momentum microscope in momentum space mode (a-b) and real space mode (c) (adapted from [65]. (d) shows the real space PEEM image of Fe_3GeTe_2 encapsulated flake measured at NanoESCA beamline at Elettra. (e) shows the Fermi surface of graphene at E_B = 1.25 eV, measured in the momentum space mode at NanoESCA beamline at Elettra.

momentum microscope offers high spatial resolution and can also be used in PEEM mode. In this thesis, the momentum microscope at NanoESCA beamline, Elettra, was used in both k–space mode, for Fermi surface maps and in PEEM mode, for domain structure mapping.

The electron trajectory in momentum microscope in momentum space mode and real space mode are shown in Figure 3.7 (a-c). The NanoESCA, which is an example of momentum microscope, consists of an objective, two projective lenses, two hemispherical analyzers, a channeltron, and a 2D image detector. A schematic diagram of the scheme of NanoESCA is shown in Figure 3.8. The objective applies a high voltage (in keV range) between the sample and extractor to extract all the photoelectrons emitted into the half sphere above the sample. A spatial image is formed at the focal plane and a reciprocal image is formed at the back focal plane of the objective (see Figure 3.7 (a)). In the PEEM mode, for high spatial resolution and to reduce aberrations, the electrons with higher angles are cut off by the *contrast aperture*, which is placed at the back focal plane of the objective, see Figure 3.7 (a). Similarly, in the k-space mode, the dimension of real

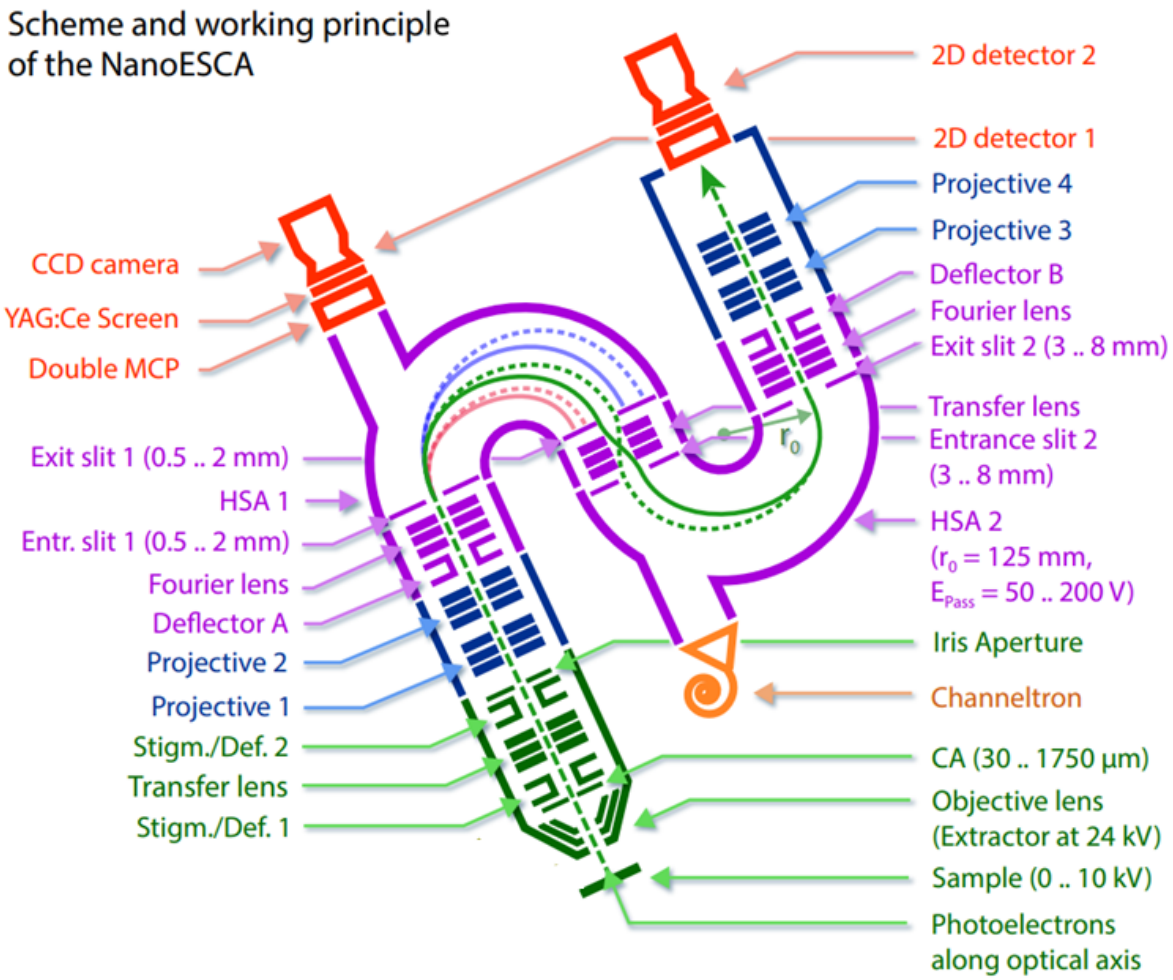

Figure 3.8: Schematic diagram of the layout of different components of NanoESCA, an example of momentum microscope. The objective lens, projective lens, two hemispherical analyzers, channeltron and 2D image detector are shown in the Figure. The Figure is adapted from [65].

space from where the electrons are collected can be reduced by closing the *iris aperture*, which is placed at the focal plane of the objective (shown in Figure 3.7 (c)). This allows to choose the spot on the sample which shows sharp features in the band structure and is extremely important for smaller or in-homogeneous samples. For the measurements on the flake samples in this thesis, the iris was closed to 5×5 μm, as the sample size was of the order of 10 μm^2 and as the beam spot at NanoESCA is approximately $15 \times 20 \mu$m.

Switching between real-space and momentum-space imaging modes is achieved by adjusting the lens voltages. The projector lens serves to project either a real-space or reciprocal-space image onto the first 2D detector, depending on the applied voltages. Specifically, the lens system directs the selected image (real or reciprocal) to the entrance slit of the energy filter. In PEEM mode, without energy filtering, the projector lens focuses the real-space image onto the 2D detector, with major contribution coming from secondary electrons.

After the first projector lens, the electrons enter the energy filter. The main use of the second hemispherical analyzer is to reduce the aberration for high resolution spatial image. The energy resolution is the highest after passing through the first hemispherical analyzer. The resolution of the momentum maps can be increased by using low E_{pass}, like 50 eV, giving a total resolution of 100 meV. This resolution is sufficient for the band structure study of many materials. The electrons after the energy filtering enter the imaging column. The real space image or the reciprocal image is then projected on the 2D detector, which consists of a MCP and a Cerium-doped Yttrium Aluminum Garnet (YAG:Ce) screen for imaging the electrons. As discussed earlier, when the electrons hit the MCP, each electron produces a bunch of electrons. These electrons from the MCP get accelerated to YAG:Ce screen, where the incident electrons produce photons. In momentum microscopy, the momentum image coordinates are directly proportional to $k_x - k_y$ units, eliminating the need for converting angles to k-scale, unlike conventional lens systems.

In momentum microscopy, an energy dispersion curve is obtained by scanning the binding energy. At each binding energy, a $k_x - k_y$ map is captured to form a 3D data set, from which the Energy versus k maps can be extracted. The momentum space range probed scales with the voltage applied between the sample and the extractor. As the extractor voltage increases, the k-scale expands. However, the real-space image scale decreases with increasing extractor voltage. For k-space mapping, a typical sample voltage of 12 keV is applied, enabling measurements across a range of ± 2 Å^{-1} over the entire MCP image in reciprocal space, covering more than one Brillouin zone of most of the materials.

3.4 Experimental geometry

In ARPES measurements the experimental geometry plays an important role. The $\vec{\epsilon} \cdot \vec{r} |\psi_i\rangle$ term in the photoemission transition matrix depends on the light polarization type and direction [41]. In all the synchrotrons the light is incident at an angle when the sample surface normal is along the lens axis. This introduces additional asymmetries in the

photoemission maps.

The key is to setup the measurements such that these additional asymmetries are minimized, for example, by aligning the mirror plane of the crystal with the light incidence direction. This requires the sample to be properly oriented. Most of the synchrotron ARPES end stations are equipped with manipulators with six degrees of freedom, three translations along x, y and z, and three rotational degree of freedom, θ, ϕ and tilt (shown in Figure 3.9). For CD-ARPES, when the light is incident perpendicular to the sample

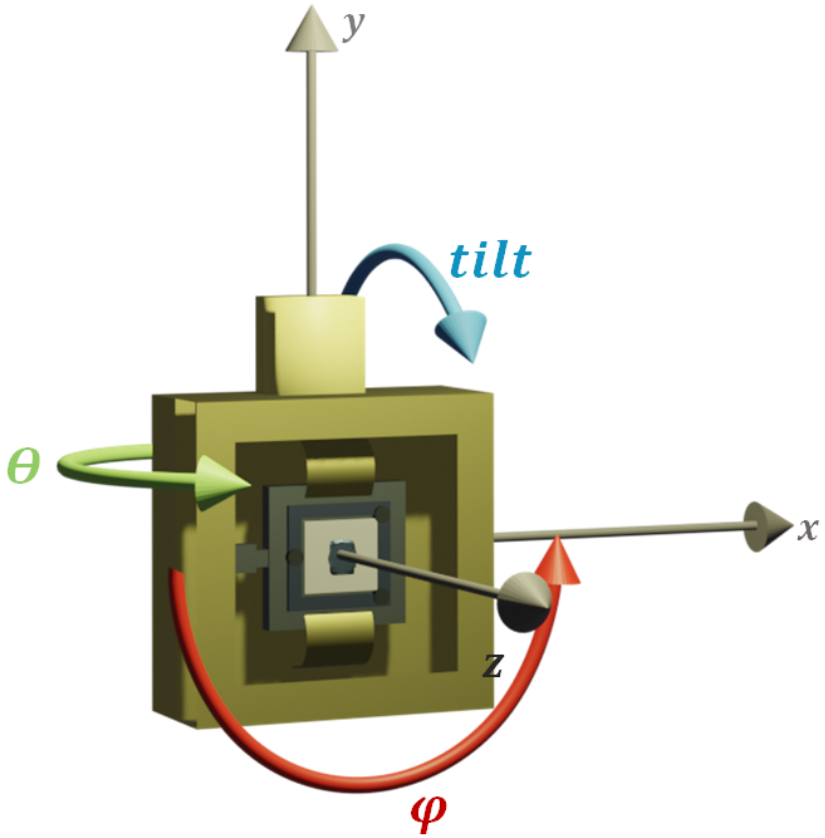

Figure 3.9: Schematic representation of a manipulator showing the sample with six degrees of freedom, the translational degree along x, y and z axis and the rotational degrees along x ($tilt$), y (θ) and z (ϕ) axis.

surface, less symmetries are broken. It is possible to rotate the sample towards the light incidence direction, using conventional hemispherical analyzers, which allow the sample to be aligned with the direction of light incidence. For most of the regular ARPES measurements, the sample normal is oriented along the lens axis. The experimental geometries at the NanoESCA beamline and at the PHELIX beamline, where most of the ARPES measurements in this thesis were performed, are shown in Figure 3.10.

Another important factor for most of the samples is the temperature of the measurement. The transition temperatures (T_C) of layered magnetic samples are often below the room

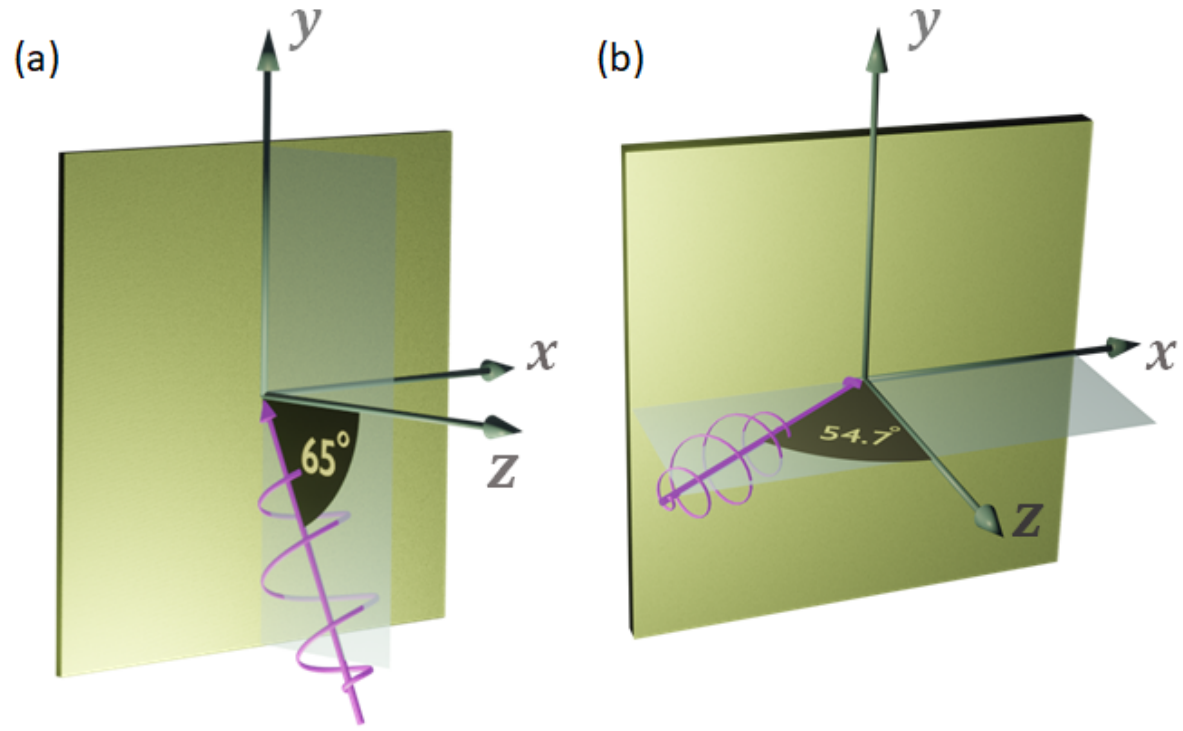

Figure 3.10: ARPES experimental geometry (a) at the NanoESCA beamline, Elettra and (b) at the PHELIX beamline, SOLARIS. In the cases, the sample surface normal is along the lens axis.

temperature. Therefore, measurements with cooling are needed to access the properties of the magnetic state. Most of the ARPES beamlines at synchrotrons offer manipulators with cooling. Depending on the beamline, the lowest sample temperature vary between 10 - 80 K, with liquid He cooling. The measurements with cooling also improves the energy resolution of the measurement, as at low temperature the thermal broadening in reduced. The thermal broadening of the bands is $\approx 4k_BT$, which is approximately 100 meV at room temperature.

All the measurements in this thesis were performed at synchrotron laboratories. The band structure measurements on bulk single crystal samples were performed at PHELIX beamline, SOLARIS, Krakow and high resolution branch of I05 beamline, Diamond Light Source, Oxforshire. The flake samples were measured at NanoESCA beamline, Elettra, Trieste, with KB optics where aperture plays an important role and MAESTRO beamline, Advanced Light Source, Berkeley, with micro-focusing capillary. Additionally, some of the measurements on the bulk samples were also performed at NanoESCA beamline. A summary of the beamline specifications is given in table 3.11.

Beamline	Focusing	Beam spot	Cooling	Photon energy	Light polarization	Light incidence
PHELIX, SOLARIS	Toroidal mirror	60 x 160 μm^2	LHe, LN	50–2000 eV	LH, LV, C_+ and C_-	54.7°
NanoESCA, Elettra	KB optics	7.2 x 3.5 μm^2	LHe, LN	5 – 1000 eV	LH, LV, C_+ and C_-	65°
MAESTRO, ALS (μARPES)	KB optics	< 10 x 10 μm^2	LHe	20 – 1000 eV	LH, LV, C_+ and C_-	Variable
MAESTRO, ALS (nARPES)	Capillary optics	1.5 x 1.5 μm^2	LHe	20 – 1000 eV	LH, LV, C_+ and C_-	Variable
I05, DLS (High resolution branch)	KB optics	50 x 50 μm^2	LHe	18 – 240 eV	LH, LV, C_+ and C_-	50°

Figure 3.11: Table shows selected specifications of PHELIX beamline, NanoESCA beamline, MAESTRO beamline (nARPES and μARPES) and i05 beamline.

3.5 PEEM at the DEMETER beamline, SOLARIS

As mentioned earlier, magnetic domain structure mapping measurements were also performed and the results will be discussed in Chapter 7. The PEEM measurements were performed at the DEMETER beamline, SOLARIS and at the NanoESCA beamline at Elettra. The light source at DEMETER beamline is an elliptically polarizing undulator, which can produce linearly and circularly polarized light. Following the undulator, there are several optical components to collimate, monochromatize and focus the beam. The beamline optics is similar to PHELIX beamline, shown in Figure 3.2 except that the focusing mirror before the monochromator is toroidal and mirror after the monochromator are cylindrical at DEMETER beamline. The PEEM endstation at DEMETER beamline is equipped with Elmitec LEEM/PEEM III (shown in Figure 3.12). It consists of an electrostatic lens, one hemispherical analyzer and an imaging column. The light is incident on the sample at an angle of 74° with respect to the surface normal. The photoelectrons emitted from the sample enter the transfer lens. The transfer lens corrects the image and transfers the real or diffraction image, depending on the lens mode, to the projective lens where the image is magnified. The electrons then pass through the entrance slit of the hemispherical analyzer for the energy filtering and reaches the imaging column. After passing through the imaging column, the electrons are detected and multiplied with MCP and are finally imaged and recorded using a CCD camera. The Elmitec at the DEMETER beamline is also equipped with LHe cooling, which makes it possible to map domain structure of samples with transition temperature below room temperature.

In this thesis, the PEEM microscope was used to study the domain structure of 2D magnetic material Fe_3GeTe_2. The measurements were performed using the X ray magnetic circular dichroism (XMCD) technique. The theory of XMCD and experimental details of the PEEM measurements will be provided in the Section 7.3.1 of Chapter 7.

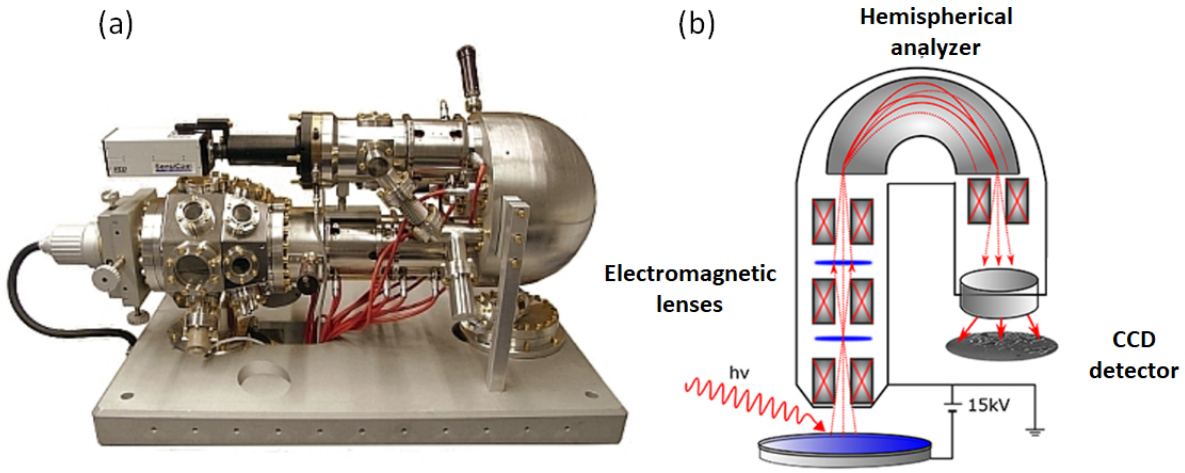

Figure 3.12: (a) shows Elmitec PEEM experimental setup. (b) shows trajectory of electrons in a PEEM apparatus. The hemispherical analyzer, electrostatic lens and detector are labelled in the schematic diagram. (a) is taken with permission from Elmitec website [66] and (b) is taken with permission from SOLARIS website [67]

.

4 Sample preparation

Characterizing monolayer and few-layer samples of technologically relevant materials is essential. Materials show different band structure features depending on the thickness of the sample. Examples are TMDCs such as MoS_2 and WSe_2, where the nature and size of band gap changes with the sample thickness [68]. In the monolayer limit, MoS_2 shows a direct band gap of 1.9 eV [69], while in the bilayer, the band gap value decreases to 1.6 eV [70]. In the bulk limit MoS_2 shows an indirect band gap of 1.3 eV [71]. Thickness-dependent studies are also important for magnetic 2D samples. In the magnetic 2D samples, for example in Fe_3GeTe_2, an increase in domain size is observed with decreasing thickness [72].

The initial monolayer of graphene was isolated through mechanical exfoliation using adhesive tape [2, 3]. This technique was later extended to the isolation of TMDC monolayers [73] and has since been extensively employed for the production of monolayers across a diverse range of materials. Exfoliation of flakes from bulk single crystal ensures high sample quality, which is important for ARPES measurements. ARPES measurements on easily oxidizing few layer samples are challenging. One of the well known examples is CrI_3, which rapidly oxidizes when exposed to air [74]. One way to measure these highly reactive samples is to use vacuum suitcase to transfer the samples to the ARPES chamber. However, this is not practical when the measurements are performed at synchrotrons. Another way is to encapsulate the few layer samples with air stable monolayers like graphene and hBN. The preparation of monolayer and few layer samples using mechanical exfoliation, the dry transfer technique, which was used for the stacking of the samples, as well as post-transfer cleaning of the sample will be discussed in this chapter in detail.

4.1 Mechanical exfoliation of 2D flakes

For the 2D heterostructure preparation, the initial step is to exfoliate the required flakes separately. There flakes are assembled to form the heterostructure in a later stage. Si wafers are the most commonly used substrate for exfoliation. The Si wafers used in this study were pre-treated at the Helmholtz Nano Faciliy (HNF), in FZ Jülich, using wet oxidation process. Carrying out the oxidation process at 1000°C for 41 minutes results in SiO_2 of thickness of 285 nm and oxidation at 850°C for 80 minutes produce SiO_2 of thickness 92 nm. Depending on the material to be exfoliated, the 285nm or 92 nm substrates were chosen. It is important that the substrates are clean before exfoliation to increase the probability of getting larger areas of monolayer or few layer flakes.

The substrates are cleaned according to a standard procedure as mentioned in the reference [75]. This involves an initial wet cleaning process, which is subsequently followed by a dry cleaning step. The Si wafers are cut into desired dimensions using a diamond scribe. These cut wafers are then transferred into acetone and are placed in an ultrasonic bath for 10 minutes. This is to remove oil, grease and other organic contaminants on the surface. After the ultrasonic bath, the wafers are washed using isopropanol, followed by another ultrasonic bath in isopropanol for 5 minutes. This is to remove the remaining acetone and the contaminants. Once this is done, the wafers are blow dried using N_2 gas. The next step is to treat the wafers in the UV/O_3 plasma. The substrates are kept in the UV/O_3 cleaner for 2 minutes. Highly intense UV radiation is used to dissociate oxygen molecule, forming atomic oxygen which combines with oxygen molecule to form ozone (O_3). Again, with the UV radiation, O_3 decomposes into oxygen molecule and atomic oxygen. At the same time, the UV radiation will break the contaminants on the surface to form ions and free radicals. The atomic oxygen which is highly oxidizing in nature and attaches to the open chain of the contaminant to form volatile molecules like H_2O, CO_2, O_2 etc, leaving a clean substrate.

Along with SiO_2 substrates, Au coated substrates are used for exfoliation. Studies show that gold assisted exfoliation can be used for obtaining large monolayers, in the order of millimeters, of almost all the materials [76]. The success rate is high when freshly prepared gold is used for exfoliation.

Next step in the exfoliation process is to prepare a 'parent' or 'mother' tape of the required material. Different kinds of tapes are used for exfoliation. The most commonly used tapes are "magic" scotch tape, blue tape ($1007R-6.0$ from Ultron Systems INC) and kapton tape. Single crystals of the 2D material is placed on the tape in such a way that the single crystal contact regions occupy the maximum space. This tape will serve as the parent tape. Another tape is then placed on the parent tape and are pressed gently to remove the air trapped between the tapes and to increase the contact. The force of pressing the tapes vary from materials. For example, relatively high force can be applied on graphite resulting in no fragmentation, whereas for materials like WSe_2, this can result in fragmentation and therefore, no force at all should be applied. This process is repeated 5-6 times, depending on the thickness of the initial crystal, to get thinner flakes. After the final exfoliation, the tape is examined under light to determine optically, if there are any large regions with relatively small thicknesses. For graphene, light gray regions indicate regions of small thickness and for WSe_2, light red regions indicate regions of small thickness. Once such regions are determined, the next step is to transfer the thin flake on to the substrate. The substrates are heated to 150°C to remove any remaining water molecules. The tape with the region of interest is placed on top of the substrate while it is still hot. When blue tape is used for exfoliation, the substrate with the tape containing flakes on top was heated to 80°C for 1 minute. Different types of adhesive tapes exhibit varying levels of adhesion, which is primarily influenced by the specific adhesive compounds utilized. The degree of adhesion directly related to the extent of adhesive residue, or glue contamination, left on surfaces upon removal. The advantage of using blue tape for the exfoliation is that the residues from the glue is minimized even when it is heated. Before taking the tape off from the substrate, it is gently pressed on to the substrate

to maximize the yield. The various stages of the exfoliation process are shown in Figure 4.1.

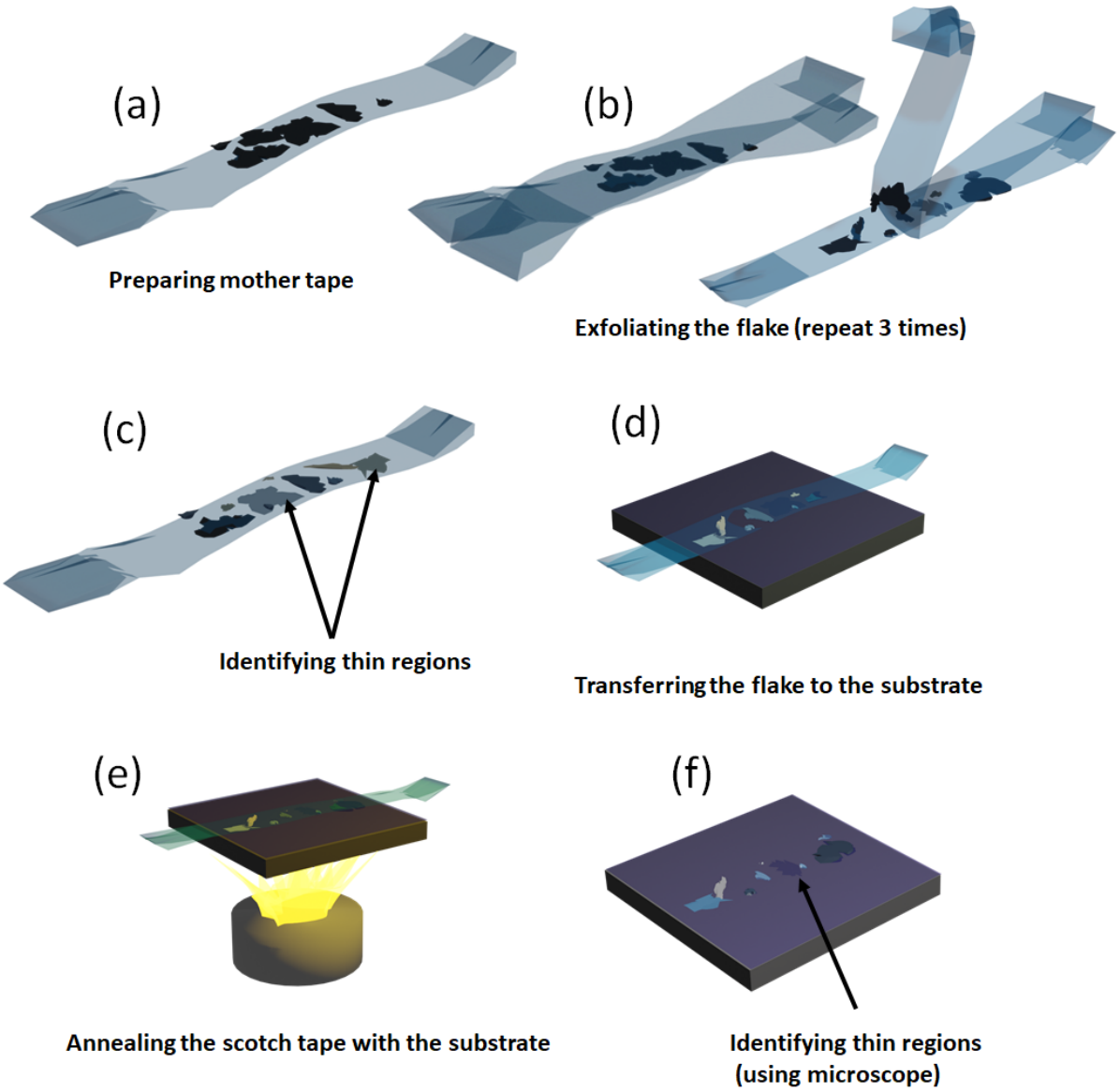

Figure 4.1: Schematic diagram of different step in the mechanical exfoliation of 2D materials. The Figure shows exfoliation, identification of few layer flakes with a microscope and transferring the flakes from the scotch tape to the SiO_2 substrate.

Once the exfoliation is performed, the next step is to identify the regions of monolayers, bilayers, or few layer regions in the substrate. This is done by examining the substrate under the optical microscope. *Axioscope*5/7 from Zeiss was used for the identification. For commonly used materials like graphene, hBN, and WSe_2, finding monolayer and bilayer is achieved through optical contrast. For other materials it might be difficult to identify monolayer or bilayer regions and often atomic force microscopy (AFM) needs to be used to calibrate the optical contrast. The contrast also depends on the thickness of the SiO_2

substrate used. Flakes of different thicknesses of graphene and WSe_2 are shown in Figure 4.2.

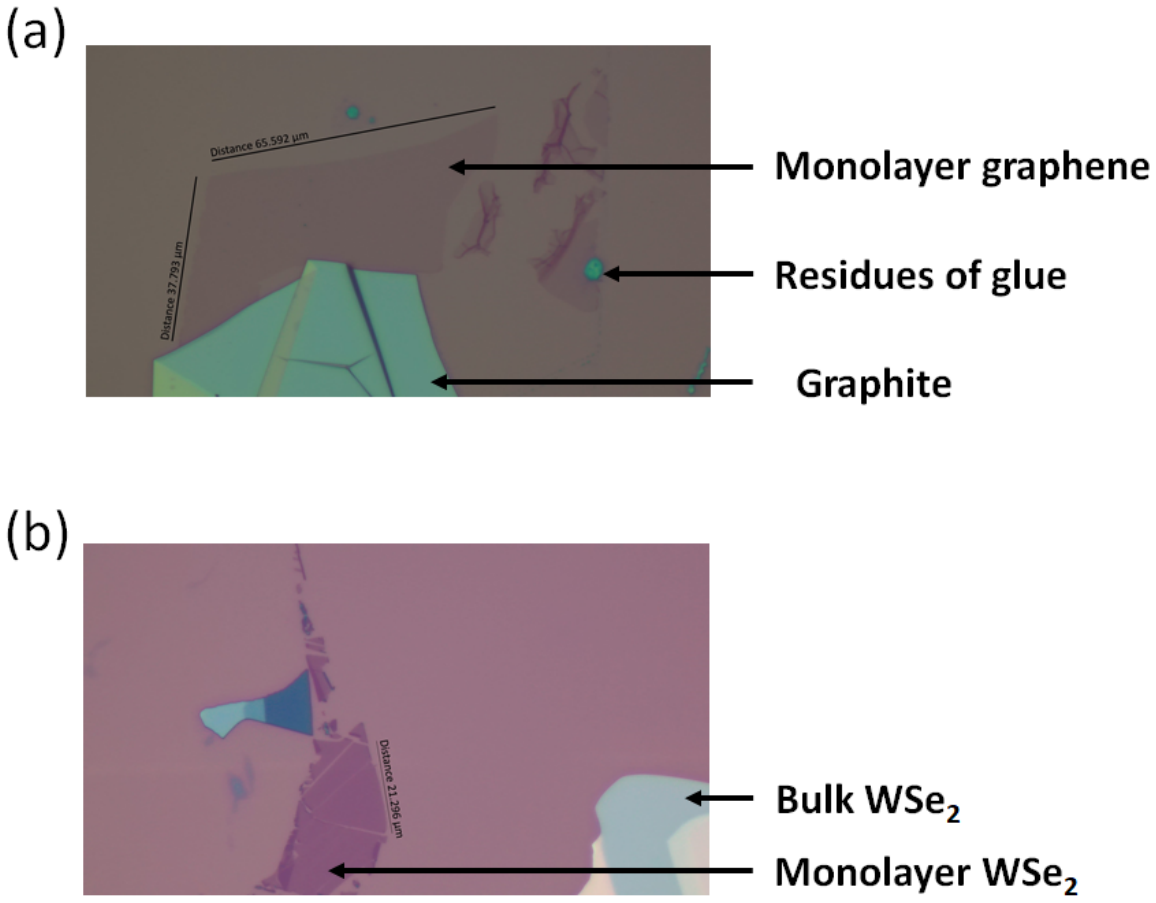

Figure 4.2: Figure shows microscopic images of exfoliated few layer flakes of (a) graphene and (b) WSe_2 on SiO_2 substrate. The monolayers of graphene and WSe_2 are identified by the optical color contrast. Figure also shows how the optical contrast of flake changes with thickness for both graphene and WSe_2.

It is not possible to exfoliate highly reactive materials in ambient condition, as they would degrade in the presence of oxygen, water etc. [44, 45]. Such materials were exfoliated under Argon atmosphere in the glove box at PGI-3, where the oxygen and and water concentration are maintained to be less than 1 ppm and 0.1 ppm, respectively. For the determination of the flakes, the glove box is equipped with another Zeiss microscope and the scanning can be controlled remotely outside the glovebox. For these reactive materials, the substrate preparation is slightly different. After the wet cleaning process the material is directly exfoliated. This is because the UV/O_3 cleaning creates a strong adhesion of the flakes to the substrate, making it difficult to pick-up the flake later. Additionally, the heating of substrates to remove the water molecules also results in strong adhesion between the flake and the substrate.

Gold assisted exfoliation [76] produced big few layer flakes of Fe_3GeTe_2 and $Cr_2Ge_2Te_6$. The adhesion between the magnetic samples and the Au substrate were strong, making it impossible to pick the flakes from the substrate. Therefore Au coated SiO_2 wafer were not used for exfoliation in this thesis.

4.2 Stacking of 2D flakes

Once all the flakes are identified, the next step is to stack these flakes together to form the heterostructure. To assemble the flakes, the *hot pick-up* technique was used with polycarbonate (PC)/polydimethylsiloxane (PDMS) stamps [77]. The first step is to prepare the stamp. For this, a PC solution is made by mixing 6% of PC by weight in chloroform. The PC film can be made from the PC solution in two ways. The first method is to pour 4-6 drops of PC on a clean glass slide using a pipette. Another glass slide is used to distribute the PC solution evenly on the first glass slide and is then placed on top of each other. The glass slides are then moved in the opposite directions to form a thin layer of PC solution on both slides. This is then kept in the oven for 5 minutes at 100° or left outside until the PC film is fully dried. Now, a smooth region is identified on the film and remaining the portions are removed. The second method for preparing PC film is by using a spin coater. A glass slide is cut into 10×10 mm pieces and is cleaned in isopropanol. This is then placed on a spin coater, two drops of PC solution is dropped on the glass slide and is spin coated for 1 minute at 1400 rpm. The spin coater method is more reliable and reproducible than first method.

For the PDMS preparation, two components, polymer A (Sylgard 184 silicone elastomer base) and polymer B (Sylgard 184 silicone elastomer curing agent) are mixed in 10:1 ratio. The polymers are vigorously mixed for a few minutes until fully combined, forming bubbles. The mixture is then placed in a desiccator for approximately one hour to eliminate the bubbles. On a clean glass slide, one drop of the solution is dropped. The glass slide is immediately turned upside down and baked in an oven at 70°C for one hour such that the PDMS forms a spherical shape because of gravity (shown in Figure 4.3 (a)).

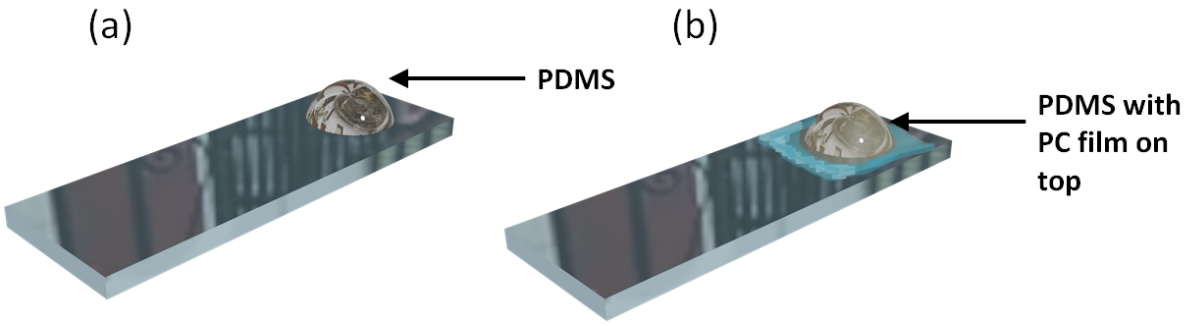

Figure 4.3: Schematic diagram of (a) PDMS and (b) PDMS/PC stamp on the glass slide

The prepared PC film is then picked from the glass slide with a scotch tape, which is punched to form a hole in the middle. The final step in the stamp preparation is to transfer this PC film (with the scotch tape) on to the PDMS droplet, such that the center of the hole without the scotch tape is placed exactly on top of the center of the PDMS droplet (shown in Figure 4.3 (b).

At PGI-3, the transferring of the flakes to produce heterostructure is performed on a transfer stage, from the manufacturer HQ Graphene, which is inside the glove box. The transfer stage consists of a sample stage, with 4 degrees of freedom, three translational degrees and one rotational degree and is also equipped with heating, a glass slide holder and a microscope, which is connected to a monitor outside the glove box, as shown in Figure 4.4. The glass slide with the stamp is attached on the glass slide holder of the

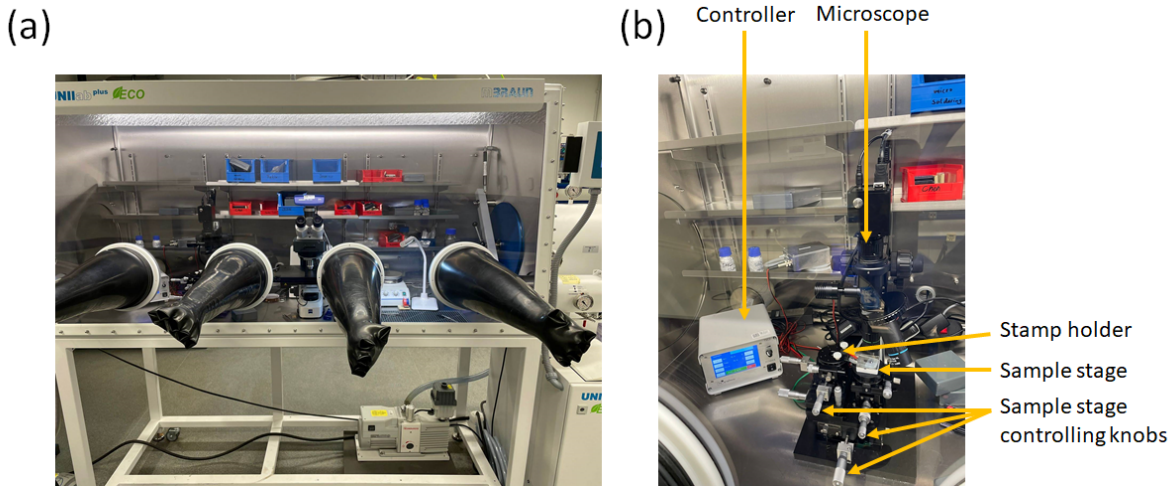

Figure 4.4: Picture of glove box setup at PGI-3. Figure (b) shows the transfer stage in the glovebox equipped with a microscope. The sample stage, stamp holder, controlling knobs and the controller are labeled in the picture.

transfer stage. The SiO_2/Si wafer with the flake of interest is placed on the sample stage. For transfers with PDMS/PC stamp, the top most flake of the heterostructure is picked up first. Since these heterostructure are made for ARPES studies, it is important to have a smooth and flat surface. And in case of insulators and semiconductors, the bottom flake should be conducting. For this reason, the bottom flake was mostly chosen to be a thick (more than 20 monolayer) and flat graphite flake. To study the band structure of monolayer graphene, less than 20 monolayer thick hBN were also used as bottom flake (see 5.1). The first step of the transfer is to identify the top most flake of the heterostructure using the microscope and align it to the center of the monitor. Then the stamp is placed directly above the flake, but separated by a vertical distance, without touching the flake. The sample is then heated to 60°C. The sample stage with the sample is slowly moved in the upward direction approaching the stamp. Once the flakes is in the close vicinity of the stamp, it should be made sure that the flake is not exactly at the center of the PC stamp. It will cause the flake to wrinkle or even get damaged if the flake region is the first to be hit by the stamp. Now the sample stage is again moved in the upward direction carefully until the PC film just touches the substrate. This can be accurately distinguished

using the microscope, as there will be concentric ring like patterns when the PC stamp is in close distance to the substrate (shown in Figure 4.5). Now the temperature is raised

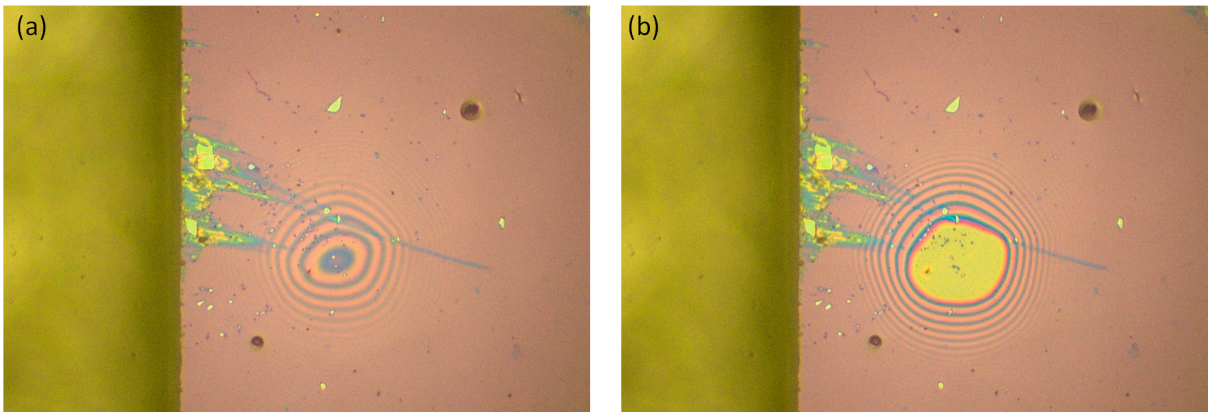

Figure 4.5: Photographs of PC film. (a) shows when the ring structures due to interference that happens when the PC film is in close distance to the substrate. (b) shows the PC in contact with the substrate. The yellow region shows the contact region.

to 120°C. This will cause the PC to expand its contact area. Initially, the temperature is ramped up at a rate of 0.1°C/s. Once the flake is covered by the PC, the rate is increased to 4°C/s. When the temperature reaches 120°C the heater is turned off. This will result in slow retraction of the PC film from the substrate. If the pick up is successful, the flake will stick to the PC film during the retraction. For samples like Fe_3GeTe_2, the substrate is heated to slightly higher temperatures in the order of 150° for successful pick up.

The above mentioned procedure is repeated for all the subsequent flakes. The only additional step is aligning the second flake exactly on top of the bottom flake. This is done optically with the microscope, but can sometimes be incorrect, as the position of the flake on the PC film may change slightly when in contact with the substrate compared to the free standing PC film. The alignment can be adjusted, even after the PC film is in contact with the substrate by retracting and repeating the steps. The topmost flake is usually monolayer of graphene or hBN which will serve as a protecting layer for the reactive materials like Fe_3GeTe_2 and $Cr_2Ge_2Te_6$. Once all the flakes are picked up, the cleaned final substrate is put on the sample stage. The final substrate is usually gold coated SiO_2, with a 2nm Ti layer in between, as ARPES requires a conducting substrate. The substrates are cleaned in a similar way as the SiO_2/Si wafers, as mentioned earlier in Section 4.1. The final substrate is heated to 60°C and is moved to be in contact with the stamp. Once in contact, the temperature is raised to 200°C. The PC film will start to melt and while it is still hot, the sample stage is retracted causing the PC film to break. The film on the contact area will remain on the final substrate. A schematic illustration of the different steps in the transfer procedure is shown in Figure 4.6.

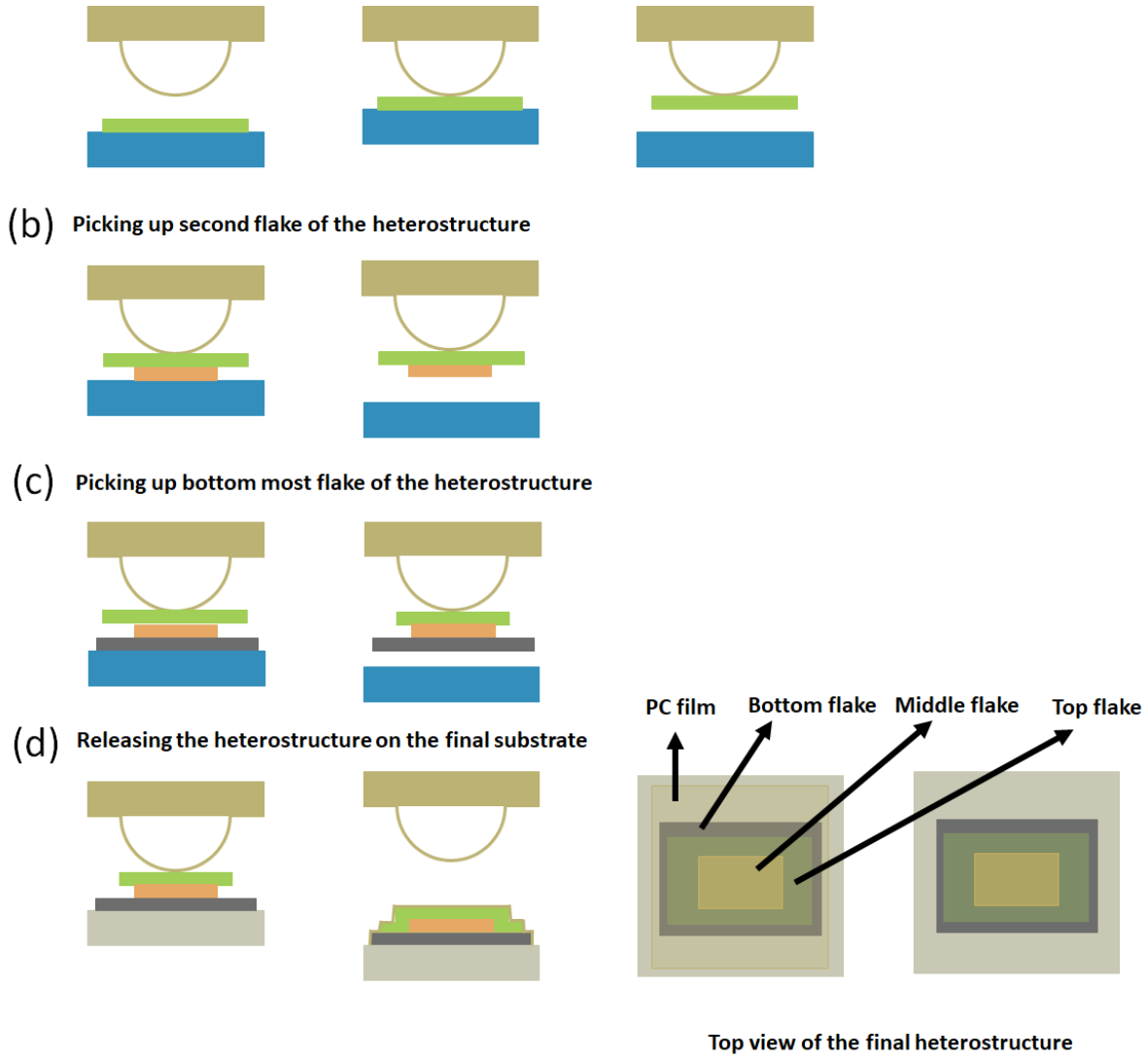

Figure 4.6: Schematic illustration of the dry transfer technique. The process of picking up of the topmost flake (a), the second flake (b), and the bottom flake (c) are shown. The dropping down of the heterostructure along with the PC film on the final substrate is shown in (d). The PC film is finally removed from the heterostructure using chloroform wash and the heterostructure is finally cleaned using AFM.

4.3 Cleaning the heterostructure

The final step is to remove the PC film from the substrate and to clean the heterostructure. For this, the sample is placed in chloroform for few hours. Because PC is soluble in chloroform, placing the final substrate in chloroform will remove most of the film residue. The substrate is then taken out of the chloroform solution to examine under the microscope. If needed, the sample is again washed in the chloroform. The photographs of different stages of transfer are shown in Figure 4.7

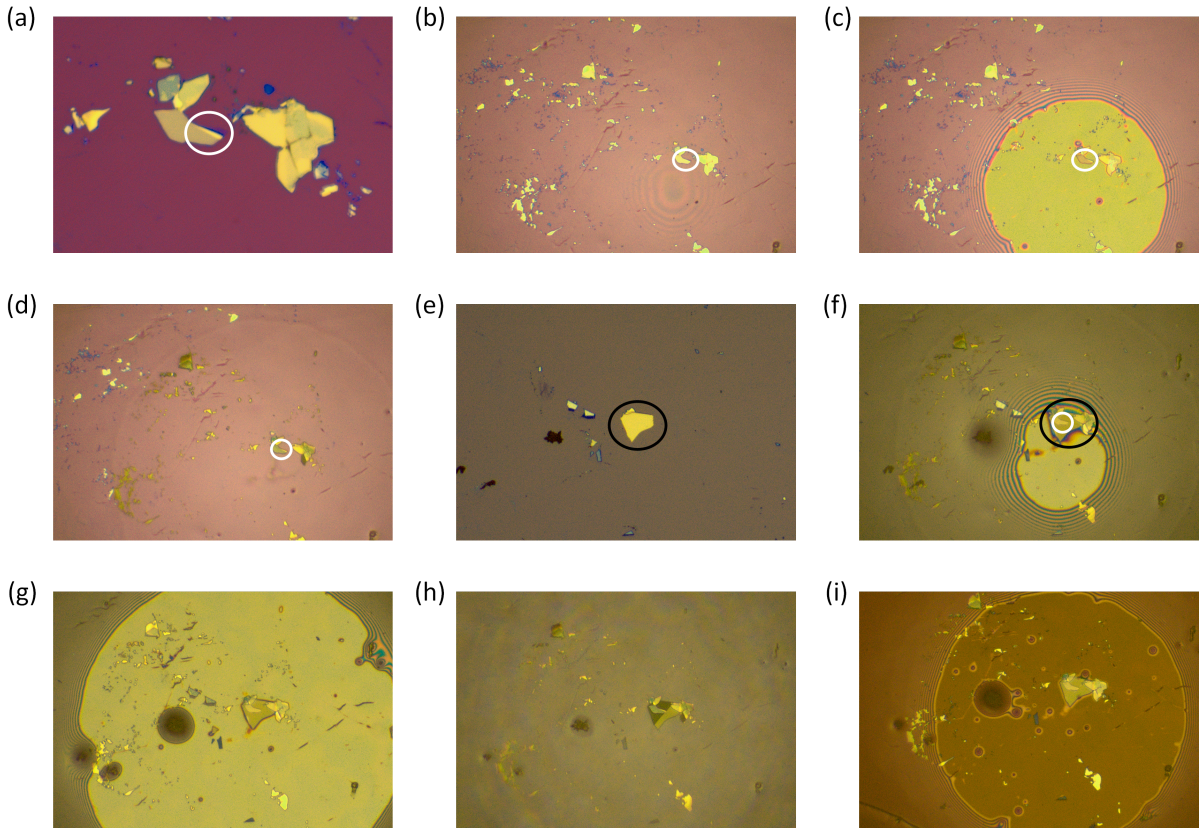

Figure 4.7: Photographs showing different stages of transfer. (a) shows the monolayer WSe_2 flake. The monolayer region is indicated by white circle. (b)-(c) show different stages of picking up monolayer WSe_2 with PC film. (d) shows the picked up monolayer flake on the PC film. (e) shows the bottom graphite flake. The region of interest is marked by black circle. (f)-(g) show different stages of picking up bottom graphite flake. (h) shows the picked up monolayer WSe_2 and graphite on the PC film. (i) shows the final step of the transfer, after the heterostructure is placed on the final substrate.

Once the sample is free from visible residues, it is taken to the AFM for further examination. The flakes will be covered with small residues even after washing in chloroform. They can be removed by sweeping the sample with AFM in the contact mode [78].

5 Circular dichroism in graphene and WSe_2

ARPES is a well-established technique for studying the band structure of solids, providing access to initial-state band dispersions through parallel momentum conservation, $\mathbf{k}_{\parallel,i} = \mathbf{k}_{\parallel,f}$, where i and f represent the initial and final states, respectively. In addition to band dispersion, ARPES maps contain valuable information about the material, which can be extracted from the intensity modulation of the measured spectral function. These intensity modulations arise from final-state scattering events and the experimental geometry. Specifically, the intensity variations in ARPES maps corresponding to dispersive bands depend on the polarization of the incident light, which influences photoemission transition matrix elements. Consequently, photon polarization-dependent ARPES measurements can provide additional insights into the electronic structure. Results presented in this chapter has been been published in [1].

Linearly ($s-$ and $p-$)polarized, circularly polarized, and elliptically polarized light are commonly used in ARPES experiments. In circular dichroic-ARPES (CD-ARPES) measurements, right circularly polarized light (RCP/C_+) and left circularly polarized light (LCP/C_-) are used. The dichroic signal is calculated as the difference between the photoemission intensities measured with C_+ and C_- lights, normalized by the total intensity ($I_{C_+} + I_{C_-}$). The CD magnitude can be expressed as:

$$CD\ magnitude = \frac{I_{C_+} - I_{C_-}}{I_{C_+} + I_{C_-}}. \tag{5.1}$$

In the atomic limit, the CD magnitude is also referred to as circular dichroism in angular distribution (CDAD), where the angular distribution is described by a linear combination of spherical harmonics.

CD-ARPES is widely used to study initial-state orbital angular momentum (OAM). Previous studies have utilized CD-ARPES to determine the chiral orbital texture of Dirac cones in topological insulators [79, 80] and to investigate spin textures in these materials [81–83]. CD-ARPES has also been applied to graphene and transition metal dichalcogenides (TMDCs) to explore OAM and orbital symmetries [84–86]. Beyond probing orbital and spin angular momentum, circularly polarized light in CD-ARPES has been shown to manipulate spins within certain photon energy ranges [87]. Additionally, CD-ARPES intensities have been linked to the Berry curvature through the OAM of the initial state [85, 86, 88, 89]. The connection between Berry curvature and OAM has been well established in reference [88].

In addition to the study of orbital and spin angular momentum, several investigations have highlighted the importance of considering final-state effects in interpreting CD-ARPES intensities and their photon energy dependence [90–95]. Final-state interference and multiple scattering have been shown to significantly influence dichroic spectra [90, 93].

From these previous studies [90, 91, 93], it is evident that the relationship between OAM (or spin angular momentum) and CD-ARPES is not straightforward. A detailed analysis is therefore required to establish a meaningful connection between CD-ARPES intensities and spin or OAM. In this chapter, various factors influencing CD-ARPES intensity and the extent of their effects across different photon energy regimes will be examined in detail. These discussions will be supported by CD-ARPES measurements on monolayer graphene and WSe_2. Furthermore, comparisons with DFT calculations and multiple scattering simulations will be presented to analyze the contributions in greater depth.

5.1 CD-ARPES on graphene/hBN

Before directly presenting the CD-ARPES measurements, it is important to examine the photoemission transition matrix element, which governs the CD-ARPES signal. It is given by

$$M_{i\to f}(\vec{k}_f) \propto \langle \psi_f(\vec{k}_f)|\vec{\epsilon}\cdot\vec{r}|\psi_i\rangle. \tag{5.2}$$

The initial state in photoemission can be approximately described as a sum of atomic-like orbitals as $|\psi_i\rangle = \sum_{n,l,m,\mathbf{R}} C_{n,l,m,\mathbf{R}}\phi_{i_{n,l,m}}(\mathbf{r})$, where $\mathbf{R}$ represent the atomic sites, and $\mathbf{r}$ is the position coordinate. When the initial state is a band with a single orbital character, the summation in $|\psi_i\rangle$ reduces to a single term, simplifying the analysis of CD-ARPES. Graphene serves as an ideal material for such an analysis, as the Dirac bands at the K points of its Brillouin zone are composed of C p_z orbitals [96]. For this reason, graphene was chosen for CD-ARPES measurements in this study.

Monolayer graphene was prepared by mechanically exfoliating bulk graphite single crystals (commercially obtained from HQ Graphene), as described in Section 4.1. Once a monolayer graphene flake was identified using an optical microscope, it was transferred onto the final substrate using the dry transfer technique (Section 4.2). The final substrate consisted of Au-coated SiO_2 chips, with a 1 nm Ti adhesion layer in between. A hexagonal boron nitride (hBN) flake of thickness 10–20 monolayers was used as the bottom layer. The hBN thickness was carefully chosen, as flakes thicker than approximately 30 monolayers can lead to charging effects due to the insulating nature of hBN. An optical micrograph of the heterostructure is shown in Figure 5.1 (a).

The CD-ARPES measurements were performed at the NanoESCA beamline at Elettra [97], where the beam spot is approximately 20x20 μm. The lateral dimension of the flake was approximately 30x30 μm, allowing the photon beam spot to be focused entirely on the graphene, thereby avoiding signals from the surrounding hBN and gold substrate. Initially, standard ARPES measurements with $p-$polarized light were performed to orient

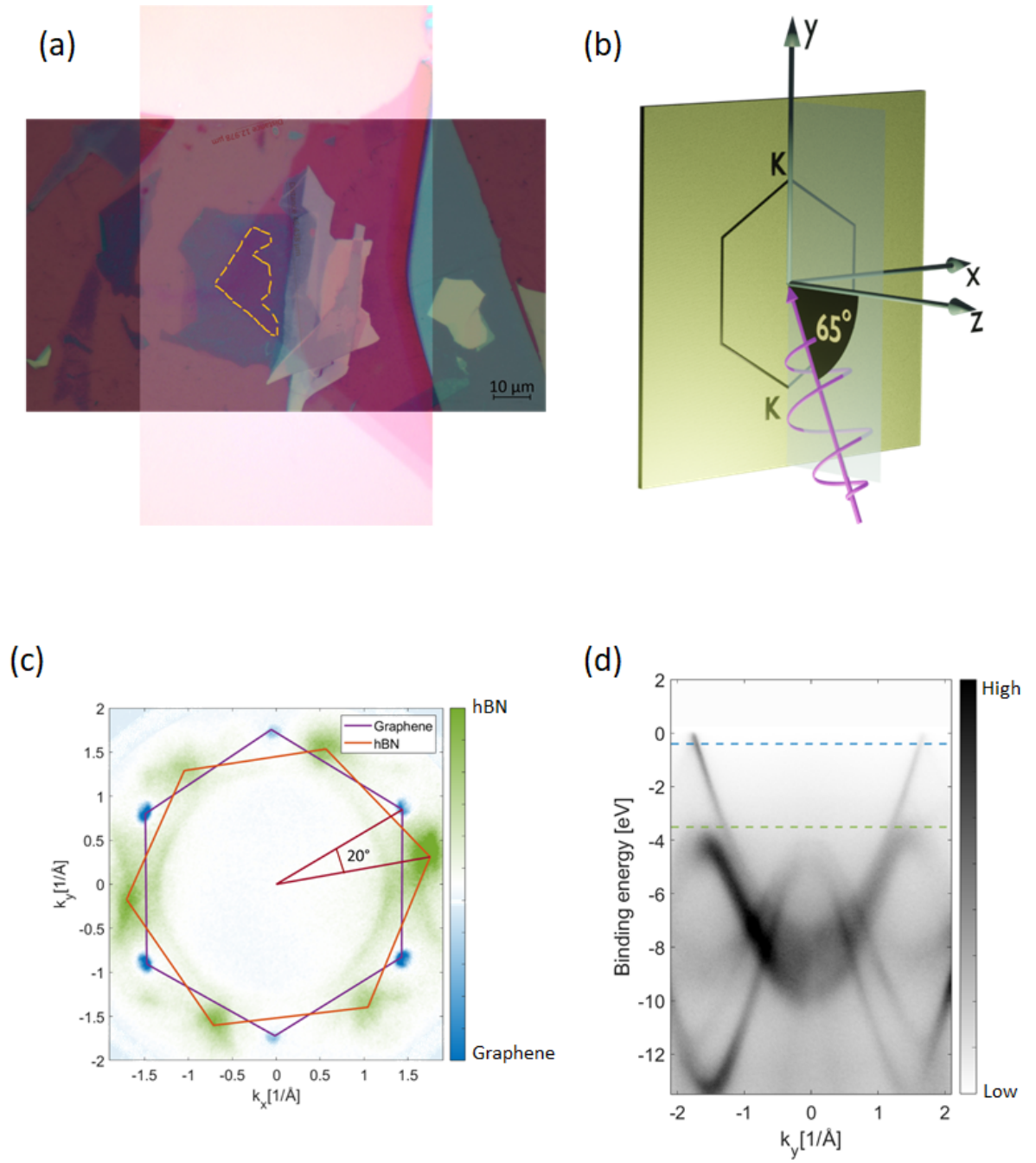

Figure 5.1: (a) Optical micrograph of graphene/hBN flake. The monolayer graphene region is indicated with yellow dotted lines. (b) Experimental geometry of the ARPES measurements on graphene/hBN sample at NanoESCA beamline. (c) Two superimposed constant energy cuts on hBN/graphene showing the Dirac cones of graphene at E_B = 0.4 eV and valence band maximum of hBN at E_B =3.3.eV. (d) shows the Energy versus $k_{||}$ maps on hBN/graphene at $h\nu$ = 40 eV. The constant energy cuts in (c) are indicated by dotted lines.

the sample. The sample was aligned such that the $K - \Gamma - K'$ direction of graphene was along the light incidence direction, as shown in Figure 5.1 (b). From the binding energy scan, both the graphene and hBN bands were identified. The hexagonal features of the graphene and hBN bands in the $k_x - k_y$ maps were used to determine the twist angle between graphene and hBN, which was found to be 20°, as shown in Figure 5.1 (c).

The measurements with $p-$ and $s-$polarized light are shown in Figure 5.2. The inten-

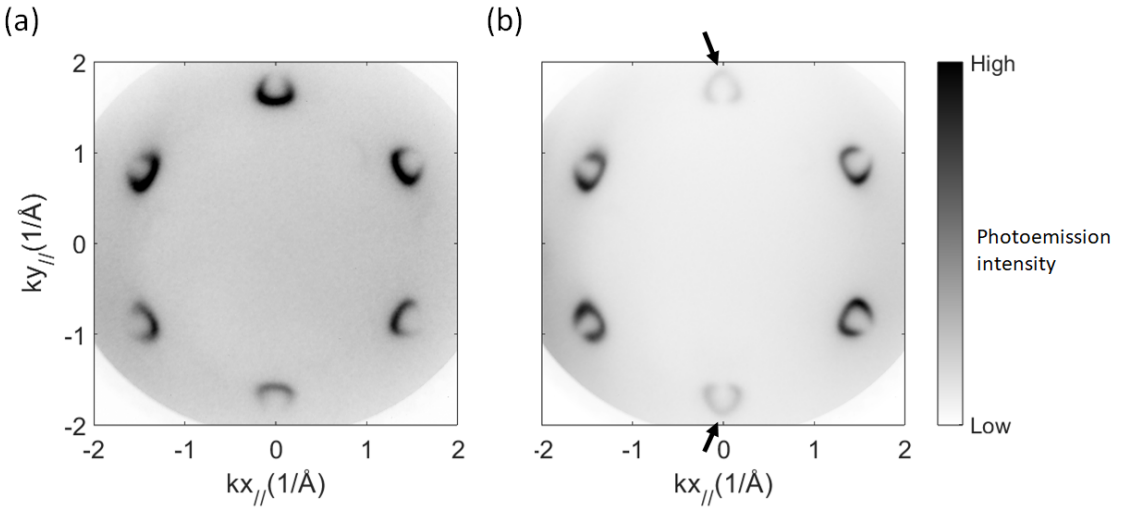

Figure 5.2: Constant energy $k_x - k_y$ maps on graphene/hBN at E_B= 1.25 eV with (a) $p-$polarized and (b) $s-$polarized light at $h\nu$ = 40 eV.

sity at the K points with $p-$-polarized light reveals the presence of dark corridors [98, 99] (see Figure 5.2 (a)). The measurements with $s-$polarized light illuminate the dark corridors at the topmost and bottommost K points, as indicated by arrows in Figure 5.2 (b).

The CD-ARPES measurements were performed at photon energies from 35 eV to 80 eV (shown in Figure 5.3). All the CD maps exhibit non-vanishing dichroism, with the dichroic signal strongly depending on the photon energy used. We focus on the CD-ARPES maps taken at photon energies of 35, 40, and 50 eV, as shown in Figures 5.3 (a), (b) and (d), respectively. At $h\nu$ = 35 eV, all the six K points exhibit a complex mixture of positive and negative values of CD magnitude, indicated by red and blue colors, respectively. The sign of the two K points reverses while moving from $h\nu$ = 35 eV to 40 eV as indicated in Figure 5.3 (a)-(b). This shift occurs around $h\nu$ = 38 eV, as depicted in Figure 5.4. At a photon energy of $h\nu$ = 60 eV, the CD signal is observed to be very weak. (see Figure 5.3 (e)). However, as the photon energy increases further to $h\nu$ = 80 eV, there is a small but noticeable increase in the CD signal (see Figure 5.3 (f)).

To confirm that the measured CD magnitude originates from graphene and is not due to backscattering from the underlying hBN flake, similar measurements were performed on a thick graphite flake (greater than 10 monolayers). Figures 5.5 (a)-(f) compare the CD-ARPES measurements on graphite and graphene/hBN. The energy versus $k_{||}$ map of

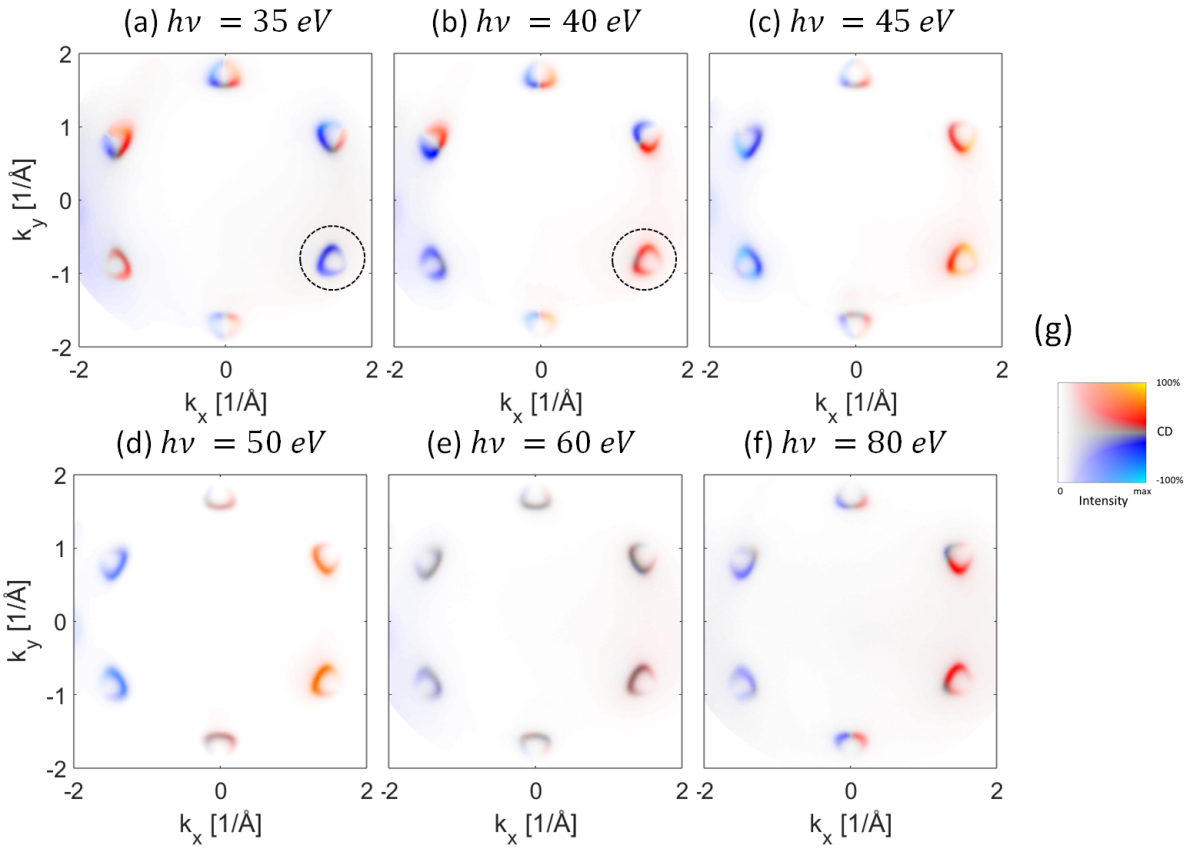

Figure 5.3: Constant energy $k_x - k_y$ CD maps on graphene/hBN at E_B= 1.25 eV at $h\nu$ = (a) 35 eV, (b) 40 eV, (c) 45 eV, (d) 50 eV, (e) 60 eV and (f) 80 eV. (g) shows the 2D color map used for the plots in (a) - (f).

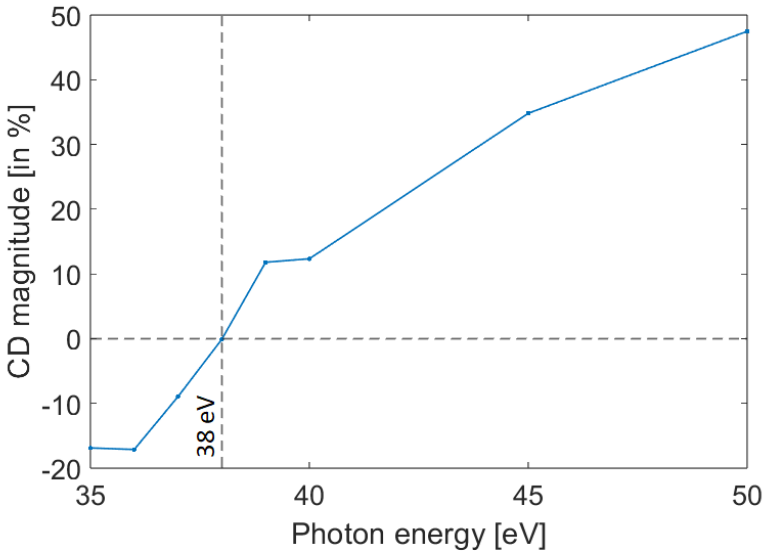

Figure 5.4: Intensity magnitude of hBN/graphene at k_x = -1.33 Å^{-1} and k_y = 0.97 Å^{-1}. The plot shows the sign reversal of dichroic signal at around $h\nu$ = 38 eV.

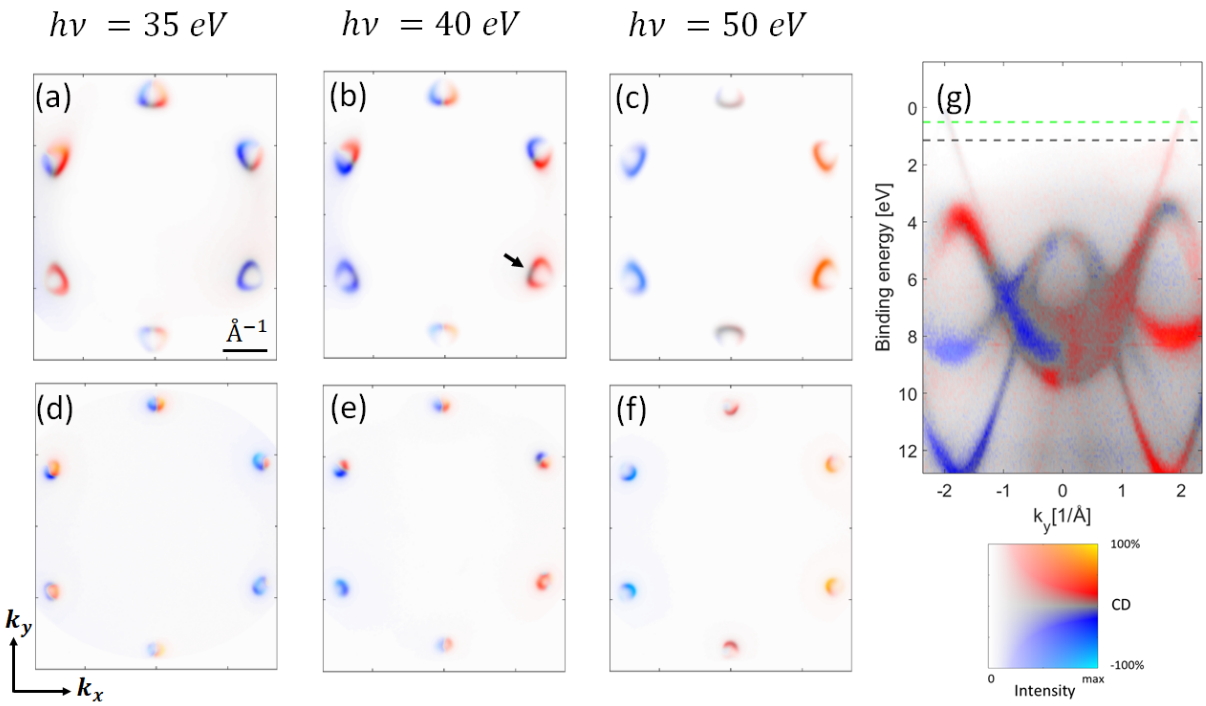

Figure 5.5: Figure shows the comparison of CD-ARPES from graphene and graphite. (a)-(c) show the constant energy $k_x - k_y$ maps at E_B = 1.25 eV on graphene/hBN at $h\nu$ = 35 eV, 40 eV and 50 eV, respectively. (d)-(f) show the CD-ARPES $k_x - k_y$ maps from graphite at E_B = 0.5 eV at $h\nu$ = 35 eV, 40 eV and 50 eV, respectively. (g) shows the E versus $k_{||}$ maps on graphene/hBN at $h\nu$ = 40 eV. The green and black dotted lines indicate the binding energies used for graphite and graphene, respectively.

graphene/hBN is also shown in Figure 5.5 (g), with the binding energies of the constant energy cuts indicated. Although the binding energies differ between the graphite and graphene measurements, the CD signals are similar in both cases, and the sign reversal at the K points is still observed for graphite. This confirms that the CD pattern in Figure 5.5 (a)-(c) originates from graphene and is not due to backscattering from the hBN substrate.

5.1.1 Free electron final state and partial wave expansion

To explain the observed CD pattern, it is essential to examine the matrix elements in detail. The form of the final state in Equation 5.2 is critical. The most commonly used approximation in photoemission is the free-electron final state (FEFS) or the plane-wave approximation (PWA) [100]. In the PWA, the final state is given by $|\psi_f\rangle = e^{i\mathbf{k}_f \cdot \mathbf{r}}$. Under the PWA, the photoemission matrix element is proportional to the Fourier transform of the initial state, directly linking the photoemission intensity to the initial-state wave function. Although the PWA successfully describes regular ARPES measurements and band dispersion, it is insufficient to account for intensity modulations in ARPES maps.

The limitations of the PWA include its inability to explain perpendicular emission, circular dichroism, and the photon energy dependence of the ARPES intensity [101–103]. In *perpendicular emission*, where $\mathbf{A}$ is perpendicular to $\mathbf{p}$, the $\mathbf{A} \cdot \mathbf{p}$ term becomes zero, resulting in zero intensity. Regarding circular dichroism, the photoemission intensity for C_+ and C_- light is the same, leading to the cancellation of the CD magnitude. Additionally, the PWA neglects all final-state scattering events, which can modify the photoemission intensity. The inability of the PWA to describe perpendicular emission and circular dichroism necessitates a more accurate representation of the photoemission final state.

The photoemission process can be treated as a scattering problem [101, 104]. Electrons emitted from a site may undergo scattering due to the screened potential of the nucleus, which is often approximated using a muffin-tin potential. Determining the scattering amplitude, which is related to the differential cross-section [105], is crucial to understanding how electrons are distributed after scattering. The differential cross-section is defined as the ratio of the scattered flux to the incident flux.

Considering the single-site scattering problem in quantum mechanics, the Schrodinger equation for the process can be written as

$$\left(-\frac{\hbar^2}{2m}\nabla^2 + V(r)\psi(\mathbf{r})\right) = E\psi(\mathbf{r}). \tag{5.3}$$

Here, $V(r)$ is typically approximated by the spherically symmetric potential and therefore, the solutions $\psi(\mathbf{r})$ can be represented in the spherical harmonic basis as $\psi(\mathbf{r}) = R_{n,l}(r)Y_{l,m}(\theta,\phi)$. The simplest case is when the potential $V(r) = 0$, corresponding to the previously discussed PWA. For a plane-wave solution, the radial part of the Schrodinger equation satisfies

$$\left(-\frac{\hbar^2}{2m}\frac{d^2}{dr^2} - \frac{\hbar^2}{2m}\frac{l(l+1)}{r^2}\right)R_{n,l}(r) = \frac{\hbar^2}{2m}R_{n,l}(r). \tag{5.4}$$

The solutions for this equation are called the spherical Bessel functions, $j_l(kr)$ and $n_l(kr)$. Because of the singularity of $n_l(r)$ at the origin ($r = 0$), the only physically possible solution is $j_l(r)$. For a potential of finite range, described by $V(r > a) = 0$, the solution can also include $n_l(kr)$ outside the range of the potential and can be written as $R_{n,l}(r) = \sum_l A_l j_l(kr) + B_l n_l(kr)$. As $r \to \infty$, the functions $j_l(kr)$ and $n_l(kr)$ become $\frac{sin(kr-l\pi/2)}{kr}$ and $\frac{cos(kr-l\pi/2)}{kr}$, respectively. By substituting A_l and B_l with $a_l cos(\sigma_l)$ and $-a_l sin(\sigma_l)$, and by using trigonometric relations, the wave function can be represented as

$$\psi(\mathbf{r}) = \sum_l \frac{a_l}{kr} sin(kr - \frac{l\pi}{2} + \sigma_l)Y_{l,m}(\theta,\phi), \tag{5.5}$$

where σ_l is the phase shift. This additional phase acquired by the scattered wave outside the potential range reveals the effect of the potential on the scattered wave [105].

The total wave function after scattering can be written as the sum of incident plane wave and the scattered spherical wave

$$\psi(\mathbf{r}) = e^{ikr} + f(\theta,\phi)\frac{e^{ikr}}{r}, \tag{5.6}$$

where the scattering amplitude is given by $|f(\theta,\phi|^2$. By representing the Equation 5.6 in spherical basis and comparing with Equation 5.5, the relation between scattering amplitude and phase shift can be obtained.

The photoemission final state can be expressed as a scattering state:

$$|\psi_f\rangle = 4\pi \sum_{l=0}^{\infty} \sum_{m=-l}^{l} i^l e^{i\sigma_l(E_{kin})} R_{n,l}(r) Y_l^{m*}(\hat{\mathbf{r}}) Y_l^m(\mathbf{k}_f), \tag{5.7}$$

where σ is the phase shift, which depends on angular momentum quantum number, l and kinetic energy, E_{kin}. $R_{n,l}$ represents the radial component, while Y_l^m are the spherical harmonics [106]. The partial wave expansion of the scattering state reduces to the free-electron plane wave when the phase shift σ_l is zero and when the radial wave functions are replaced by spherical Bessel functions. By considering the initial state as a sum of atomic orbitals and the final state as a scattering state, along with the dipole selection rules, the photoemission matrix elements for C_+ light, for $l \pm 1$ channel can be written as

$$M_{i\to f} \propto i^{l\pm1} e^{i\sigma_{l\pm1}(E_{kin})} R_{l\to l\pm1}(E_{kin}) Y_{l\to l\pm1}^{m\to m+1} Y_{l\pm1}^{m+}(\mathbf{k}_f). \tag{5.8}$$

Here the $R_{l\to l\pm1}(E_{kin})$ is the radial integral and $Y_{l\to l\pm1}^{m\to m+1}$ is the angular integral given by

$$\begin{aligned} R_{l\to l\pm1}(E_{kin}) &= \int_0^{\infty} r^2 R_{nl} r R_{E_{kin},l\pm1} dr, \\ Y_{l\to l\pm1}^{m\to m+1} &= \langle Y_{l\pm1}^{m+1} | C_+ | Y_l^m \rangle, \end{aligned} \tag{5.9}$$

respectively. The transition matrix element in Equation 5.8 contains the phase shift term, the radial integral, and the angular integral. The last term, $Y_{l\to l\pm1}^{m+1}(\mathbf{k}_f)$, can be considered a constant for a particular $\mathbf{k}_f$ direction. The matrix element depends on the quantum number l through the σ_l term and radial integral. This dependence is crucial for circular dichroism and plays a critical role in sign reversals in CD-ARPES maps. The angular integral determines the angular profile of the photoemission intensity, which will be discussed in detail in the next section.

The independent atomic center approximation (IACA) assumes that the final state is an atomic-like scattering state, neglecting the effects of neighboring atomic potentials [107]. In IACA, all contributions from atomic-like sites are added coherently without any additional scattering. However, in reality, electrons in a solid experience additional scattering due to neighboring potentials [101]. The most accurate description of the photoemission final state treats it as a time-reversed LEED state [108, 109]. In a LEED experiment, a sample is probed with an electron beam, and the electrons undergo multiple scattering events with atomic potentials. In the time-reversed LEED state, these multiply scattered spherical waves accumulate at the emission site, generating a free electron. Time-reversed LEED states are employed in one-step model calculations such as the KKR method [110] and are also employed in multiple scattering codes [111].

5.1.2 Photoionization pattern

Using tabulated phase shifts, radial integrals, and angular integrals [112], the circular dichroism in angular distribution can be calculated for atomic orbitals. Depending on the initial orbitals, the matrix elements are determined by the polarization of the incident light. When only one of the $l \pm 1$ channels is available, the phase shift and radial integrals can be regarded as constants and therefore do not affect the angular distribution of the dichroic pattern. This occurs for the initial state orbital Y_1^0. Here only the $l+1$ channel exists with both C_+ and C_- lights with final states Y_2^1 and Y_2^{-1}. The angular dependence and phases of these profiles are shown in Figure 5.6 (a) and (b), respectively. Both Y_2^1 and

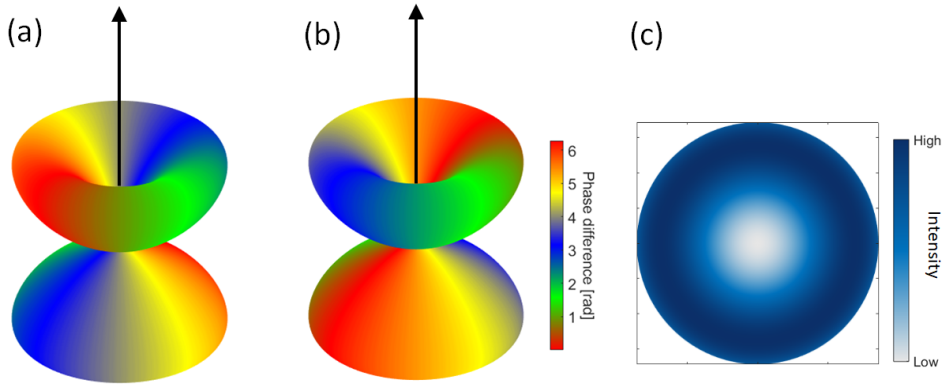

Figure 5.6: Photoionization patterns from Y_1^0 initial state with (a) C_+ and (b) C_- light. The final states has the form Y_2^1 and Y_2^{-1}. The intensity pattern of both (a) and (b) is the same and is shown in (c).

Y_2^{-1} profiles, when squared, yield the same intensity profile, as shown in Figure 5.6 (c), representing the emission distribution over the upper half-space. In this scenario, where only the $l+1$ channel exists, the angular integral fully determines the angular distribution of the CD pattern.

For other orbitals where both $l+1$ and $l-1$ channels are available, the phase shift difference can influence the sign of the CD pattern. When the phase shift difference crosses zero or π, $e^{i\sigma_l}$ term changes sign. Similarly, differences in the radial integrals for the $l \pm 1$ channels also affect the sign of CD pattern. The phase shift and radial integral for the C $2p$ $l \pm 1$ channels are shown in Figure 5.7. For the C $2p$ orbital, the phase shift difference reaches zero around $h\nu = 40$ eV (marked in Figure 5.7 (a)), indicating a CD signal reversal at this photon energy. The radial integral for the C $2p$ for the $l \pm 1$ channels can be considered constant since the difference remains nearly the same for the photon energy range considered in Figure 5.7 (b).

5.1.3 Experimental geometry induced circular dichroism

The photoionization pattern can be calculated using the multiple scattering code, "Electron Diffraction in Atomic Clusters" (EDAC) [111]. The photoionization pattern corresponds

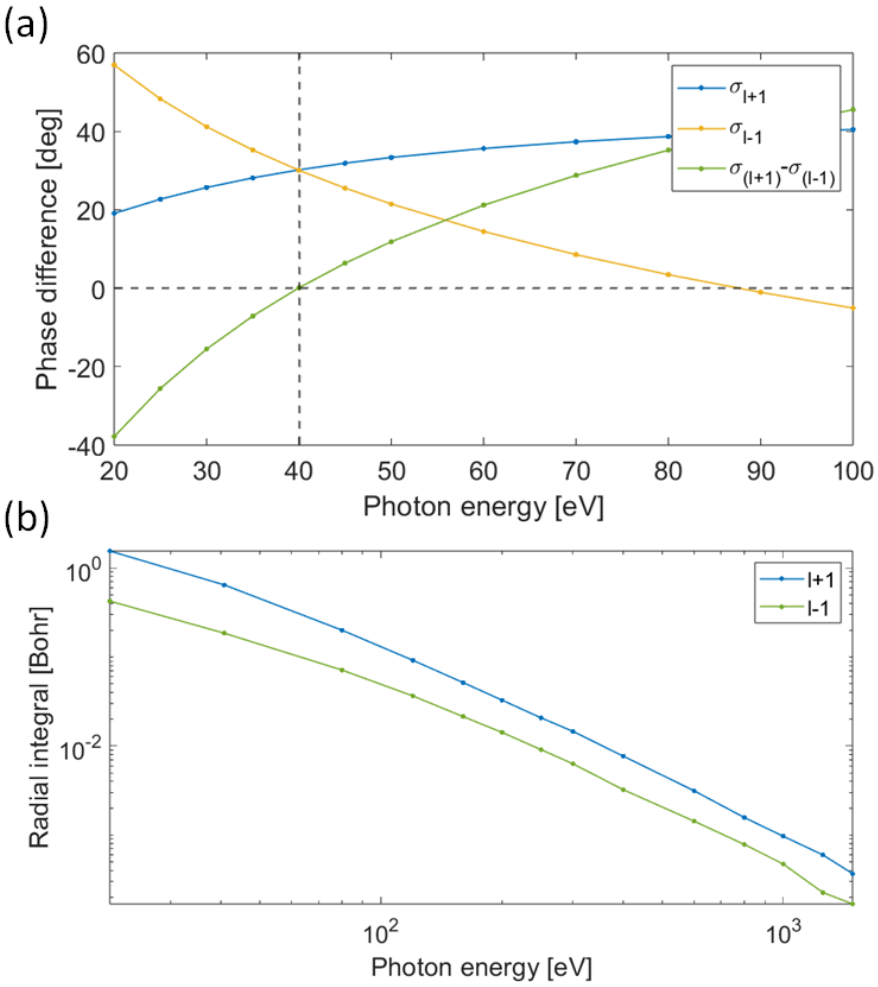

Figure 5.7: Phase shift (a) and radial integral (b) of C $2p$ orbital for the $l \pm 1$ channels. The phase difference between $l \pm 1$ channel is shown in (a), and the photon energy at which the phase shift difference becomes zero is also marked. The phase shift values for the photon energy range shown in (a) is obtained from EDAC and the radial integral values are from [112].

to a zero-order scattering pattern. For the CD-ARPES measurements shown in Figure 5.3, where the primary contribution comes from $2p_z$ (that is Y_1^0), the photoionization patterns were calculated for the photon energies used. The intensity patterns for the C Y_1^0 orbital with C_+ and C_- light, with quantization axis taken as surface normal (that is the z axis), at $h\nu = 100$ eV are shown in Figure 5.8 (a) and (b). The pattern remains exactly the same for $C_\pm$ light. When taking the difference between the two light polarizations, the result shows only numerical noise, indicating zero dichroism from the C Y_1^0 (as seen in Figure 5.8 (c) and (d)). This calculation contrasts with the measurements on graphene.

So far, the experimental setup has been considered such that the light is incident perpendicular to the sample surface. Previous studies have shown the importance of experimental geometry on CDAD from oriented orbitals (or molecules) [113]. It has been demonstrated that a non-chiral molecule or atomic orbital can still exhibit nonzero dichroism due to

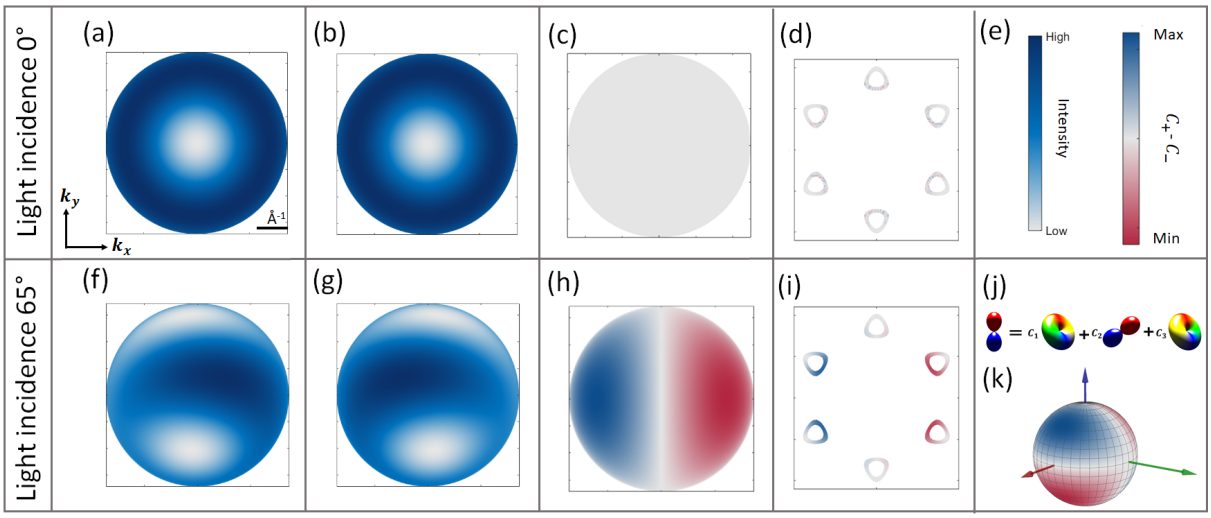

Figure 5.8: Calculated photoionization pattern from C p_z orbital at $h\nu$ = 100 eV. (a)-(d) are calculated with light incidence along the surface normal. (f)-(i) are calculated with light incidence direction taken as 65° with respect to the surface normal. (a) and (b) ((f) and (g)) are the intensity profiles from Cp_z at 0° (65°). (c) and (h) show difference of C_+ and C_- calculations from C p_z at 0° and 65°, respectively. (d) and (i) are the difference of C_+ and C_- calculations combined with tight binding calculation, at binding energy E_B = 1.25 eV. The colormaps used for the intensity plots and intensity difference plots are shown in (e). (j) shows a schematic diagram of transforming the p_z orbital to a new coordinate system. (k) shows the photoionization pattern in the full emission sphere from initial state Y_1^0.

the chirality induced by the experimental geometry. When the axis of the oriented orbital (or molecule), **n**, the photon propagation direction (light incidence direction), **q** and electron propagation direction, **k** are non-coplanar, the experimental geometry itself induces chirality, even if the orbital (or molecule) lacks intrinsic chirality. This effect is only visible in the angular distribution and cancels out in angle-integrated measurements.

The measurements were performed at the NanoESCA beamline, where the light was incident at an angle of 65° with respect to the surface normal. The graphene $K - \Gamma - K'$ direction was aligned along the light incidence direction, as shown in Figure 5.1 (b). Dipole selection rules are valid when the quantization axis of the orbitals aligns with the light incidence direction, which is conventionally the z axis. When this is not the case, the orbitals must be decomposed along the light incidence direction. The experimental geometry can also be analyzed by decomposing the light into Cartesian coordinates. In this thesis, the approach of decomposing atomic orbitals along the light incidence direction was adopted. The graphene p_z orbital needs to be defined in the new quantization axis, z', which is tilted by 65° from the surface normal.

The decomposition of orbitals in the new quantization axis can be performed using the Wigner D-matrix. For p_z orbitals, it is convenient to use trigonometric relations, and the

transformation is given by

$$(Y_1^0)_z = C_{1,1}(Y_1^1)_{z'} + C_{1,0}(Y_1^0)_{z'} + C_{1,-1}(Y_1^{-1})_{z'}, \tag{5.10}$$

where $C_{1,1} = \frac{sin\theta}{\sqrt{2}}$, $C_{1,0} = cos\theta$ and $C_{1,-1} = -\frac{sin\theta}{\sqrt{2}}$. For the light incidence at NanoESCA beamline the Equation 5.10 becomes

$$(1,0)_z = 0.5846(Y_1^1)_{z'} - 0.5624(Y_1^0)_{z'} - 0.5846(Y_1^{-1})_{z'}. \tag{5.11}$$

Since Y_1^0 in the new coordinates contains $(Y_1^1)_{z'}$, $(Y_1^0)_{z'}$ and $(Y_1^{-1})_{z'}$ (shown in Figure 5.8 (j)), both $l \pm 1$ channels exist with $C_\pm$ light. According to dipole selection rules, the possible final states for $(Y_1^{-1})_{z'}$ with C_+ light are $(Y_0^0)_{z'}$ and $(Y_2^0)_{z'}$. Similarly, for the $(Y_1^1)_{z'}$ with C_- light, the possible final states are $(Y_0^0)_{z'}$ and $(Y_2^0)_{z'}$. The calculated intensity patterns with $C_\pm$ light and with light incidence along 65° with respect to the surface normal are shown in Figure 5.8 (f) and (g). One possible reason for the nonzero dichroism observed in the CD-ARPES measurements could be the influence of experimental geometry. With the quantization axis set by the light incidence direction, the calculated CD pattern shows a nonzero difference, as seen in Figure 5.8 (h) and (i).

5.1.4 Multiple scattering in graphene

A detailed inspection of the photon energy dependence of the CD-ARPES measurements, as shown in Figure 5.5 (a)-(c), reveals that the map at $h\nu$ = 50 eV exhibits a relatively simple CD pattern: the left side of the map shows negative CD values (indicated in blue), while the right side shows positive CD values (indicated in red). The calculated pattern for the Y_1^0 orbital at 65° similar behavior (see Figure 5.8 (g) and (h)). However, at other photon energies, such as $h\nu$ = 35 eV and 40 eV, the CD pattern at different K points appears as a complex mixture of positive and negative CD values (indicated in red and blue), which was not replicated in the calculated CD pattern from Y_1^0. This suggests an additional source of dichroism.

Photoelectrons emitted from a site can undergo scattering by neighboring atomic potentials [101]. Multiple scattering has been shown to modify the intensity of bands in photoemission spectra. Final-state scattering (backscattering) effects have been observed in ARPES spectra from adsorbed atoms, which also reveal the substrate geometry [104, 114]. Similar scattering effects have also been observed in core-level spectra of single crystals using circularly polarized light [115]. Such final-state scattering effects also contribute to valence band spectra. Since valence-band wave functions are not as localized as core-level wave functions, multiple scattering in valence band photoemission exhibits additional complexity [101].

Different levels of approximation exist for describing the photoemission final state. The simplest is the Plane Wave Approximation (PWA), where all final-state scattering effects are ignored, and the emitted electron does not retain any memory of the initial state. A more refined description is the Independent Atomic Center Approximation (IACA), where

the final state is described as an atomic-like scattering state with phase shifts depending on the l quantum number of the final state. This results in intensity modulations due to $l \pm 1$ interference in the photoionization pattern. However, IACA neglects the influence of neighboring atoms. The limitation of IACA is addressed by multiple scattering theory, which provides the most accurate description of the photoemission final state by considering all possible scattering events. Inelastic scattering effects can also be included in multiple scattering formalism by considering the inelastic mean free path [111].

To determine the extent of multiple scattering effects in CD patterns of graphene, a multiple scattering calculation was performed. Graphene consists of a honeycomb lattice of carbon atoms with two non-equivalent sites per unit cell, labeled as site A and site B. The distance between adjacent carbon atoms is approximately 1.42 Å. The transition matrix element for graphene is given by

$$M_{i\to f}(\mathbf{k}_f) \propto (A(\mathbf{k}_\parallel)\cdot M_A(\mathbf{k}_f) + B(\mathbf{k}_\parallel)\cdot M_B(\mathbf{k}_f)) \times \delta(h\nu - E_k - W - E_B), \tag{5.12}$$

where $A(\mathbf{k}_\parallel)$ and $B(\mathbf{k}_\parallel)$ are complex coefficients, the initial state of graphene is written as $|\psi_i\rangle = A(\mathbf{k}_\parallel)|C_A\rangle + B(\mathbf{k}_\parallel)|C_B\rangle$, $M_A(\mathbf{k}_f)$ and $M_B(\mathbf{k}_f)$ are the atomic-like transition matrix elements of site A and site B, respectively and is defined as $M_{A/B}(\mathbf{k}_f) = \langle\psi_f(\mathbf{k}_f)|\vec{\epsilon}\cdot\vec{r}|\psi_{A/B}\rangle$. The photon energy, kinetic energy of the emitted electron, work function and binding energy with respect to the Fermi energy in Equation 5.12 are represented by $h\nu$, E_k, W and E_B, respectively. For the calculations, it is important to coherently add the contributions from site A and site B. This means that the transition matrix elements from site A and site B are combined before squaring to obtain the total intensity. Coherent addition will result in interference effects due to the phases of the wave functions from site A and site B. By adding multiple scattering, the atomic transition matrix elements are replaced by multiple scattering transition matrix elements, $M_{A,MS}(\mathbf{k}_f)$ and $M_{B,MS}(\mathbf{k}_f)$ for site A and site B, respectively. The multiple scattering matrix elements are obtained from multiple scattering calculations and in this study, EDAC code was used [111].

The complex coefficients $A(\mathbf{k}_\parallel)$ and $B(\mathbf{k}_\parallel)$ are obtained from tight binding calculation for π bands of graphene near the Fermi level. The nearest neighbour hopping Hamiltonian for carbon p_z orbital is given by

$$H(\mathbf{k}) = t\sum_i(\sigma_x \cos\mathbf{k}\cdot\mathbf{a}_i - \sigma_y \sin\mathbf{k}\cdot\mathbf{a}_i), \tag{5.13}$$

where t is the hopping parameter and was taken as 2.7 eV, the vectors $\mathbf{a}_i$ are the real space vectors and $\sigma_{x,y}$ are the Pauli spin matrices [116]. This tight binding Hamiltonian can approximately describe the π bands derived from p_z orbitals near the K points of the graphene Brillouin zone. The coherently added graphene CD calculation (without scattering) is shown in Figure 5.9 (a) and (b). Figure 5.9 (b) shows a constant energy cut at E_B = 1.2 eV. The calculation shows regions of vanishing intensity near the K points. These regions of vanishing intensity are called the dark corridors [98, 99]. These are the regions where the wave function from site A and site B enters with a phase difference of 180°. Because of the identical spherical muffin tins and because of the coherent addition, the total intensity vanishes at the dark corridor. The dark corridor regions are represented

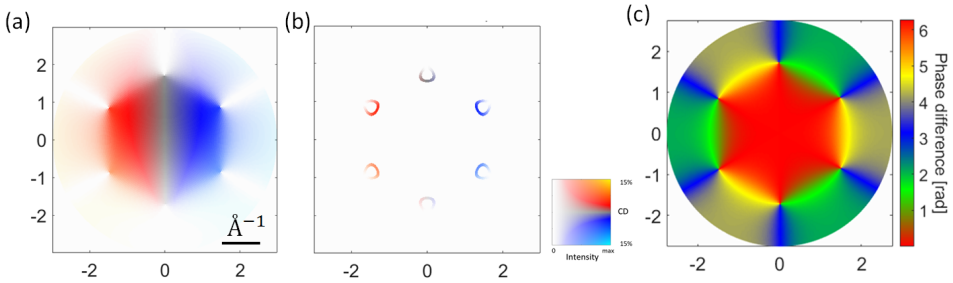

Figure 5.9: (a) CD pattern from C Y_1^0 at $h\nu$ = 40 eV, from site A and site B coherently added with the phases from tight binding calculation. Energy conservation is not taken into account and therefore (a) shows an energy integrated CD pattern over the entire p_z band. (b) shows the coherently added CD pattern same as (a) with constant energy cut at E_B = 1.2 eV. (c) Difference of the complex phases of the coefficients corresponding to A and B site for p_z bands near the Fermi level. The blue regions show that the phase difference from site A and site B is π, which will result in cancellation of the signal from site A and site B.

in Figure 5.9 (c) as blue areas, indicating a phase difference of 180° between the wave functions from site A and site B.

The coherently added photoionization plot 5.9 (b), as discussed earlier, does not agree with the experimental CD-ARPES patterns. The calculations in Figure 5.10 show the intensity profiles and CD patterns where the $M_A(\mathbf{k}_f)$ and $M_B(\mathbf{k}_f)$ are replaced by $M_{A,MS}(\mathbf{k}_f)$ and $M_{B,MS}(\mathbf{k}_f)$ in 5.12 with light incidence perpendicular to the sample surface and at 65° with respect to the surface normal, performed using EDAC. A cluster of 481 atoms was used with the radius of 20 Å. An inner potential (V_0) of 15 eV was used for the calculations shown in Figure 5.10. The multiple scattering CD pattern shows the symmetry of the crystal structure through the neighbouring atom scattering. There are three nearest neighbours in graphene as shown in Figure 5.11. When scattering from the nearest neighbours are considered, the intensity pattern also shows trigonal symmetry. The symmetry of the intensity patterns from site A and site B are inverted as the local geometry of the A and B sites are inverted with respect to each other (see Figure 5.11). The calculation clearly shows that the CD is no longer zero at normal incidence, due to the multiple scattering effects. The CD signal at normal incidence is not related to the initial state OAM, as in the normal incidence one would expect the intensity patterns to be the same for both C $_+$ and C$_-$ light. The CD asymmetry, with multiple scattering, becomes ≈ 80%.

The non-zero CD signals at normal incidence from Y_1^0 can be explained by the Daimon effect [115]. In reference [115], photoelectron diffraction measurements on the $2p$ core levels of non-magnetic Si single crystals were shown to exhibit chiral patterns, with the sense of chirality changing depending on the use of $C_\pm$ polarized light. This is due to the forward scattering of the emitted electrons. Considering the initial state as Y_1^0, the possible final states are Y_2^1 and Y_2^{-1} with C_+ and C_- light, respectively. The angular dependence of Y_2^1 is given by $\frac{1}{2}\sqrt{\frac{15}{2\pi}} \cdot e^{-i\phi} \cdot sin\theta \cdot cos\theta$. In the $x-y$ plane, the angular

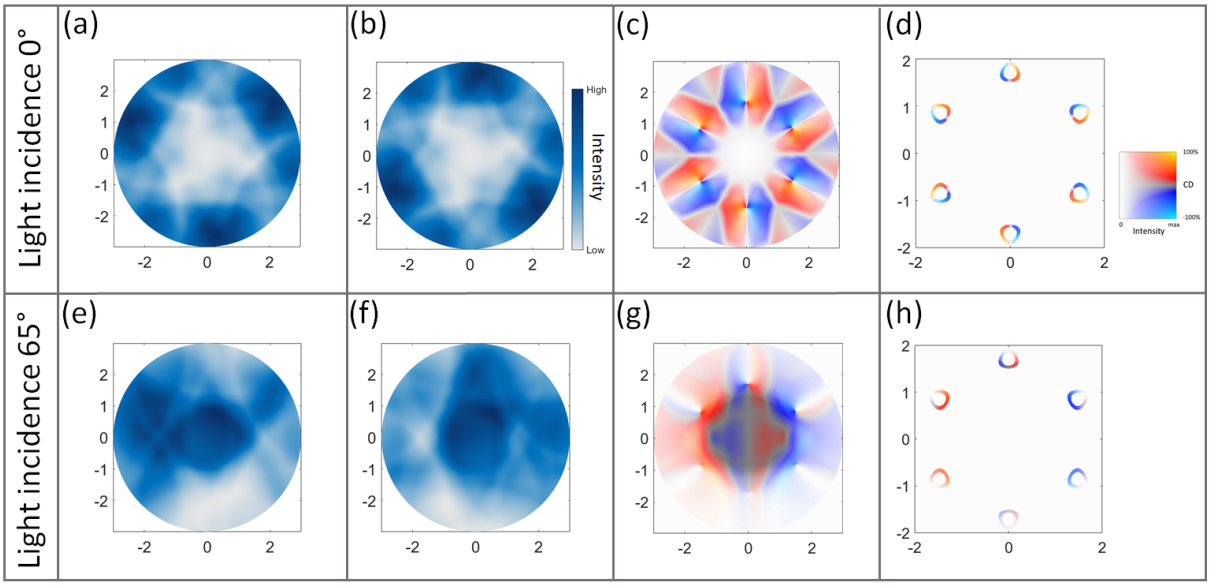

Figure 5.10: Multiple scattering calculation of C p_z orbital from graphene using EDAC code at $h\nu$ = 50 eV. (a) and (b) shows the intensity profile of emission from site A with C_+ and C_- light. (c) is CD pattern the site A and site B added coherently. For the plot from (a)-(c) the quantization axis is taken as the surface normal (z axis) and are energy integrated over the entire p_z band of graphene. (d) shows the constant energy cut at E_B = 1.25 eV similar to experimental spectra in Figure 5.5 (a)-(c). The lower panel shows the similar calculation as in the top panel with quantization axis taken as 65° with respect to the surface normal.

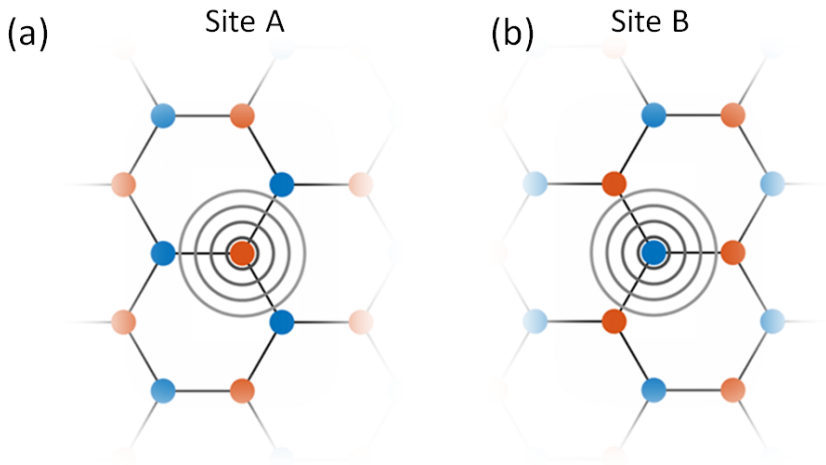

Figure 5.11: Top view of graphene lattice showing (a) site A (represented by orange color) and (b) site B (represented by blue color).

pattern is proportional to $e^{-i\phi}$. When this angular pattern is combined with the outgoing spherical wave, a spiral phase structure is obtained. The direction of propagation can be obtained by using the current operator, $\frac{i\hbar}{2m}(\psi\nabla\psi^* - \psi^*\nabla\psi)$, on the wave function. The

wavefront direction depends on the quantum number m and the distance of scatterer from the emitter. If the emitter is at position A (origin) and the scatterer is at position B, at a distance $R_{\parallel}$ from the origin on the x axis, the angle, α, between the wave propagation direction and x axis can be written as

$$tan\alpha = \frac{m}{k_{\parallel}R_{\parallel}}, \tag{5.14}$$

where $k_{\parallel}$ is the parallel component of the propagation vector and m is the azimuthal angular momentum quantum number [115]. When the scatterer is at the infinity, the angle of deviation from the x axis becomes

$$\Delta\phi_{\infty} = \frac{m}{k_{\parallel}R_{\parallel}}, \tag{5.15}$$

where $\Delta\phi_{\infty}$ is the deviation of the wave propagation direction from the x axis at infinity, m is the azimuthal angular momentum quantum number and $R_{\parallel}$ is the position of the scatterer [115]. When the chirality of the light is reversed, the forward scattering direction also reverses to $-\Delta\phi_{\infty}$. This change in the direction of forward peak direction with respect to $C_{\pm}$ light results in dichroism. The reversal of the chirality of the intensity with $C_{\pm}$ light is also visible in multiple scattering calculation at normal light incidence direction (shown in Figure 5.10 (a) and (b)). A general quantum mechanical description of the rotation of the feature with circular polarized light is given in [117], where it is shown that the rotation is related to the photoelectron diffraction.

The calculations presented in Figure 5.10 show a modulation of intensity within the contours at the K points, for both normal and off-normal light incidence. This is close to the observed experimental CD patterns, suggesting the importance of considering multiple scattering effects in graphene. With multiple scattering taken into account, the dark corridors show non-zero intensity, and a CD asymmetry of ≈ 5 % is predicted by the calculations.

The comparison between the graphene and graphite circular dichroism (CD) maps reveals significant differences in symmetry, particularly the presence of mirror symmetry along the M_x plane in graphene that is absent in graphite. This discrepancy can be attributed to the distinct crystal structures of the two materials. Graphite belongs to the space group 187, which has three mirror planes. In contrast, graphene belongs to space group 191, which features six mirror planes. This structural difference is a key factor in the differing symmetries observed in their CD maps. However, in graphene, the mirror symmetry might be broken due to the influence of the underlying hBN substrate. The hBN layer introduces back scattering effects, which can break the mirror symmetry of the CD maps. The region highlighted in Figure 5.5 (b) is likely a result of this back scattering, indicating that the hBN substrate plays a role in the observed asymmetries in graphene CD maps.

To validate the calculation made with EDAC, one step model calculation using *omni* code [98] were also performed on graphene at $h\nu$ = 35, 40 and 50 eV. The results are shown in Figure 5.12. The one step model calculation at $h\nu$ = 35 eV is in agreement with the CD pattern calculated with the PED patterns from EDAC, combined with the

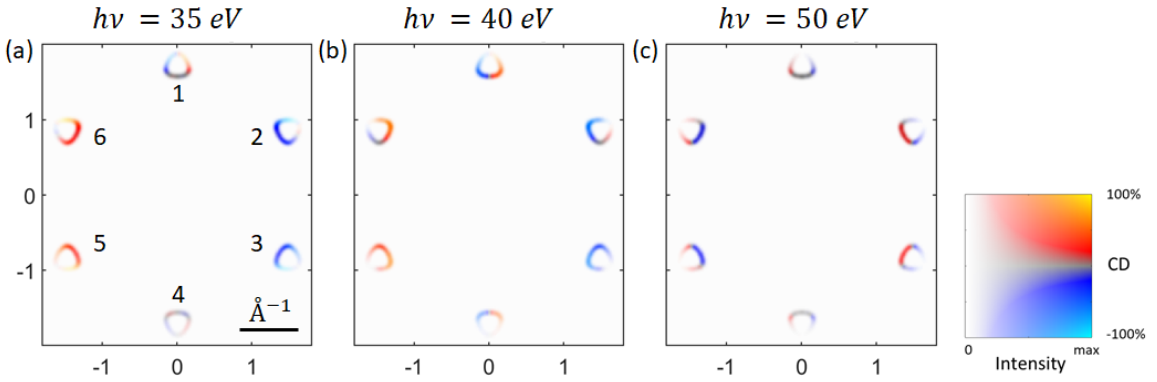

Figure 5.12: One step model calculation on graphene at $h\nu$ = (a) 35 eV, (b) 40 eV and (c) 50 eV. The calculations are performed at E_B = 0.8 eV with light incidence at 65° with respect to the surface normal.

tight binding model, at $h\nu$ = 50 eV. The one step model calculation could replicate the experimental data at K points at k_x = 0 Å^{-1} (marked as 1 in Figure 5.12 (a)) and at k_x = ± 1.48 eV, k_y = 0.78 Å^{-1} (marked as 2 and 6 in Figure 5.12 (a)) at $h\nu$ = 40 eV. The sign reversal between $h\nu$ = 35 and 40 eV at k_x = ± 1.48 eV, k_y = -0.78 Å^{-1} (marked as 3 and 5 in Figure 5.12 (a)) could not be replicated with the one step model calculation. The one step model calculation shown in Figure 5.12, used a continuously varying surface barrier, V_0, in contrast to the step potential used in the EDAC code. This can influence the CD pattern. Going beyond the muffin tin potential description may also improve the calculations and could potentially allow to reproduce the experimental results [118, 119].

5.2 CD-ARPES on WSe_2

The Dirac bands in graphene serve as an example of initial state orbital angular momentum (OAM) with a quantum number m=0, leading to a vanishing CD signal. CD-ARPES measurements on graphene highlight the significant impact of experimental geometry and multiple scattering effects on the observed CD signal. However, an important question remains unresolved regarding bands that possess a finite OAM and how the initial state OAM influences CD-ARPES measurements. To address this question, it is necessary to identify a material that exhibits non-zero OAM character, preferably with a band dominated by a single orbital character, to simplify the analysis.

WSe_2 is a two-dimensional semiconducting transition metal dichalcogenide (TMDC) with spin-orbit-split bands at the K/K' points of the Brillouin zone [120, 121]. WSe_2 is particularly interesting because of its non-vanishing orbital angular momentum (OAM) band character, primarily derived from W 5d orbitals. Additionally, WSe_2 exhibits the well-known phenomenon of hidden spin polarization [122].

The hidden spin polarization arises from the crystal structure, where both inversion sym-

metry and time-reversal symmetry are present in the bulk crystal, preventing any bulk spin polarization due to Kramer's degeneracy. However, local spin polarization can still exist in the bulk state. In the monolayer limit, the inversion symmetry is broken, leading to lifting of the Kramer's degeneracy and resulting in spin polarization of the bands. In AB-stacked monolayers, the opposite spin polarization at the K/K' points results in zero net spin polarization in the bulk crystal. Moreover, the spin-orbit-split bands at the K (or K') points exhibit opposite signs of spin polarization, as shown in Figure 5.13 (a). The

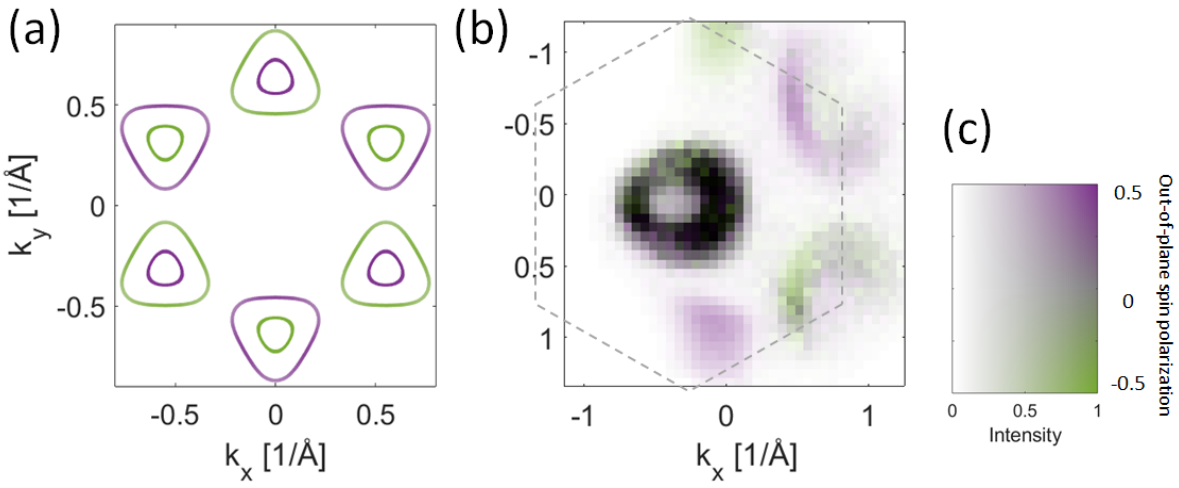

Figure 5.13: (a) Calculated out-of-plane spin angular momentum of WSe_2 monolayer using WIEN2k[33]. (b) The constant energy $k_x - k_y$ map at E_B = 0.7 eV below the valence band maximum. The spin polarized ARPES measurement shows the out of plane spin polarization in bulk WSe_2 using p–polarized at $h\nu$ = 100 eV. Only part of Brillouin zone is covered at $h\nu$ = 100 eV. The first Brillouin zone is marked in dotted lines. (c) shows the 2D colormap used in (b).

whole spin polarization reverses while moving from K to K' points.

Figure 5.13 (b) shows the spin polarized ARPES measurement at $h\nu$ = 100 eV, at ≈ 85K on bulk single crystal of WSe_2 showing out-of-plane spin polarization, where the photon beamspot is focused on a single terrace. Large single terraces are easily obtainable by scotch tape cleaving. The spin polarized $k_x - k_y$ map shows the predicted spin polarization in WSe_2 at K and K' points. Even though the measurements were performed on cleaved bulk crystal, the surface sensitivity of ARPES makes it possible to measure the spin polarization from the topmost WSe_2 layer with smaller contributions from the layer below.

In contrast to spin polarized measurements, the CD-ARPES measurements on WSe_2 show a complicated pattern at the K/K' points, which also show a strong photon energy dependence (see Figure 5.11). There is an intermixing of positive and negative values of CD magnitude at each of the K/K' points. From the photoionization cross section (shown in Figure 5.15) [123] it is clear that at the photon energies that were used for the CD-ARPES measurements, the main contributions come from W 5d, Se 4s and Se 4p. Below $h\nu$ = 130 eV, the dominating contribution comes from W 5d and above $h\nu$ = 130 eV,

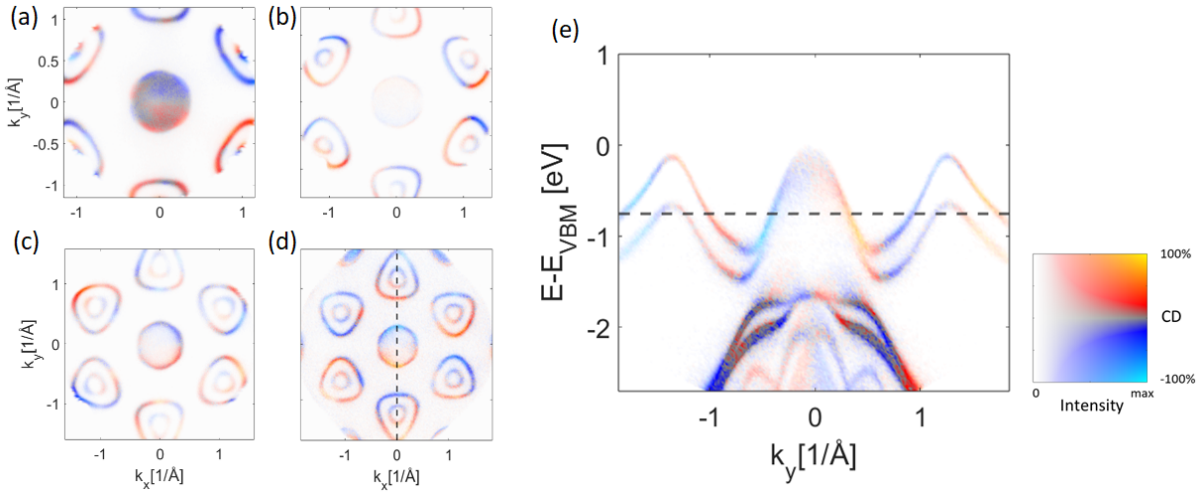

Figure 5.14: Photon energy-dependent CD-ARPES measurements on bulk WSe_2 showing constant energy cuts at $E - E_{VBM}$ = 0.7 eV at $h\nu$ = (a) 80 eV, (b) 120 eV, (c) 150 eV and (d) 200 eV. (e) shows the E versus $k_{||}$ along the vertical line of (d) at k_x = 0 Å^{-1}. The dotted line in (e) shows the binding energy for the plots in (a)-(d).

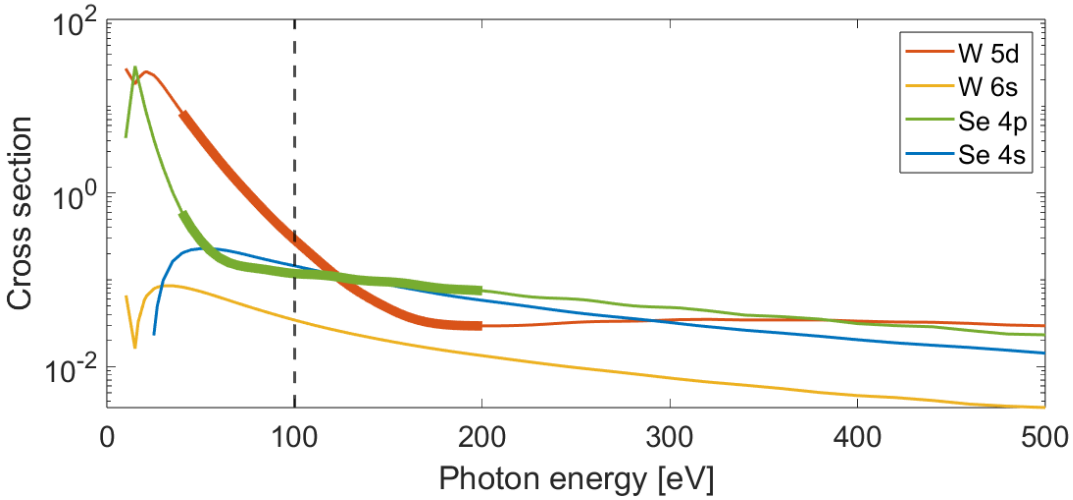

Figure 5.15: Photo ionization cross section of W 5d, W 6s, Se 4p and Se 4s for $h\nu$ = 10 eV to 500 eV. The W 5d and Se 4p cross sections in the photon energy range used for the CD-ARPES measurements are highlighted. The cross sections at $h\nu$ = 100 eV is marked with the vertical dotted line. Cross section values are taken from [123].

the Se 4p is not negligible.

Further, Y_l^m decomposition of the band structure of bulk WSe_2 were performed using Wien2k [33]. The initial state wave functions were projected onto the basis of atomic orbitals, to study the orbital character of the bands. In the study of the electronic structure near the K/K' points in WSe_2, it was found that the orbital characters are primarily

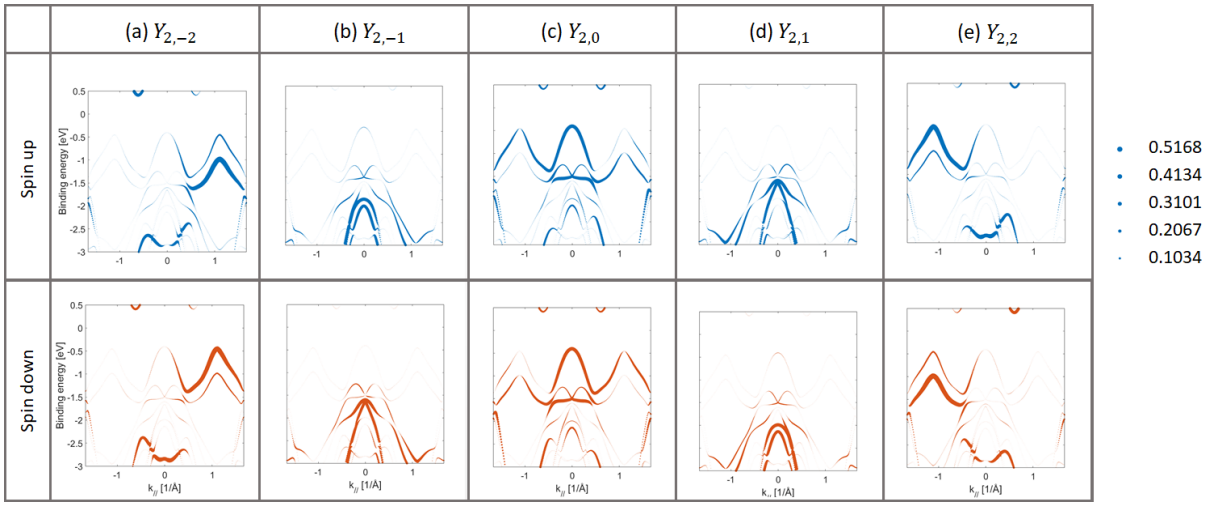

Figure 5.16: The calculated Y_l^m decomposition W $5d$ orbitals of bulk WSe_2 using WIEN2k [33]. The top panels show the spin up bands, and the columns from (a)-(e) show the Y_2^{-2}, Y_2^{-1}, Y_2^0, Y_2^1 and Y_2^2 values, respectively. The bottom panels show the spin down bands, and the columns from (a)-(e) show the Y_2^{-2}, Y_2^{-1}, Y_2^0, Y_2^1 and Y_2^2 values, respectively.

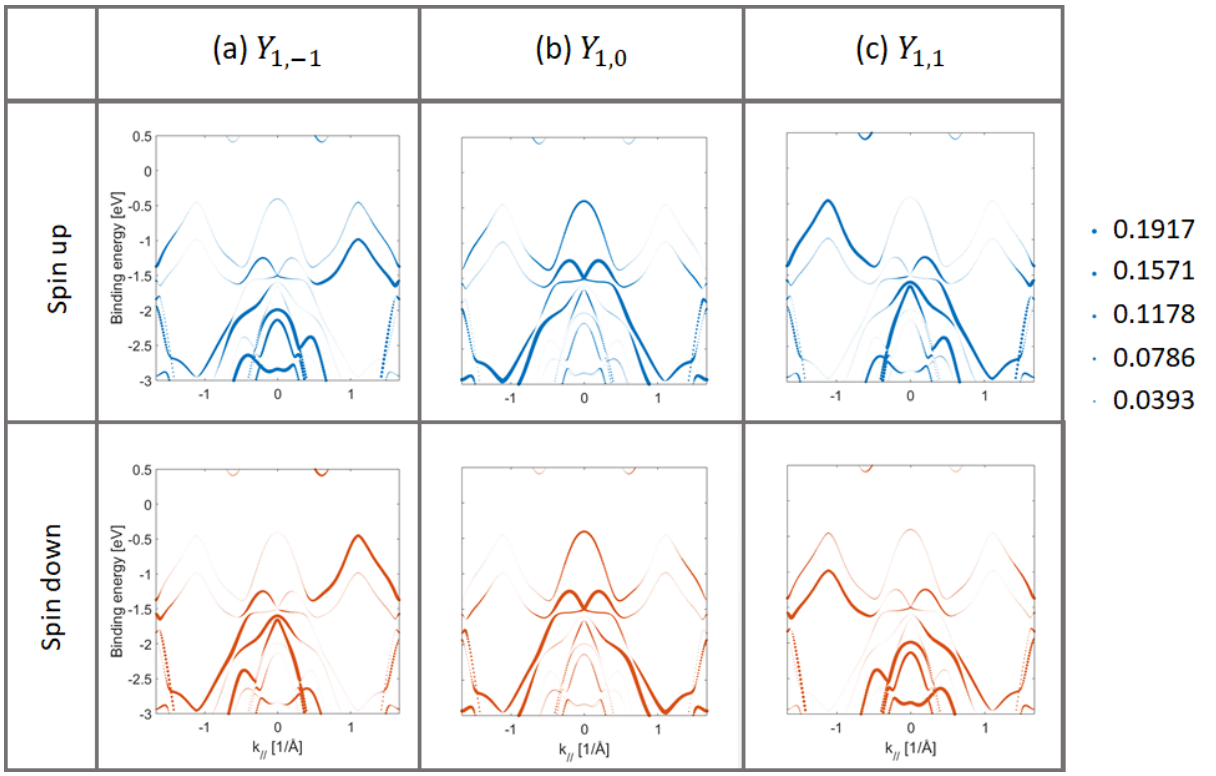

Figure 5.17: The calculated Y_l^m decomposition Se $4p$ orbitals of bulk WSe_2 using WIEN2k [33]. The top panels show the spin up bands, and the columns from (a)-(c) show the Y_1^{-1}, Y_1^0 and Y_1^1 values, respectively. The bottom panels show the spin down bands, and the columns from (a)-(c) show the Y_1^{-1}, Y_1^0 and Y_1^1 values, respectively.

mixed between W 5*d* and Se 4*p* orbitals, with negligible contributions from W 6*s* and Se 4*s* orbitals. The Figure 5.16 and Figure 5.17 show the W 5*d* and Se 4*p* contributions near the valence band maximum. The charge contribution to each eigenvalue within the respective muffin-tin spheres for W and Se atoms was analyzed. For the Wien2k calculations, the radii of the muffin-tin spheres were set to 2.45 Bohr for W and 2.33 Bohr for Se. Within these spheres, approximately 73% of the W 5*d* electron charge and 59% of the Se 4*p* electron charge were enclosed. At the K/K' points, the W 5*d* $Y_2^{\pm 2}$ orbital contributions are 0.51 and 0.47 for the upper and lower spin-split bands, respectively. For the Se 4*p* $Y_1^{\pm 1}$ orbitals, the contributions are 0.06 and 0.07 for the upper and lower bands, respectively. These values are for bulk WSe_2 at $k_z = 0$, and similar values were observed for the WSe_2 monolayer.

While the Se 4*p* contribution within the muffin-tin spheres is small, it can be adjusted to account for the overall occupancy within the spheres, potentially increasing the relative contribution to about 10-20% that of W 5*d* $Y_2^{\pm 2}$ orbitals. Additionally, Se atoms contribute more significantly to the photoemission signal due to the short inelastic mean free path (IMFP) at the relevant kinetic energies. Even though there is a non-zero contribution of Se 4*p*, especially from the $Y_1^{\pm 1}$ orbitals, for simplicity and clarity, only W 5*d* contributions will be considered for the analysis below.
From the Y_l^m decomposition of the W 5*d* orbitals (see Figure 5.16), it is evident that at the K/K' points, the $Y_2^{\pm 2}$ contribution is predominant. A constant energy cut at $E - E_{VBM} = 0.7$ eV, showing the difference in character between the W 5*d* Y_2^2 and Y_2^{-2} orbitals in monolayer WSe_2 is illustrated in Figure 5.18. The pattern shows negative CD value at

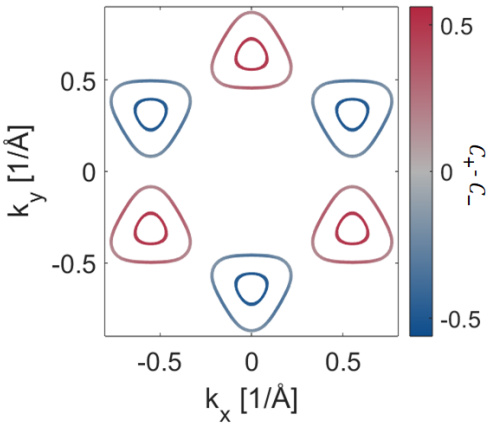

Figure 5.18: The theoretical constant energy maps at $E - E_{VBM} = 0.7$ eV shows difference of the orbital characters Y_2^2 and Y_2^{-2} of W *d* orbital of monolayer WSe_2 calculated in WIEN2k [33].

K points and positive CD value at K' points. The measured CD maps show a strong deviation from the calculated Y_l^m decomposition of the initial state. To further study the influence of initial state OAM, photoionization CD patterns from W 5*d* $Y_2^{\pm 2}$ with normal light incidence and 54.7° light incidence were calculated using EDAC code (see Figure 5.19). For the light incidence along 54.7°, the photoionization pattern displays a variation in color from red to blue, indicating a sign change in the CD value, except at photon energies $h\nu = 100$ eV and 120 eV (see Figure 5.19). At $h\nu = 100$ eV and 120 eV, the entire

emission space shows the same sign of CD. The switching of the sign of the CD value

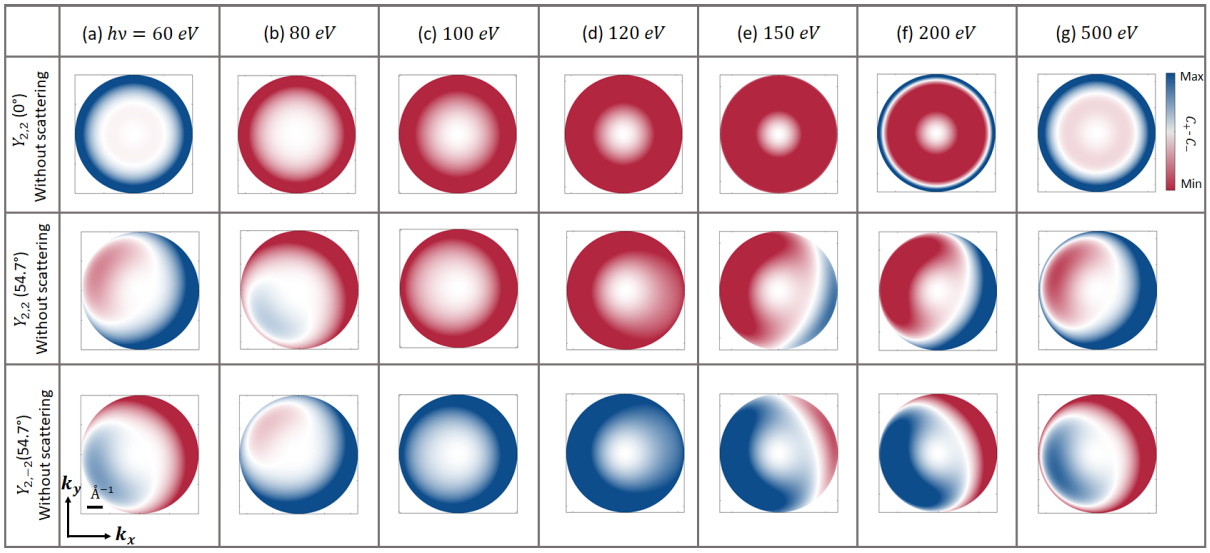

Figure 5.19: Photon energy-dependent CDAD patterns of W 5*d* orbital at $h\nu$ = 60 eV (a), 80 eV (b), 100 eV (c), 120 eV (d), 150 eV (e), 200 eV (f) and 500 eV (g). The top panels show CD patterns from Y_2^2 with quantization along 0°, the second panels show CD patterns from Y_2^2 with quantization along 54.7° and bottom panels show CD patterns from Y_2^{-2} orbitals.

in the photoionization patterns are gradual and no rapid changes are observed. But in contrast, the experimental data shows sudden changes in sign of the CD value, and this suggest that these patterns might have a different origin other than the initial state OAM.

The measurements on the cleave bulk single crystal of WSe_2 were performed at PHELIX beamline at SOLARIS [124], where the light is incident at an angle 54.7° with respect to surface normal. Like in the case of graphene, the experimental geometry itself will influence the measured spectra. The photoionization patterns at light incidence at 54.7° (second row of Figure 5.19) are similar to the normal incidence (top panel of Figure 5.19) other than a rotation of pattern in the direction of the new quantization axis, and do not show any sudden reversal of sign.

So far the final state scattering effects were not considered. A multiple scattering calculation was performed on a cluster of 463 atoms with a cluster radius of 15 Å. An atomic cluster distributed over three monolayers of WSe_2 was created. The V_0 was taken as 15 eV. The results are shown in Figure 5.20. Similar to the experimental results, a rapid change of the sign is observed in the multiple scattering CD patterns, suggesting the complex patterns might be originating from multiple scattering events. From $h\nu$ = 120 eV onwards, the forward scattering peak becomes visible (as marked in Figure 5.20 (d) bottom panel), revealing the local environment of the W atom. In the WSe_2 monolayer, the W atom is positioned beneath three Se atoms. Additionally, a calculation was performed at higher photon energy of $h\nu$ = 1000eV. The atomic photoionization pattern and multiple scattering pattern of W 5*d* Y_2^2 is shown in Figure 5.21. Both CD patterns show similar features. This

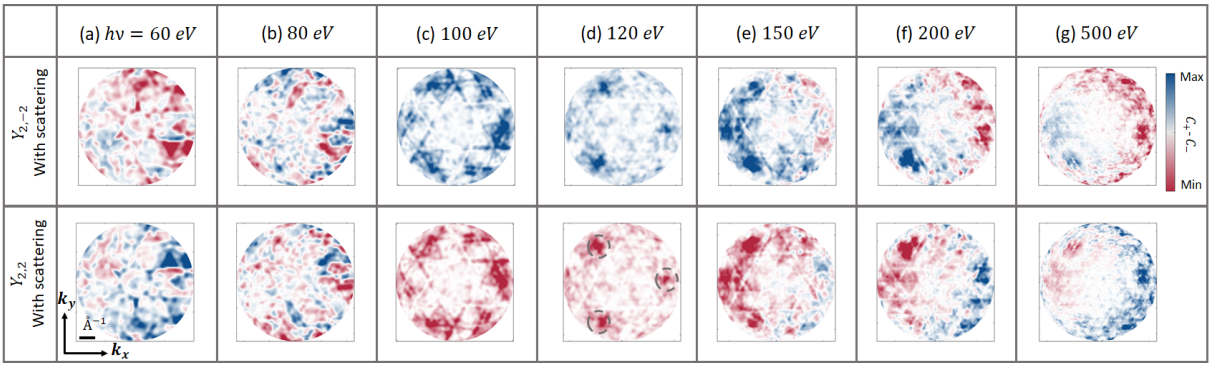

Figure 5.20: Photon energy-dependent multiple scattering calculation of W 5*d* orbital at $h\nu$ = 60 eV (a), 80 eV (b), 100 eV (c), 120 eV (d), 150 eV (e), 200 eV (f) and 500 eV (g). The top panels show CD patterns from Y_2^{-2} and bottom panels show CD patterns from Y_2^2 orbitals. The quantization axis is taken as the light incidence direction, which is at 54.7° with respect to the surface normal, along the horizontal direction.

is due to the dominance of forward scattering at higher photon energies. The multiple scattering pattern still exhibits intensity modulation, however, at higher kinetic energies, it more closely resembles the atomic photoionization pattern compared to lower kinetic energies. Consequently, using measurements at higher photon energies may offer a better opportunity to predict the initial state OAM. The problem at higher photon energies is that the photoionization cross sections become small for the orbitals. Additionally, with conventional ARPES setups only a portion of the pattern will be covered at higher photon energies as indicated by black circle in Figure 5.21

In order to reduce the contribution of Y_2^0 near the K/K' points and therefore, to minimize the experimental geometry induced dichroism in WSe_2, normal light incidence measurements were performed on WSe_2. The normal light incidence measurements are possible with conventional ARPES setups, if the sample can be rotated towards the light incidence direction. Our measurements were performed at the PHELIX beamline, the sample was rotated by 54.7° away from the normal emission direction towards the light incidence direction. However, as a consequence of rotating the sample, only higher emission angles can be detected. This means that the ARPES maps will not be centered at Γ point of the first Brillouin zone. With 54.7° rotation the ARPES maps on WSe_2 cover part of the second Brillouin zone at $h\nu$ = 60 eV, as shown in Figure 5.22 (a). Similar normal incidence measurements were performed at photo energies $h\nu$ = 100 eV, 120 eV and 200 eV, as shown in Figure 5.24. The 3D plot, showing $k_x - k_y$–energy, at normal incidence and normal emission are shown in Figure 5.23. All the maps show a complex CD pattern with sign changes within K/K' points. The normal incidence spectra still does not match the calculated initial state OAM, showing the influence of multiple scattering.

As described earlier, one unit cell of WSe_2 is made up of AB stacked monolayers of WSe_2 (see Figure 5.22 (b)), which are rotated by 180° with respect to each other. A monolayer of WSe_2 contains three atomic layers of one W and two Se atoms. The three dimensional

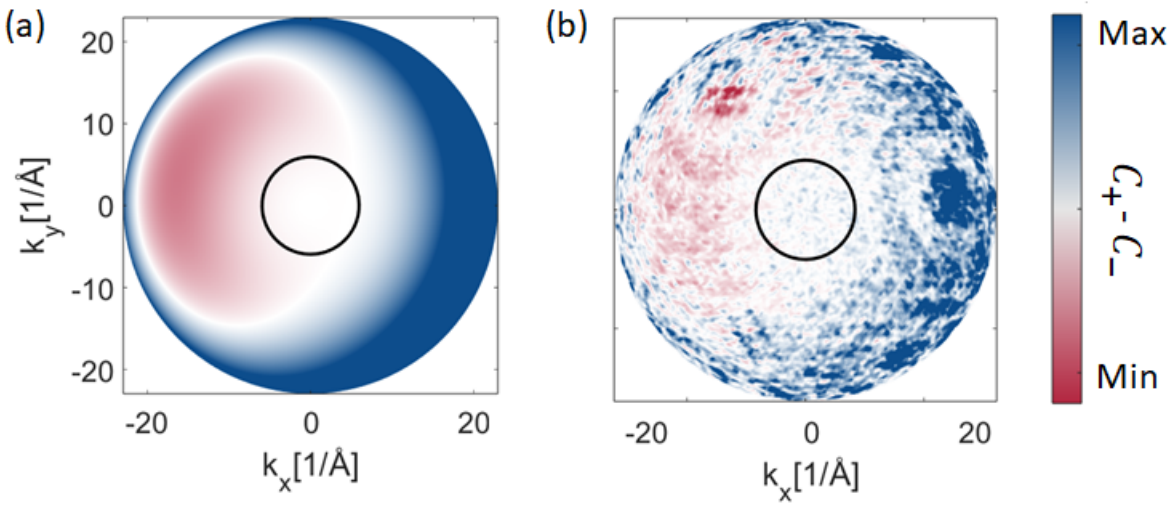

Figure 5.21: (a) Photo ionization pattern of W 5*d* Y_2^{-2} orbital from three layer WSe_2 cluster using EDAC at $h\nu$ = 1000 eV. (b) Multiple scattering CD pattern from W 5*d* Y_2^{-2} orbital from three layer WSe_2 cluster at $h\nu$ = 1000 eV. The black circles indicate the portion of the momentum space that will covered by a conventional ARPES setup with ± 15° acceptance angle.

arrangement of the atoms create a zigzag chain of W and Se, as shown in Figure 5.22 (b). The asymmetric arrangement of Se atoms with respect to the W atoms break the mirror symmetry along the z axis (see Figure 5.22 (b)). Cleaving of the bulk single crystal of WSe_2 results in two possibilities, which are named as terrace A and terrace B in this thesis. The terrace A and terrace B show different intensities at K/K' points with $C_\pm$ light. The CD-ARPES measurements on the two terraces are shown in Figure 5.25 (a) and (b). Comparing the CD maps from terraces A and B, it is evident that the sign of the CD signal is not identical on both terraces. A closer examination of the outer spin-orbit-split hole bands at the K/K' points in Figure 5.25 (a) and (b) reveals a reversal of the CD signal sign. However, not all bands exhibit the same reversal, for instance, the inner spin-orbit-split hole bands do not display the same CD patterns between terrace A and terrace B. This discrepancy arises from the broken mirror symmetry in WSe_2. The asymmetry in CD patterns originates from inter atomic interference, which occurs due to the coherent addition of emissions from different atomic sites that carry a position-dependent phase [125].

This broken symmetry effectively divides the Brillouin zone of WSe_2 into two distinct sectors, illustrated in beige and green in Figure 5.22 (a). The energy versus k_x maps, shown in Figure 5.25 (c) and (d) along the dotted line indicated in Figure 5.25 (a), reveal an interesting change in the CD signal in the spin-orbit-split bands at the K/K' points. The intensity difference of C_+ and C_- along the dotted lines in (c) is plotted in (e) for clarity. Given that the spin-polarized ARPES measurements (Figure 5.13 (b)) and spin-polarized band structure calculations (Figure 5.13 (a)) both confirm that the spin-orbit-split bands are of spin-up and spin-down character, and considering that the Y_l^m decomposition shows virtually the same or very similar OAM for both bands at the K (or K') points, the observed differences in the CD signal (Figure 5.25 (c) and (d)) should be attributed to

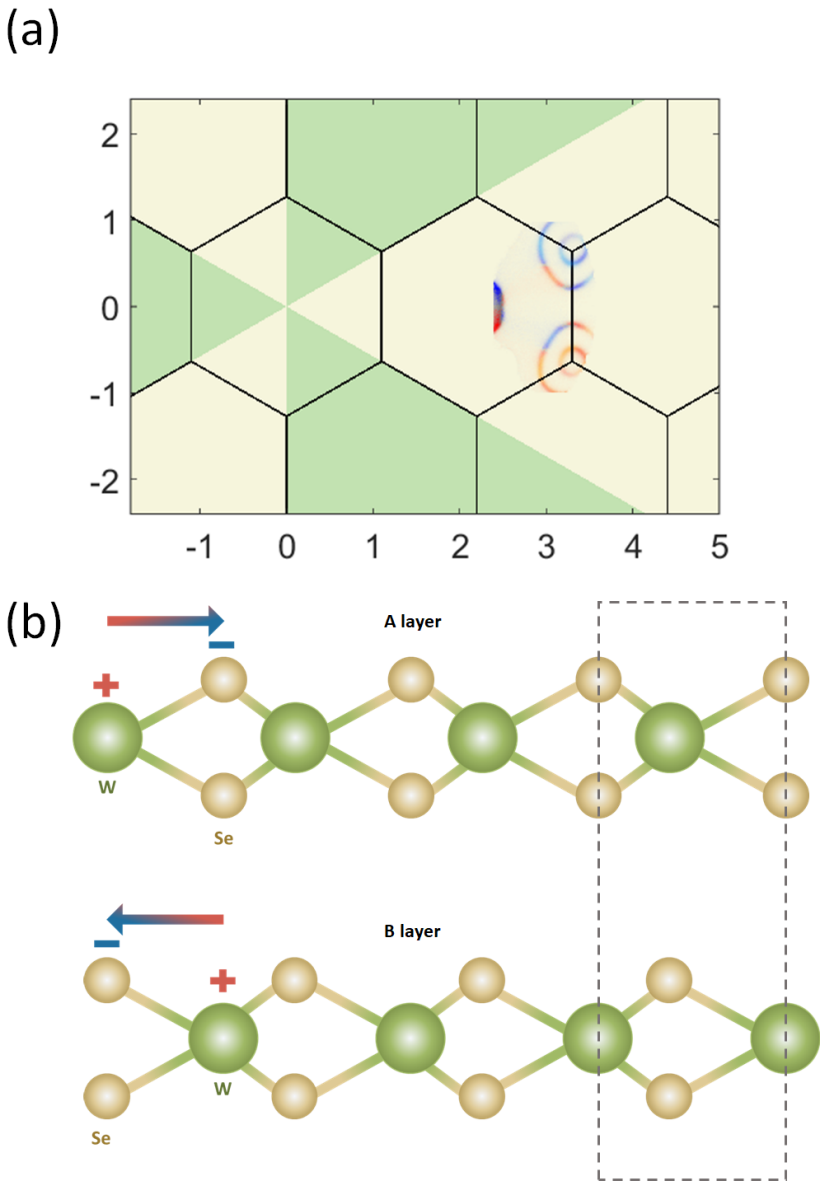

Figure 5.22: (a) Normal incidence CD-ARPES measurement on bulk WSe_2 at $h\nu$ = 60 eV. The part of the Brillouin zone measured with different regions protected by the mirror symmetry is indicated in beige and green colors. (b) side view of the crystal structure of WSe_2 showing AB stacking and resulting terrace A and terrace B are marked. The dotted lines in (b) shows the unit cell of WSe_2. The polarity of the A layer and the B layer are indicated by the arrows.

spin-dependent scattering effects.

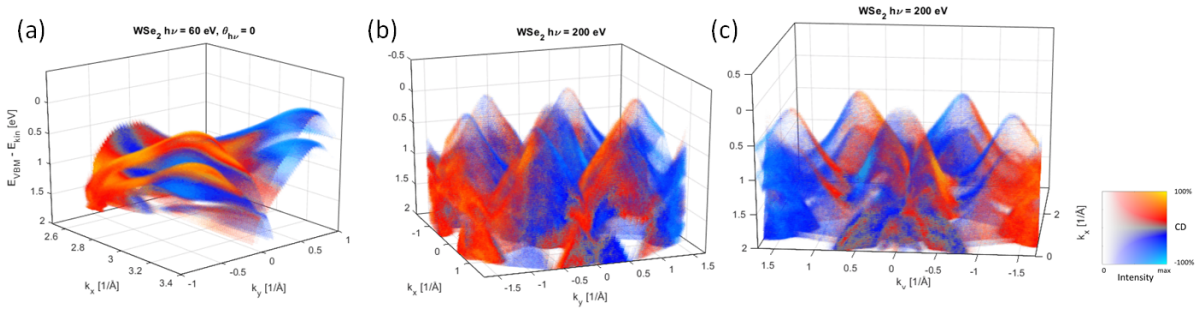

Figure 5.23: 3D plots of the experimental CD-ARPES spectra showing $k_x - k_y$–energy (a) at $h\nu$= 100 eV at normal incidence and (b) at $h\nu$ = 200 eV at normal emission. (c) shows part of the plot in (b) from k_x 0 to 2 Å^{-1}. The CD-ARPES magnitude at the spin-orbit-split bands at K/K' are shown in (c)

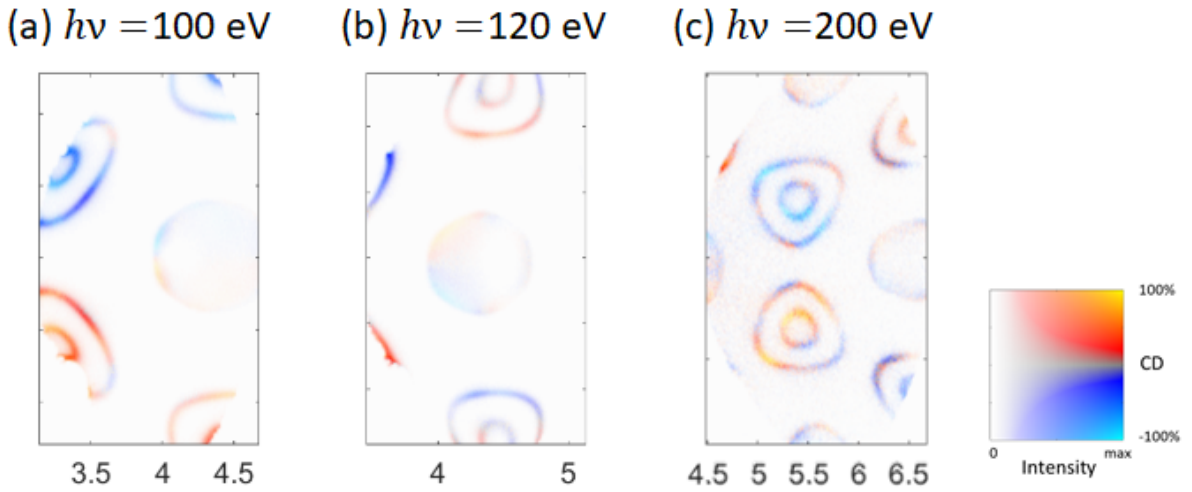

Figure 5.24: Normal incidence CD-ARPES measurements on single terrace of bulk WSe_2 at $h\nu$ = 100 eV (a), 120 eV (b), and 200 eV.

5.3 Conclusion

In conclusion, CD-ARPES studies of two distinct materials, graphene and WSe_2 reveal the complexities involved in interpreting circular dichroism signals, particularly concerning the initial state orbital angular momentum (OAM).

In graphene, where the initial state OAM is zero, the CD-ARPES maps are significantly influenced by the experimental geometry and final state scattering effects. A comprehensive theoretical analysis conducted on graphene highlights the importance of considering photoemission matrix element effects when interpreting these maps. This study demonstrates that CD-ARPES results cannot always be directly correlated with the initial OAM, highlighting the need for caution in making such associations.

For WSe_2, the initial state exhibits a well-defined OAM. However, the experimental

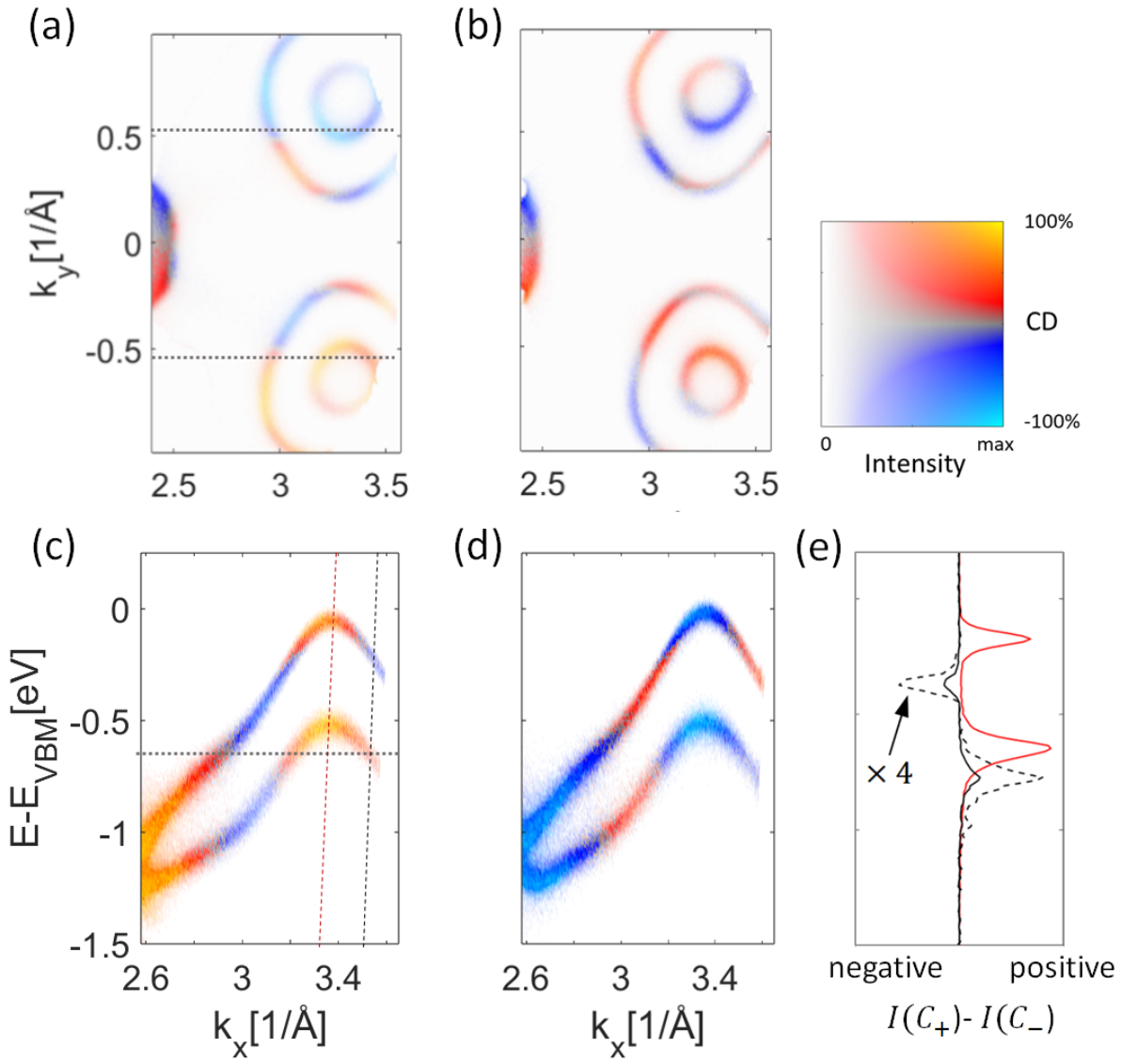

Figure 5.25: Normal incidence CD-ARPES measurement on bulk WSe_2 at $h\nu$ = 60 eV on (a) terrace A and (b) terrace B. (c) and (d) are the E versus k_x spectra along the dotted line shown in (a). The constant energy cut in (a)-(b) is at $E - E_{VBM}$ = 0.7 eV as shown in dotted lines in (c). (e) the red and black curves shows the intensity difference between C_+ and C_- along the red and black dotted lines in (c). The black dotted line is black solid line multiplied by 4.

CD-ARPES maps display a complex pattern that is not directly related to the initial OAM but rather shows a strong influence of multiple scattering. Notably, measurements taken at normal incidence reveal indications of spin-dependent scattering, suggesting that CD-ARPES can be utilized for spin detection.

The scattering effects discussed in this chapter provide valuable insights for improving experimental techniques, particularly in the development of more effective spin detectors.

These findings emphasize the complex nature of CD-ARPES and its potential applications beyond simple OAM analysis.

6 Magnetism and orbital angular momentum of $Cr_2Ge_2Te_6$

$Cr_2Ge_2Te_6$ (CGT) is a 2D magnetic semiconductor [10] with a reported indirect band gap ranging from 0.2 to 0.74 eV [126–128] and a Curie temperature (T_C) of approximately 61 K [126, 129, 130]. CGT is an interesting material not only because of its magnetic properties but also due to the possibility of tuning its magnetic and electronic properties through external perturbations. Electrostatic gating [74, 131, 132], intercalation of organic molecules [133], adsorption of molecules [134, 135], interfaces in heterostructure with magnetic oxides [136, 137], pressure [138, 139] and strain [140] all influence the properties of CGT.

An enhancement of T_C up to 200 K has been observed in double-layer transistor devices using CGT with electrostatic gating [131]. It has also been observed that the application of pressure and intercalation of organic molecules change the easy axis from the c axis to the ab plane and makes CGT metallic in nature [133, 139]. Additionally, the application of external strain increases the T_C of CGT [140].

There exist experimental band structure studies focusing on the 2D nature of the bands, Coulomb interactions in Cr d electrons and atomic (Cr and Te) contributions in CGT band structure [127, 141–144]. However, a detailed analysis of the orbital character of the bands is still lacking. This study aims to understand the atomic and orbital composition of the band structure using photon energy-dependent and light polarization-dependent ARPES measurements. To investigate the origin and stabilization of magnetism in CGT, temperature-dependent ARPES measurements have been performed and analyzed, covering the transition from the paramagnetic to the ferromagnetic state. Additionally, the experimental findings are supported by theoretical band structure calculations.

6.1 Structural properties of $Cr_2Ge_2Te_6$

CGT belongs to the space group number 148 ($R\bar{3}$) with lattice constants $a = b = 0.690$ nm and c= 2.18 nm [126, 129]. In the crystal, Cr ions and Ge-Ge dimers are inside the distorted octahedral voids formed by AB stacked Te layers (see figure 6.1 (a) and (b)). These Te layers form the van der Waals gap between CGT monolayers. Three ABC stacked monolayers form one primitive rhombohedral unit cell of CGT, as shown in figure 6.1 (c). The conventional hexagonal Brillouin zone and primitive rhombohedral Brillouin zone of

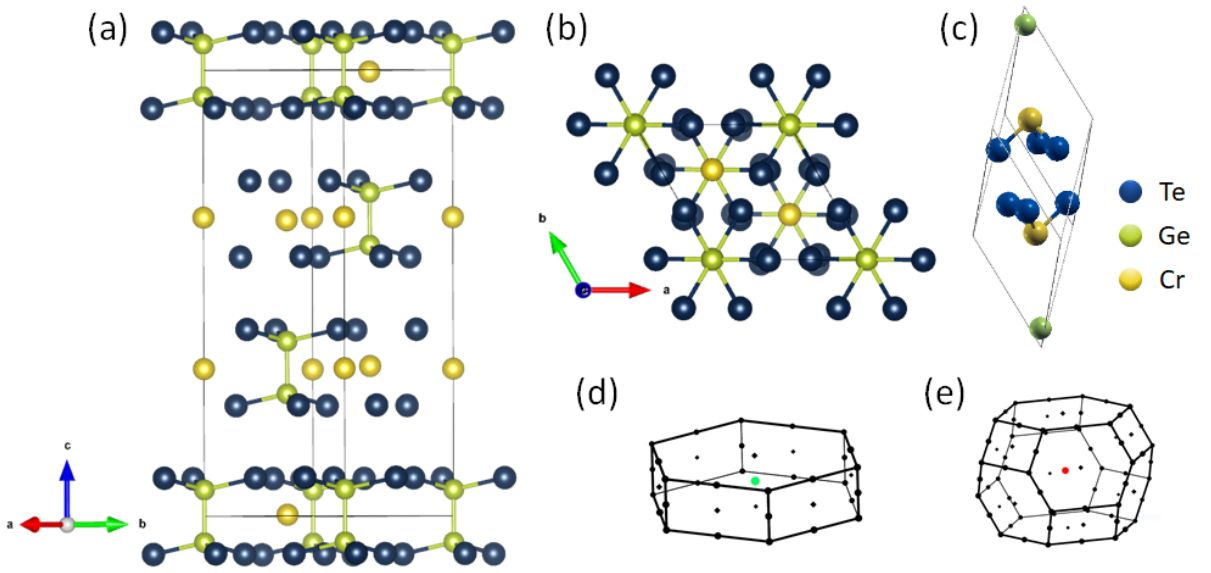

Figure 6.1: Crystal structure of $Cr_2Ge_2Te_6$ (a) side view and (b) top view. The conventional unit cell is indicated in (a) and (b). (c) shows the primitive rhombohedral unit cell of CGT. (d) and (e) are the conventional and primitive Brillouin zones of CGT respectively.

CGT are shown in figure 6.1 (d) and (e), respectively. There are no mirror planes in either the bulk or monolayer forms of CGT. However, the CGT crystal structure is inversion symmetric.

The Cr ions is the magnetic atom in CGT. The easy axis is along the out-of-plane direction [128], and magnetism is observed even in the bi-layer limit [10]. CGT exhibit domain patterns such as stripe domains and magnetic chiral bubbles below T_C with applied magnetic field [145, 146].

6.2 ARPES measurements on $Cr_2Ge_2Te_6$

A commercially grown single crystal of CGT from *HQ graphene*, a company specializing in single crystals, was cleaved inside an ultra-high vacuum chamber using Scotch tape. The ARPES measurements were performed at the PHELIX beamline at the SOLARIS synchrotron. The sample was cooled using liquid helium, and the temperature was initially stabilized at 65 K for ARPES measurements in the non-magnetic state. For all measurements, the sample was oriented such that the $M - \Gamma - M'$ direction was parallel to the entrance slit of the analyzer (see chapter 3). The photon beam was incident at an angle of 54.7° with respect to the surface normal, along the $K - \Gamma - K'$ direction, as shown in Figure 6.2.

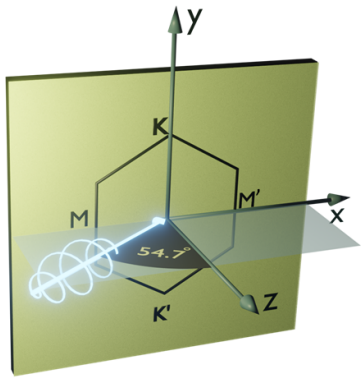

Figure 6.2: Schematic diagram of the experimental geometry for the CGT measurement at PHELIX beamline. The light is incident at an angle 54.7° with respect to the surface normal, along the $M - \Gamma - M'$ direction of the Brillouin zone.

6.2.1 Atomic and orbital composition of the band structure

To study the origin of magnetism and the orbital angular momentum of the bands, a deeper understanding of the atomic contributions to the band structure is required. For this purpose, a photon energy-dependent ARPES measurement was performed by selecting an energy range that passes through one of the absorption edges. The advantage of using this energy range is the enhancement in intensity when the photon energy matches the core-level energy, a phenomenon known as resonance enhancement.

At resonance, two possible photoemission channels exist. The first is the direct channel, which corresponds to normal photoemission, where an electron is emitted from the valence band. The second is the indirect channel, an Auger-like emission process caused by the excitation and de-excitation of a core electron. These two channels interfere coherently, resulting in an increase in the intensity of the bands contributed by the specific core-level atom. This enhancement makes it easier to study atomic contributions to the band structure [141]. The physics and process of resonant photoemission are discussed in detail in Chapter 7. Cr 3p core level at ≈ ore level at approximately 50 eV was chosen, as Cr is the magnetic atom and is therefore directly related to the magnetic properties of CGT. The experimental results of photon energy-dependent measurements, conducted within the range at $h\nu$ = 46 eV and 60 eV are shown in figure 6.3. There is a clear intensity enhancement while moving through the core level absorption edge energy. For a detailed analysis, the intensity versus photon energy curves for the selected regions of the $E(k)$ have been plotted in figure 6.4. An intensity enhancement up to 6-8 times is observed in bands at binding energies around 1.3 eV and 2.08 eV (shown in green in figure 6.4) below valence band maximum (VBM). In contrast, the intensity enhancement of the bands at the VBM is only approximately threefold, as shown in Figure 6.4. From the observed intensity enhancement, it is evident that the bands at $E - E_{VBM} \approx$ 1.3 eV and 2.08 eV below the VBM are primarily derived from Cr orbitals, whereas the top of the VBM is likely contributed by Te or Ge orbitals. These conclusions are based on the assumption that the monochromator or the undulator flux remains constant over the entire photon energy range used for the measurements shown in Figure 6.4.

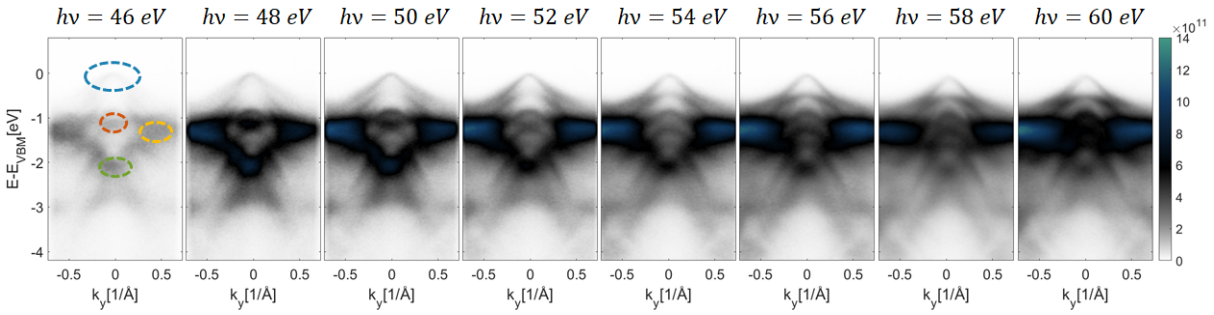

Figure 6.3: Photon energy-dependent ARPES spectra on CGT from $h\nu$ = 46 eV to $h\nu$ = 60 eV. The E vs. k maps show the intensity enhancement of the selected bands while approaching the $3p$ core level binding energy at $h\nu$ = 55eV.

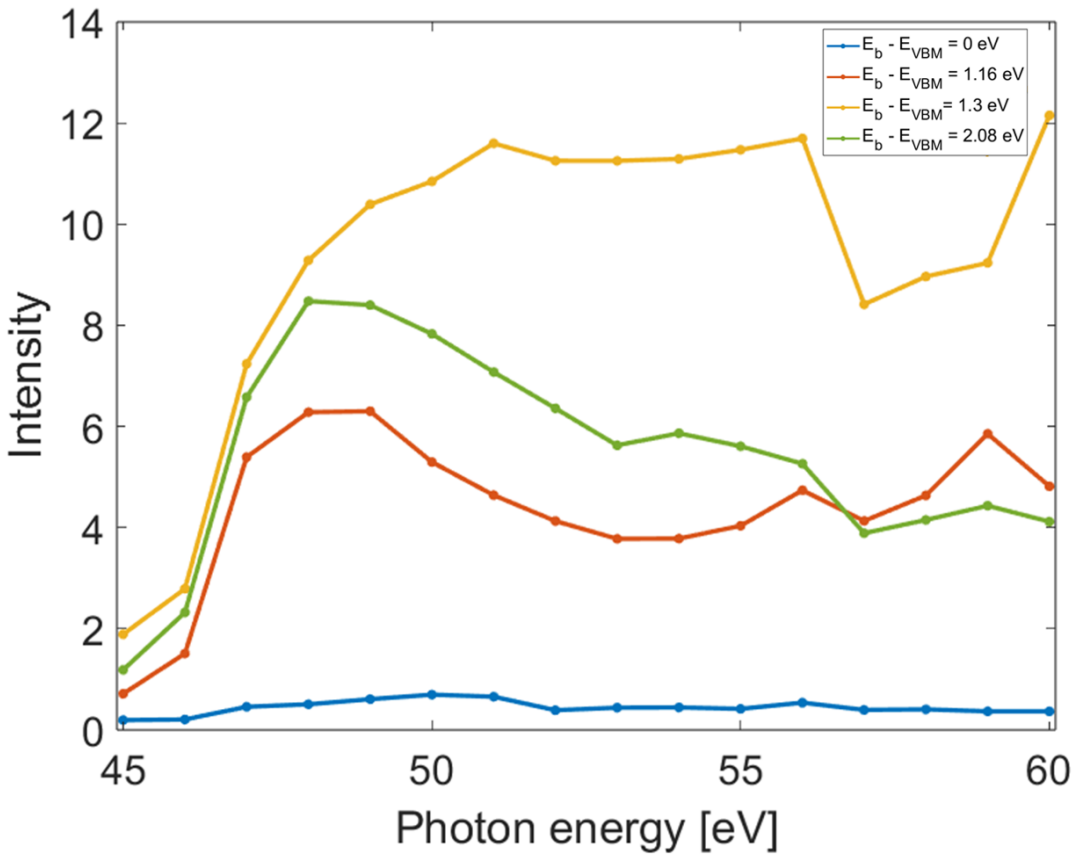

Figure 6.4: Intensity vs. photon energy plots of CGT experimental spectral functions at $E_b - E_{VBM}$ = 0 eV and $k_{||}$ = 0 Å^{-1} (blue), $E - E_{VBM}$ = 1.16 eV and $k_{||}$ = 0 Å^{-1} (red), $E_b - E_{VBM}$ = 1.3 eV and $k_{||}$ = 0.66 Å^{-1} (yellow) and $E_b - E_{VBM}$ = 2.08 eV and $k_{||}$ = 0 Å^{-1} (green). The regions considered for the plots are marked in figure 6.3 ($h\nu$ =46 eV).

To confirm these experimental findings a DFT slab calculations for 9 monolayer CGT slab was performed and are shown in figure 6.5. The atomic positions of CGT can be found in

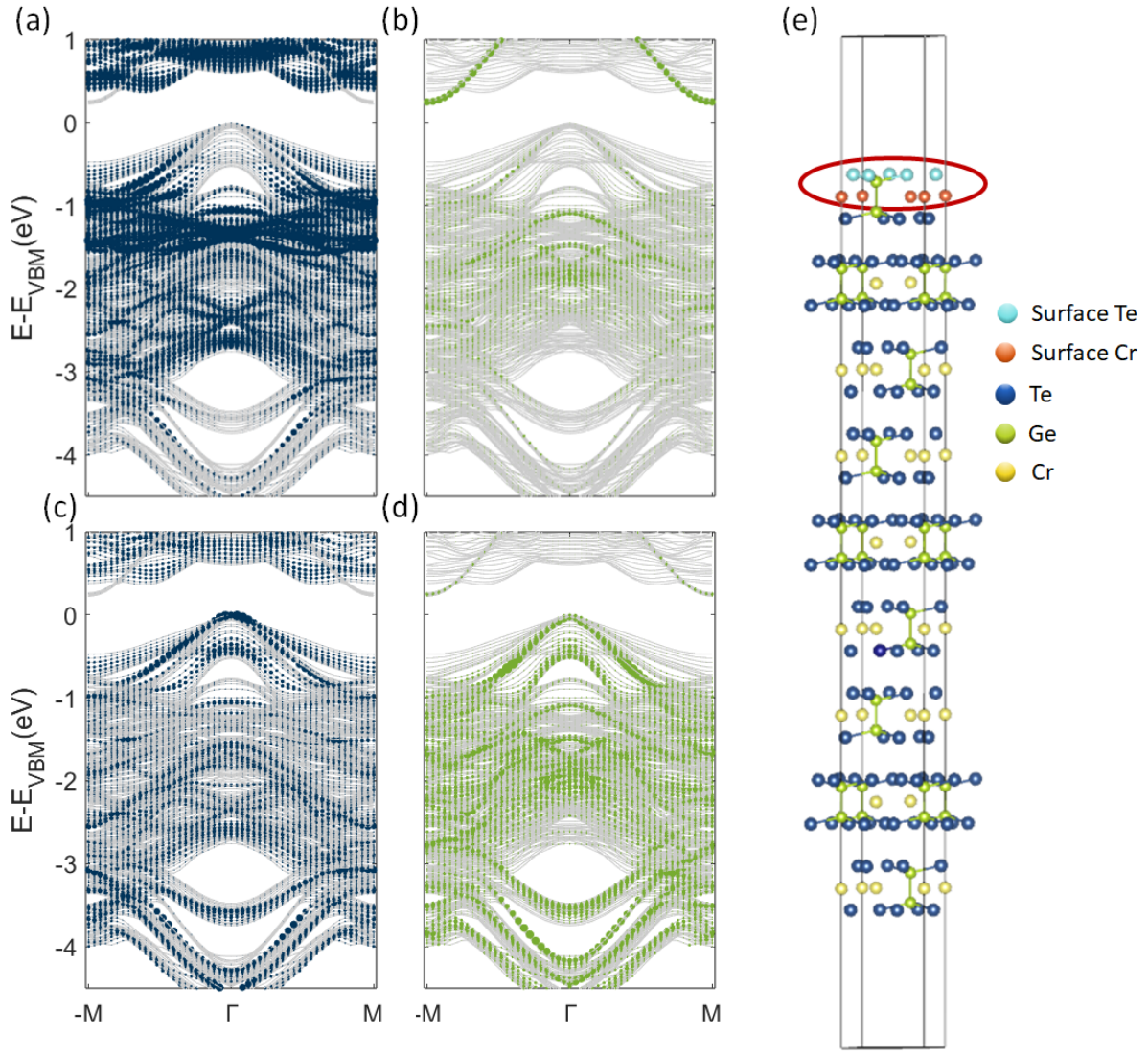

Figure 6.5: 9 monolayers (shown in (e)) DFT slab calculation of CGT. (a) and (b) shown Cr 3*d* spin and spin down contributions respectively in the band structure. (c) and (d) show the Te 5*p* spin up and spin down contributions respectively. The plots shows the contribution from the surface atoms, that are marked in (e).

references [126, 129, 147]. For the calculations presented in figure 6.5, the atomic positions from reference [126] were used. Due to the surface sensitivity of ARPES, only the band characters of Cr and Te from the surface of the slab are plotted in Figure 6.5 (a)-(d). The surface Cr and Te atoms are marked in Figure 6.5 (e). In agreement with the experimental results, the DFT calculations indicate the dominance of Cr 3*d* contributions at energies 3 eV to 0.5 eV below the VBM. The top of the valence band is mainly formed by the Te 5p orbitals as shown in figure 6.5 (c) and (d).
To understand the long-range magnetic ordering in CGT crystals, it is necessary to examine the electronic configuration and the local environment of the magnetic ion. The presence of neighboring atoms can alter the energy levels of the magnetic ions. The intra-atomic exchange-correlation energy and Coulomb repulsion, along with inter-atomic interactions,

influence the spin moment on these magnetic ions. This phenomenon is explained by crystal field theory or ligand field theory. Crystal field theory or ligand field theory is widely used to describe magnetism in transition metal oxides, where the transition metal ion is surrounded by oxygen atoms. The effect of neighboring atoms can be considered as a perturbation field acting on the central atom (see chapter 7 of [148]). Tetrahedral and octahedral geometries are the most common configurations in transition metal oxides. In these structures, the d orbitals of the transition metal interact with the p orbitals of oxygen, leading to the splitting of the d orbitals. This splitting strongly depends on the spatial configuration of the d orbitals. In tetrahedral geometries, where the bonds are formed along the diagonals of a cube, the d_{xy}, d_{yz} and d_{xz} orbitals experience greater Coulomb repulsion from neighboring atoms. As a result, the energy of these orbitals increases relative to the $d_{x^2-y^2}$ and d_{z^2} orbitals. A schematic diagram of tetrahedral and octahedral geometries, along with the corresponding crystal field splittings, is shown in Figure 6.6. The d_{xy}, d_{yz} and d_{xz} orbitals with higher energy are called the t_{2g} orbitals and the $d_{x^2-y^2}$ and d_{z^2} with lower energy are called the e_g orbitals. On the other hand, for an octahedral complex, the neighboring atoms approach along the principle axis, increasing the energy of the e_g orbitals with respect to the t_{2g} orbitals [148].
In case of CGT, as mentioned earlier, the magnetic Cr^{3+} ions are located inside the distorted octahedral voids formed by the Te atoms [141]. This geometry lifts the degeneracy of the Cr d orbitals by increasing the energy of e_g orbitals and lowering the energy of t_{2g} orbitals. Consequently, the three electrons in the Cr^{3+} ions, which have a $3d^3$ electronic configuration, will occupy the lower-energy t_{2g} orbitals. Since the t_{2g} orbitals do not participate in bond formation with the neighboring Te $5p$ orbitals, the bands derived from these orbitals are expected to show the highest intensity enhancement in the resonant ARPES spectra due to their dominant Cr contribution [141]. Examining the intensity versus photon energy plots shown in Figure 6.4, the non-dispersive bands at approximately 1.3 eV below the VBM exhibit the highest intensity enhancement. Therefore, the feature at 1.3 eV below the VBM can be attributed to the t_{2g} bands of Cr, whereas the feature at approximately 2.08 eV below the VBM, which shows some dispersion, originates from the e_g derived bands. The dispersion of the neighboring e_g orbitals is related to their overlap with the neighboring Te $5p$ orbitals.
In general, the Cr^{3+} derived bands are expected to be near the Fermi level due to their $3d^3$ configuration. However, based on both experimental data and DFT calculations, the highest-energy band derived from Cr is centered at approximately 1.3 eV below the VBM. The bands from -3 eV to -1 eV exhibit relatively small dispersion, with a bandwidth of approximately 0.6 eV, which may be related to the partial localization of Cr d orbitals in CGT. As a result, both itinerant and localized electron theories must be considered to explain magnetism in CGT. Previous theoretical studies have also highlighted the importance of incorporating the Hubbard U parameter in calculations to achieve better agreement with experimental results [142, 149]. This strong intra-atomic interaction significantly influences the magnetism in CGT, which will be discussed in the following section.

To investigate the $k_\perp$ dispersion of the bands and confirm the 2D nature of CGT bands, a broad photon energy range scan was performed. The band dispersion at $k_\parallel = 0$ as a function of photon energy is shown in Figure 6.7. The results essentially show nearly flat bands with very small k_z dispersion. Figure 6.7 (b) presents the calculated k_z dispersion

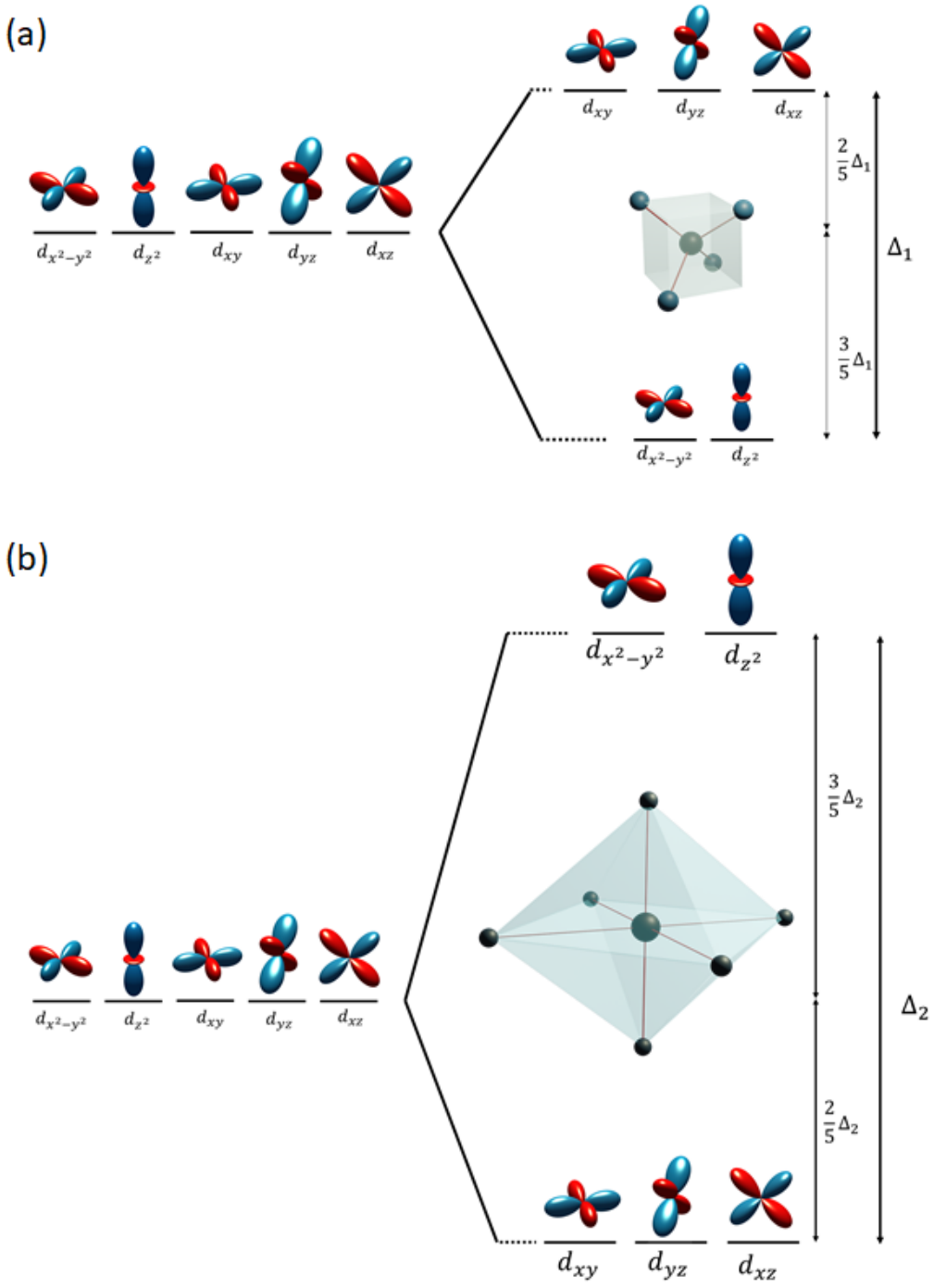

Figure 6.6: Schematic diagram of crystal field splitting in (a) tetrahedral and (b) octahedral complexes. The energy of d orbitals along the bond direction ($d_{x^2-y^2}$, d_{z^2} decreases (increases) and energy of orbitals along off diagonal directions (d_{xy},d_{yz} and d_{xz}) increases (decreases) in a tetrahedral (octahedral) complex.

of the CGT bands. The calculations indicate a small k_z dispersion, consistent with the experimental data, confirming the two-dimensional nature of CGT.

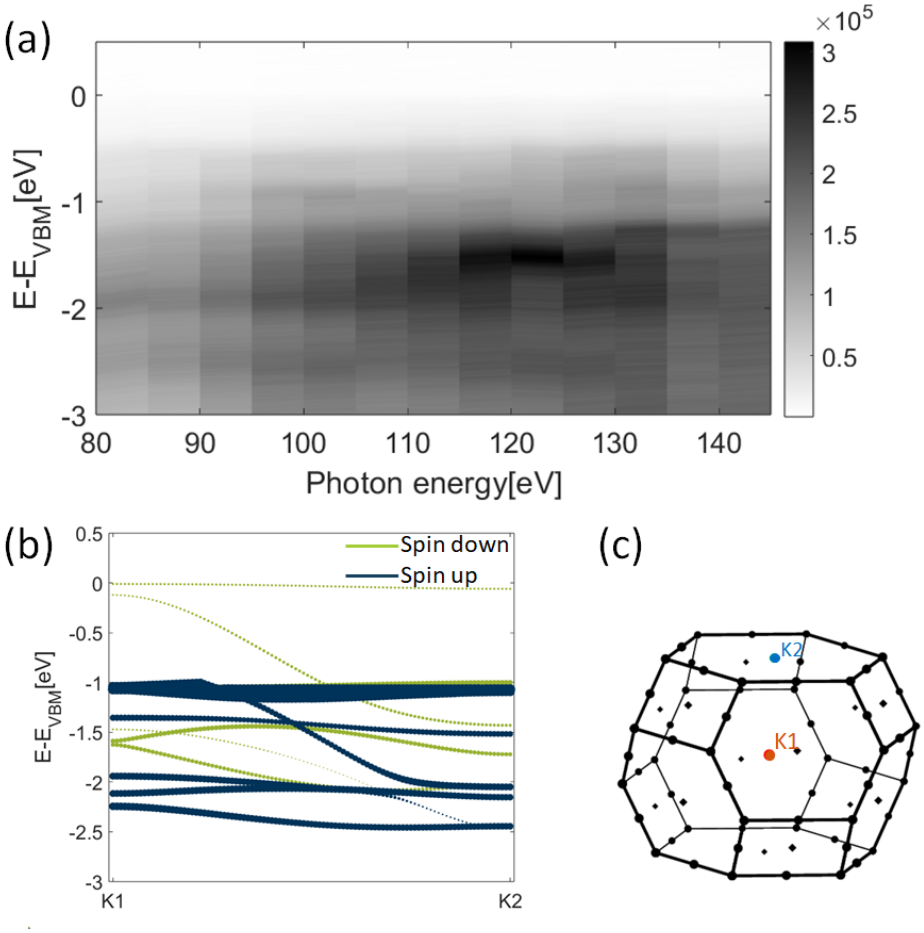

Figure 6.7: (a) k_z dispersion of CGT bands at $k_{||}$ = 0 measured with photon energies $h\nu$ = 80 to 100 eV in steps of 5 eV. (b) shows the calculated k_z dispersion of CGT bands between K1 and K2 points in the Brillouin zone as indicated in (c).

The orbital character of the bands was further analyzed using polarization-dependent ARPES measurements with linearly polarized light. The transition matrix element, $M_{i\to f} \propto \langle\psi_f|\vec{\varepsilon}\cdot\vec{r}|\psi_i\rangle$, depends on the direction of the light polarization vector $\vec{\varepsilon}$ [41]. For p–polarized light (horizontal polarization in our experimental geometry), the polarization direction is parallel to the plane of incidence, which is defined by the incident light and the surface normal. When the light is incident at an angle, as is typically the case in ARPES setups, p–polarized light acquires an out-of-plane component in addition to its in-plane component, as illustrated in Figure 6.8 (a). For s–polarized light (vertical polarization in our experimental geometry), the polarization vector is perpendicular to the plane of incidence—that is, parallel to the sample surface, as shown in Figure 6.8 (b). The intensity of emission with s–polarized light is typically lower than that with p–polarized light, particularly near normal emission angles [41]. Since most ARPES measurements are performed at angles close to normal emission, the intensity of s–polarized light is correspondingly reduced. The sensitivity of orbitals to the s– and p–polarized light depends on the experimental geometry. s–polarized light is primarily sensitive to in-plane orbitals, such as p_x and p_y orbitals. p–polarized light is more sensitive to out-of-plane orbitals, with a small contribution from in-plane orbitals due to its out-of-plane polarization component.

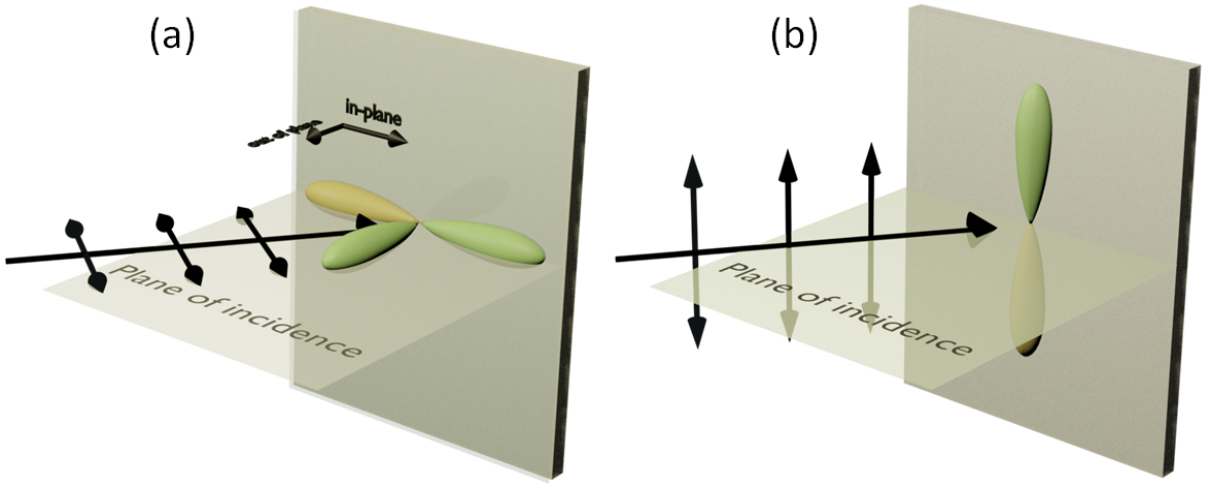

Figure 6.8: The in plane and out of plane components of the light polarization of (a) p–polarized light and (b) s–polarized light and its sensitivity to in plane and out of plane p orbitals.

This sensitivity can be utilized to determine the real orbital characters (orbitals represented in Cartesian coordinates) of the band structure. However, the above discussion applies mainly to atomic-like photoemission. In solids, the photoemission spectra also contain contributions from multiple scattering, which can modify the measured spectral function. Figure 6.9 (a) and (b) show the Energy versus $k_{||}$ maps obtained with p– and s–polarized

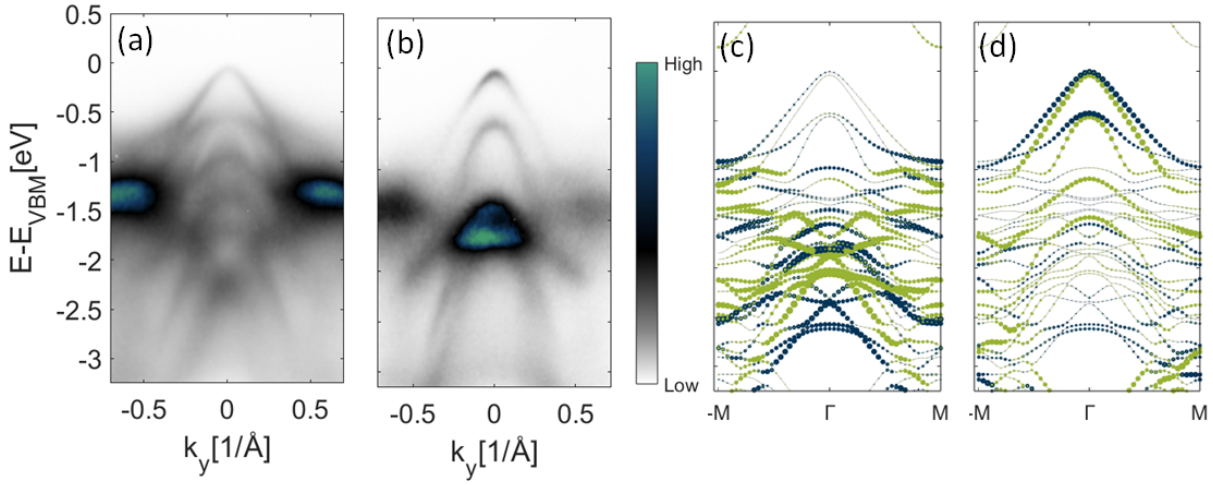

Figure 6.9: Polarization dependent measurements on CGT using (a) p–polarized light and (b) s– polarized light at $h\nu$ = 56 eV at 60 K. The calculated real orbital decomposition of Te p orbitals are shown in (c) and (d). The out of plane orbital, p_z is shown in (c) and in-plane orbitals, p_x and p_y are shown in (d). This shows the sensitivity of p–polarized light to the out of plane orbitals and s–polarized light to in-plane orbitals. The green and blue bands in (c) and (d) are spin up and spin down bands.

light, respectively. With the p–polarized light, the slightly dispersive band in the k_z

dispersion map (Figure 6.7)is clearly visible, confirming the contribution of the p_z orbital in the lower part of the valence band maximum (VBM), as shown in Figure 6.9 (c). The tip of the VBM appears more intense with s–-polarized light, indicating an in-plane orbital character. The incoherent sum of the p_x and p_y orbitals is shown in Figure 6.9 (d). Given our experimental geometry, s–polarized light is primarily sensitive to the p_y orbital due to the sample orientation. The nonzero intensity observed with s–polarized light further suggests that atomic-like polarization selection rules do not strictly apply in solids. Otherwise, one would expect zero intensity at normal emission [41].

6.2.2 Signatures of magnetism in the band structure

To study the magnetic interactions in CGT, temperature-dependent ARPES measurements were performed. The bulk transition temperature of CGT, as mentioned earlier, is approximately 61 K [126, 129, 130]. With LHe cooling, the temperature was lowered from 65 K to approximately 15 K in steps of 5 K. Figure 6.10 shows the temperature-dependent experimental band structure as it transitions from the paramagnetic state to the ferromagnetic state.

In these temperature-dependent spectra, distinct changes in the band structure are observed, including intensity renormalization, energy shifts, and band splittings, mainly from the Cr-derived bands. For detailed analysis, the energy distribution curves (EDCs) at $k_{\|}$= 0 Å^{-1} (Γ point, cut 1 in figure 6.10 (a)) and $k_{\|}$= 0.4 Å^{-1} (cut 2 shown in figure 6.10) are shown in Figures 6.10 (d) and (e), respectively.

The band at 2.25 eV below the VBM at 65 K exhibits a temperature-dependent shift to lower binding energy. The EDC at the Γ point shows a pronounced energy shift of the band at 2.25 eV below the VBM with the onset of the ferromagnetic transition. An energy shift of approximately 0.25 eV is observed. The EDC at ≈0.4 Å^{-1} (see Figure 6.10 (e)) reveals a splitting of the band at approximately 1 eV below the VBM as the system approaches the ferromagnetic transition temperature. Since the changes in the band structure correlate with the ferromagnetic transition temperature, the energy shifts and band splittings can be considered signatures of magnetism in the band structure. These findings provide insights into the origin of magnetism in CGT, as discussed in the following paragraph.

The energy shift of the e_g bands indicates that the overlap of e_g orbitals with Te $5p$ orbitals influences magnetism in CGT [141]. In a fully ionic picture, the Cr electrons occupy t_{2g} orbitals with all electron spins aligned in the same direction, as dictated by Hund's rule. Previous XAS studies on CGT [141, 143] have shown a shift in the peak positions of core levels to lower photon energies, indicating a higher occupation (3.5 electrons per atom, compared to 3 electrons) of Cr d orbitals. This suggests a partially covalent nature of the Cr-Te bonds.

In the case of partial covalency, the fully filled Te (Te^+ ion) p orbitals share one electron

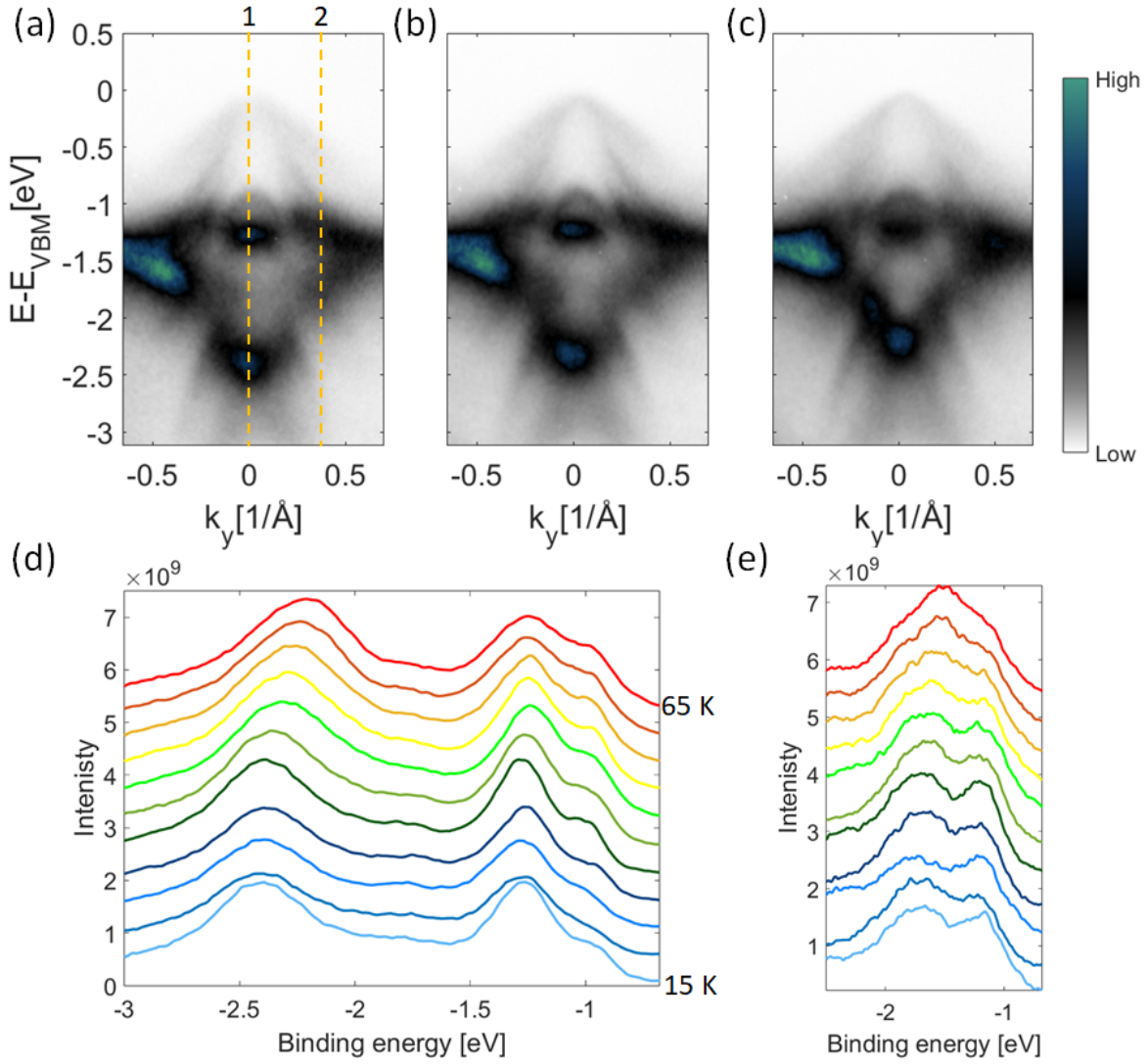

Figure 6.10: Temperature-dependent ARPES measurements on CGT at (a) 15 K, (b) 40 K and (c) 65 K. (d) and (e) shows the energy distribution curves (EDCs) at $k_{\|}$ = 0 Å^{-1} (cut 1 shown in (a)) and at $k_{\|}$ = 0.4 Å^{-1} (cut 2 shown in (a)), respectively, for temperatures 15 to 65 K. All the measurements were performed at $h\nu$= 48 eV.

with the Cr d orbital. Due to the Pauli exclusion principle, this additional electron can only occupy either the t_{2g} orbital with an opposite spin or the empty e_g orbital with the same spin. The distribution of this electron is determined by intra-atomic exchange interaction and Coulomb repulsion. In CGT, since Coulomb interaction is significantly large [142, 149], the electron moves to the e_g orbital, resulting in a high-spin state (see Figure 6.11). This transition lowers the overall energy of the e_g bands due to Hund's energy gain. The Hund's energy gain is evident in the temperature-dependent experimental spectra, where the e_g band shifts to a lower binding energy by approximately 0.25 eV. This confirms that magnetic ordering in CGT arises from interactions between the Cr and Te orbitals (see Figure 6.11 (c)). Such magnetic ordering, mediated through indirect interactions between magnetic atoms via neighboring non-magnetic atoms, is called indirect exchange interaction.

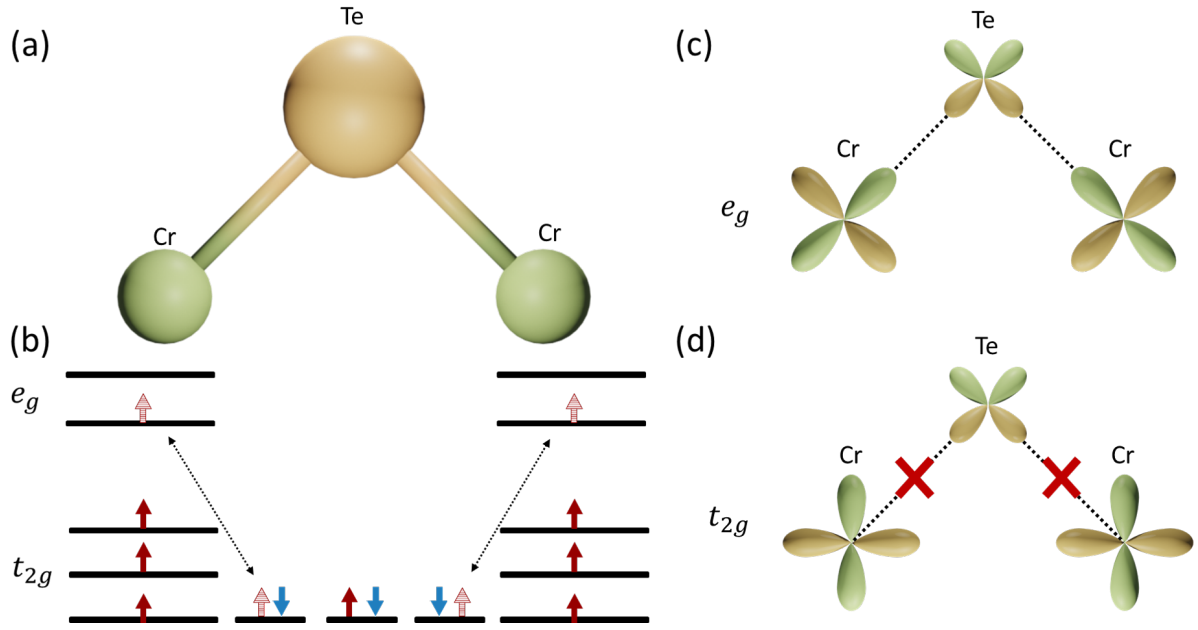

Figure 6.11: (a) The bond between Cr and Te atoms in CGT. The 90.4° bond angle between Cr-Te-Cr makes the interaction between neighboring Cr atoms ferromagnetic in nature. The electron sharing between Cr and Te atoms are shown in (b) [141]. The overlap of Te p orbital and Cr e_g and t_{2g} are shown in (c) and (d), respectively.

There are different types of magnetic interactions in solids. When electrons from a magnetic atom interact directly with neighboring magnetic atoms, it is called direct exchange interaction. Direct exchange is possible when the wavefunctions of the magnetic atoms overlap. However, when magnetic atoms are not in close proximity and their magnetic moments are localized, their wavefunctions overlap only through the intermediate orbitals of non-magnetic atoms. This type of interaction is called indirect exchange interaction.

In insulators, where conduction electrons are absent, the most favorable interaction is superexchange interaction. In superexchange interactions in transition metal oxides, electrons from the d orbitals of transition metal ions interact with non-magnetic oxygen p orbitals. The strength of the magnetic interaction in superexchange interactions depends on the magnetic moments of the atoms, the angle between the magnetic-non-magnetic-magnetic atoms, and the overlap of the wavefunctions.

When the angle between the magnetic-non-magnetic-magnetic atoms is 180°, as shown in figure 6.12 (a), the ground state is an antiferromagnetic state [150, 151]. When the angle is close to 90°, as shown in Figure 6.12 (b), the ground state is ferromagnetic. Compared to antiferromagnetic superexchange interaction, ferromagnetic superexchange interaction is weaker and results in a lower Curie temperature [152, 153].

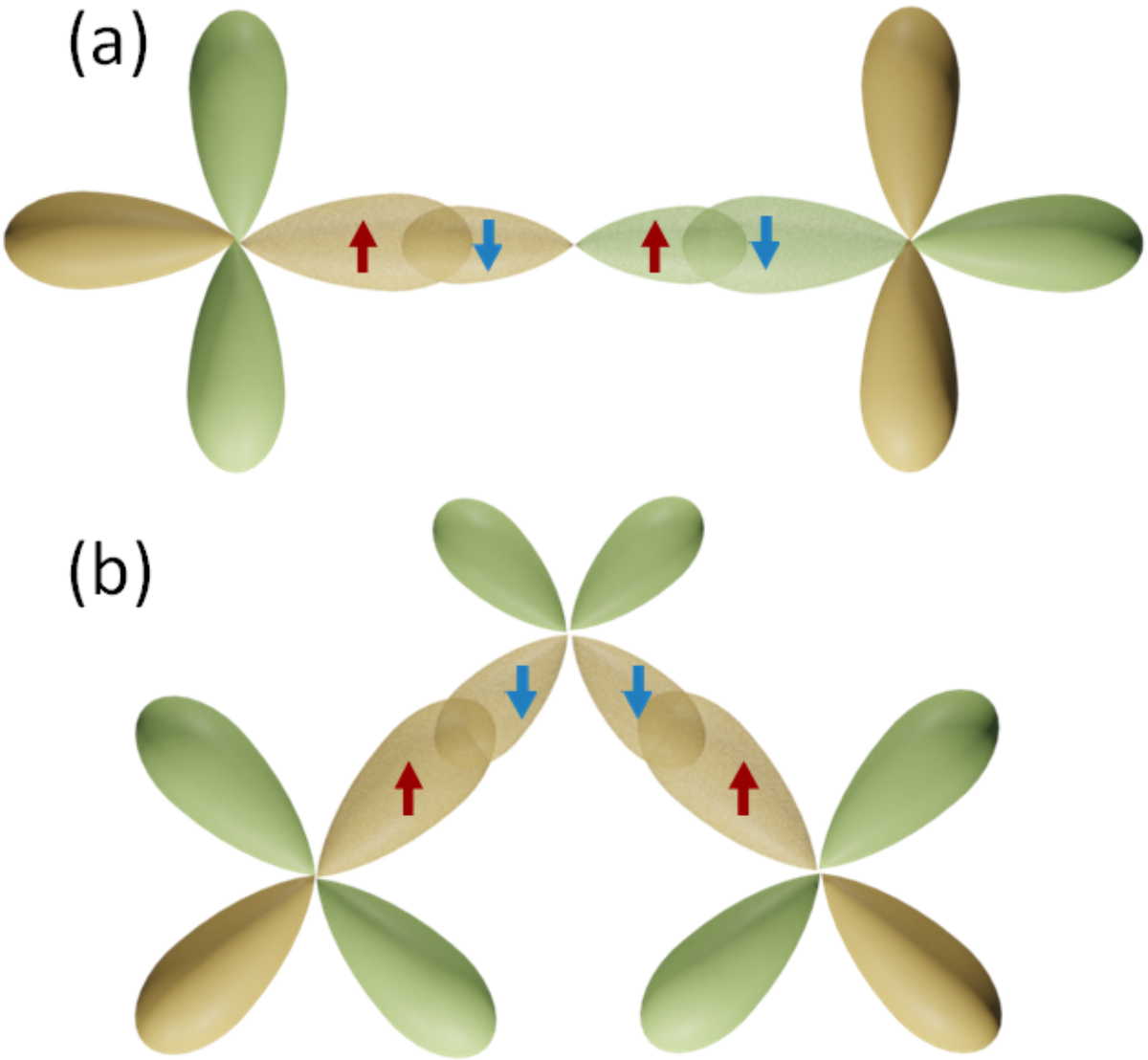

Figure 6.12: (a) shows the schematic diagram of antiferromagnetic superexchange interaction. The angle between the magnetic - non-magnetic - magnetic atom is 180°. (b) shows the schematic diagram of ferromagnetic superexchange interaction. The angle between the magnetic - non-magnetic - magnetic atom is 90°.

In transition metal insulators like CGT, the d electrons are localized to the transition metal atoms, making hopping feasible only to orbitals that are spatially close. In this case, direct exchange is not possible due to the large distance between transition metal atoms. Similarly, interactions through conduction electrons, as seen in conductors, are not feasible in insulators. Given CGT's insulating nature, the most favorable interaction is the superexchange interaction [150, 154].

There are two possible long-range magnetic orderings that can occur between Cr atoms: ferromagnetic and antiferromagnetic. The nature of this ordering strongly depends on the Cr-Te-Cr bond angle, as discussed earlier. In CGT, the experimentally determined

bond angle is close to 90°. The symmetry-allowed overlap between the e_g orbitals and the p_x and p_y orbitals, as shown in Figure 6.11 (c), stabilizes a ferromagnetic ordering in CGT [141]. The low Curie temperature of CGT may also result from the ferromagnetic superexchange interaction, which is relatively weaker compared to the antiferromagnetic superexchange interaction [152, 153].

6.2.3 CD-ARPES measurements on CGT

Circular dichroic ARPES measurements were performed on CGT to gain insight into the initial-state orbital angular momentum characteristics of CGT bands from the CD patterns. The sample was oriented so that the incident light was along the $M - \Gamma - M'$ direction, as shown in Figure 6.2. Initially, photon energy-dependent E versus $k_{\|}$ maps were obtained at 65K, above the Curie temperature of CGT. The results are shown in Figure 6.13 (top panel). The results indicate nonzero dichroism in the VBM bands and Cr d bands at the photon energies used. Additionally, a strong photon energy dependence of the dichroic pattern is observed when moving from $h\nu$ = 44 eV to 56 eV. A notable difference is the disappearance of strong dichroism at 1.5 to 2.5 eV below the valence band maximum at $h\nu$ = 56 eV. This could be due to the k_z dispersion of the bands or due to the photoemission transition matrix element effect.

To study the effect of magnetism, the sample was cooled to 30 K, below the Curie temperature, and the measurements were repeated (shown in Figure 6.13, bottom panel). The CD patterns show discernible changes above and below the Curie temperature. The most prominent change occurs at $h\nu$ = , at 2.1 eV below the valence band maximum, where the distribution of the CD pattern shifts. This could be a consequence of magnetic ordering in CGT. Additionally, band splitting (as indicated in Figures 6.13 (b) and (e) and intensity renormalization were observed below the Curie temperature, in agreement with previous work [141]. Three dimensional ($k_x - k_y - E$ spectra) measurements were also performed on CGT. Figure 6.14 (a) shows the $k_x - k_y$ maps with $E - E_{VBM}$ ranging from -1 to -0.1 eV at 0.1 eV intervals. The constant energy cut at 0.8 eV below the valence band maximum from the CD-ARPES measurement is shown in Figure 6.14 (b). The features visible in these maps can be interpreted as three hole-like pockets, as shown in Figure 6.14 (b). While the inner hole band (marked as 1 in Figure 6.14 (b)) of CGT shows only one sign reversal, the outer hole bands (marked as 2 and 3 in Figure 6.14 (b)) exhibit multiple sign changes.

Understanding the initial-state orbital angular momentum values is essential for analyzing the CD-ARPES results. However, this is not straightforward, as CGT bands have contributions from multiple orbitals of multiple nonequivalent atoms. Precisely determining the various contributions to the CD pattern requires considering all participating atoms, their orbitals, and their respective phase shifts. Given the complexity of CGT, which contains ten nonequivalent atoms per unit cell, such an exact approach is impractical. Therefore, certain approximations must be made to interpret the CD patterns in CGT.

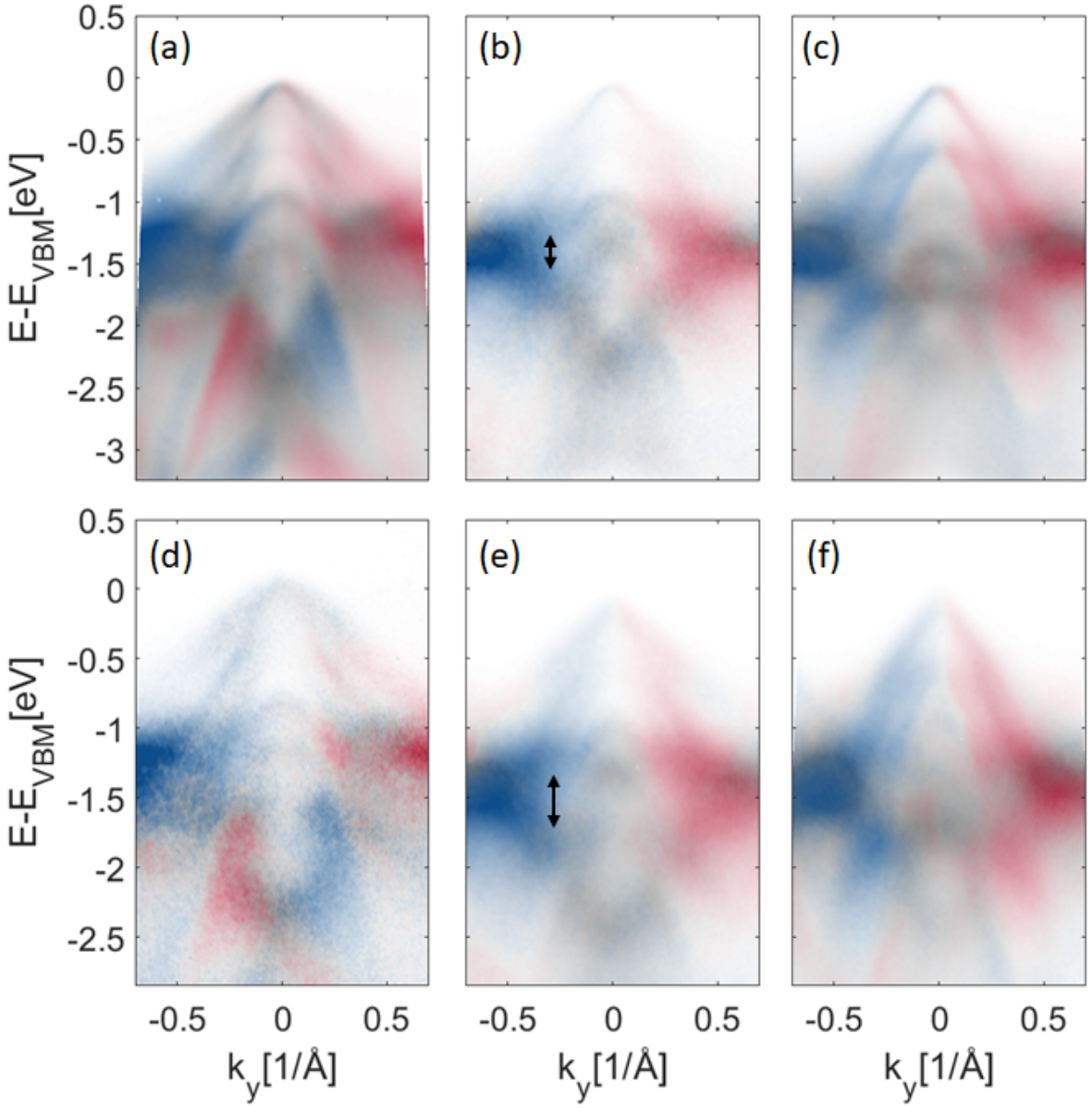

Figure 6.13: Photon energy-dependent CD-ARPES E vs $k_{||}$ maps on CGT at $h\nu$ = (a) and (d) 44 eV, (b) and (e) 50 eV and (c)and (f) 56 eV. The top panel are measurements performed at 65 K and the bottom panel are the measurements performed at 30 K. The splitting of the bands are indicated in (b) and (e).

Resonant ARPES and polarization-dependent measurements indicate that the bands at the valence band maximum are primarily of Te 5p character. Due to their dominant contribution at the valence band maximum, only the Te 5p orbitals were considered for the plots of Y_l^m decomposition, as discussed below. Initially, a Y_l^m decomposition of the Te p orbitals was performed along the three equivalent $M-\Gamma-M$ directions in a 9-monolayer CGT slab (shown in Figure 6.15 (a)). When the quantization axis is taken as the surface normal (001 direction), one might naively assume that all three $M-\Gamma-M'$directions are equivalent. However, calculations reveal an asymmetry, showing that the Y_l^m compositions along the

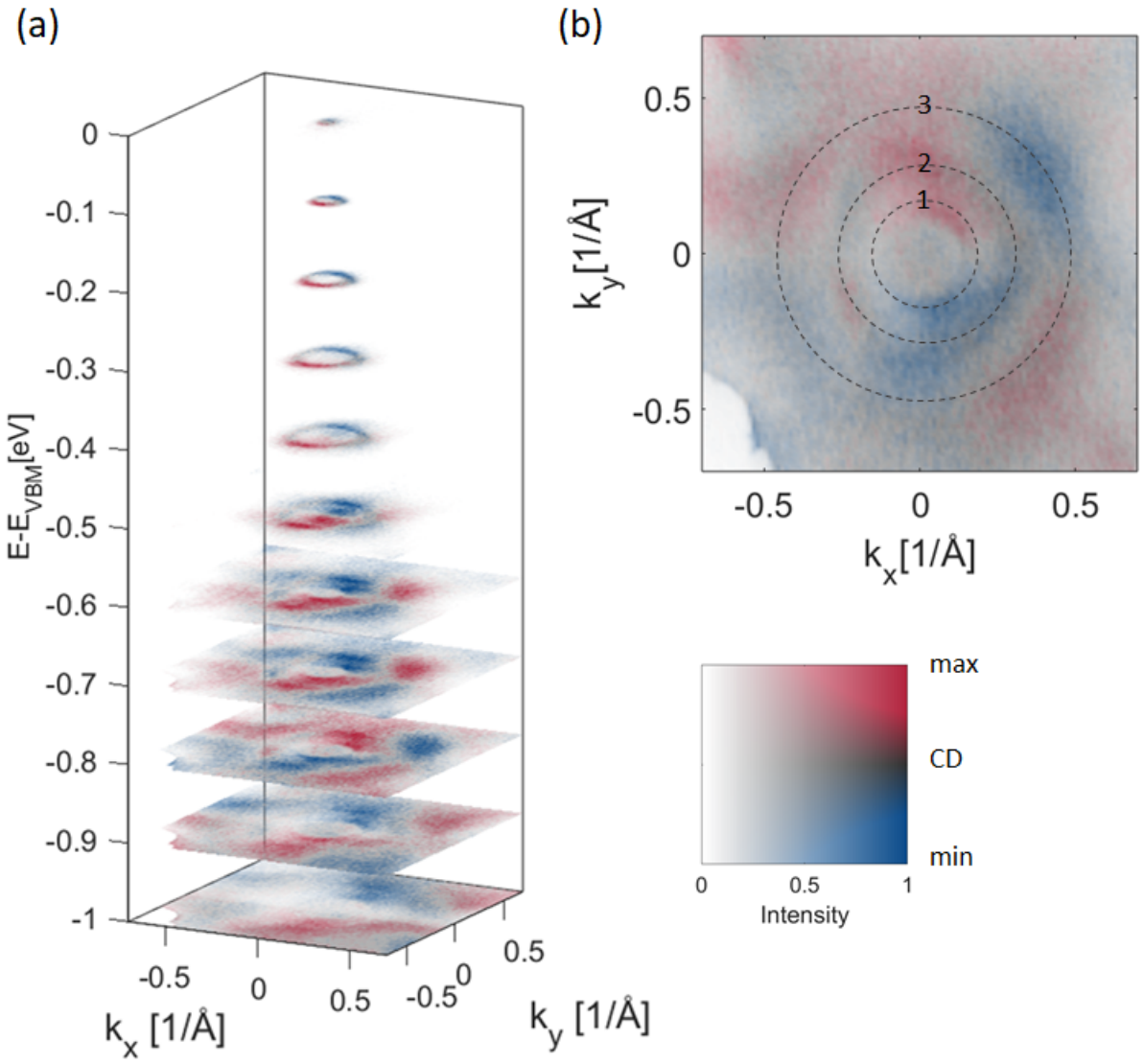

Figure 6.14: $k_x - k_y$ cuts of CD-ARPES dataset from CGT at $h\nu$ = 56 eV and 65K at binding energies 0 to 1 ev in steps of 01 eV and (b) $k_x - k_y$ map at binding energy 0.8 eV at $h\nu$ = 56 eV. The 2D colormap used for the plots is also shown.

three directions differ. To further investigate this asymmetry, a similar calculation was performed for a monolayer CGT (shown in Figure 6.15 (b)). The results are in close agreement with those of the slab calculation. In all the above calculations, contributions were considered from only one of the six Te atoms (schematic diagram shown in Figure 6.15 (c)) The contributions from the remaining Te atoms can be obtained using symmetry operations, which were not explicitly applied in the calculations presented in Figure 6.15. This asymmetry highlights the importance of computing the Y_l^m contributions from all six Te atoms separately (or utilizing symmetry operations to determine their individual contributions) to enable meaningful comparison with experimental results.

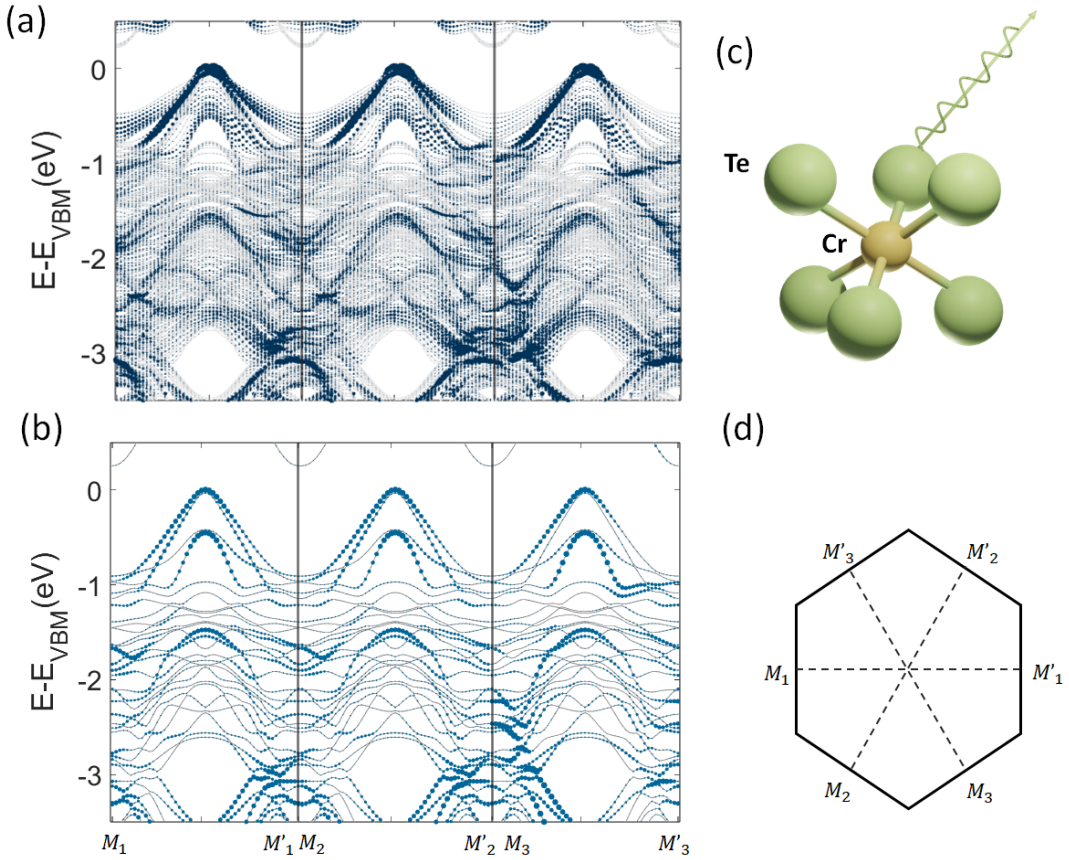

Figure 6.15: The Y_l^m decomposition of the CGT bands showing Te Y_1^1 orbital in (a) for a 9 monolayer slab calculation and (b) for a monolayer calculation, along the three equivalent $M - \Gamma - M'$ directions. (c) shows a schematic diagram of the Cr and the surrounding Te atoms. The contribution from only one of the six Te atoms are plotted in (a) and (b). (d) shows the three $M - \Gamma - M'$ directions in the Brillouin zone, that were considered for the plots in (a) and (b).

One approach to obtain contributions from all six Te atoms is to treat each atom separately, but this would make the computation significantly more expensive. Additionally, the calculations require a dense k-points. Comparing the results from the 9 monolayer slab calculation, shown in figure 6.15 (a), and monolayer calculations, shown in figure 6.15 (b), one can see that the results are similar, in accordance with the quasi-2D nature of CGT. Additionally, from the polarization-dependent studies(see Figure 6.9), the in-plane and out-of-plane contributions of the orbitals near the valence band maximum have been verified. At the tip of the valence band maximum, the in-plane p_x and p_y contributions dominate. Therefore, a calculation on monolayer CGT is sufficient to approximately determine the CD features in the CGT valence band region. In this case, the monolayer can be considered the outermost layer of the bulk CGT. Compared to the slab calculations, the monolayer calculations require significantly less computational time. Considering

these factors, calculations on a monolayer provide a practical solution for comparison with experimental data.

To understand how the Y_l^m distribution varies in momentum space, a calculation was performed using a 51 × 51 k point mesh, covering the entire 2D Brillouin zones. Figure 6.16 (a) shows the constant energy cut Y_l^m decomposition of the three Te atoms on the surface of the CGT monolayer, with spin-orbit coupling taken into account. The plots show the sum of spin-up and spin-down bands.

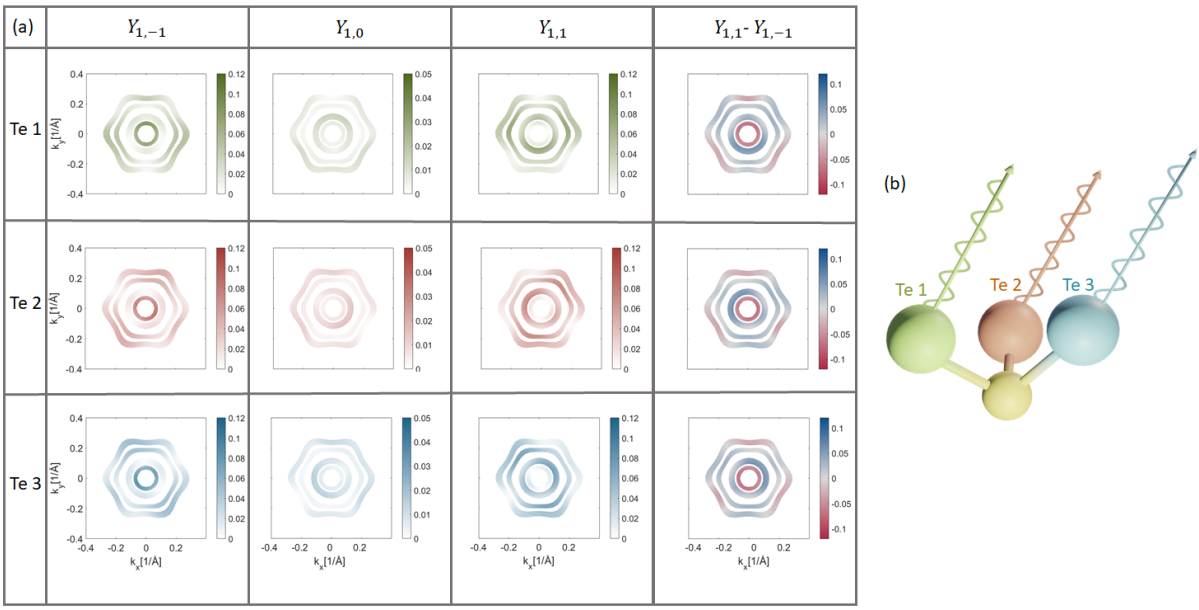

Figure 6.16: Figure shows the constant energy cut Y_l^m decomposition of Te p orbitals in CGT monolayers, with quantization axis taken as surface normal (001). The contributions from three Te atoms at the surface of the monolayer are shown separately in the rows. The columns represent the $Y_{1,-1}$, $Y_{1,0}$, $Y_{1,1}$ and $Y_{1,1} - Y_{1,-1}$. The energy cut is at 0.8 eV below the valence band maximum. The plots in (a) show the sum of spin up and spin down bands. (b) shows a schematic diagram of arrangement of Te around the Cr atoms. The three Te atoms atoms used for the calculation in (a) are indicated.

From the Y_l^m decomposition shown in Figure 6.16,it is clear that the contributions of the three Te atoms on the surface are different, as expected. The weight of the Y_l^m contribution depends on the position of the Te atom in the unit cell, even when the light is incident normal to the surface. The calculated initial-state CD pattern, shown in the fourth column of Figure 6.16 (a), also varies depending on the position of the Te atom. This leads to an important point that for meaningful comparison with experimental results, it is crucial to consider all contributing atoms separately (or calculate the contributions using symmetry operations separately).

Comparing the experimental $k_x - k_y$ CD maps (see in Figure 6.14)with the calculated OAM

patterns, shown in Figure 6.17 (a), the calculated OAM patterns do not show the sign reversal of the hole bands observed in the experimental spectra. So far, the quantization axis has been taken as the surface normal (001 direction). However, in the experimental geometry, the light is incident at an angle of 54.7° with respect to the surface normal. Therefore, it may be insightful to perform the orbital decomposition along this quantization axis (the experimental geometry-induced CD is discussed using the example of graphene p_z orbitals in Section 5.1.3). The Y_l^m decomposition with the quantization axis set along the light incidence direction is shown in Figure 6.17 (b). With the quantization axis taken as

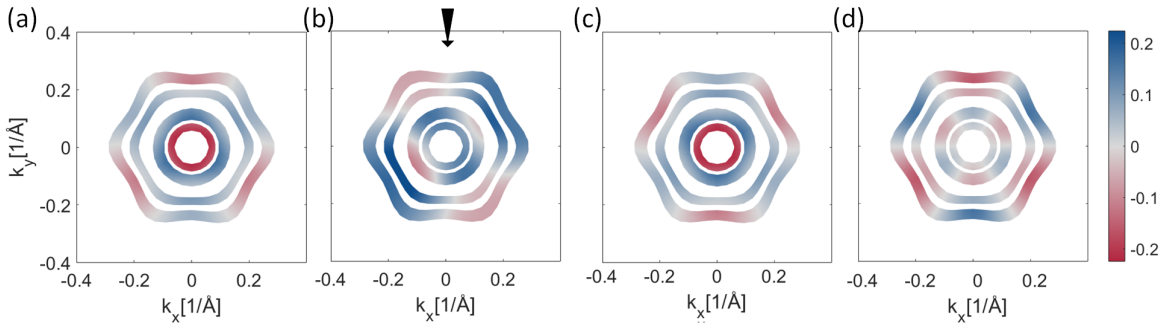

Figure 6.17: Constant energy cut at 0.8 eV below the valence band maximum of the monolayer CGT band showing the $Y_{1,1}$ contribution of Te atom with quantization axis taken as (a) surface normal (001 direction) and (b) 54.7° from the surface normal (the direction is shown by black arrow). The magnetization axis for the calculation is taken as (a)-(b) 001 direction. (c) shows the calculated OAM of Te 5p with quantization axis taken as surface normal and magnetization axis taken as 00-1 direction. (d) shows the difference of the CD patterns with magnetization axis [001] (a) and [00-1] (c). For all maps the contribution from the three Te atoms were calculated separately and added incoherently.

the light incidence direction, the OAM pattern for the Te 5p orbital shows a sign change in all the hole-like bands, agreeing with the experimental results. Even if the CD patterns do not completely match, the qualitative agreement with the experimental results highlights the importance of considering the correct quantization axis when determining the CD pattern in complex material systems like CGT.

To explain the changes in the CD pattern above and below the Curie temperature, a magnetization-axis-dependent calculation was performed on CGT. CGT has perpendicular magnetic anisotropy [128], meaning that the domains orient in the out-of-plane direction. Below the Curie temperature, the magnetization direction of CGT is either along the [001] or [00-1] direction. To calculate the Y_l^m contributions from the spin-up and spin-down domains, calculations were carried out with the magnetization axis set to [001] and [00-1], respectively, as shown in Figure 6.17 (a) and (c). Interestingly, the calculations show that the contributions from the spin-up and spin-down domains are neither exactly the same nor exactly opposite.

Although experimental CD patterns are related to the initial-state Y_l^m of the bands, many

other factors may also play a role, including interference between $l \pm 1$ channels (which depends on the radial integral and phase shifts) and multiple scattering effects. These factors could significantly impact the experimental results. A detailed discussion of these effects is provided in Section 5.1 for the case of graphene Dirac bands; however, they are not considered in this chapter due to the complex mixture of orbital characters in CGT. In reality, emitted electrons from different sites undergo mutual interference due to position-dependent phase shifts [125], as illustrated in Figure 6.18 for Te atoms in CGT. This interference modulates the intensity and, consequently, affects the CD pattern.

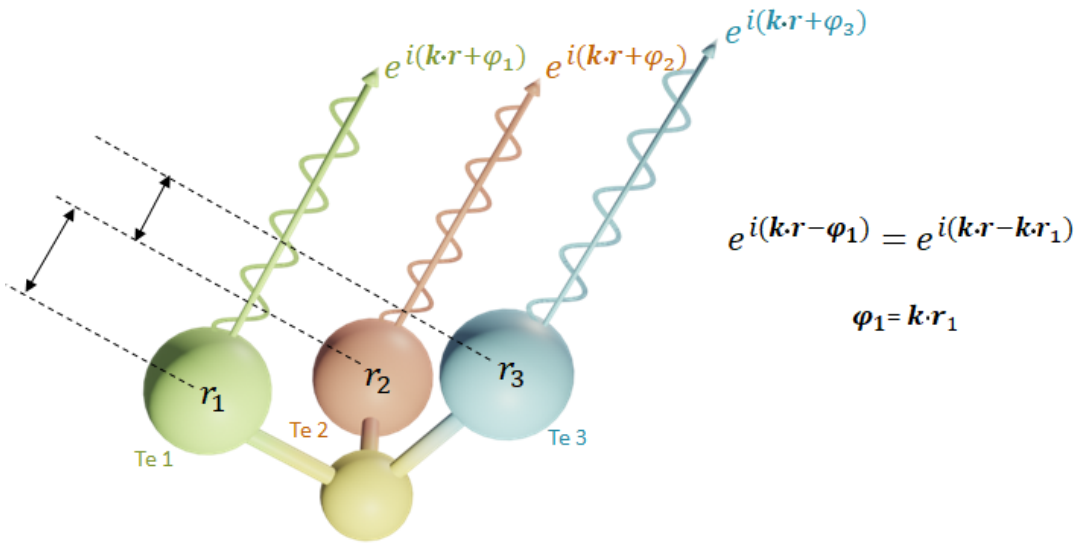

Figure 6.18: Schematic diagram of emission from Te atoms with initial phases ϕ_1, ϕ_2 and ϕ_3, related to the position of the Te atoms as $\phi_i = \mathbf{k} \cdot \mathbf{r}_i$.

Determining the phases of all atoms and contributing orbitals is extremely challenging for a material like CGT, whose crystal structure lacks symmetry. This problem can be partially addressed through core-level experiments, where the primary contribution comes from a specific atom [101]. Circular dichroism from core levels will be discussed in the following section.

6.2.4 Circular dichroism from core levels

In contrast to valence band photoemission, where contributions come from different atomic sites, core-level photoemission is element-specific [101]. In the case of valence bands, the initial state wave function is delocalized, meaning that for a complete description of the initial state, a summation of all contributions from different atomic sites needs to be considered:

$$\psi_i = \sum_A C_A \phi_A, \tag{6.1}$$

where A represents the atomic site, C_A is the complex coefficient corresponding to the site A and ϕ_A is the wave function centered at site A. For core levels, the wave function is localized to the specific atom corresponding to the core level that is considered. For core

levels, the wave function is localized to the specific atom corresponding to the core level under consideration. Core-level CD-ARPES measurements, along with element selectivity, can provide important information about the local geometry of atoms through X-ray photoelectron diffraction (XPD) effects. Core-level CD-ARPES can be used to study final-state effects in CGT.

In this subsection, core-level angle-resolved photoemission measurements performed to understand the scattering processes in CGT will be discussed. The measurements were conducted at the i05 beamline at Diamond Light Source. Single bulk crystals of CGT were cleaved in the main chamber using a ceramic post. ARPES measurements were performed with light incidence along both the $M-\Gamma-M'$ and $K-\Gamma-K'$ directions. The light was incident at an angle of 50° with respect to the surface normal. Initially, a long energy-range survey scan was taken to determine the positions of the core levels, as shown in Figure 6.19. The Ge 3d and Te 4d core levels were the only accessible core levels due to

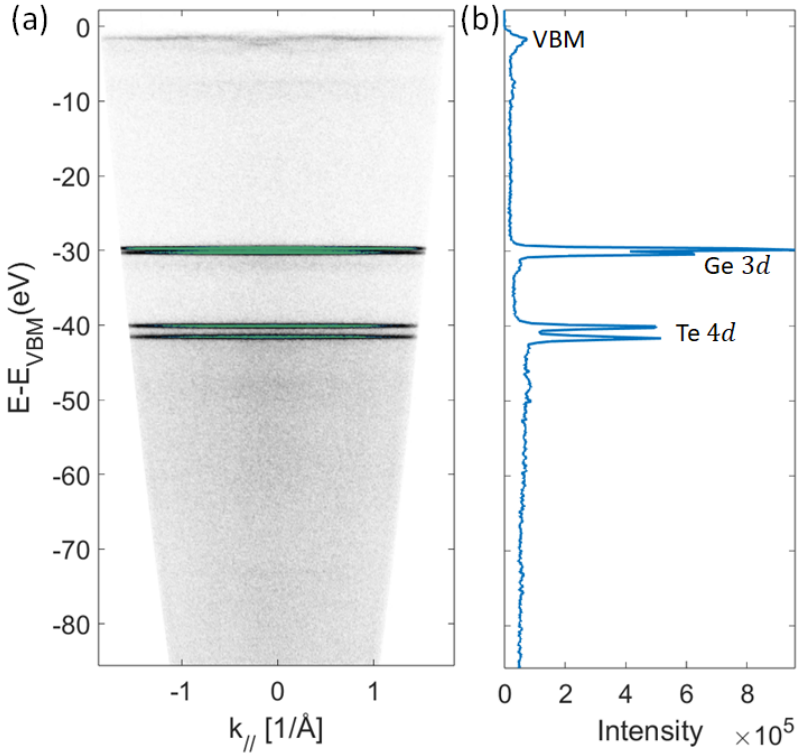

Figure 6.19: Long energy range ARPES spectra of CGT obtained with $h\nu$ =140 eV (a) and the energy distribution curve (b). The Te 4d and Ge 3d core levels are indicated in (b).

the maximum photon energy limit of $h\nu$ = 180 eV at the i05 beamline. The Cr 3p core level is located at approximately 43 eV, overlapping with the Te 4d core level. Figure 6.20 (a) shows the core-level CD-ARPES spectra at Ge 3d at E_B = 34.5 and 34.2 eV, with light incidence along $M-\Gamma-M'$ direction, measured at 45K with LHe cooling. The CD maps at $3d_{3/2}$ and $3d_{5/2}$ show rich dichroic pattern and do not show any notable differences between them. CD-ARPES measurements were also performed in another orientation, where the

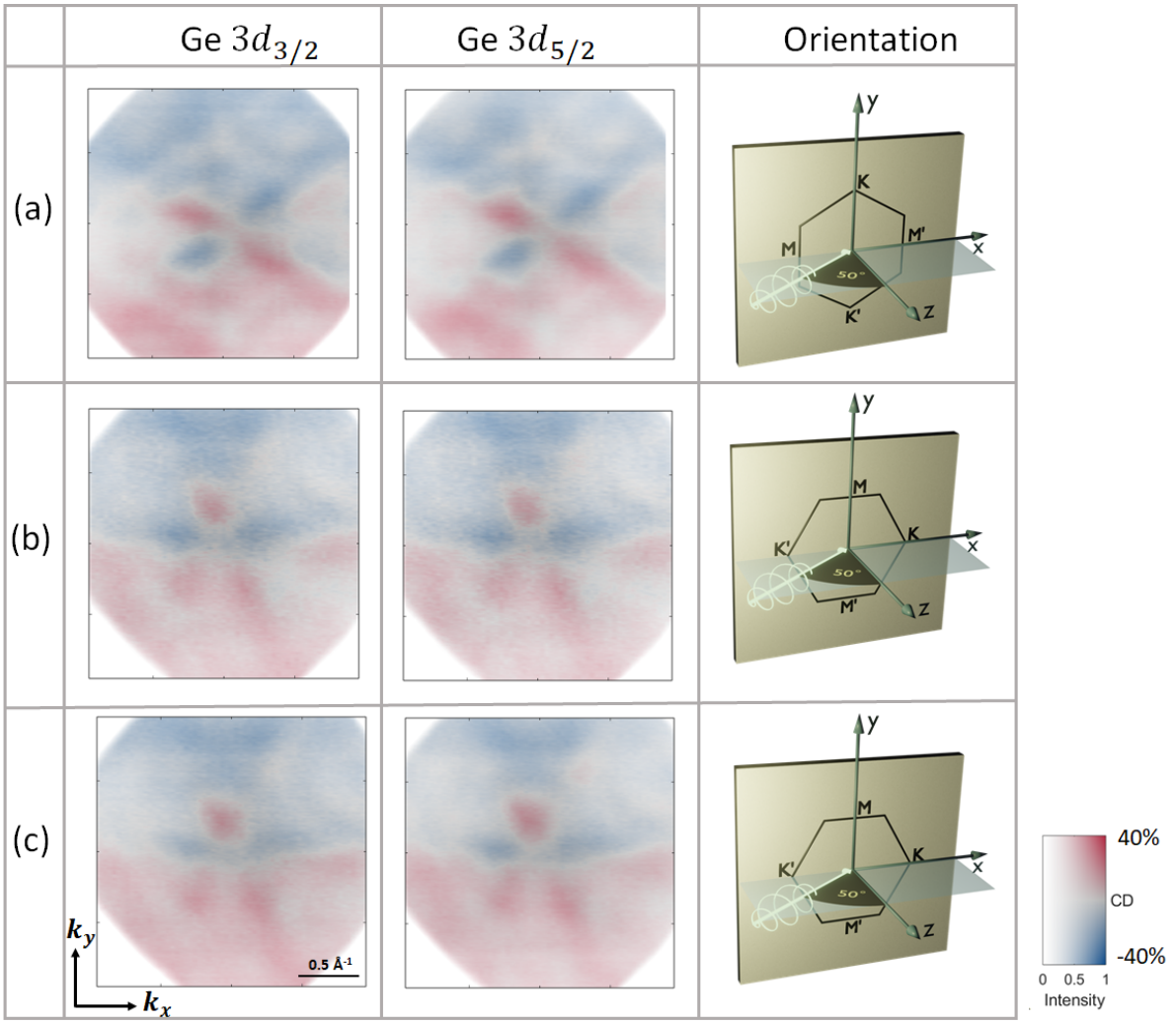

Figure 6.20: CD ARPES spectra on CGT at Ge $3d$ core levels. (a) shows the measurements with light incidence along $M-\Gamma-M'$ direction at 45K. (b) show the measurements with light incidence along $K-\Gamma-K'$ direction at 45K. (c) same as the measurements in (c) but performed at 70K. The first column shows the Ge $3d_{3/2}$, the second column shows the Ge $3d_{5/2}$ and the third column show the schematic diagram of the experimental geometry of the measurements. The measurements were performed with $h\nu$ = 140 eV. The core levels $3d_{3/2}$ and $3d_{5/2}$ are at binding energies 34.5 and 34.2 eV respectively.

sample was rotated by 30°, resulting in light incidence along the $K-\Gamma-K'$ direction at 45 K (below the Curie temperature) and at 70 K (above the Curie temperature), as shown in Figures6.20 (b) and (c). By inspecting the maps in figure 6.20, a mirror symmetry is observed in (a) about $y = 0$ even though there are no mirror planes in CGT. Since ARPES is a surface-sensitive technique and, at the photon energy used ($h\nu$ = 140 eV), the inelastic mean free path is only a few angstroms, the main contribution to the CD map comes from the topmost layer of bulk CGT. In the crystal structure of monolayer CGT, the mirror symmetries about the $M-\Gamma-M'$ directions (see Figure 6.21 (a)) are broken due to the small displacement ($\approx$ 0.03646 Å) of one of the two nonequivalent Cr atoms in the

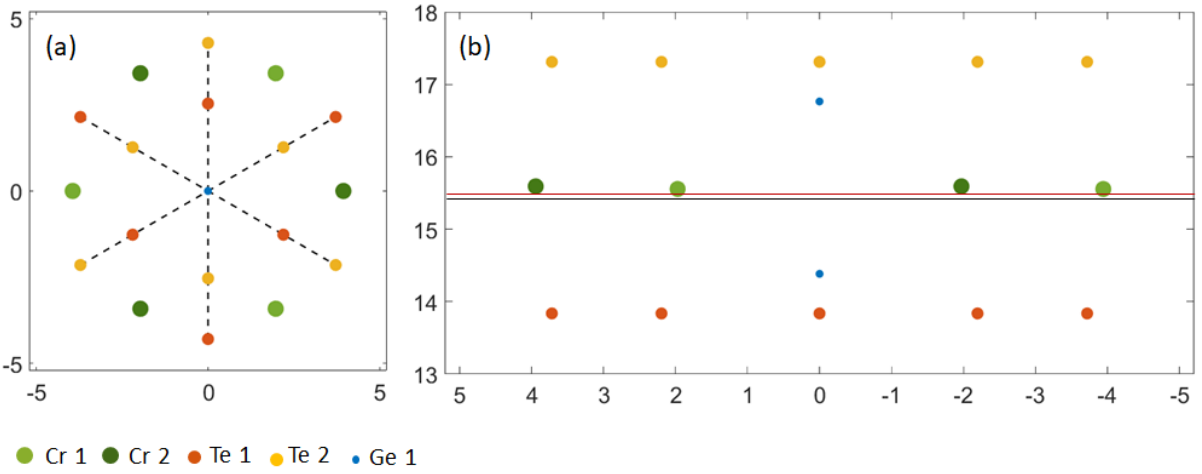

Figure 6.21: (a) and (b) show the top and side views of crystal structure of monolayer CGT respectively. The dotted lines in (a) are the three $M-\Gamma-M'$ directions. The vertical displacement of Cr atoms can be seen in the side view using the horizontal red and black lines.

unit cell along the vertical (z) direction (see Figure 6.21 (b)). This small displacement of Cr atoms might explain why the ARPES maps appear symmetric about the $M-\Gamma-M'$ direction. No significant changes were observed in the CD feature in the measurements above and below the Curie temperature (see Figures 6.20 (b) and (c)).Although Ge is not a magnetic atom, the exchange splitting of Cr may have an effect on Ge core levels; however, these magnetic splittings are too small to be resolved. Additionally, exchange scattering can influence diffraction patterns above and below the Curie temperature, but no such changes were observed in the temperature-dependent data. To observe the effect of exchange scattering, a spin-split core level that produces spin-polarized electrons is required (in this case, the Cr core level). However, this is difficult to verify due to the very small core-level splitting; for instance, in Fe, the 3p $3p$ core-level splitting is on the order of 0.26 - 0.7 eV [155, 156].

The CD-ARPES measurements were repeated on the Te $4d$ core levels at E_B = 46 and 44.5 eV with $h\nu$ = 140 eV (see Figure 6.22 (a) and (b)). The light was incident along $M-\Gamma-M'$ direction at 50° with respect to surface normal. The CD maps reveal multiple features, including a hexagonal-like pattern near the Γ point and high-intensity spots at the K points of CGT (as indicated in Figure 6.22 (a)). The hexagonal symmetry observed in the Te $4d$ spectra might be related to the local geometry of the Te atoms in the crystal structure. Similarly, in the case of Te, the CD patterns are consistent across both core-level components.

TTo study the effect of scattering in the core-level CD-ARPES spectra, calculations were performed on a monolayer CGT using EDAC [111]. A CGT monolayer cluster was created using atomic positions obtained from the crystal structure available in the Materials Project database [157]. For the calculation, a cluster with a radius (R_{max}) 20 Å(307 atoms

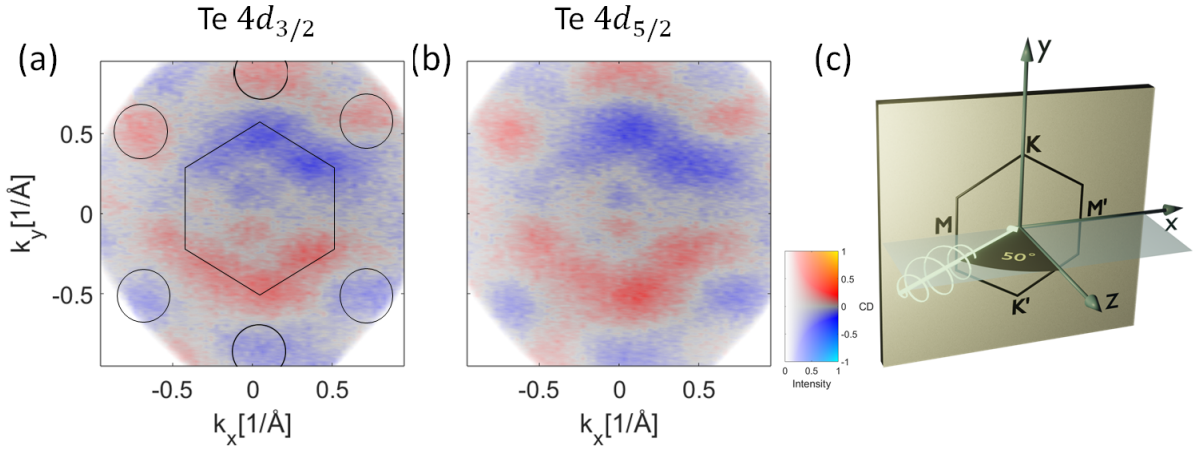

Figure 6.22: (a) and (b) show the CD-ARPES measurements on Te $4d$ core levels at E_B = 46 and 44.5 eV respectively. The measurements were performed at $h\nu$ = 140 eV at 45 K, below Curie temperature. The experimental geometry of the measurement is shown in (c).

in total) was considered, as shown in Figure 6.23. In EDAC, atoms are represented by

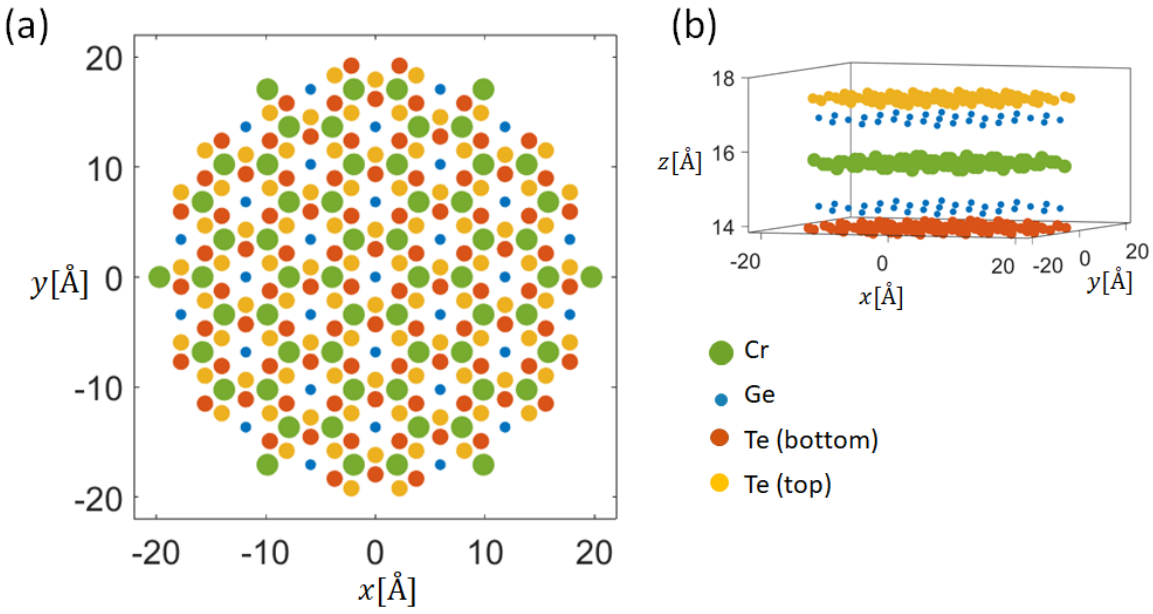

Figure 6.23: Top view (a) and side view (b) of the CGT cluster used for the EDAC calculations.

muffin-tin potentials, which are used to determine the scattering phase shifts. The inner potential V_0, defined as the muffin-tin zero relative to the vacuum level, was set to 10 eV for this case. The light incidence direction can be specified and was chosen to be 50° with respect to the surface normal to match the experimental conditions at the i05 beamline. A scattering order of 20 was used for multiple scattering calculations, and inelastic scattering effects were accounted for by incorporating an inelastic mean free path of 5 Å.

Since the spin-orbit-split core levels do not exhibit significant differences in the CD-ARPES pattern, both core levels were integrated using a Gaussian envelope function to reduce background noise, as shown in Figures 6.24 (a)-(c). These integrated data were then used for comparison with theoretical modeling.

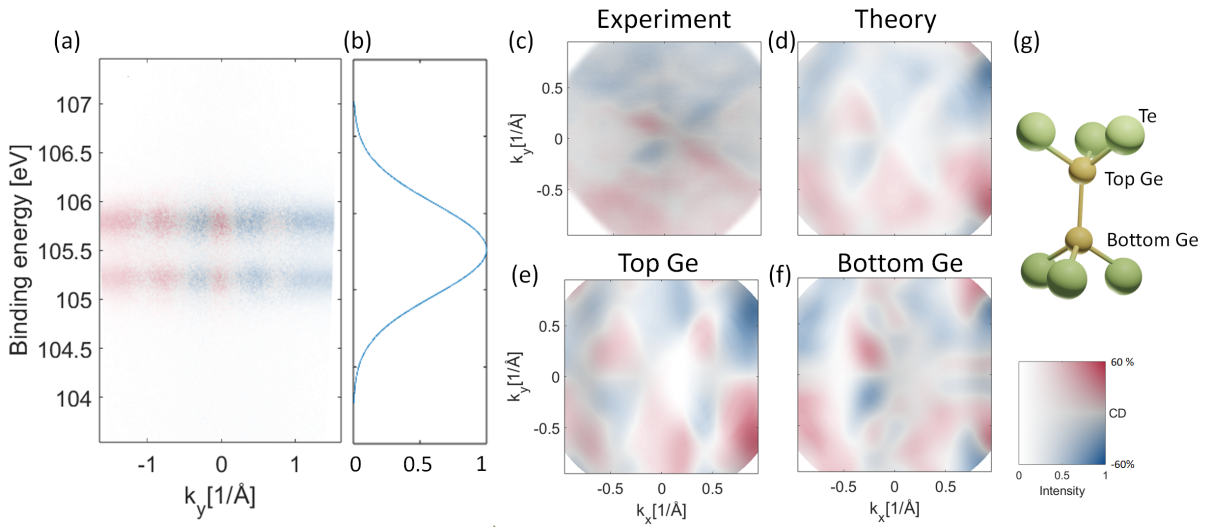

Figure 6.24: (a) shows the Ge 3d core level E versus $k_{||}$ CD map at $h\nu$ = 140 eV along k_x = 0.5 Å^{-1}. (b) shows the Gaussian function used to integrate the two core levels. (c) shows the core level integrated CD map of Ge 3d at $h\nu$ = 140 eV. (d)-(f) show the multiple scattering calculations at E_{kin} = 105.6 eV. (d) shows the coherently added Ge 3d orbital contribution from two nonequivalent Ge sites in CGT monolayer. (e) and (f) are the individual contribution from top Ge atom and bottom Ge atom respectively.

The Ge 3d core level was chosen as the initial state, with light incidence along the $M-\Gamma-M'$ direction. The kinetic energy of the emitted photoelectrons was taken as 105.6 eV, corresponding to the photon energy used in the measurements ($h\nu$ = 140 eV). The calculated CD-ARPES core-level patterns with multiple scattering are shown in Figures 6.24 (d)-(f). The total contribution from the two nonequivalent Ge atoms is shown in Figure 6.24 (d), while the individual contributions from each Ge atom are plotted separately in (e) and (f). With the inclusion of multiple scattering in the calculations, most of the experimental CD features were successfully reproduced, demonstrating the influence of multiple scattering in core-level CD-ARPES measurements.

A preliminary analysis was also performed for the Te 4d core levels. The experimental CD-ARPES map, integrated over both doublet features, is shown in Figure 6.25 (a). The multiple scattering calculations from Te 4d in a monolayer CGT are presented in Figures 6.25 (b)-(d). The coherently added total contribution from all six nonequivalent Te atoms is shown in (b), while (c) and (d) display the contributions from the top three and bottom three Te atoms, respectively. However, the calculated maps differ from the

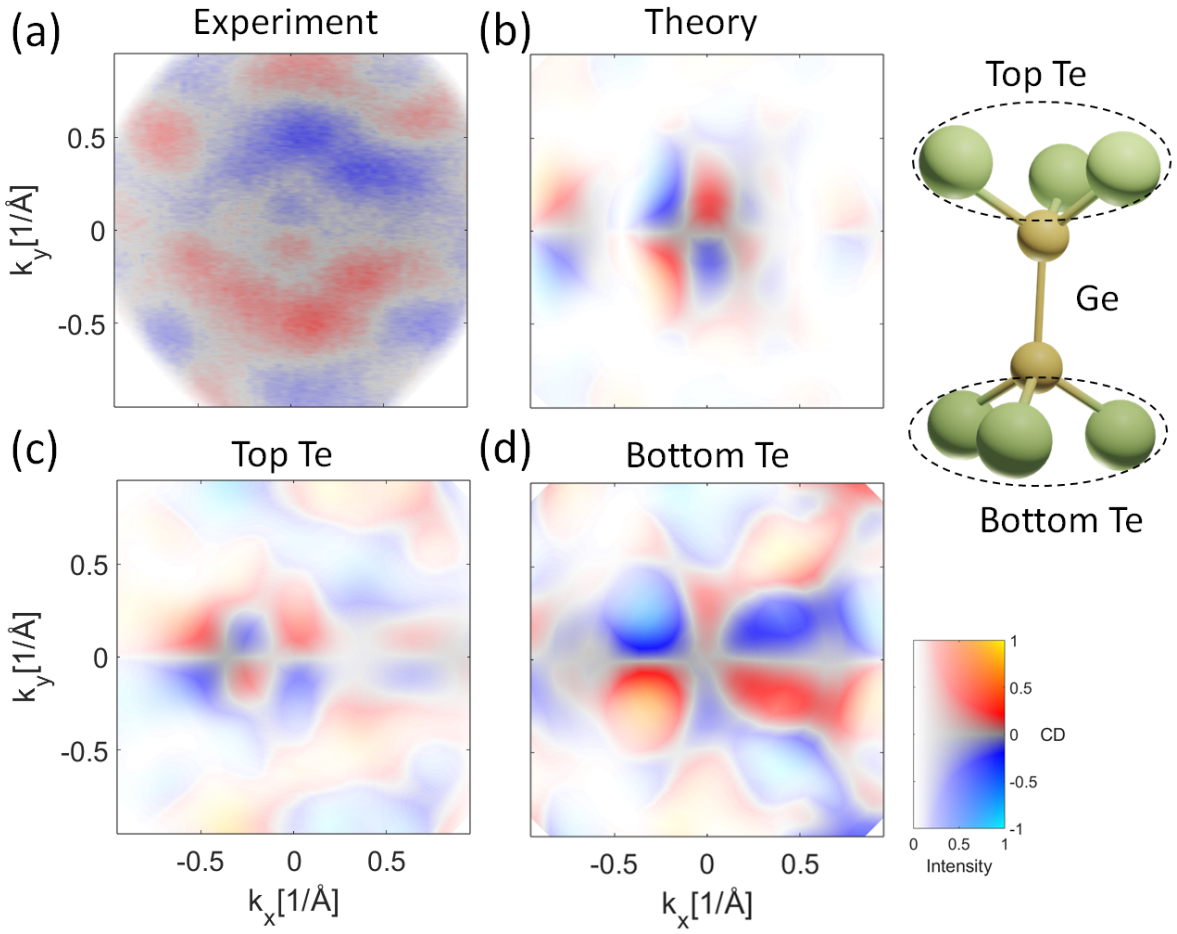

Figure 6.25: (a) shows the core level integrated CD map of Te 4*d* at $h\nu$ = 140 eV. (b)-(d) show the multiple scattering calculations at E_{kin} = 94.8 eV. (b) shows the coherently added Te 4*d* orbital contribution from six non equivalent Te sites in CGT monolayer. (c) and (d) are the contributions from the three top Te atoms (marked with yellow color in figure 6.23) and three bottom Te atom (marked with red color in figure 6.23), respectively. A schematic diagram of top and bottom Te atoms are shown in (e).

experimental results, and the experimental CD-ARPES features could not be replicated in the calculations. Since the Ge 3*d* simulations align well with the experimental data, it is unlikely that the cleaved surface exhibits twinning. A potential improvement for the calculations in Figure 6.25 could be achieved by including additional CGT layers in the cluster.

Core-level CD-ARPES highlights the importance of multiple scattering in the photoemission process. The differences in the CD patterns of the Ge 3*d* and Te 4*d* core levels may also be linked to the local atomic geometry through scattering. The angular limit of ± 15° in the measurements makes direct comparisons challenging. Performing core-level CD-ARPES measurements at higher photon energies, where forward scattering dominates, would further enhance the study of structural properties due to XPD effects. Additionally, conducting photoelectron diffraction over a larger angular range would enable a more

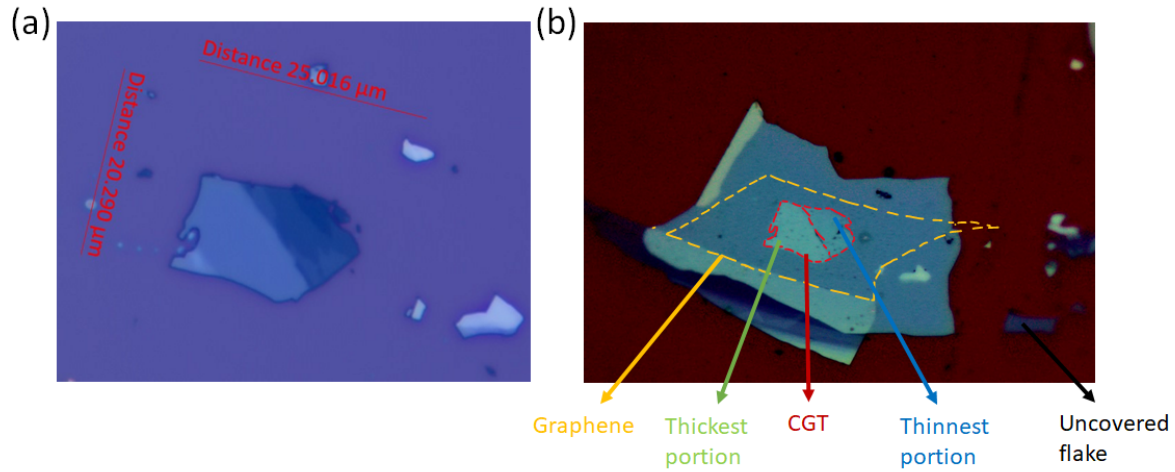

Figure 6.26: Optical image of exfoliated CGT flake (a) and graphene/CGT/graphite heterostructure (b). The different regions in the heterostructure are labelled.

comprehensive evaluation of forward scattering features, which are often more pronounced at higher emission angles.

6.2.5 ARPES measurements on exfoliated CGT flakes

In addition to the bulk measurements on CGT, preliminary measurements were also performed on exfoliated CGT flakes. Most 2D magnetic systems, including CGT, exhibit a decrease in Curie temperature with decreasing sample thickness [158]. Our primary objective was to study the connection between magnetic interactions and sample thickness.

For the flake measurements, the samples were prepared in a glove box due to the sensitivity of CGT to ambient conditions. The CGT crystals were not of sufficient quality to prepare millimeter-scale flat surfaces, which are essential for flake preparation. As a result, only small flakes, on the order of a few micrometers, were obtained by exfoliation. No monolayer CGT flakes were obtained due to the quality of the bulk crystal. However, by repeated exfoliation, CGT flakes with a thickness of less than 20 monolayers and lateral dimensions of 5–6 micrometers were successfully obtained (see Figure 6.26 (a)). As explained in Section 4.2, the CGT flakes were transferred onto exfoliated thick graphite and subsequently encapsulated with monolayer graphene. An optical micrograph of the final heterostructure sample is shown in Figure 6.26 (b), where the thick and thin portions of the flakes are indicated.

Measurements on the flake samples were conducted at the nano-ARPES branch of the MAESTRO beamline at ALS, using a beam spot size of approximately $2\mu m$. This beam spot allowed for selective probing of different portions of the flake. ARPES measurements with p–polarized light on both the thin and thick portions of the flake are shown in Figure 6.27 (a) and (b).

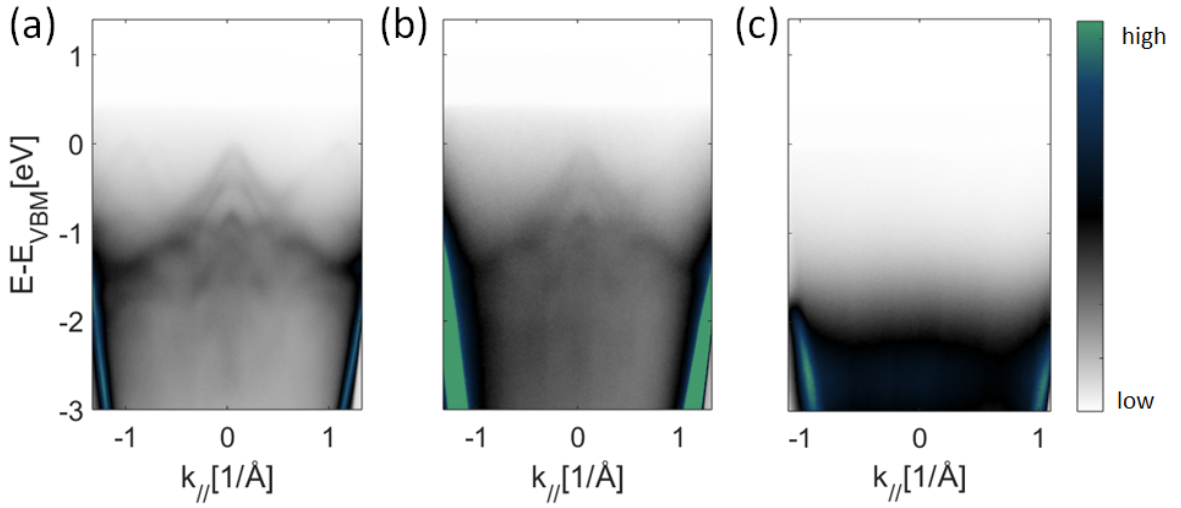

Figure 6.27: ARPES measurements on (a) bulk encapsulated CGT flake, (b) less than 20 monolayer encapsulated flake and (c) uncovered flake exposed to air. All the measurements were performed at 20 K at $h\nu$ = 56 eV.

To assess the extent of oxidation in the CGT flakes, measurements were also performed on an uncovered flake located near the encapsulated one (shown in Figure 6.26 (b)). The ARPES measurement revealed no observable bands from the uncovered flake, as shown in Figure 6.27 (c). This confirms that encapsulation with monolayer graphene enables measurements on few-layer CGT and could potentially be applied to other air-sensitive magnetic 2D materials.

Unfortunately, due to limited beamtime and technical difficulties at the beamline, the measurements could not be fully completed. Further thickness-dependent measurements are required to better understand the relationship between the strength of magnetic interactions and sample thickness. Additionally, such measurements would provide insight into the stabilization of magnetism in the true 2D limit.

7 Electronic and magnetic domain structure of Fe_3GeTe_2

Fe_3GeTe_2 (FGT) is a 2-dimensional ferromagnetic metal with a bulk Curie temperature of 220K [159, 160]. It is one of the rare 2D materials that exhibit near-room-temperature ferromagnetism. Recently, there has been growing interest in FGT due to its metallic nature, with magnetism observed even in the monolayer limit [161, 162], the observation of large anomalous Hall effect [163], significant perpendicular magnetic anisotropic energy [159, 164], and the tunability of the magnetic and electronic properties through doping [165], gating [166], patterning [72], and the application of strain [167].

Bulk FGT is a hard magnet with a coercive field of 21.6 mT [164]. It exhibits a large perpendicular magnetic anisotropy of $\approx$ 3 meV/f.u., which is comparable to that of transition metal permanent magnetic systems [168]. Studies have shown that hole doping in FGT reduces both the perpendicular magnetic anisotropy and the coercive field [165]. Similarly, the application of an in-plane current alters the coercive field due to large spin-orbit torque, which can be used for future magnetic memory storage devices [169].

FGT, in addition to its potential for practical device applications, also exhibits rich physics in terms of its electronic band structure. Electronic correlations play a crucial role in this system, and it is considered a rare-earth-free heavy fermion system [170, 171]. Previous specific heat data from FGT show a Sommerfeld coefficient of 110 mJ/mol, indicating enhanced mass renormalization, which is directly related to electronic correlations in FGT [172]. However, there remains a discrepancy between the experimental Sommerfeld coefficient and theoretical predictions, which has yet to be resolved. The origin of the higher experimental Sommerfeld coefficient values is still unclear.

Additionally, there are claims that FGT exhibits Kondo lattice behavior, supported by Fano resonances observed in STM data [171]. The large anomalous Hall effect observed in transport measurements is attributed to the presence of a topological nodal line and significant Berry curvature [163]. Furthermore, FGT develops a domain structure below its Curie temperature, with this structure being dependent on thickness [164], temperature [173, 174] and applied external magnetic field [72, 175]. The domain pattern and its size play a crucial role in determining the magnetic and electronic properties of FGT.

A deeper understanding of FGT's electronic band structure, along with its underlying domain structure, is essential to fully unveil its rich physics. These factors make FGT an

intriguing system for further study. In this Chapter, we present the results of study on the magnetic domain structure and electronic properties of bulk single-crystal and encapsulated few-layer samples of FGT. Resonant ARPES was used to determine the contribution of Fe-derived bands to the electronic structure of bulk FGT. These measurements were further complemented by CD-ARPES studies. The magnetic domain structure of FGT was investigated using PEEM with X-ray magnetic circular dichroism (XMCD) on exfoliated and encapsulated few-layer FGT samples, and the results will be presented toward the end of the Chapter. Additionally, a brief overview of the Stoner model of ferromagnetism, along with the theoretical background of resonant photoemission and XMCD, will be provided in the relevant sections of this Chapter.

7.1 Properties of FGT

7.1.1 Crystal structure

FGT crystallizes in a hexagonal structure within the space group $P6_3/mmc$ [159, 176]. Its structure consists of Fe_3Ge hexagonal nets sandwiched between Te layers. The crystal structure of FGT is shown in Figure 7.1. There are two nonequivalent Fe atoms in FGT, denoted as Fe1 and Fe2. Each monolayer consists of five sublayers: Fe1 forms a hexagonal net on its own, while Fe2 is covalently bonded with Ge atoms, maintaining hexagonal symmetry. The adjacent Te layers interact via van der Waals forces, giving FGT its characteristic 2D nature. The most probable cleavage occurs between the Te layers, breaking the van der Waals bonds. A unit cell of FGT consists of two monolayers stacked in an AB stacking order, as illustrated in Figure 7.1.The structure exhibits three mirror planes along the three equivalent $M-\Gamma-M$, and the bulk crystal is inversion symmetric.

The AB stacking of FGT monolayers in the bulk crystal, where the B layer is rotated by 180° relative to the A layer, preserves inversion symmetry. This stacking behavior is similar to that of other transition metal dichalcogenides (TMDCs) such as WSe_2 [177–179]. In monolayer FGT, inversion symmetry is broken, but it is restored in bilayer FGT due to the AB stacking. As a result, FGT exhibits a spin polarization behavior similar to WSe_2, where spin polarization is observed in monolayer samples, while bilayer samples exhibit spin-layer locking [122]. In WSe_2, spin polarization in the A layer is opposite to that in the B layer at each k point, leading to exact cancellation when summed over both layers. This effect can be observed when spin-polarized measurements are performed separately on the A and B layers. In FGT, however, the presence of intrinsic ferromagnetism alters this balance. The spin polarization in the A and B layers differs due to ferromagnetic ordering, resulting in a net spin polarization even in the bulk crystal.

7.1.2 Magnetism in FGT

While most of the 2D magnets such as CrI_3 [180], $Cr_2Ge_2Te_6$ [10], $Cr_2Si_2Te_6$ [181] are insulating in nature, FGT is metallic and has bands crossing the Fermi level [163]. This

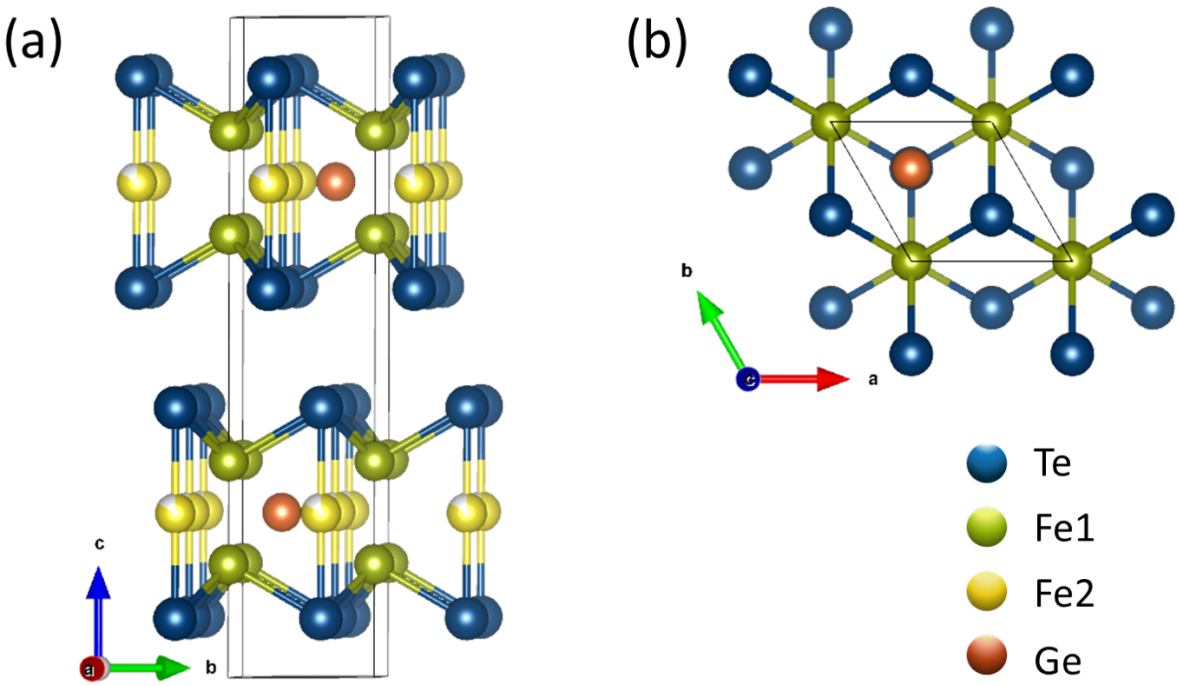

Figure 7.1: Side view (a) and top view (b) of FGT crystal structure.

distinction makes the magnetic interactions in FGT fundamentally different from those in insulating materials, where localized magnetism dominates. The presence of delocalized or itinerant electrons near the Fermi level classifies FGT as a Stoner magnet, a concept that will be explained in detail in this section (and is also discussed in Chapter 7 of [148]).

The itinerant or localized nature of electrons is determined by the effective potential of the atom. The Hamiltonian of an electron in a central potential in spherical coordinates is given by:

$$H(r) = \underbrace{\frac{-\hbar^2}{2m_e}\frac{d^2P_{nl}(r)}{dr^2}}_{I} + \underbrace{V(r)P_{nl}(r)}_{II} + \underbrace{\frac{l(l+1)\hbar^2}{2m_e r^2}P_{nl}(r)}_{III}, \tag{7.1}$$

where $P_{nl}(r)$ is r times the radial part of the wave function. The second term in 7.1 is a Coulomb potential term, which pulls the electron towards the center of the nucleus and the third term is a centrifugal term that points away from the nucleus. The Coulomb potential varies depending on the electron's position relative to the nucleus. Core electrons, which are located close to the nucleus, experience the full nuclear charge, given by $-\frac{Ze^2}{4\pi\epsilon_0 r}$. However, in the valence shell, the core electrons screen the nuclear charge, so the effective potential experienced by valence electrons is reduced to $-\frac{e^2}{4\pi\epsilon_0 r}$. At intermediate distances from the nucleus, the $\mathbf{V}(r)$ assumes a complex form. Slater proposed an approximate form of the effective potential:

$$V_{eff}(r) = -\frac{Z^* e^2}{4\pi\epsilon_0 r} + \frac{l(l+1)\hbar^2}{2m_e r^2}, \tag{7.2}$$

where $Z^* = (Z - \sigma)$, with σ being the screening coefficient. This expression accounts for

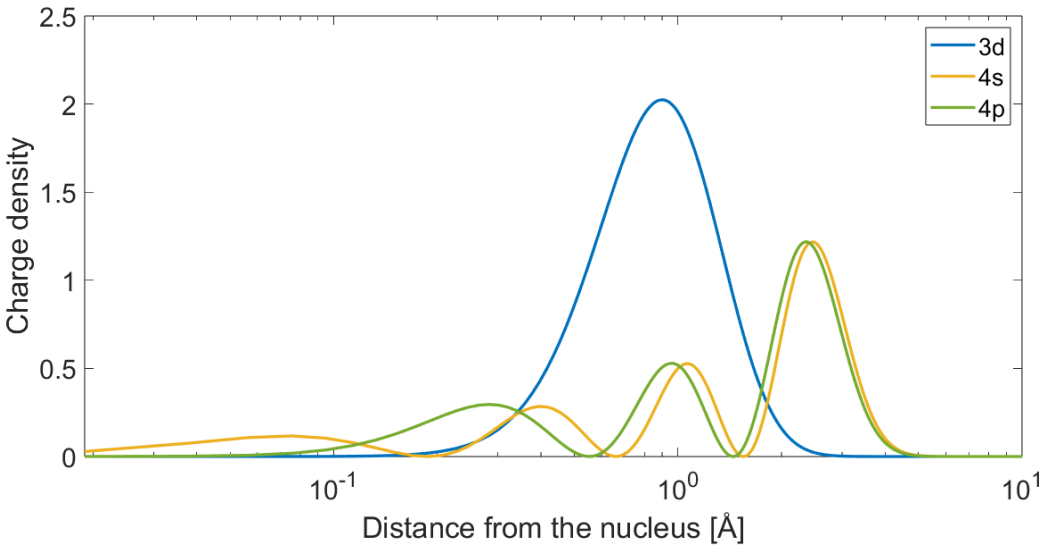

Figure 7.2: The plot show radial wave functions of $3d$, $4s$ and $4p$ orbitals of $3d$ transition metals.

the screening effect caused by core electrons. In transition metal compounds like FGT, a Z^* value of approximately 10 is obtained from calculations [182]. Figure 7.2 illustrates the radial wave functions of the $3d$, $4s$ and $4p$ orbitals, clearly showing that d-electrons are more localized than s- and p-electrons. However, while d-electrons exhibit some degree of localization, they are not as strictly localized as the $4f$-electrons in rare-earth compounds. In those systems, the high l quantum number creates a centrifugal barrier, effectively trapping the f-electrons (see Chapter 7 of [148]).

The partially delocalized nature of the d-electrons can be further confirmed by the deviation of the experimental magnetic moment values from those calculated using the spin and orbital angular momentum quantum numbers, given by $\mathbf{m} = (2\mathbf{s} + \mathbf{l})\mu_B/\hbar$. In the $3d$ transition metals, the magnetic moments are non integer multiples of $\mu_B/\hbar$, which arises from the overlap of d-electron wave functions with surrounding atoms. In these materials, the d-orbitals are split by the surrounding charges, a phenomenon known as crystal field splitting. The extent of this splitting depends on the geometry of the neighboring atoms. When d-orbitals split into real orbitals (such as d_{xy},d_{yz}, d_{xz}, etc.), the orbital angular momentum is partially quenched. Due to the nonzero overlap between d-electrons and bonding atoms, transition metals cannot be adequately described using a purely atomic model. Instead, a band model is necessary to accurately describe their magnetic properties.

The band model for ferromagnetism was developed by Mott [183], Slater [184, 185] and Stoner [186, 187], and is known as the *Stoner model*. In transition metals, the Fermi level is primarily populated by the d-electrons (a schematic representation of the density of states of d-electrons is shown in Figure 7.3 (a)). When the exchange interaction is included, the spin up and spin down states are split by an energy ΔE, also known as the *Stoner splitting* as illustrated in Figure 7.3 (b). This exchange interaction arises purely

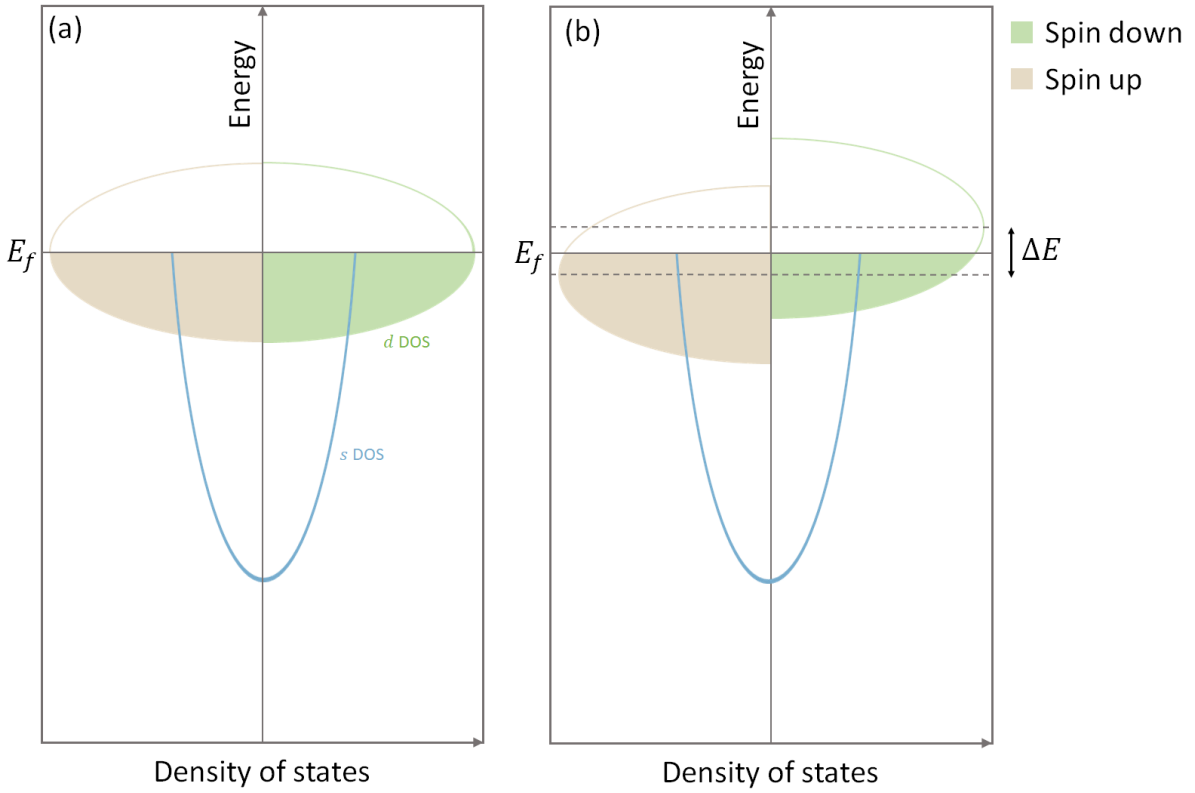

Figure 7.3: Schematic diagram showing the Stoner model of ferromagnetism. (a) show the schematic diagram of spin up and spin down density of states of the d- and s-bands in a non magnetic material near the Fermi level (E_F). The shaded regions show the filled density of states below the Fermi level and the unshaded regions show the hole states above the Fermi level. (b) show the schematic diagram of spin up and spin down density of states of the d-bands in a magnetic material. Compared to the non magnetic case, the magnetic density of states are shifted due to the exchange interaction, and this energy is indicted as ΔE in the Figure.

from the Pauli exclusion principle, which states that no two electrons can occupy the same quantum state. As a result, the splitting creates an imbalance of electron spins, leading to a net magnetic moment given by

$$|\mathbf{m}| = \mu_B(N^{maj} - N^{min}), \tag{7.3}$$

where the N^{maj} and N^{min} are the number the majority and minority spin electrons. The majority and minority spins are determined by the magnetization direction. Equation 7.3 gives the magnetic moment of the Stoner magnet which is a non integer multiple of μ_B, agreeing with $3d$ electron magnets. However, not all transition metals are ferromagnetic. For a material to exhibit ferromagnetism, it must satisfy the Stoner criterion, defined as

$$ID(E_f) \geq 1, \tag{7.4}$$

where I is defined as the ratio of number of spin up or spin down electrons to the total number of electrons, and is called the *Stoner parameter*. The $D(E_f)$ term in Equation 7.4 is the density of states at the Fermi level. This equation implies that only systems in which the total energy is reduced by the Stoner splitting—creating an imbalance of spins near E_f—will be ferromagnetic. This condition is satisfied by elements such as Fe, Co, and Ni.

In the case of FGT, where magnetism is due to the magnetic Fe atom, the magnetic interaction is quite complex. Previous band structure studies show that magnetism in FGT can not be fully explained by Stoner model alone [172]. Instead, a combination of localized and itinerant magnetism is required to explain the temperature-dependent evolution of band structure of FGT [170].

7.2 Electronic band structure of Fe_3GeTe_2

7.2.1 Resonant photoemission

When photoemission is performed at photon energies close to the absorption edge of an atom in the solid, the intensity of the emission from this atom will be enhanced and the enhancement is called *resonant enhancement*. The technique used to exploit this effect is called *resonant photoemission*, which is closely related to the core levels of the atoms present in the material. Core levels, located at deeper binding energies, are highly localized to specific atoms. Because of this localization, resonant photoemission is element-specific, allowing selective enhancement of the photoemission signal from different atomic species by tuning the photon energy to the corresponding atomic core levels. This makes resonant photoemission a powerful tool for determining the atomic contributions to a material's band structure.

As mentioned earlier, resonant photoemission is closely related to the X-ray absorption spectroscopy (XAS). In XAS, the sample is illuminated with photons of varying energies. When the photon energy becomes high enough to excite an electron from a core level to an

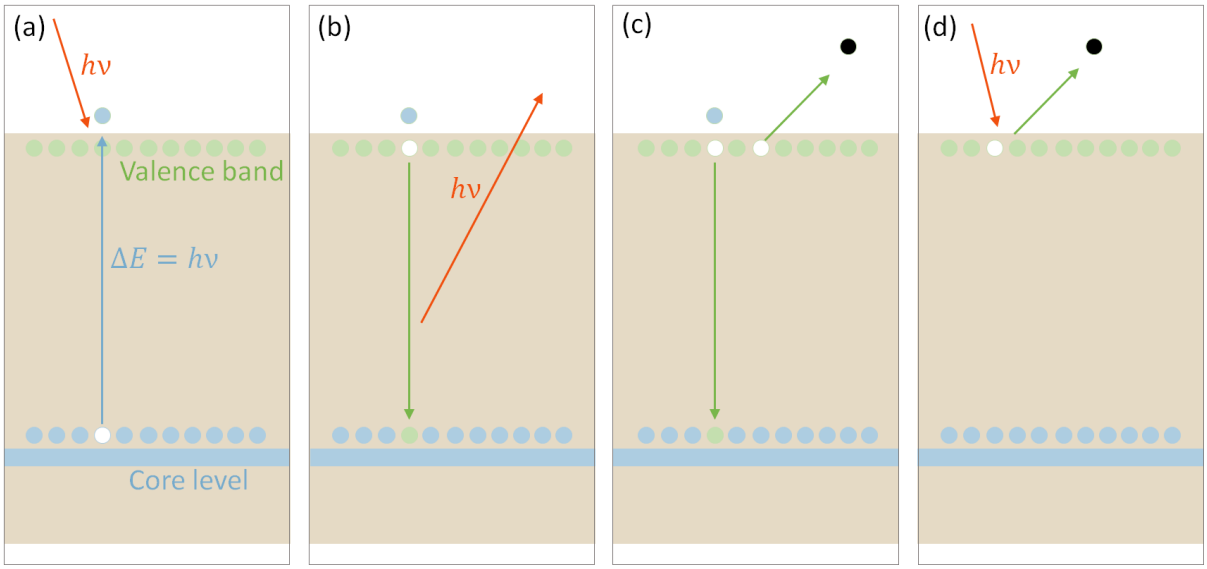

Figure 7.4: Schematic diagram showing (a) excitation of core electron in X-ray absorption, (b) decay of core hole through fluorescence, (c) decay of core hole through Auger emission and (d) direct photoemission final state.

unoccupied state above the Fermi level (see Figure 7.4 (a)), a peak appears in the X-ray absorption cross-section. XAS spectra can be recorded by measuring the current between the sample and ground, known as the *drain current*. These transitions can be described using time-dependent perturbation theory and are governed by the dipole selection rules: $\Delta l = \pm 1$ and $\Delta m = 0$ or ± 1. In the final state, a hole is created in the core level, while an electron occupies a previously unoccupied state above the Fermi level.

The lifetime of the hole in the core level is of the order of few femto-seconds. The core hole is rapidly filled by an electron from either a higher-lying core level or the valence band. The filling of the core level by another electron will result in emission of a photon or in emission of an electron. In case of the photon channel, a photon of wavelength corresponding to the energy difference of the core level (from which the electron is emitted to the unoccupied state) and the core level or valence band (from which the electron is refilled), is emitted (see Figure 7.4 (b)), and can be measured using a X-ray fluorescence spectrometer. The other channel, where an electron is emitted, is called the Auger channel. Here the electron decay results in the emission of an electron from another core level or from valence band, above the vacuum level as a free electron. When the refilling electron and emitted electron are from the valence band, it is called CVV (core-valence-valence) Auger emission (see Figure 7.4 (c)). Since the core level is a localized state of the atom, the electron that is emitted will be also from the same atom. This electron can be detected as photoelectron in an ARPES setup. In resonant photoemission, the sample is probed with the photon energy that matches the absorption edge of an atom in the solid. There are two possible emissions. The first one is the regular emission, which is the direct emission from the valence band (see Figure 7.4 (d)). The second one is the Auger emission, as discussed earlier. In both the cases the final state of the emission is the same and the energy of the emitted electrons are also the same. These two processes can happen at the same

time and will interfere coherently [141, 188], resulting in an intensity enhancement of the bands from the corresponding atom. In this way, resonant photoemission can be used for determining the atomic character of the band structure of solids. Resonant photoemission was used in subsection 6.2.1 to determine the Cr derived bands in CGT and was also used in other studies for the atomic composition of the band structure [141, 188].

A theoretical calculation of resonant photoemission is difficult because of the complexity of the physics involving the interaction between core and valence holes with the remaining electrons. Especially in the case of materials like FGT and CGT, where the electronic correlations and onsite Coulomb repulsion plays an important role, the resonant photoemission would be extremely complex to calculate.

7.2.2 Resonant ARPES on Fe_3GeTe_2

In the ARPES maps, FGT shows broad bands near the valence band due to electronic correlations, and therefore, it is difficult to determine the band characters. This issue can be tackled by performing resonant ARPES. As mentioned in the previous section, resonant ARPES is element-specific because of the localized nature of the core levels. This property of resonant ARPES can be used to study the atomic composition of the band structure of FGT. The electronic correlation effects in FGT can also be studied to some extend using this technique.

A commercially available bulk single crystal of FGT (from HQ Graphene company) was glued on Mo plate using silver epoxy glue. Since FGT is a very reactive material, the entire procedure of gluing was performed in a glovebox, to avoid any interaction with air and to avoid chances of oxidation. The sample was then prepared for cleaving using the scotch tape. the ARPES measurements were performed at PHELIX beamline at SOLARIS. To align the sample along the high-symmetry direction, constant-energy $k_x - k_y$ cuts were acquired at a photon energy of $h\nu$ =114 eV. The sample was aligned such that the $M - \Gamma - M$direction coincided with the plane defined by the light incidence direction and the sample surface normal. The Fermi surface map of FGT at $h\nu$ = 114 eV with horizontally ($p-$) and vertically ($s-$) polarized light averaged over ΔE = 0.16 eV is shown in Figure 7.5 (a) and (b), respectively. The maps exhibit mirror symmetry along the $M - \Gamma - M$ direction, consistent with the sample's crystal symmetry. At $h\nu$ = 114 eV, FGT show Fermi surface features with elements of trigonal symmetry (see Figure 7.5 (a)). The trigonal symmetry indicates that the photoemission is from a single terrace of FGT.

Before the resonant ARPES measurements, an XPS measurement at $h\nu$ = 1000 eV was performed to identify the core level energies of FGT. The Fe 2p, Fe 3p, Te 4d and Ge 3p peaks were observed in the XPS spectra, as shown in Figure 7.6 (a). The peak positions agree with elemental core level energies of Fe, Ge and Te [189], confirming the chemical composition of the measured crystal. The Te core level peaks show the highest intensity as the cross section of the Te 3d orbitals are higher than Fe 3p and Ge 3d orbitals at $h\nu$ =

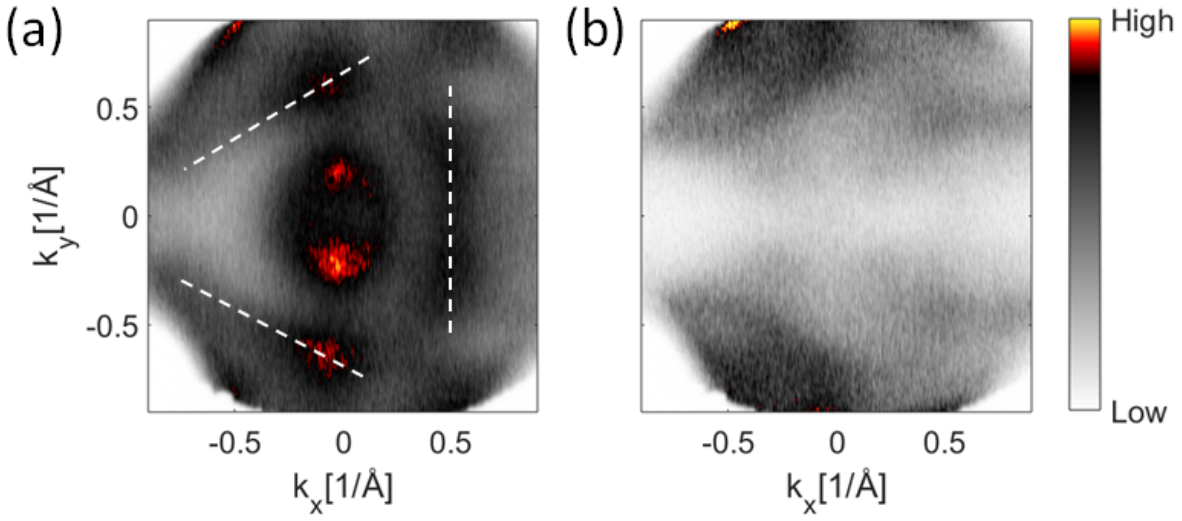

Figure 7.5: (a) p–polarized and (b) s–polarized light spectra from FGT at $h\nu$ = 114 eV. The map shows the Fermi surface with $\Delta E = 0.16$ eV. The horizontal direction corresponds to $M - \Gamma - M$ direction. The dotted lines in (a) show the trigonal symmetry of the Fermi surface.

1000 eV, as plotted in Figure 7.7.

The Fe 2p and Fe 3p core levels were chosen for the resonant ARPES measurements. Figure 7.6 (b) shows the XPS measurement at $h\nu$ = 1000 eV with binding energy ranging from 700 eV to 736 eV, performed to cover the Fe 2p core level. To precisely determine the absorption edges of Fe 3p and Fe 2p, an XAS measurement was performed as shown in Figure 7.8. The Fe 3p shows a broad absorption edge starting from $h\nu$ = 52 eV. The spin-orbit-split Fe $2p_{3/2}$ and $2p_{1/2}$ components were found to be at $h\nu$ = 706 eV and at $h\nu$ = 718 eV, respectively.

The resonant ARPES spectra around the Fe 2p edge using p–polarized light are shown in Figure 7.9 (a). The Auger peak can be seen moving in the binding energy with respect to the photon energy used, which is also visible in the EDC plot in Figure 7.9(b). Within this photon energy range, there were no clear dispersive band structure features visible other than the flat band near the Fermi level. Moving through the resonance, the flat bands show a clear increase in intensity as the Auger peak moves through the band. The intensity of the band at the Fermi level with respect to the photon energy is plotted in Figure 7.9 (c). The intensity versus photon energy plot resembles the XAS spectra of Fe 2p core level (Figure 7.8 (b)) and show the spin-orbit-split $2p_{1/2}$ and $2p_{3/2}$ features. This resemblance might be because of the Fe contribution in the band or might be also an increase in intensity simply because of the Auger peak passing by. A theoretical calculation is required to determine the actual reason and to decouple the influence of Auger emission from the Fe related enhancement of the bands.

Further resonant ARPES measurements were performed on the Fe 3p core level, around

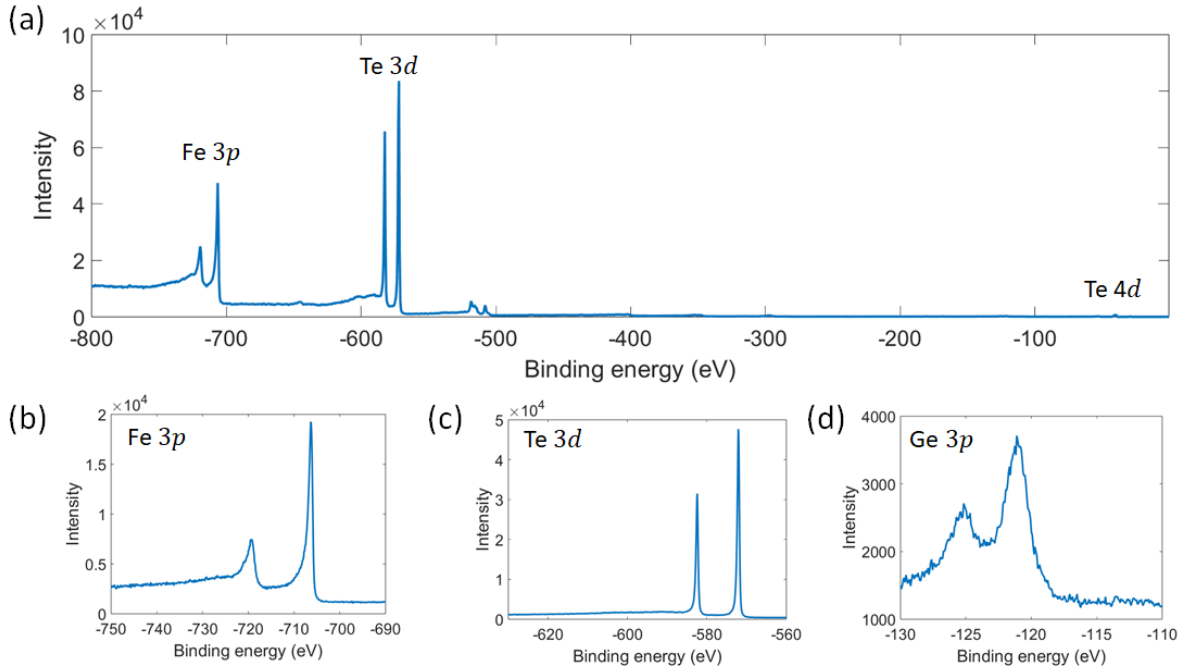

Figure 7.6: (a) XPS spectra on bulk Fe_3GeTe_2 crystal showing Fe 2p, Te 3d and Te 4d core levels, at $h\nu$ = 1000 eV. (b), (c) and (d) shows XPS spectra from bulk FGT showing Fe 3p, Te 3d and Ge 3p core levels respectively.

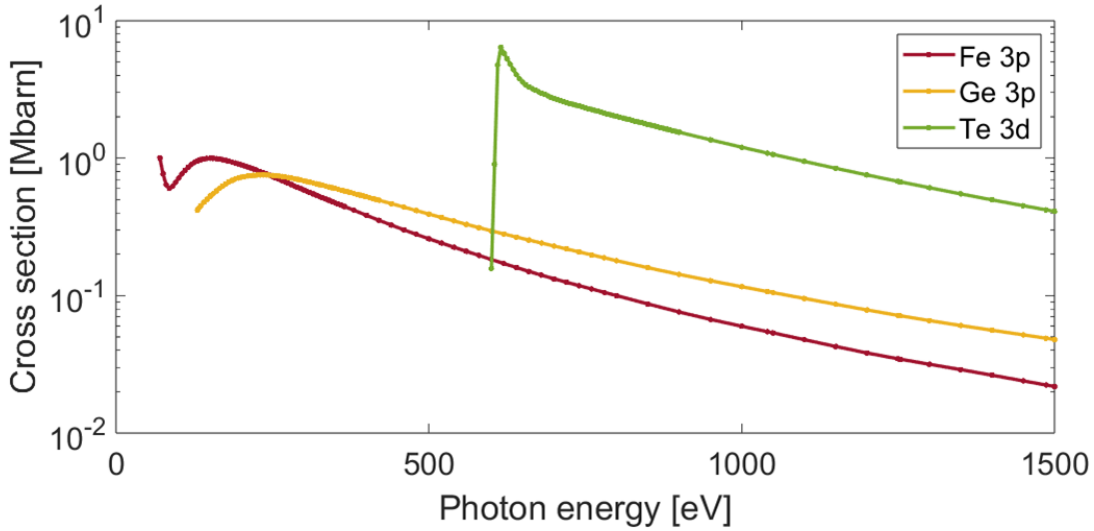

Figure 7.7: Cross section of Fe 3p, Ge 3p and Te 3d at photon energy ranging from $h\nu$ = 10 eV to 1500 eV [123].

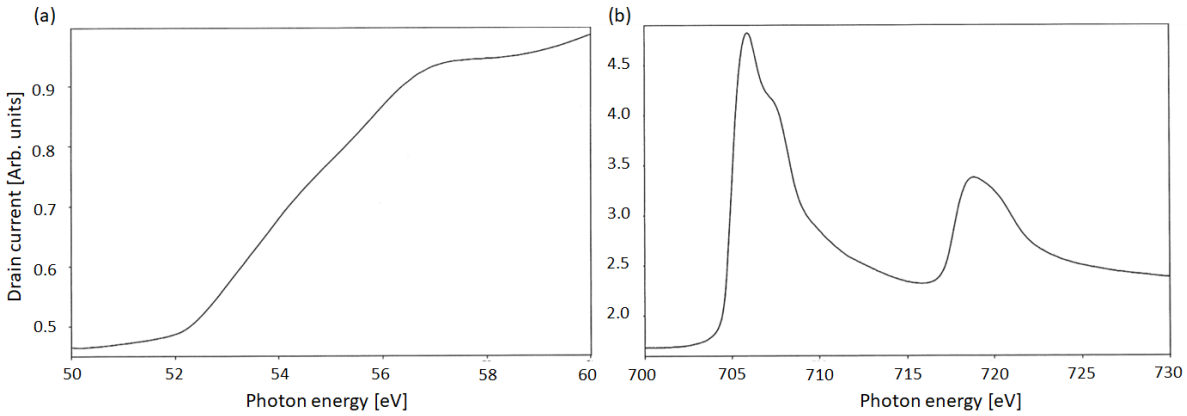

Figure 7.8: XAS measurement from FGT showing (a) Fe $3p$ edge and (b) Fe $2p$ edge. The photon energy range of $h\nu$ = 50 to 60 eV was chosen for (a) and $h\nu$ = 700 to 725 eV was chosen for (b).

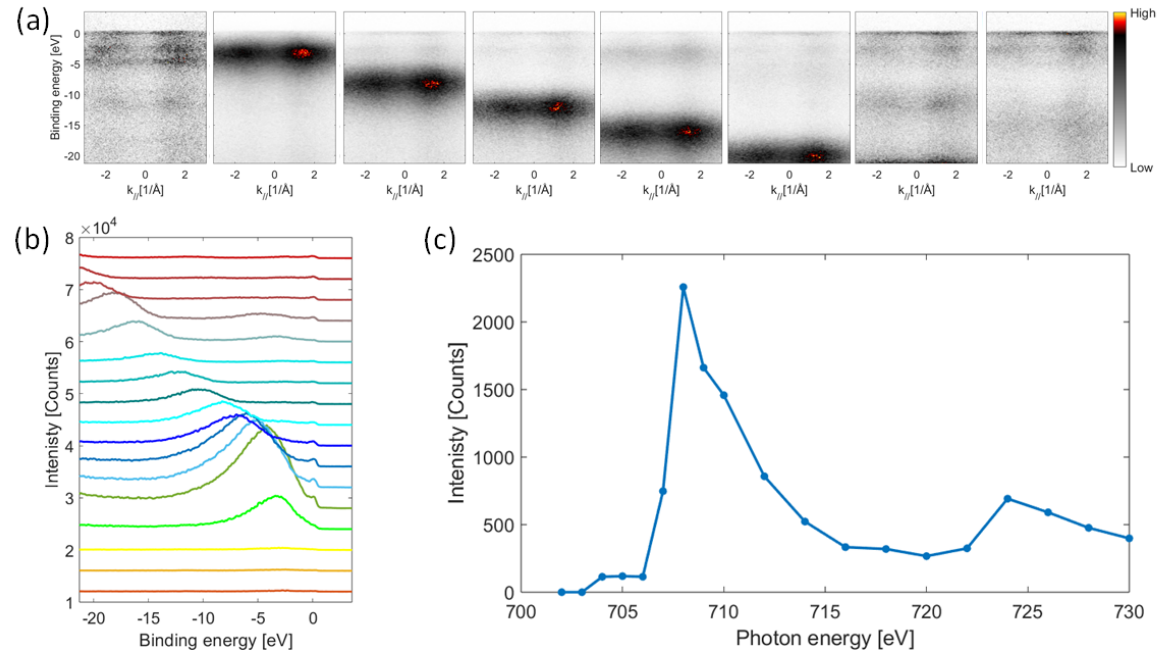

Figure 7.9: (a) Resonant ARPES measurements from FGT at $h\nu$ = 700, 705, 710, 714, 718, 722, 726 and 730 eV. (b) EDC plots of resonant ARPES measurements at $h\nu$ = 700-736 eV, at $k_{||}$ = 0 Å^{-1}. The measurements were performed at ≈ 60 K. (c) shows the intensity versus photon energy of the band at $k_{||}$ = 0 Å^{-1} at the Fermi level.

$h\nu$ = 56 eV. The polarization-dependent resonant ARPES maps measured using p– and s–polarized light are shown in Figure 7.10 (a) and (b), respectively. Additionally, CD-ARPES measurements were also performed at these photon energies (shown in Figure 7.10 (c)). Both the horizontal and vertical polarization measurements show the Auger peaks moving with respect to the photon energies. The EDC plot for the horizontal and vertical polarization are shown in Figure 7.11 (a) and (b), respectively. For the horizontal polarization, the E versus $k_{||}$ spectra show several bands near the Fermi level. The bands at the Fermi level show no dispersion or minimal dispersion, when measured with p–polarized light. In contrast to the p–polarized measurements, the s–polarized measurements show dispersing bands near the Fermi level, as shown in Figure 7.10 (b). The intensity of these bands increases as the photon energy moves through the resonance. The intensity versus photon energy plot for the topmost band at the Fermi level at $k_{||}$ = 0 Å^{-1} is shown in the Figure 7.11 (c) and (d). A particularly notable feature appears at a binding energy of E_b = 10 eV. This band is visible only under horizontal polarization, which may be due to a combination of atomic final-state effects and multiple scattering processes. The intensity of this band exhibits a sharp peak near resonance (at $h\nu$ = 56 eV) and drops by approximately a factor of 12.5 after the resonance, as shown in the EDC plot in Figure 7.11 (e). Similar to the p– and s– polarization measurements, CD-ARPES also reveals several bands near the Fermi level. The emergence of the band at E_b= 10 eV near resonance is particularly evident in the CD-ARPES maps.

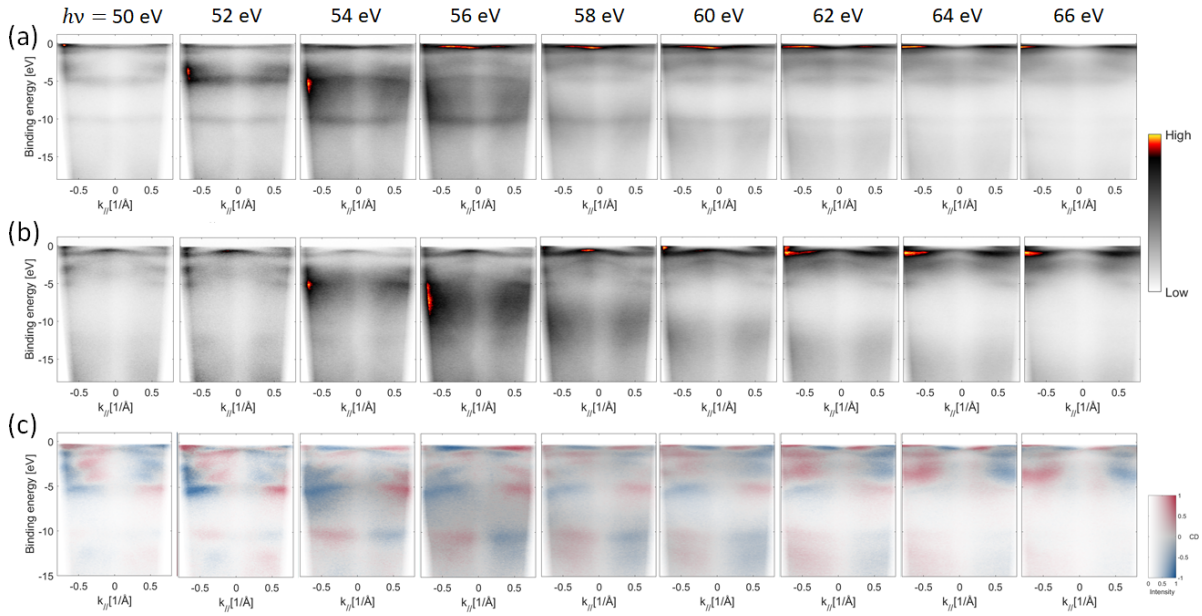

Figure 7.10: Resonant ARPES measurement from FGT with (a) p– polarized light and (b) with s–polarized light, at photon energies from $h\nu$ = 50 to 66 eV in steps of 2 eV. (c) show the CD-ARPES spectra from FGT at same energies as in (a) and (b). The measurements were performed at ≈ 60 K.

To study the atomic composition of the band structure of FGT, DFT calculations were performed in WIEN2k [33], with atomic positions obtained from materials project database [157]. The density of states (DOS) of FGT at binding energies ranging from -20 eV to

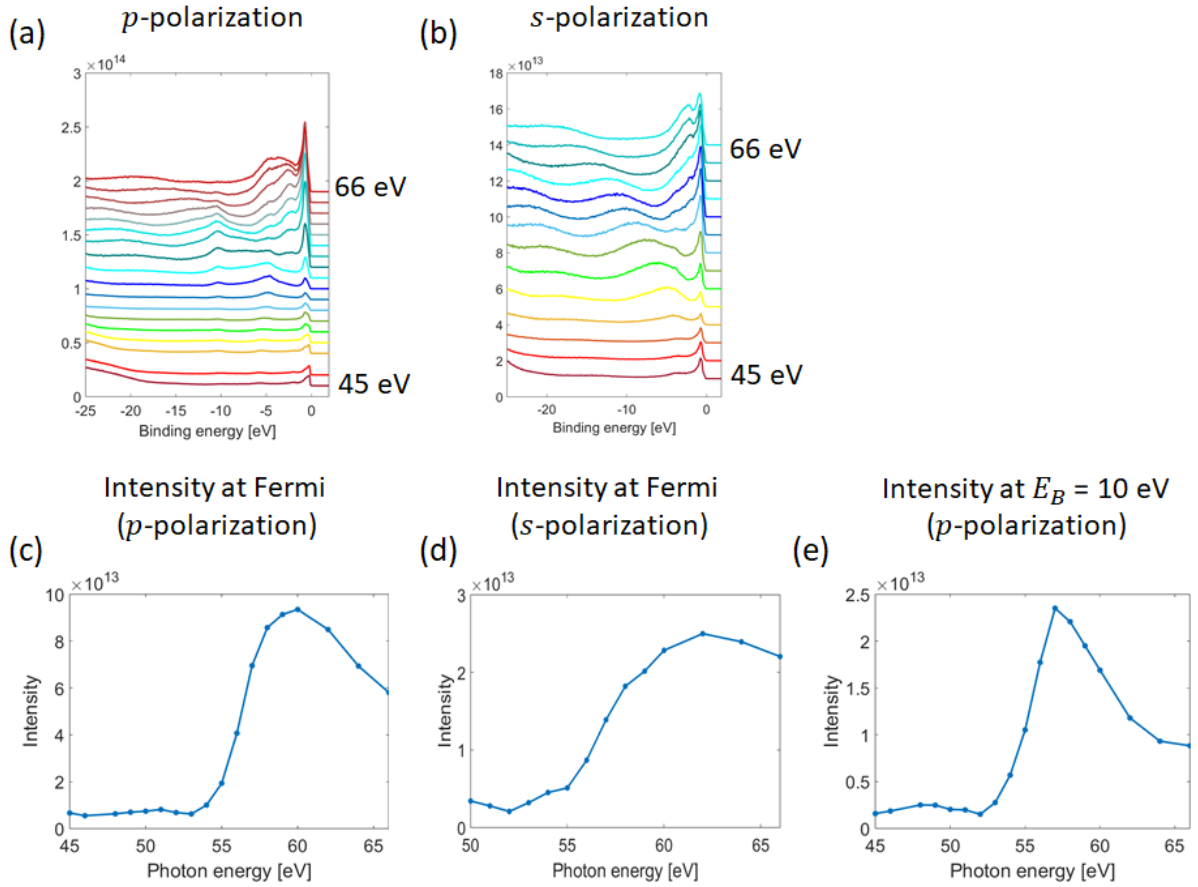

Figure 7.11: Energy distribution curves (EDCs) of resonant ARPES maps at the normal emission for (a) horizontally and (b) vertically polarized light at photon energies $h\nu$= 45 eV to 66 eV. The intensity versus photon energy plots in (c) and (d) show the intensity enhancement of the bands at the Fermi level at $k_{||}$ = 0 Å^{-1}, with horizontally and vertically polarized light, respectively. (e) shows the intensity versus photon energy of the band at E_b = 10 eV.

10 eV are shown in Figure 7.12. From the DOS, it is clear that the main contribution at the Fermi level is from Fe, with a smaller contribution from Te. The band at E_b = -10 eV is derived from Ge and the enhancement of the intensity of the band is unrelated to the resonance effects.

However, based on intensity variations alone, it is not possible to definitively determine the atomic contributions to the band structure of FGT. As discussed earlier, the observed intensity enhancements could result from the Auger peak passing through the bands during resonance. A more detailed theoretical analysis would be required to disentangle these effects. Resonant ARPES calculations, which involve complex many-body interactions with two-hole final states, present a significant computational challenge. A practical approach would be to develop a method to assess whether the resonance enhancement is due to coherent effects or merely an incoherent sum of bands and Auger emission.

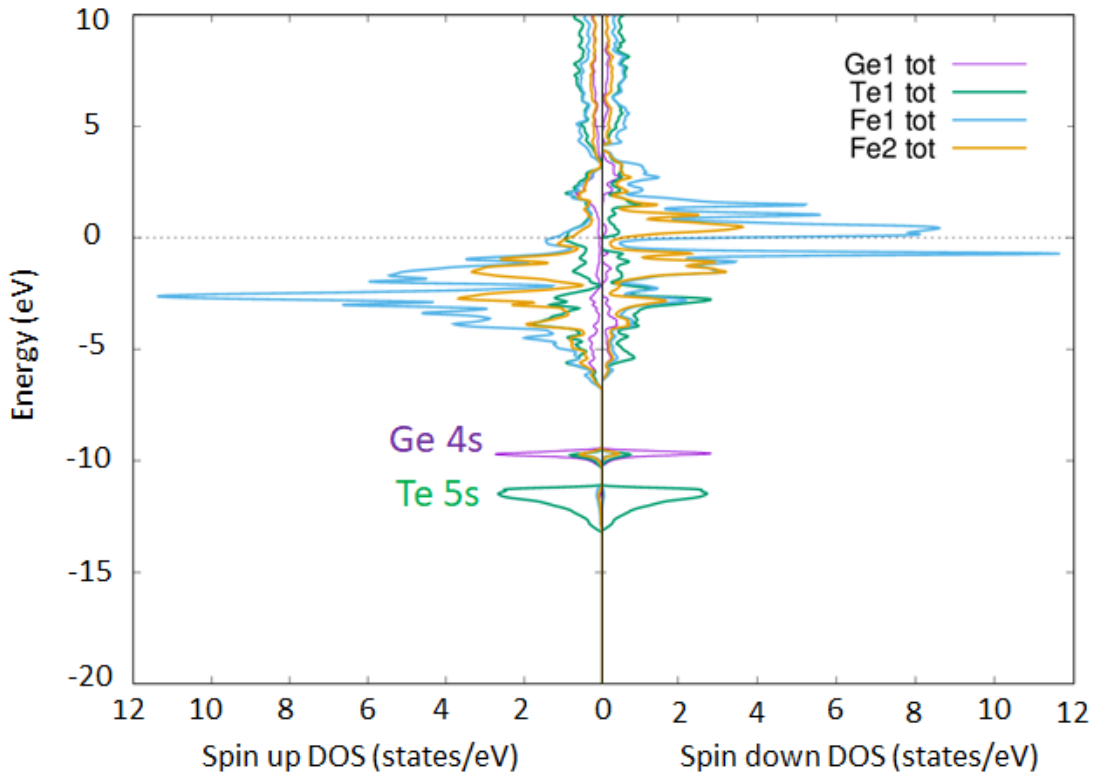

Figure 7.12: Density of states (DOS) of Fe, Te and Ge atoms in FGT band structure. The spin up and spin down states are plotted separately. Ge and Te DOS at ≈ -10 eV and ≈ -12 eV are indicated.

7.3 Magnetic domain structure of Fe_3GeTe_2

In a collinear magnetic material, magnetic moments align along a preferred axis below the Curie temperature, known as the easy axis. The easy axis is determined by the material's magnetic anisotropy (see Chapter 11 of [148]). The energy associated with magnetic anisotropy is expressed as:

$$E_{ani} = K_1 sin^2\alpha + K_2 sin^4\alpha + K_3 sin^6\alpha + ..., \tag{7.5}$$

where the constants K_i with i = 1,2,3,.. are anisotropy constants, which depend on the material, and α is defined as the angle between the easy axis and the magnetic crystallography axis. Since magnetic anisotropy remains unchanged upon magnetization reversal, E_{ani} is an even function of α. For materials exhibiting uniaxial anisotropy (where there is only one magnetic easy axis), all other terms except the first term in Equation 7.5 vanish. The anisotropy constant in this case is given by $K_1 = K_{cry} + K_{sh}$, where K_{cry} and K_{sh} are the magneto crystalline anisotropy and shape anisotropy, respectively.

The magneto crystalline anisotropy originates from the spin orbit coupling, which couples

otherwise isotropic spins to the crystal lattice, introducing directional dependence in magnetic behavior. Since this anisotropy is linked to bonding interactions, it is inherently tied to the material's crystal structure. The shape anisotropy originates from the interaction between the spin moments, given by the dipole-dipole interaction. The dipole-dipole interaction energy is given by

$$E_{dip-dip} \propto \sum_{i \neq j} \frac{1}{r_{ij}^3} \left(\mathbf{m}_i . \mathbf{m}_j - 3 \frac{(r_{ij} . \mathbf{m}_i)(r_{ij} . \mathbf{m}_j)}{r_{ij}^2} \right), \tag{7.6}$$

where r_{ij} is the distance between the two magnetic moments m_i and m_j. Additionally, the shape anisotropy includes contribution from the stray field, or the demagnetizing field, and effects from the surface, which arise from the pseudo charges at the surface due to the breaking of the bonds at the surface. Since the dipole-dipole interaction energy is lowest when the magnetic moments ($\mathbf{m}_i/\mathbf{m}_j$) are aligned along the inter nuclear axis, $\mathbf{r}_{ij}$ (ie., when $\mathbf{r}_{ij}.\mathbf{m}_{i,j}$ term in Equation 7.6 becomes $r_{ij}m_{i,j}$), the shape anisotropy prefers the spin to be in plane. On the other hand, the magneto-crystalline anisotropy which is related to the spin-orbit coupling, generally align the spins in thin films and 2D materials in the out-of-plane direction, due to the broken bonds at the surface. The final orientation of the spins is determined by the competition between shape anisotropy and magneto crystalline anisotropy. Dominance of shape anisotropy results in in-plane easy axis and dominance of magneto crystalline anisotropy results in out-of-plane easy axis.

In equilibrium, a magnetic sample does not exist in a completely uniform magnetic state due to the presence of a stray field. In a uniformly magnetized state, the stray field emerging from the sample is nonzero, making it energetically unfavorable. To minimize this energy, the system naturally reorganizes into magnetic domains—regions of uniform magnetization—thereby reducing the stray field [190]. Domain size and pattern depends on the material thickness and shape. By moving from domain to domain, the spins rotate. The region where the spins are not along the magnetic easy axis is called the domain wall. The domain wall thickness strongly depends on the magneto crystalline anisotropy and the exchange interaction. The magneto crystalline anisotropy tends to decrease the size of the domain wall, whereas the exchange interaction, which forces the spin to align parallel to each, forces the domain wall size to increase.

FGT exhibits rich domain structure patterns. Previous domain structure studies indicate that below the Curie temperature FGT shows stripe domains [72, 160, 162, 191, 192], spin bubbles, and skyrmion spin textures [174, 175, 193]. The out-of-plane stripe domains indicate the high magneto-crystalline anisotropy in FGT. In FGT, the domain structure depends on many factors, which includes the thickness of the sample, the applied external magnetic field and temperature at which the measurement is performed [194]. Bulk-like samples of FGT, with thickness greater than 30 nm, exhibit the out-of-plane stripe domains [194]. When the thickness is reduced to below 30 nm or below, the bubble domains were observed [194]. Similarly, with field cooling and field warming, transitions from spiral to spin bubble and vise versa were observed in FGT [174]. Transmission electron microscopy (TEM) studies also show that FGT exhibits both Néel type and Bloch type skyrmions [191]. An interesting PEEM study has shown a transition of out-of-plane spin to the

in-plane direction in FGT by changing the shape of the FGT nanoflakes [72]. In this paper [72], the in-plane spin ordering is observed even up to 300K. In the same study, an increase in the domain size has been observed with decreasing sample thickness. Apart from the domains itself, the domain walls of FGT has also been an interesting field of research [195, 196].

This thesis aims to identify single domains or large-area domains with lateral dimensions of the order of micrometers, making them suitable for micro-ARPES measurements. To achieve this, FGT flakes with thicknesses below 4 nm (corresponding to 4–5 monolayers) were prepared. Since FGT is highly reactive, mechanical exfoliation was performed inside a glove box under an argon atmosphere. The flakes were encapsulated with graphene, with a thick, flat graphite flake serving as the bottom layer of the heterostructure. The sample preparation process is detailed in Chapter 4. Figure 7.13 (a) presents an optical image of the heterostructure sample, where regions with 3–4 monolayers and bulk-like regions are marked. The lateral dimensions of the exfoliated flakes are approximately 8×8.

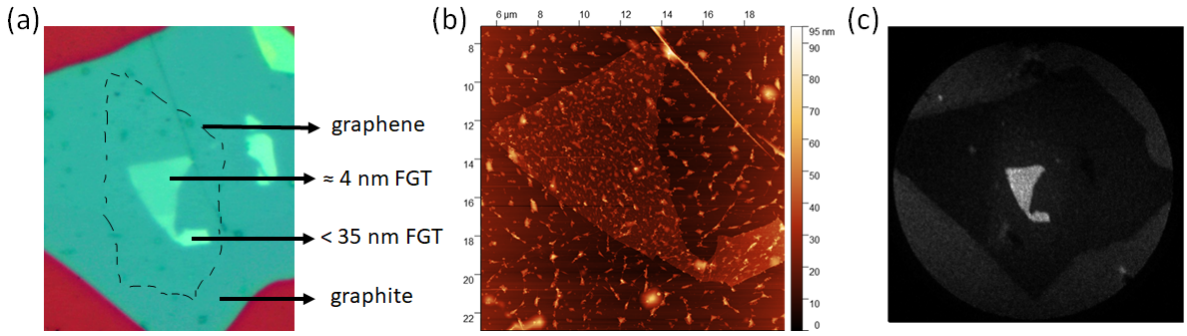

Figure 7.13: (a) Optical microscope image of graphene/FGT/graphite hetero structure. (b) AFM image of the hetero structure. The bubbles trapped during the stacking of flakes are visible. (c) PEEM image of FGT flake.

Photoemission electron microscopy at DEMETER beamline at SOLARIS and NanoESCA beamline at Elettra synchrotron were used to map the domain patterns in FGT. PEEM was performed using the x-ray magnetic circular dichroism (XMCD) mode to obtain the magnetic contrast. In the following section, a brief description of XMCD technique will be given.

7.3.1 X-ray magnetic circular dichorism

In both x-ray absorption spectroscopy (XAS) and in XPS, the intensity of the peaks is given by the square of the transition matrix element, which depends on the polarization and direction of the photon source used. The photoemission transition matrix is given by $\langle \psi_f | P_q^\alpha | \psi_i \rangle$, where ψ_i and ψ_f are initial and final state wave functions, and P_q^α is the dipole operator. The photoemission intensity depends on three factors, the orientation of the sample with respect to the incident photon, the polarization of the photon (q) and the direction of the polarization (α). The fully angle integrated intensity in XAS or XPS is related to the total number of the unoccupied states above the Fermi level. The angle average is often

approximately obtained by summing the three direction-dependent measurements along the orthogonal axes (x, y and z axis in case of crystals with symmetries higher than that of monoclinic structure) or by summing the polarization dependent measurements ($q = 0, \pm 1$) [148]. However, this approximation does not account for photoelectron diffraction effects.

In the case of L edge spectroscopy, where the initial states are p levels, the allowed $l \pm 1$ transitions are given by the dipole selection rules, which are the p to s and p to d transitions. In transition metals, the main contribution in the L edge spectra comes from p to d transitions. The intensity of the transition corresponds to the total number of unoccupied d levels above the Fermi level. This is particularly interesting for transition metals, where the d-orbitals are partially filled. The intensity of the peaks decreases while going from Fe to Cu because of the fully filled d-orbital configuration towards Cu.

In the transition metal magnets, there is an imbalance of spin up and spin down states, as explained in the Stoner model (see section 7.1.2). The magnetic moment of the Stoner magnets can be determined by the difference of spin up and spin down density of states of the d levels near the Fermi level given by the Equation 7.3. If the excitation can be made spin selective, then from the measured intensity, the spin up and spin down unoccupied states can be determined. This is possible by using circularly polarized light to excite the core levels. The angular momentum of the photons (± 1 for $C_\pm$ light), couples with the spin angular momentum through the spin-orbit coupling, which excites selected spins. This can be used to obtain the magnetic contrast measurements.

For the PEEM measurements in this thesis, the $2p$ core levels of Fe were used. The spin-orbit splitting of the $2p$ core levels can be obtained by calculating the $H = \mathbf{L} \otimes \mathbf{S}$ Hamiltonian. Here $\mathbf{L} = (\mathbf{L}_x, \mathbf{L}_y, \mathbf{L}_z)$ is a vector of 3×3 matrices given by

$$\begin{aligned} L_x &= \frac{\hbar}{\sqrt{2}} \begin{pmatrix} 0 & 1 & 0 \\ 1 & 0 & 1 \\ 0 & 1 & 0 \end{pmatrix} \\ L_y &= \frac{\hbar}{\sqrt{2}i} \begin{pmatrix} 0 & 1 & 0 \\ -1 & 0 & 1 \\ 0 & -1 & 0 \end{pmatrix} \\ L_z &= \hbar \begin{pmatrix} 1 & 0 & 0 \\ 0 & 0 & 0 \\ 0 & 0 & -1 \end{pmatrix} \end{aligned} \tag{7.7}$$

and $\mathbf{S} = (\sigma_x, \sigma_y, \sigma_z)$ is the vector of Pauli spin matrices given by

$$\sigma_x = \begin{pmatrix} 0 & 1 \\ 1 & 0 \end{pmatrix}, \sigma_y = \begin{pmatrix} 0 & -i \\ i & 0 \end{pmatrix}, \sigma_z = \begin{pmatrix} 1 & 0 \\ 0 & -1 \end{pmatrix}. \tag{7.8}$$

The Kronecker product of $\mathbf{L}$ and $\mathbf{S}$ gives the 6×6 matrix. By diagonalizing this 6×6 Hamiltonian matrix, two energy eigenvalues are obtained, and are found to be corresponding to the $p_{1/2}$ and $p_{3/2}$ states. These are 2-fold and 4-fold degenerate, respectively

(shown in Figure 7.14). As shown in the Figure 7.14, it is clear that only $p_{3/2}(3/2)$ and $p_{3/2}(-3/2)$ are pure spin states, the rest of the states are a mixture of spin up and spin down states. With the initial $p_{3/2}(3/2)$ and $p_{3/2}(-3/2)$ states, the angular component of the transition matrix elements simplifies to a single term. Unlike in the case of valence band photoemission, where both p to d and p to s transitions are relevant, in the core levels p to d transitions dominate because of the availability of d levels immediately above the Fermi level. The p to s transitions are weaker than the p to d by a factor of 20 in this case. Therefore, one can consider only p to d channel, with its radial part and angular part. This allows to avoid complexities related to the interference of $l \pm 1$ channels. The calculated transition probabilities from $2p$ states with $C_{\pm}$ light and the difference between the two intensities are shown in Figure 7.15. The selection rules are applicable to the l and m_l quantum numbers and therefore the j, m_j states need to be rewritten in the l, m_l basis. The coefficients can be obtained by solving the Hamiltonian or are readily available in the textbooks and are called the Clebsch-Gordan coefficients. The intensity of spin up and spin down electrons from $p_{3/2}$ is 36.5 % and 65.5 %, respectively and $p_{1/2}$ states it is 75 % and 25 %. In the case of $p_{1/2}$, the net spin polarization is 50 %, whereas for the $p_{3/2}$, the net spin polarization is 25 %. The sign of the polarization is opposite for $p_{3/2}$ and $p_{1/2}$, this is obvious because the spin-orbit-split states correspond to the l+s and l−s energy levels.

In XMCD measurements, the detected photoelectrons primarily result from Auger cascades, undergoing multiple inelastic scattering, which leads to a fully integrated angular distribution. While the magnetization direction is typically assumed to align with the light incidence, in practice, the light is incident at an angle. As a result, only the spin component along the light incident direction is measured, meaning that a projection of the spin along the light incidence direction is recorded. Because spin-flip transitions are forbidden and electronic states near the Fermi level are highly spin-polarized, the net CD signal is directly linked to the magnetization of the sample.

For the PEEM measurements on FGT, the $2p$ core level energies were first determined by XPS. The $2p_{3/2}$ and $2p_{1/2}$ were found at 718.6 eV and 705.8 eV binding energies. An XMCD measurement was performed at room temperature and as expected, no dichroism was observed, confirming that FGT is in the paramagnetic sate in the room temperature. The XMCD result at room temperature is shown in Figure 7.16 (a). Additionally, an XMCD image was obtained at room temperature at $h\nu$ = 706 eV and is shown in Figure 7.16 (b). The room temperature XMCD image confirms that there is no signature of domains. The field of view is adjusted by the voltage applied on the electrostatic lens and was adjusted to be 37.5 μm for Figure 7.16 (b). These measurements were performed at the DEMETER beamline at SOLARIS.

The sample was then cooled to 70 K using liquid nitrogen and the XMCD image was measured at $h\nu$ = 706 eV (shown in Figure 7.17 (a)). There are clear indications of domains at 70 K, which confirms that the sample is in the ferromagnetic state. The thicker regions of the flake exhibit the stripe domains, as expected. The 3-4 monolayer regions show small bubble-like structures and a single domain region was observed as indicated in Figure 7.17 (a) (marked in yellow circle). The field of view of the PEEM

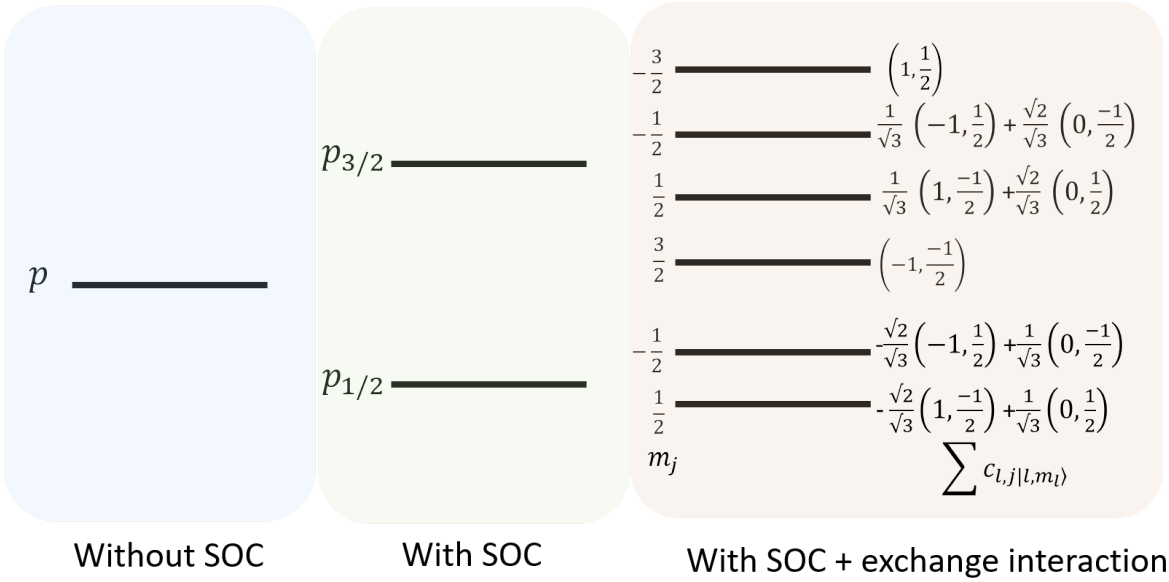

Figure 7.14: Figure shows the $2p$ core levels without spin orbit coupling (blue region), with spin orbit coupling (green regions) and with spin orbit coupling and exchange interaction (beige region).

image shown in Figure 7.17 is 20 micrometers. The dimensions of the single domain region was determined from the field of view and was found to be approximately 3×4 micrometers. This is comparable to the available size of the micro-ARPES beamspot when the focusing capillary is used. To confirm the magnetic nature of the domains observed, the measurements were repeated at $h\nu$ = 718 eV where the signs of the dichroic signal should reverse (shown in Figure 7.17 (b)). The demonstrated reversal of the sign while moving from $h\nu$ = 706 eV to $h\nu$ = 718 eV confirms the magnetic nature of the measured domains.

In conclusion, the XMCD measurements on few layer FGT flake show relatively large single domain region which could be used in micro-ARPES measurements. Spin polarized ARPES measurement on bulk 2D materials are always averaging the spin up and spin down domains making it impossible to study the single domain spin polarized bands. Observation of single domain regions, of the order of micro ARPES beam spot in the flake samples, paves a new path to study the spin polarized bands with micro ARPES setups, where the spin polarized bands could be potentially studied using $C_{\pm}$ light. As a possible extension, making 2D magnetic heterostructure samples on magnetic multilayer substrate with out-of-plane magnetization will further increase the size of the domains due to the proximity effect. This would allow spin polarized measurements, with slightly larger beam spots, possible. An important requirement for the studies is the protection of the FGT flakes by encapsulation with monolayer graphene, which allows to measure these, otherwise readily oxidizing, samples. The sample with encapsulation is convenient as it does not require a vacuum suitcase, use of which is difficult when the measurements are performed at different synchrotrons.

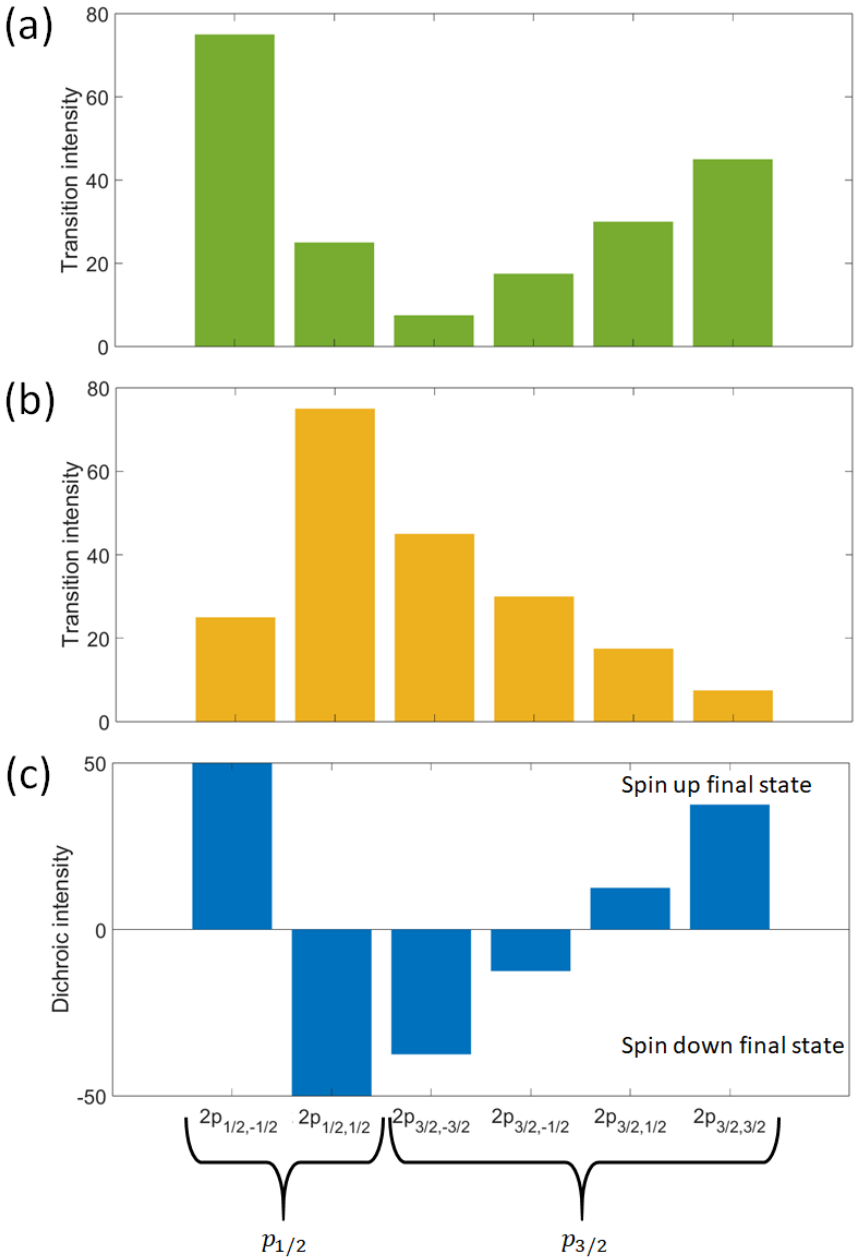

Figure 7.15: Calculated transition probabilities from $2p$ core level with (a) C_+ light and (b) C_- light. (c) is the dichroic intensity, $C_+ - C_-$.

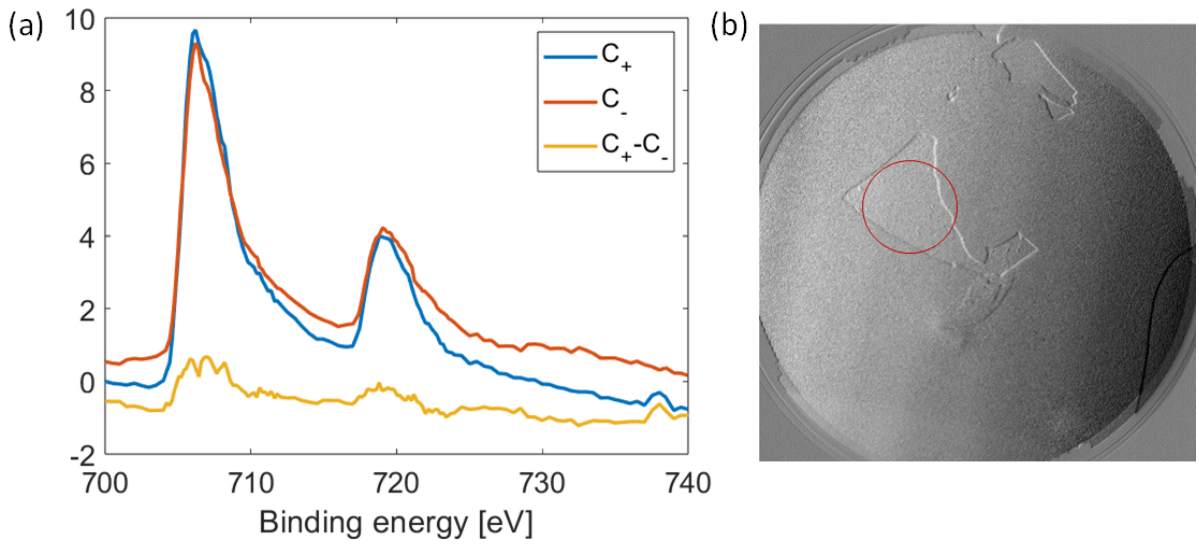

Figure 7.16: (a) XMCD spectra on FGT flake at room temperature. (b) XMCD PEEM image of FGT flake taken at $h\nu$ = 706 eV, with field of view 37.5 μm. No magnetic domains were observed at room temperature. The red circle indicates approximately the portion of the flake used for the measurement in (a).

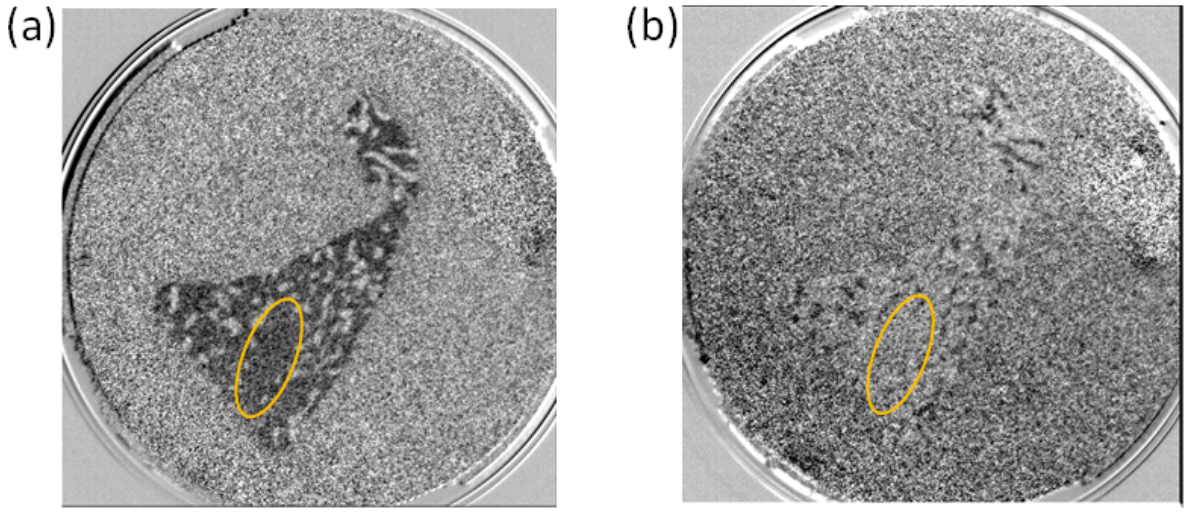

Figure 7.17: XMCD PEEM image of FGT flake at 70 K at (a) $h\nu$ = 706 eV and (b) $h\nu$ = 718 eV. The Figure show the out-of-plane domains in FGT. In thicker regions, with more 10 monolayers, the image show stripe domains. The yellow circle indicates the region of single domain regions, where the thickness is 3-4 monolayers. The field of the view is 20 micrometers.

8 Summary and outlook

Next-generation quantum devices exploit spin and orbital degrees of freedom in addition to charge degrees of freedom [16]. For instance, spin transport in graphene [197], which has small spin-orbit coupling, and the ability to manipulate spin and valley degrees of freedom using polarized light in 2D transition metal dichalcogenides (TMDCs) [177], which exhibit large spin-orbit coupling, represent two technologically relevant classes of materials. The large spin-orbit coupling in 2D materials makes them ideal candidates for these advanced devices [198]. In TMDCs, two circularly polarized lights can be used to selectively populate the K and K' points of the conduction band, creating an electron imbalance between these K/K' points. The Hall voltage generated in this scenario depends on the polarity of the light, and the sign of the Hall voltage can be reversed by reversing the light polarization. This valley-dependent Hall current can be harnessed in future devices, known as *valleytronic* devices [199, 200]. devices. The effective magnetic field experienced by the excited electrons differs at the K/K' points and is influenced by the Berry curvature of the band structure. Similarly, for spintronic and orbitronic devices, the spin and orbital properties of the initial state band structure are crucial.

The development of spintronic, orbitronic, and valleytronic devices is based on quantum transport phenomena such as the quantum anomalous Hall effect, spin Hall effect, orbital Hall effect, and valley Hall effect, all of which are closely related to the Berry curvature of the material. One of the major challenges in developing next-generation devices is accurately predicting the quantum mechanical properties of materials, including Berry curvature. Circular dichroic angle-resolved photoemission spectroscopy (CD-ARPES) [88], along with spin-polarized ARPES [201], has been the most commonly used technique to study the Berry curvature of band structures due to its connection with the orbital and spin angular momentum of the bands, respectively. However, the effects of external factors, including photoemission final state effects, have not been adequately considered in CD-ARPES data, posing a challenge in accurately predicting the Berry curvature of materials.

In this thesis, various contributions to the CD-ARPES measurements have been discussed. The origin of the non-zero CD signal from the p_z orbitals in graphene is attributed to the experimental geometry of the measurements and multiple scattering in the photoemission final state. The CD-ARPES data from bulk WSe_2 demonstrate how the initial state orbital angular momentum of the bands influences the measurements. Additionally, the CD-ARPES data from the K/K' points of WSe_2 at normal incidence suggest that spin-orbit scattering can introduce spin sensitivity into CD-ARPES measurements, which are much faster than traditional spin-polarized measurements.

In conclusion, the data from both graphene and WSe_2 indicate that determining orbital angular momentum is challenging and requires detailed theoretical calculations to separate the initial state contributions from other factors affecting the measurements. A careful examination of the data across different photon energy regimes and experimental geometries, supported by theoretical calculations can enable, at least to some extent, determination of the initial state characteristics of the bands.

In the future, spin-orbit scattering and exchange scattering could be harnessed to generate beams with both orbital angular momentum polarization and spin polarization, potentially revolutionizing next-generation quantum devices. These scattering mechanisms may prove useful for creating electron beams with single spin and orbital polarization by transmitting electrons through atomic layers of materials with strong spin-orbit coupling. However, further research is required to fully understand and exploit these phenomena. Additionally, spin-orbit and exchange scattering could enhance the development and efficiency of experimental setups for detecting electron spin.

Another technologically relevant class of materials is the 2D magnetic materials. The manipulation of spin density in these materials can be used in spin-dependent transport devices such as spin filters, spin valves [17], and tunnel junctions [16]. However, a fundamental understanding of many aspects of the magnetic interactions are still lacking, and understanding the temperature evolution of the band structure is crucial for further advancements in this field. The temperature- and polarization-dependent band structure of the magnetic 2D material $Cr_2Ge_2Te_6$ has been demonstrated, providing insights into the magnetic interactions present in the material. Additionally, CD-ARPES measurements from the valence band and core levels were performed for the first time. These CD maps from the valence band region reveal the influence of experimental geometry. In the case of Fe_3GeTe_2, both the band structure and domain structure were explored. Notably, the encapsulated few-layer FGT exhibits a single domain region of approximately 3×4 μm in size.

The CD-ARPES maps from core levels can be employed to study exchange scattering in magnetic materials like $Cr_2Ge_2Te_6$ and Fe_3GeTe_2. Thickness-dependent and substrate-dependent band structure studies will also help clarify their influence on the magnetic properties of these materials. A strong thickness dependence of the domain pattern has already been observed in the PEEM measurements on Fe_3GeTe_2. Furthermore, using a magnetic substrate could enhance the domain structure size, as observed in recent studies [175]. This would also facilitate the study of spin polarization with standard ARPES setups.

Acknowledgment

I would like to express my deepest gratitude to my supervisor, Dr. Lukasz Plucinski, for his unwavering support throughout my entire PhD journey. As someone new to the field of photoemission, I greatly benefited from our insightful discussions and your continuous guidance. I also extend my heartfelt thanks to our institute director, Prof. Claus Michael Schneider, for his consistent support. I would also like to thank Prof. Markus Morgenstern for reviewing my thesis.

Special thanks go to my colleagues, Mohammed Qahosh and Xiao Hou, for making my PhD journey both easier and more enjoyable. It was a pleasure working with such wonderful individuals, and I will always cherish the synchrotron beam times and sleepless nights we spent together. I also extend my gratitude to Jeff Strasdas and Benjamin Pestka from RWTH Aachen University for their support and assistance during the beamtimes. I would like to thank the technical staff at PGI-6 for their invaluable support throughout my research. A warm thank you to my friends at FZJ, especially Daisy, Amal, Reza, Faranak, Khattab, and Christian, for making my time at FZJ truly memorable.

The Glovebox lab at PGI-3 was always a fun and collaborative environment, filled with amazing people. Thank you to Keda Jin, Tobias Wichmann, Dr. Jose Martinez Castro, and Dr. Felix Lüpke for their assistance in preparing my 2D samples. A special mention to Tobias for dedicating his valuable time to reviewing the sample preparation chapter of this thesis.

I would also like to thank the beamline scientists at the PHELIX beamline at SOLARIS, NanoESCA beamline at Elettra, I05 beamline at Diamond Light Source, DEMETER beamline at SOLARIS, and MAESTRO beamline at ALS, where all the measurements for this thesis were performed. A special mention to Dr. Magdalena Szczepanik-Ciba (PHELIX beamline, SOLARIS), Tomasz Sobol (PHELIX beamline, SOLARIS), Dr.Vitaly Feyer (NanoESCA beamline, Elettra), Dr.Daniel Baranowski (NanoESCA beamline, Elettra), Simone Mearini (NanoESCA beamline, Elettra), and Yan Grisan (NanoESCA beamline, Elettra) for their constant support during the beamtime.

This PhD journey would not have been possible without the support of my friends in Jülich. A heartfelt thank you to the "Team Jülich" for standing by me through the toughest times and supporting me at every step of my PhD. Ashish, Vidhya Chechi, Shilpa, Varun, Akshay, Nikhil, and Nithya, I am deeply grateful for your friendship and encouragement. I would also like to thank Vishakettan, Sindhu Chechi, little Shanvick, Godwin, Sourav, Anjana, Amal, Supriya, Kavya, and Mahesh for their companionship and support.

Finally, thank you to Ameer, my closest friend, for motivating and supporting me throughout this journey. To my family, who have always been my backbone, I cannot imagine

functioning without you. No amount of thanks would suffice to express my gratitude for your patience and understanding in dealing with me.

Bibliography

[1] H. Boban et al., "Scattering makes a difference in circular dichroic angle-resolved photoemission," *Phys. Rev. B*, vol. 111, p. 115 127, 11 Mar. 2025. DOI: 10.1103/PhysRevB.111.115127. [Online]. Available: https://link.aps.org/doi/10.1103/PhysRevB.111.115127.

[2] K. S. Novoselov et al., "Electric field effect in atomically thin carbon films," *Science*, vol. 306, no. 5696, pp. 666–669, 2004. DOI: 10.1126/science.1102896. eprint: https://www.science.org/doi/pdf/10.1126/science.1102896. [Online]. Available: https://www.science.org/doi/abs/10.1126/science.1102896.

[3] A. K. Geim and K. S. Novoselov, "The rise of graphene," *Nature Materials*, vol. 6, no. 3, pp. 183–191, 2007. DOI: 10.1038/nmat1849. [Online]. Available: https://doi.org/10.1038/nmat1849.

[4] X. Chen et al., "Electrically tunable physical properties of two-dimensional materials," *Nano Today*, vol. 27, pp. 99–119, 2019, ISSN: 1748-0132. DOI: https://doi.org/10.1016/j.nantod.2019.05.005. [Online]. Available: https://www.sciencedirect.com/science/article/pii/S1748013219300672.

[5] Q. Ma, G. Ren, K. Xu, and J. Z. Ou, "Tunable optical properties of 2d materials and their applications," *Advanced Optical Materials*, vol. 9, no. 2, p. 2 001 313, 2021. DOI: https://doi.org/10.1002/adom.202001313. [Online]. Available: https://onlinelibrary.wiley.com/doi/abs/10.1002/adom.202001313.

[6] Y. Yu, Y. Yu, L. Huang, H. Peng, L. Xiong, and L. Cao, "Giant gating tunability of optical refractive index in transition metal dichalcogenide monolayers," *Nano Letters*, vol. 17, no. 6, pp. 3613–3618, 2017, PMID: 28505462. DOI: 10.1021/acs.nanolett.7b00768. eprint: https://doi.org/10.1021/acs.nanolett.7b00768. [Online]. Available: https://doi.org/10.1021/acs.nanolett.7b00768.

[7] A. Pal et al., "Quantum-engineered devices based on 2d materials for next-generation information processing and storage," *Advanced Materials*, vol. 35, no. 27, p. 2 109 894, 2023. DOI: https://doi.org/10.1002/adma.202109894. [Online]. Available: https://onlinelibrary.wiley.com/doi/abs/10.1002/adma.202109894.

[8] P. Kumbhakar et al., "Prospective applications of two-dimensional materials beyond laboratory frontiers: A review," *iScience*, vol. 26, no. 5, p. 106 671, 2023, ISSN: 2589-0042. DOI: https://doi.org/10.1016/j.isci.2023.106671. [Online]. Available: https://www.sciencedirect.com/science/article/pii/S2589004223007484.

[9] S. Manzeli, D. Ovchinnikov, D. Pasquier, O. V. Yazyev, and A. Kis, "2D transition metal dichalcogenides," *Nature Reviews Materials*, vol. 2, no. 8, 2017. DOI: 10.1038/natrevmats.2017.33. [Online]. Available: https://doi.org/10.1038/natrevmats.2017.33.

[10] C. Gong et al., "Discovery of intrinsic ferromagnetism in two-dimensional van der waals crystals," *Nature*, vol. 546, pp. 265–269, 7657 Jun. 2017. DOI: 10.1038/nature22060. [Online]. Available: https://doi.org/10.1038/nature22060.

[11] B. Huang et al., "Layer-dependent ferromagnetism in a van der waals crystal down to the monolayer limit," *Nature*, vol. 546, no. 7657, pp. 270–273, 2017.

[12] C.-Z. Chang, C.-X. Liu, and A. H. MacDonald, "Colloquium: Quantum anomalous hall effect," *Reviews of Modern Physics*, vol. 95, no. 1, p. 011 002, 2023.

[13] M. I. Dyakonov and V. I. Perel, "Possibility of orienting electron spins with current," *JETP Letters*, vol. 13, p. 657, 11 1971. [Online]. Available: http://jetpletters.ru/ps/0/article_24366.shtml.

[14] M. Dyakonov and V. Perel, "Current-induced spin orientation of electrons in semiconductors," *Physics Letters A*, vol. 35, no. 6, pp. 459–460, 1971, ISSN: 0375-9601. DOI: https://doi.org/10.1016/0375-9601(71)90196-4. [Online]. Available: https://www.sciencedirect.com/science/article/pii/0375960171901964.

[15] A. Pezo, D. Garcia Ovalle, and A. Manchon, "Orbital hall physics in two-dimensional dirac materials," *Phys. Rev. B*, vol. 108, p. 075 427, 7 Aug. 2023. DOI: 10.1103/PhysRevB.108.075427. [Online]. Available: https://link.aps.org/doi/10.1103/PhysRevB.108.075427.

[16] S. Bandyopadhyay and M. Cahay, "Electron spin for classical information processing: A brief survey of spin-based logic devices, gates and circuits," *Nanotechnology*, vol. 20, no. 41, p. 412 001, 2009.

[17] Y. K. Luo et al., "Opto-valleytronic spin injection in monolayer MoS_2/few-layer graphene hybrid spin valves," *Nano letters*, vol. 17, no. 6, pp. 3877–3883, 2017.

[18] M. Popinciuc et al., "Electronic spin transport in graphene field-effect transistors," *Physical Review B—Condensed Matter and Materials Physics*, vol. 80, no. 21, p. 214 427, 2009.

[19] M. Gmitra and J. Fabian, "Proximity effects in bilayer graphene on monolayer WSe_2: Field-effect spin valley locking, spin-orbit valve, and spin transistor," *Physical review letters*, vol. 119, no. 14, p. 146 401, 2017.

[20] Y. Liu and Q. Shao, "Two-dimensional materials for energy-efficient spin–orbit torque devices," *ACS Nano*, vol. 14, no. 8, pp. 9389–9407, 2020, PMID: 32692151. DOI: 10.1021/acsnano.0c04403. eprint: https://doi.org/10.1021/acsnano.0c04403. [Online]. Available: https://doi.org/10.1021/acsnano.0c04403.

[21] D. Das, "Orbitronics in action," *Nature Physics*, vol. 19, no. 8, p. 1085, 2023. DOI: 10.1038/s41567-023-02183-4. [Online]. Available: https://doi.org/10.1038/s41567-023-02183-4.

[22] D. Go, D. Jo, H.-W. Lee, M. Kläui, and Y. Mokrousov, "Orbitronics: Orbital currents in solids," *Europeanphysics Letters*, vol. 135, 3 Sep. 2021. DOI: 10.1209/0295-5075/ac2653. [Online]. Available: https://iopscience.iop.org/article/10.1209/0295-5075/ac2653/meta.

[23] D. Go, D. Jo, C. Kim, and H.-W. Lee, "Intrinsic spin and orbital hall effects from orbital texture," *Phys. Rev. Lett.*, vol. 121, p. 086 602, 8 Aug. 2018. DOI: 10.1103/PhysRevLett.121.086602. [Online]. Available: https://link.aps.org/doi/10.1103/PhysRevLett.121.086602.

[24] J. Sohn, J. M. Lee, and H.-W. Lee, "Dyakonov-perel-like orbital and spin relaxations in centrosymmetric systems," *Phys. Rev. Lett.*, vol. 132, p. 246 301, 24 Jun. 2024.

DOI: 10.1103/PhysRevLett.132.246301. [Online]. Available: https://link.aps.org/doi/10.1103/PhysRevLett.132.246301.

[25] N. Nagaosa, J. Sinova, S. Onoda, A. H. MacDonald, and N. P. Ong, "Anomalous hall effect," *Rev. Mod. Phys.*, vol. 82, pp. 1539–1592, 2 May 2010. DOI: 10.1103/RevModPhys.82.1539. [Online]. Available: https://link.aps.org/doi/10.1103/RevModPhys.82.1539.

[26] W. L. Lee, S. Watauchi, V. L. Miller, R. J. Cava, and N. P. Ong, "Dissipationless anomalous hall current in the ferromagnetic spinel $CuCr_2Se_{4-x}Br_x$," *Science*, vol. 303, no. 5664, pp. 1647–1649, 2004. DOI: 10.1126/science.1094383. [Online]. Available: https://www.science.org/doi/abs/10.1126/science.1094383.

[27] P. Drude, "Zur elektronentheorie der metalle," *Annalen der Physik*, vol. 306, no. 3, pp. 566–613, 1900. DOI: https://doi.org/10.1002/andp.19003060312. eprint: https://onlinelibrary.wiley.com/doi/pdf/10.1002/andp.19003060312. [Online]. Available: https://onlinelibrary.wiley.com/doi/abs/10.1002/andp.19003060312.

[28] N. Ashcroft and N. Mermin, *Solid State Physics* (HRW international editions). Holt, Rinehart and Winston, 1976, ISBN: 9780030839931. [Online]. Available: https://books.google.de/books?id=oXIfAQAAMAAJ.

[29] F. Bloch, "Über die quantenmechanik der elektronen in kristallgittern," *Zeitschrift für Physik*, vol. 52, pp. 555–600, 1929.

[30] C. Kittel, *Introduction to Solid State Physics*. Wiley, 1986, ISBN: 9780471874744.

[31] W. Kohn and L. J. Sham, "Self-consistent equations including exchange and correlation effects," *Phys. Rev.*, vol. 140, A1133–A1138, 4A Nov. 1965. DOI: 10.1103/PhysRev.140.A1133. [Online]. Available: https://link.aps.org/doi/10.1103/PhysRev.140.A1133.

[32] P. Hohenberg and W. Kohn, "Inhomogeneous electron gas," *Phys. Rev.*, vol. 136, B864–B871, 3B Nov. 1964. DOI: 10.1103/PhysRev.136.B864. [Online]. Available: https://link.aps.org/doi/10.1103/PhysRev.136.B864.

[33] K. Schwarz and P. Blaha, "Solid state calculations using wien2k," *Computational Materials Science*, vol. 28, no. 2, pp. 259–273, 2003, Proceedings of the Symposium on Software Development for Process and Materials Design, ISSN: 0927-0256. DOI: https://doi.org/10.1016/S0927-0256(03)00112-5. [Online]. Available: https://www.sciencedirect.com/science/article/pii/S0927025603001125.

[34] A. J. Freeman, R. Asahi, A. Continenza, and R. Wu, "Electronic structure theory for ground and excited state properties of materials," in *Solid-State Photoemission and Related Methods*. John Wiley and Sons, Ltd, 2003, ch. 1, pp. 1–49, ISBN: 9783527602506. DOI: https://doi.org/10.1002/9783527602506.ch1. eprint: https://onlinelibrary.wiley.com/doi/pdf/10.1002/9783527602506.ch1. [Online]. Available: https://onlinelibrary.wiley.com/doi/abs/10.1002/9783527602506.ch1.

[35] I. Aguilera, I. A. Nechaev, C. Friedrich, S. Blugel, and E. V. Chulkov, "Many-body effects in the electronic structure of topological insulators," in *Topological Insulators*. John Wiley and Sons, Ltd, 2015, ch. 7, pp. 161–189, ISBN: 9783527681594. DOI: https://doi.org/10.1002/9783527681594.ch7. [Online]. Available: https://onlinelibrary.wiley.com/doi/abs/10.1002/9783527681594.ch7.

[36] H. Hertz, "Ueber einen einfluss des ultravioletten lichtes auf die electrische entladung," *Annalen der Physik*, vol. 267, no. 8, pp. 983–1000, 1887. DOI: https://doi.org/10.1002/andp.18872670827. eprint: https://onlinelibrary.wiley.com/doi/pdf/10.1002/andp.18872670827. [Online]. Available: https://onlinelibrary.wiley.com/doi/abs/10.1002/andp.18872670827.

[37] A. Einstein, "Ueber einen die erzeugung und verwandlung des lichtes betreffenden heuristischen gesichtspunkt," *Annalen der Physik*, vol. 322, no. 6, pp. 132–148, 1905. DOI: https://doi.org/10.1002/andp.19053220607. eprint: https://onlinelibrary.wiley.com/doi/pdf/10.1002/andp.19053220607. [Online]. Available: https://onlinelibrary.wiley.com/doi/abs/10.1002/andp.19053220607.

[38] S. Hufner, *Photoelectron Spectroscopy: Principles and Applications*. springer, 2003.

[39] C. N. Berglund and W. E. Spicer, "Photoemission studies of copper and silver: Theory," *Phys. Rev.*, vol. 136, A1030–A1044, 4A Nov. 1964. DOI: 10.1103/PhysRev.136.A1030. [Online]. Available: https://link.aps.org/doi/10.1103/PhysRev.136.A1030.

[40] W. E. Spicer and A. Herrera-Gomez, "Modern theory and applications of photocathodes," in *Photodetectors and Power Meters*, K. J. Kaufmann, Ed., International Society for Optics and Photonics, vol. 2022, SPIE, 1993, pp. 18–35. DOI: 10.1117/12.158575. [Online]. Available: https://doi.org/10.1117/12.158575.

[41] S. Moser, "An experimentalist's guide to the matrix element in angle resolved photoemission," *Journal of Electron Spectroscopy and Related Phenomena*, vol. 214, pp. 29–52, 2017, ISSN: 0368-2048. DOI: https://doi.org/10.1016/j.elspec.2016.11.007. [Online]. Available: https://www.sciencedirect.com/science/article/pii/S0368204816301724.

[42] M. P. Seah and W. A. Dench, "Quantitative electron spectroscopy of surfaces: A standard data base for electron inelastic mean free paths in solids," *Surface and Interface Analysis*, vol. 1, no. 1, pp. 2–11, 1979. DOI: https://doi.org/10.1002/sia.740010103. eprint: https://analyticalsciencejournals.onlinelibrary.wiley.com/doi/pdf/10.1002/sia.740010103. [Online]. Available: https://analyticalsciencejournals.onlinelibrary.wiley.com/doi/abs/10.1002/sia.740010103.

[43] J. Braun, J. Minar, and H. Ebert, "Correlation, temperature and disorder: Recent developments in the one-step description of angle-resolved photoemission," *Physics Reports*, vol. 740, pp. 1–34, 2018, Correlation, temperature and disorder: Recent developments in the one-step description of angle-resolved photoemission, ISSN: 0370-1573. DOI: https://doi.org/10.1016/j.physrep.2018.02.007. [Online]. Available: https://www.sciencedirect.com/science/article/pii/S0370157318300358.

[44] Y. Li et al., "Visualizing the effect of oxidation on magnetic domain behavior of nanoscale Fe_3GeTe_2 for applications in spintronics," *ACS Applied Nano Materials*, vol. 6, no. 6, pp. 4390–4397, 2023. DOI: 10.1021/acsanm.2c05479. eprint: https://doi.org/10.1021/acsanm.2c05479. [Online]. Available: https://doi.org/10.1021/acsanm.2c05479.

[45] Y. Liu et al., "The environmental stability characterization of exfoliated few-layer $CrXTe_3$ (x = Si, Ge) nanosheets," *Applied Surface Science*, vol. 511, p. 145 452, 2020, ISSN: 0169-4332. DOI: https://doi.org/10.1016/j.apsusc.2020.145452.

[Online]. Available: https://www.sciencedirect.com/science/article/pii/S0169433220302087.

[46] M. Szczepanik-Ciba, T. Sobol, and J. Szade, "Phelix – a new soft x-ray spectroscopy beamline at solaris synchrotron," *Nuclear Instruments and Methods in Physics Research Section B: Beam Interactions with Materials and Atoms*, vol. 492, pp. 49–55, 2021, ISSN: 0168-583X. DOI: https://doi.org/10.1016/j.nimb.2021.01.021. [Online]. Available: https://www.sciencedirect.com/science/article/pii/S0168583X21000598.

[47] G. Brown, K. Halbach, J. Harris, and H. Winick, "Wiggler and undulator magnets — a review," *Nuclear Instruments and Methods in Physics Research*, vol. 208, no. 1, pp. 65–77, 1983, ISSN: 0167-5087. DOI: https://doi.org/10.1016/0167-5087(83)91105-5. [Online]. Available: https://www.sciencedirect.com/science/article/pii/0167508783911055.

[48] J. Bahrdt et al., "In-vacuum apple ii undulator," in *9th International Particle Accelerator Conference*, Jun. 2018. DOI: 10.18429/JACoW-IPAC2018-THPMF031.

[49] R. Hudec, "Kirkpatrick-baez (kb) and lobster eye (le) optics for astronomical and laboratory applications," *X-Ray Optics and Instrumentation*, vol. 2010, no. 1, p. 139 148, 2010. DOI: https://doi.org/10.1155/2010/139148. eprint: https://onlinelibrary.wiley.com/doi/pdf/10.1155/2010/139148. [Online]. Available: https://onlinelibrary.wiley.com/doi/abs/10.1155/2010/139148.

[50] P. Engstrom et al., "A submicron synchrotron x-ray beam generated by capillary optics," *Nuclear Instruments and Methods in Physics Research Section A: Accelerators, Spectrometers, Detectors and Associated Equipment*, vol. 302, no. 3, pp. 547–552, 1991, ISSN: 0168-9002. DOI: https://doi.org/10.1016/0168-9002(91)90373-X. [Online]. Available: https://www.sciencedirect.com/science/article/pii/016890029190373X.

[51] J. Avila, A. Boury, B. Caja-Munoz, C. Chen, S. Lorcy, and M. C. Asensio, "Optimal focusing system of the fresnel zone plates at the synchrotron soleil nanoarpes beamline," *Journal of Physics: Conference Series*, vol. 849, no. 1, p. 012 039, Jun. 2017. DOI: 10.1088/1742-6596/849/1/012039. [Online]. Available: https://dx.doi.org/10.1088/1742-6596/849/1/012039.

[52] A. Bjeoumikhov and S. Bjeoumikhova, "Capillary optics for x-rays," in *Modern Developments in X-Ray and Neutron Optics*. Springer Berlin Heidelberg, 2008, pp. 287–306, ISBN: 978-3-540-74561-7. DOI: 10.1007/978-3-540-74561-7_18. [Online]. Available: https://doi.org/10.1007/978-3-540-74561-7_18.

[53] F. Pfeiffer, C. David, J. F. van der Veen, and C. Bergemann, "Nanometer focusing properties of fresnel zone plates described by dynamical diffraction theory," *Phys. Rev. B*, vol. 73, p. 245 331, 24 Jun. 2006. DOI: 10.1103/PhysRevB.73.245331. [Online]. Available: https://link.aps.org/doi/10.1103/PhysRevB.73.245331.

[54] G. Schonhense and U. Heinzmann, "A capillary discharge tube for the production of intense vuv resonance radiation," *Journal of Physics E: Scientific Instruments*, vol. 16, no. 1, p. 74, Jan. 1983. DOI: 10.1088/0022-3735/16/1/015. [Online]. Available: https://dx.doi.org/10.1088/0022-3735/16/1/015.

[55] S. Suga et al., "High resolution, low hν photoelectron spectroscopy with the use of a microwave excited rare gas lamp and ionic crystal filters," *Review of*

Scientific Instruments, vol. 81, no. 10, p. 105 111, Oct. 2010, ISSN: 0034-6748. DOI: 10.1063/1.3488367.

[56] T. Iwata et al., "Laser-based angle-resolved photoemission spectroscopy with micrometer spatial resolution and detection of three-dimensional spin vector," *Scientific Reports*, vol. 14, no. 1, p. 127, Jan. 2024, ISSN: 2045-2322. DOI: 10.1038/s41598-023-47719-z. [Online]. Available: https://doi.org/10.1038/s41598-023-47719-z.

[57] R. Z. Xu et al., "Development of a laser-based angle-resolved-photoemission spectrometer with sub-micrometer spatial resolution and high-efficiency spin detection," *Review of Scientific Instruments*, vol. 94, no. 2, p. 023 903, Feb. 2023. DOI: 10.1063/5.0106351. eprint: https://pubs.aip.org/aip/rsi/article-pdf/doi/10.1063/5.0106351/16684200/023903_1_online.pdf. [Online]. Available: https://doi.org/10.1063/5.0106351.

[58] I. M. Vishik et al., "Doping-dependent nodal fermi velocity of the high-temperature superconductor $Bi_2Sr_2CaCu_2\mathbf{O}_{8+\delta}$ revealed using high-resolution angle-resolved photoemission spectroscopy," *Phys. Rev. Lett.*, vol. 104, p. 207 002, 20 May 2010. DOI: 10.1103/PhysRevLett.104.207002. [Online]. Available: https://link.aps.org/doi/10.1103/PhysRevLett.104.207002.

[59] Y. He et al., "Invited article: High resolution angle resolved photoemission with tabletop 11 ev laser," *Review of Scientific Instruments*, vol. 87, no. 1, p. 011 301, Jan. 2016. DOI: 10.1063/1.4939759. eprint: https://pubs.aip.org/aip/rsi/article-pdf/doi/10.1063/1.4939759/13907608/011301_1_online.pdf. [Online]. Available: https://doi.org/10.1063/1.4939759.

[60] F. Schmitt et al., "Transient electronic structure and melting of a charge density wave in TbTe," *Science*, vol. 321, no. 5896, pp. 1649–1652, 2008. DOI: 10.1126/science.1160778. eprint: https://www.science.org/doi/pdf/10.1126/science.1160778. [Online]. Available: https://www.science.org/doi/abs/10.1126/science.1160778.

[61] M. Na, A. K. Mills, and D. J. Jones, "Advancing time- and angle-resolved photoemission spectroscopy: The role of ultrafast laser development," *Physics Reports*, vol. 1036, pp. 1–47, 2023, Advancing time- and angle-resolved photoemission spectroscopy: The role of ultrafast laser development, ISSN: 0370-1573. DOI: https://doi.org/10.1016/j.physrep.2023.09.005. [Online]. Available: https://www.sciencedirect.com/science/article/pii/S0370157323003010.

[62] S. Peli, D. Puntel, D. Kopic, B. Sockol, F. Parmigiani, and F. Cilento, "Time-resolved vuv arpes at 10.8ev photon energy and mhz repetition rate," *Journal of Electron Spectroscopy and Related Phenomena*, vol. 243, p. 146 978, 2020, ISSN: 0368-2048. DOI: https://doi.org/10.1016/j.elspec.2020.146978. [Online]. Available: https://www.sciencedirect.com/science/article/pii/S0368204820300463.

[63] R. Imhof, A. Adams, and G. King, "Energy and time resolution of the 180 degrees hemispherical electrostatic analyser," *Journal of Physics E: Scientific Instruments*, vol. 9, p. 138, Feb. 2001. DOI: 10.1088/0022-3735/9/2/024.

[64] M. Escher et al., "Nanoesca: A novel energy filter for imaging x-ray photoemission spectrosocpy," *Journal of Physics-condensed Matter - J PHYS-CONDENS MATTER*, vol. 17, Apr. 2005. DOI: 10.1088/0953-8984/17/16/004.

[65] M. Patt, *Bulk and surface sensitive energy-filtered photoemission microscopy using synchrotron radiation for the study of resistive switching memories*. Apr. 2016, ISBN: 978-3-95806-130-9.

[66] *Peem iii with analyzer*. [Online]. Available: https://elmitec.de/Peem.php?Bereich=PEEMAnalyzer.

[67] *Demeter: End station and experiment*. [Online]. Available: https://synchrotron.uj.edu.pl/en_GB/linie-badawcze/demeter/eksperyment.

[68] S. K. Pandey, R. Das, and P. Mahadevan, "Layer-dependent electronic structure changes in transition metal dichalcogenides: The microscopic origin," *ACS Omega*, vol. 5, no. 25, pp. 15 169–15 176, 2020, PMID: 32637790. DOI: 10.1021/acsomega.0c01138. eprint: https://doi.org/10.1021/acsomega.0c01138. [Online]. Available: https://doi.org/10.1021/acsomega.0c01138.

[69] K. F. Mak, C. Lee, J. Hone, J. Shan, and T. F. Heinz, "Atomically thin MoS_2: A new direct-gap semiconductor," *Phys. Rev. Lett.*, vol. 105, p. 136 805, 13 Sep. 2010. DOI: 10.1103/PhysRevLett.105.136805. [Online]. Available: https://link.aps.org/doi/10.1103/PhysRevLett.105.136805.

[70] S. Tongay et al., "Thermally driven crossover from indirect toward direct bandgap in 2d semiconductors: $MoSe_2$ versus MoS_2," *Nano Letters*, vol. 12, no. 11, pp. 5576–5580, 2012, PMID: 23098085. DOI: 10.1021/nl302584w. eprint: https://doi.org/10.1021/nl302584w. [Online]. Available: https://doi.org/10.1021/nl302584w.

[71] T. Boker et al., "Band structure of MoS_2, $MoSe_2$ and α- $MoTe_2$: Angle-resolved photoelectron spectroscopy and ab initio calculations," *Phys. Rev. B*, vol. 64, p. 235 305, 23 Nov. 2001. DOI: 10.1103/PhysRevB.64.235305. [Online]. Available: https://link.aps.org/doi/10.1103/PhysRevB.64.235305.

[72] Q. Li et al., "Patterning-induced ferromagnetism of Fe_3GeTe_3 van der waals materials beyond room temperature," *Nano Letters*, vol. 18, no. 9, pp. 5974–5980, 2018, PMID: 30114354. DOI: 10.1021/acs.nanolett.8b02806. [Online]. Available: https://doi.org/10.1021/acs.nanolett.8b0280.

[73] K. S. Novoselov et al., "Two-dimensional atomic crystals," *Proceedings of the National Academy of Sciences*, vol. 102, no. 30, pp. 10 451–10 453, 2005. DOI: 10.1073/pnas.0502848102. eprint: https://www.pnas.org/doi/pdf/10.1073/pnas.0502848102. [Online]. Available: https://www.pnas.org/doi/abs/10.1073/pnas.0502848102.

[74] Z. Wang et al., "Very large tunneling magnetoresistance in layered magnetic semiconductor CrI_3," *Nature Communications*, vol. 9, no. 1, p. 2516, Jun. 2018, ISSN: 2041-1723. DOI: 10.1038/s41467-018-04953-8. [Online]. Available: https://doi.org/10.1038/s41467-018-04953-8.

[75] B. Bera, "Silicon wafer cleaning: A fundamental and critical step in semiconductor fabrication process," *International Journal of Applied Nanotechnology (IJAN)*, vol. 5, 2019.

[76] M. Velicky et al., "Mechanism of gold-assisted exfoliation of centimeter-sized transition-metal dichalcogenide monolayers," *ACS Nano*, vol. 12, no. 10, pp. 10 463–10 472, 2018, PMID: 30265515. DOI: 10.1021/acsnano.8b06101. eprint: https://doi.org/10.1021/acsnano.8b06101. [Online]. Available: https://doi.org/10.1021/acsnano.8b06101.

[77] P. J. Zomer, M. H. D. Guimaraes, J. C. Brant, N. Tombros, and B. J. van Wees, "Fast pick up technique for high quality heterostructures of bilayer graphene and hexagonal boron nitride," *Applied Physics Letters*, vol. 105, no. 1, p. 013 101, Jul. 2014, ISSN: 0003-6951. DOI: 10.1063/1.4886096. eprint: https://pubs.aip.org/aip/apl/article-pdf/doi/10.1063/1.4886096/13901964/013101_1_online.pdf. [Online]. Available: https://doi.org/10.1063/1.4886096.

[78] D.-G. Kim, S. Lee, and K. Kim, "Mechanical removal of surface residues on graphene for tem characterizations," *Applied Microscopy*, vol. 50, no. 1, p. 28, Nov. 2020, ISSN: 2287-4445. DOI: 10.1186/s42649-020-00048-1. [Online]. Available: https://doi.org/10.1186/s42649-020-00048-1.

[79] S. R. Park et al., "Chiral orbital-angular momentum in the surface states of Bi_2Se_3," *Phys. Rev. Lett.*, vol. 108, p. 046 805, 4 Jan. 2012. DOI: 10.1103/PhysRevLett.108.046805.

[80] L. Nicolai et al., "Bi ultra-thin crystalline films on inas(1 1 1)a and b substrates: A combined core-level and valence-band angle-resolved and dichroic photoemission study," *New Journal of Physics*, vol. 21, no. 12, p. 123 012, Dec. 2019. DOI: 10.1088/1367-2630/ab5c14. [Online]. Available: https://dx.doi.org/10.1088/1367-2630/ab5c14.

[81] Y. H. Wang et al., "Observation of a warped helical spin texture in Bi_2Se_3 from circular dichroism angle-resolved photoemission spectroscopy," *Phys. Rev. Lett.*, vol. 107, p. 207 602, 20 Nov. 2011. DOI: 10.1103/PhysRevLett.107.207602. [Online]. Available: https://link.aps.org/doi/10.1103/PhysRevLett.107.207602.

[82] H. Mirhosseini and J. Henk, "Spin texture and circular dichroism in photoelectron spectroscopy from the topological insulator Bi_2Se_3: First-principles photoemission calculations," *Phys. Rev. Lett.*, vol. 109, p. 036 803, 3 Jul. 2012. DOI: 10.1103/PhysRevLett.109.036803. [Online]. Available: https://link.aps.org/doi/10.1103/PhysRevLett.109.036803.

[83] K. Takahashi, M. Imamura, I. Yamamoto, and J. Azuma, "Circular dichroism in angle-resolved photoemission mapping of surface state on bi(111)," *AIP Conference Proceedings*, vol. 2054, no. 1, p. 040 011, Jan. 2019, ISSN: 0094-243X. DOI: 10.1063/1.5084612. eprint: https://pubs.aip.org/aip/acp/article-pdf/doi/10.1063/1.5084612/14174699/040011_1_online.pdf. [Online]. Available: https://doi.org/10.1063/1.5084612.

[84] S. Beaulieu et al., "Revealing hidden orbital pseudospin texture with time-reversal dichroism in photoelectron angular distributions," *Phys. Rev. Lett.*, vol. 125, p. 216 404, 21 Nov. 2020. DOI: 10.1103/PhysRevLett.125.216404. [Online]. Available: https://link.aps.org/doi/10.1103/PhysRevLett.125.216404.

[85] M. Schuler et al., "How circular dichroism in time- and angle-resolved photoemission can be used to spectroscopically detect transient topological states in graphene," *Phys. Rev. X*, vol. 10, p. 041 013, 4 Oct. 2020. DOI: 10.1103/PhysRevX.10.041013. [Online]. Available: https://link.aps.org/doi/10.1103/PhysRevX.10.041013.

[86] S. Cho et al., "Studying local berry curvature in 2H-WSe_2 by circular dichroism photoemission utilizing crystal mirror plane," *Scientific Reports*, vol. 11, 1 Jan. 2021. DOI: 10.1038/s41598-020-79672-6. [Online]. Available: https://doi.org/10.1038/s41598-020-79672-6.

[87] J. Sanchez-Barriga et al., "Photoemission of Bi_2Se_3 with circularly polarized light: Probe of spin polarization or means for spin manipulation?" *Phys. Rev. X*, vol. 4, p. 011 046, 1 Mar. 2014. DOI: 10.1103/PhysRevX.4.011046. [Online]. Available: https://link.aps.org/doi/10.1103/PhysRevX.4.011046.

[88] M. Schuler, U. D. Giovannini, H. Hubener, A. Rubio, M. A. Sentef, and P. Werner, "Local berry curvature signatures in dichroic angle-resolved photoelectron spectroscopy from two-dimensional materials," *Science Advances*, vol. 6, no. 9, eaay2730, 2020. DOI: 10.1126/sciadv.aay2730. eprint: https://www.science.org/doi/pdf/10.1126/sciadv.aay2730. [Online]. Available: https://www.science.org/doi/abs/10.1126/sciadv.aay2730.

[89] S. Cho et al., "Experimental observation of hidden berry curvature in inversion-symmetric bulk 2H-WSe_2," *Phys. Rev. Lett.*, vol. 121, p. 186 401, 18 Oct. 2018. DOI: 10.1103/PhysRevLett.121.186401. [Online]. Available: https://link.aps.org/doi/10.1103/PhysRevLett.121.186401.

[90] F. Vidal et al., "Photon energy dependence of circular dichroism in angle-resolved photoemission spectroscopy of Bi_2Se_3 dirac states," *Phys. Rev. B*, vol. 88, p. 241 410, 24 Dec. 2013. DOI: 10.1103/PhysRevB.88.241410. [Online]. Available: https://link.aps.org/doi/10.1103/PhysRevB.88.241410.

[91] I. Gierz, M. Lindroos, H. Hochst, C. R. Ast, and K. Kern, "Graphene sublattice symmetry and isospin determined by circular dichroism in angle-resolved photoemission spectroscopy," *Nano Letters*, vol. 12, no. 8, pp. 3900–3904, 2012, PMID: 22784029. DOI: 10.1021/nl300512q. eprint: https://doi.org/10.1021/nl300512q. [Online]. Available: https://doi.org/10.1021/nl300512q.

[92] R. Sagehashi, G. Park, and P. Kruger, "Theory of circular dichroism in angle-resolved resonant photoemission from magnetic surfaces," *Phys. Rev. B*, vol. 107, p. 075 407, 7 Feb. 2023. DOI: 10.1103/PhysRevB.107.075407. [Online]. Available: https://link.aps.org/doi/10.1103/PhysRevB.107.075407.

[93] P. Kruger and F. Matsui, "Observation and theory of strong circular dichroism in angle-revolved photoemission from graphite," *Journal of Electron Spectroscopy and Related Phenomena*, vol. 258, p. 147 219, 2022, ISSN: 0368-2048. DOI: https://doi.org/10.1016/j.elspec.2022.147219. [Online]. Available: https://www.sciencedirect.com/science/article/pii/S0368204822000561.

[94] H. Rostami et al., "Layer and orbital interference effects in photoemission from transition metal dichalcogenides," *Phys. Rev. B*, vol. 100, p. 235 423, 23 Dec. 2019. DOI: 10.1103/PhysRevB.100.235423. [Online]. Available: https://link.aps.org/doi/10.1103/PhysRevB.100.235423.

[95] M. R. Scholz et al., "Reversal of the circular dichroism in angle-resolved photoemission from Bi_2Se_3," *Phys. Rev. Lett.*, vol. 110, p. 216 801, 21 May 2013. DOI: 10.1103/PhysRevLett.110.216801. [Online]. Available: https://link.aps.org/doi/10.1103/PhysRevLett.110.216801.

[96] A. H. Castro Neto, *Selected Topics in Graphene Physics*, D. C. Cabra, A. Honecker, and P. Pujol, Eds. Berlin, Heidelberg: Springer Berlin Heidelberg, 2012, pp. 117–144. [Online]. Available: https://doi.org/10.1007/978-3-642-10449-7_3.

[97] C. Wiemann et al., "A new nanospectroscopy tool with synchrotron radiation: Nanoesca at elettra," *e-Journal of Surface Science and Nanotechnology*, vol. 9, pp. 395–399, 2011. DOI: 10.1380/ejssnt.2011.395.

[98] I. Gierz, J. Henk, H. Hochst, C. R. Ast, and K. Kern, "Illuminating the dark corridor in graphene: Polarization dependence of angle-resolved photoemission spectroscopy on graphene," *Phys. Rev. B*, vol. 83, p. 121 408, 12 Mar. 2011. DOI: 10.1103/PhysRevB.83.121408. [Online]. Available: https://link.aps.org/doi/10.1103/PhysRevB.83.121408.

[99] E. L. Shirley, L. J. Terminello, A. Santoni, and F. J. Himpsel, "Brillouin-zone-selection effects in graphite photoelectron angular distributions," *Phys. Rev. B*, vol. 51, pp. 13 614–13 622, 19 May 1995. DOI: 10.1103/PhysRevB.51.13614. [Online]. Available: https://link.aps.org/doi/10.1103/PhysRevB.51.13614.

[100] P. Puschnig and D. Luftner, "Simulation of angle-resolved photoemission spectra by approximating the final state by a plane wave: From graphene to polycyclic aromatic hydrocarbon molecules," *Journal of Electron Spectroscopy and Related Phenomena*, vol. 200, pp. 193–208, 2015, Special Anniversary Issue: Volume 200, ISSN: 0368-2048. DOI: https://doi.org/10.1016/j.elspec.2015.06.003. [Online]. Available: https://www.sciencedirect.com/science/article/pii/S0368204815001309.

[101] P. Krüger, "Photoelectron diffraction from valence states of oriented molecules," *Journal of the Physical Society of Japan*, vol. 87, no. 6, p. 061 007, 2018. DOI: 10.7566/JPSJ.87.061007. [Online]. Available: https://doi.org/10.7566/JPSJ.87.061007.

[102] L. Wagner, Z. Hussain, and C. Fadley, "Direct-transition interpretation of angular-dependent valence-band photoemission from single-crystal copper in the energy range 40 ≤ hv ≤ 200 ev," *Solid State Communications*, vol. 21, no. 3, pp. 257–261, 1977, ISSN: 0038-1098. DOI: https://doi.org/10.1016/0038-1098(77)90181-8. [Online]. Available: https://www.sciencedirect.com/science/article/pii/0038109877901818.

[103] M. Dauth et al., "Perpendicular emission, dichroism, and energy dependence in angle-resolved photoemission: The importance of the final state," *Phys. Rev. Lett.*, vol. 117, p. 183 001, 18 Oct. 2016. DOI: 10.1103/PhysRevLett.117.183001. [Online]. Available: https://link.aps.org/doi/10.1103/PhysRevLett.117.183001.

[104] A. Liebsch, "Theory of angular resolved photoemission from adsorbates," *Phys. Rev. Lett.*, vol. 32, pp. 1203–1206, 21 May 1974. DOI: 10.1103/PhysRevLett.32.1203. [Online]. Available: https://link.aps.org/doi/10.1103/PhysRevLett.32.1203.

[105] R. L. Dubs, S. N. Dixit, and V. McKoy, "Circular dichroism in photoelectron angular distributions from adsorbed atoms," *Phys. Rev. B*, vol. 32, pp. 8389–8391, 12 Dec. 1985. DOI: 10.1103/PhysRevB.32.8389. [Online]. Available: https://link.aps.org/doi/10.1103/PhysRevB.32.8389.

[106] S. Moser, "A toy model for dichroism in angle resolved photoemission," *Journal of Electron Spectroscopy and Related Phenomena*, vol. 262, p. 147 278, 2023, ISSN: 0368-2048. DOI: https://doi.org/10.1016/j.elspec.2022.147278. [Online]. Available: https://www.sciencedirect.com/science/article/pii/S0368204822001116.

[107] W. D. Grobman, "Angle-resolved photoemission from molecules in the independent-atomic-center approximation," *Phys. Rev. B*, vol. 17, pp. 4573–4585, 12 Jun. 1978. DOI: 10.1103/PhysRevB.17.4573. [Online]. Available: https://link.aps.org/doi/10.1103/PhysRevB.17.4573.

[108] P. Kruger, F. Da Pieve, and J. Osterwalder, "Real-space multiple scattering method for angle-resolved photoemission and valence-band photoelectron diffraction and its application to Cu(111)," *Phys. Rev. B*, vol. 83, p. 115 437, 11 Mar. 2011. DOI: 10.1103/PhysRevB.83.115437. [Online]. Available: https://link.aps.org/doi/10.1103/PhysRevB.83.115437.

[109] J. Pendry, "Theory of photoemission," *Surface Science*, vol. 57, no. 2, pp. 679–705, 1976, ISSN: 0039-6028. DOI: https://doi.org/10.1016/0039-6028(76)90355-1. [Online]. Available: https://www.sciencedirect.com/science/article/pii/0039602876903551.

[110] J. Braun, "The theory of angle-resolved ultraviolet photoemission and its applications to ordered materials," *Reports on Progress in Physics*, vol. 59, no. 10, p. 1267, Oct. 1996. DOI: 10.1088/0034-4885/59/10/002. [Online]. Available: https://dx.doi.org/10.1088/0034-4885/59/10/002.

[111] F. J. García de Abajo, M. A. Van Hove, and C. S. Fadley, "Multiple scattering of electrons in solids and molecules: A cluster-model approach," *Phys. Rev. B*, vol. 63, p. 075 404, 7 Jan. 2001. DOI: 10.1103/PhysRevB.63.075404. [Online]. Available: https://link.aps.org/doi/10.1103/PhysRevB.63.075404.

[112] S. Goldberg, C. Fadley, and S. Kono, "Photoionization cross-sections for atomic orbitals with random and fixed spatial orientation," *Journal of Electron Spectroscopy and Related Phenomena*, vol. 21, no. 4, pp. 285–363, 1981, ISSN: 0368-2048. DOI: https://doi.org/10.1016/0368-2048(81)85067-0. [Online]. Available: https://www.sciencedirect.com/science/article/pii/0368204881850670.

[113] G. Schonhense, "Circular dichroism and spin polarization in photoemission from adsorbates and non-magnetic solids," *Physica Scripta*, vol. 1990, no. T31, p. 255, Jan. 1990. DOI: 10.1088/0031-8949/1990/T31/035. [Online]. Available: https://dx.doi.org/10.1088/0031-8949/1990/T31/035.

[114] J. Gadzuk, "Angle resolved photoemission from chemisorbed layers: Further theoretical considerations," *Surface Science*, vol. 53, no. 1, pp. 132–143, 1975, ISSN: 0039-6028. DOI: https://doi.org/10.1016/0039-6028(75)90121-1. [Online]. Available: https://www.sciencedirect.com/science/article/pii/0039602875901211.

[115] H. Daimon, T. Nakatani, S. Imada, S. Suga, Y. Kagoshima, and T. Miyahara, "Strong circular dichroism in photoelectron diffraction from nonchiral, nonmagnetic material–direct observation of rotational motion of electrons," *Japanese Journal of Applied Physics*, vol. 32, no. 10A, p. L1480, Oct. 1993. DOI: 10.1143/JJAP.32.L1480. [Online]. Available: https://dx.doi.org/10.1143/JJAP.32.L1480.

[116] S. Reich, J. Maultzsch, C. Thomsen, and P. Ordejon, "Tight-binding description of graphene," *Phys. Rev. B*, vol. 66, p. 035 412, 3 Jul. 2002. DOI: 10.1103/PhysRevB.66.035412. [Online]. Available: https://link.aps.org/doi/10.1103/PhysRevB.66.035412.

[117] A. P. Kaduwela, H. Xiao, S. Thevuthasan, C. S. Fadley, and M. A. Van Hove, "Circular dichroism in the angular distribution of core photoelectrons from si(001): A photoelectron-diffraction analysis," *Phys. Rev. B*, vol. 52, pp. 14 927–14 934, 20 Nov. 1995. DOI: 10.1103/PhysRevB.52.14927. [Online]. Available: https://link.aps.org/doi/10.1103/PhysRevB.52.14927.

[118] J. Henk, W. Schattke, H. Cartensen, R. Manzke, and M. Skibowski, "Surface-barrier and polarization effects in the photoemission from GaAs(110)," *Phys. Rev. B*, vol. 47, pp. 2251–2264, 4 Jan. 1993. DOI: 10.1103/PhysRevB.47.2251. [Online]. Available: https://link.aps.org/doi/10.1103/PhysRevB.47.2251.

[119] J. Henk, A. M. N. Niklasson, and B. Johansson, "Multiple-scattering theoretical approach to magnetic dichroism and spin polarization in angle-resolved core-level photoemission," *Phys. Rev. B*, vol. 59, pp. 13 986–14 000, 21 Jun. 1999. DOI: 10.1103/PhysRevB.59.13986. [Online]. Available: https://link.aps.org/doi/10.1103/PhysRevB.59.13986.

[120] J. Kang, S. Tongay, J. Zhou, J. Li, and J. Wu, "Band offsets and heterostructures of two-dimensional semiconductors," *Applied Physics Letters*, vol. 102, no. 1, p. 012 111, Jan. 2013, ISSN: 0003-6951. DOI: 10.1063/1.4774090. eprint: https://pubs.aip.org/aip/apl/article-pdf/doi/10.1063/1.4774090/14263519/012111_1_online.pdf. [Online]. Available: https://doi.org/10.1063/1.4774090.

[121] K. Koifmmode acuteselse sfimider, J. W. Gonzalez, and J. Fernandez-Rossier, "Large spin splitting in the conduction band of transition metal dichalcogenide monolayers," *Phys. Rev. B*, vol. 88, p. 245 436, 24 Dec. 2013. DOI: 10.1103/PhysRevB.88.245436. [Online]. Available: https://link.aps.org/doi/10.1103/PhysRevB.88.245436.

[122] J. M. Riley et al., "Direct observation of spin-polarized bulk bands in an inversion-symmetric semiconductor," *Nature Physics*, vol. 10, no. 11, pp. 835–839, 2014.

[123] J. Yeh and I. Lindau, "Atomic subshell photoionization cross sections and asymmetry parameters: $1 \leq z \leq 103$," *Atomic Data and Nuclear Data Tables*, vol. 32, no. 1, pp. 1–155, 1985, ISSN: 0092-640X. DOI: https://doi.org/10.1016/0092-640X(85)90016-6. [Online]. Available: https://www.sciencedirect.com/science/article/pii/0092640X85900166.

[124] M. Szczepanik-Ciba, T. Sobol, and J. Szade, "Phelix – a new soft x-ray spectroscopy beamline at solaris synchrotron," *Nuclear Instruments and Methods in Physics Research Section B: Beam Interactions with Materials and Atoms*, vol. 492, pp. 49–55, 2021, ISSN: 0168-583X. DOI: https://doi.org/10.1016/j.nimb.2021.01.021. [Online]. Available: https://www.sciencedirect.com/science/article/pii/S0168583X21000598.

[125] T. Heider et al., "Geometry-induced spin filtering in photoemission maps from WTe_2 surface states," *Phys. Rev. Lett.*, vol. 130, p. 146 401, 14 Apr. 2023. DOI: 10.1103/PhysRevLett.130.146401. [Online]. Available: https://link.aps.org/doi/10.1103/PhysRevLett.130.146401.

[126] H. Ji et al., "A ferromagnetic insulating substrate for the epitaxial growth of topological insulators," *Journal of Applied Physics*, vol. 114, p. 114 907, 0 2013. DOI: 10.1063/1.4822092. [Online]. Available: https://doi.org/10.1063/1.4822092.

[127] Y. F. Li et al., "Electronic structure of ferromagnetic semiconductor $CrTe_3$ by angle-resolved photoemission spectroscopy," *Phys. Rev. B*, vol. 98, p. 125 127, 12 Sep. 2018. DOI: 10.1103/PhysRevB.98.125127. [Online]. Available: https://link.aps.org/doi/10.1103/PhysRevB.98.125127.

[128] X. Zhang, Y. Zhao, Q. Song, S. Jia, J. Shi, and W. Han, "Magnetic anisotropy of the single-crystalline ferromagnetic insulator $Cr_2Ge_2Te_6$," *Japanese Journal of Applied Physics*, vol. 55, p. 3, 0 Feb. 2019. DOI: 10.7567/JJAP.55.033001. [Online]. Available: http://dx.doi.org/10.7567/JJAP.55.033001.

[129] V. Carteaux, D. Brunet, G. Ouvrard, and G. Andre, "Crystallographic, magnetic and electronic structures of a new layered ferromagnetic compound $Cr_2Ge_2Te_6$," *Journal of Physics: Condensed Matter*, vol. 7, no. 1, p. 69, Jan. 1995. DOI: 10.1088/0953-8984/7/1/008. [Online]. Available: https://dx.doi.org/10.1088/0953-8984/7/1/008.

[130] B. Siberchicot, S. Jobic, V. Carteaux, P. Gressier, and G. Ouvrard, "Band structure calculations of ferromagnetic chromium tellurides $CrSiTe_3$ and $CrGeTe_3$," *The Journal of Physical Chemistry*, vol. 100, no. 14, pp. 5863–5867, 1996. DOI: 10.1021/jp952188s. [Online]. Available: https://doi.org/10.1021/jp952188s.

[131] I. Verzhbitskiy et al., "Controlling the magnetic anisotropy in $Cr_2Ge_2Te_6$ by electrostatic gating," *Nature Electronics*, vol. 3, pp. 460–465, 0 Jun. 2020. DOI: 10.1038/s41928-020-0427-7. [Online]. Available: https://doi.org/10.1038/s41928-020-0427-7.

[132] W. Zhuo et al., "Manipulating ferromagnetism in few-layered $Cr_2Ge_2Te_6$," *Advanced Materials*, vol. 33, p. 2 008 586, 0 Jun. 2021. DOI: 10.1002/adma.202008586. [Online]. Available: https://doi.org/10.1002/adma.202008586.

[133] N. Wang et al., "Transition from ferromagnetic semiconductor to ferromagnetic metal with enhanced curie temperature in $Cr_2Ge_2Te_6$ via organic ion intercalation," *Journal of the American Chemical Society*, vol. 141, no. 43, pp. 17 166–17 173, 2019. DOI: 10.1021/jacs.9b06929. [Online]. Available: https://doi.org/10.1021/jacs.9b06929.

[134] J. Zhang, C. Zhang, K. Ren, X. Lin, and Z. Cui, "Tunable electronic and magnetic properties of $Cr_2Ge_2Te_6$ monolayer by organic molecular adsorption," *Nanotechnology*, vol. 33, p. 34, 0 Jun. 2022. DOI: 10.1088/1361-6528/ac715d. [Online]. Available: https://doi.org/10.1088/1361-6528/ac715d.

[135] C. Song et al., "Tunable band gap and enhanced ferromagnetism by surface adsorption in monolayer $Cr_2Ge_2Te_6$," *Phys. Rev. B*, vol. 99, p. 214 435, 21 Jun. 2019. DOI: 10.1103/PhysRevB.99.214435. [Online]. Available: https://link.aps.org/doi/10.1103/PhysRevB.99.214435.

[136] A. E. L. Allcca, H. Idzuchi, X. C. Pan, K. Tanigaki, and Y. P. Chen, "Modified magnetism in heterostructures of $Cr_2Ge_2Te_6$ and oxides," *AIP Advances*, vol. 13, p. 015 031, 0 2023. DOI: 10.1002/adma.202008586. [Online]. Available: https://doi.org/10.1063/9.0000413.

[137] H. Idzuchi, A. E. L. Allcca, X. C. Pan, K. Tanigaki, and Y. P. Chen, "Increased curie temperature and enhanced perpendicular magneto anisotropy $Cr_2Ge_2Te_6$/NiO heterostructures," *Appl. Phys. Lett.*, vol. 115, p. 232 403, 0 Jun. 2019. DOI: 10.1063/1.5130930. [Online]. Available: https://doi.org/10.1063/1.5130930.

[138] Z. Lin et al., "Pressure-induced spin reorientation transition in layered ferromagnetic insulator $Cr_2Ge_2Te_6$," *Physical Review Materials*, vol. 2, p. 051 004, 5 Jun. 2019. DOI: 10.1103/physrevmaterials.2.051004. [Online]. Available: http://dx.doi.org/10.1103/physrevmaterials.2.051004.

[139] E. Dong et al., "Effects of pressure on the structure and properties of layered ferromagnetic $Cr_2Ge_2Te_6$," *Physica B: Condensed Matter*, vol. 595, p. 412 344, 0921-4526 2020. DOI: 10.1016/j.physb.2020.412344. [Online]. Available: https://www.sciencedirect.com/science/article/pii/S0921452620303550.

[140] M. Šiškins et al., "Nanomechanical probing and strain tuning of the curie temperature in suspended $Cr_2Ge_2Te_6$-based heterostructures," *npj 2D Materials and Applications*, vol. 6, no. 1, 2397-7132 2022. DOI: 10.1038/s41699-022-00315-7. [Online]. Available: https://doi.org/10.1038/s41699-022-00315-7.

[141] M. D. Watson et al., "Direct observation of the energy gain underpinning ferromagnetic superexchange in the electronic structure of $CrGeTe_3$," *Phys. Rev. B*, vol. 101, p. 205 125, 20 May 2020. DOI: 10.1103/PhysRevB.101.205125. [Online]. Available: https://link.aps.org/doi/10.1103/PhysRevB.101.205125.

[142] M. Suzuki et al., "Coulomb-interaction effect on the two-dimensional electronic structure of the van der waals ferromagnet $Cr_2Ge_2Te_6$," *Phys. Rev. B*, vol. 99, p. 161 401, 16 Apr. 2019. DOI: 10.1103/PhysRevB.99.161401. [Online]. Available: https://link.aps.org/doi/10.1103/PhysRevB.99.161401.

[143] T. Yilmaz et al., "Multi-hole bands and quasi–two-dimensionality in $Cr_2Ge_2Te_6$ studied by angle-resolved photoemission spectroscopy," *Europhysics Letters*, vol. 133, no. 2, p. 27 002, Mar. 2021. DOI: 10.1209/0295-5075/133/27002. [Online]. Available: https://dx.doi.org/10.1209/0295-5075/133/27002.

[144] W. Jiang et al., "Spin-split valence bands of the ferromagnetic insulator $Cr_2Ge_2Te_6$ studied by angle-resolved photoemission spectroscopy," *Journal of Applied Physics*, vol. 127, no. 2, Jan. 2020, 023901, ISSN: 0021-8979. DOI: 10.1063/1.5135759. [Online]. Available: https://doi.org/10.1063/1.5135759.

[145] A. R. C. McCray et al., "Direct observation of magnetic bubble lattices and magnetoelastic effects in van der waals $Cr_2Ge_2Te_6$," *Advanced Functional Materials*, vol. 0, p. 2 214 203, 0 Mar. 2023. DOI: 10.1002/adfm.202214203. [Online]. Available: https://doi.org/10.1002/adfm.202214203.

[146] M.-G. Han et al., "Topological magnetic-spin textures in two-dimensional van der waals $Cr_2Ge_2Te_6$," *Nano Letters*, vol. 19, no. 11, pp. 7859–7865, 2019, PMID: 31661617. DOI: 10.1021/acs.nanolett.9b02849. [Online]. Available: https://doi.org/10.1021/acs.nanolett.9b02849.

[147] Y. Liu et al., "Polaronic conductivity in $Cr_2Ge_2Te_6$ single crystals," *Advanced Functional Materials*, vol. 32, no. 19, p. 2 105 111, 2022. DOI: https://doi.org/10.1002/adfm.202105111. eprint: https://onlinelibrary.wiley.com/doi/pdf/10.1002/adfm.202105111. [Online]. Available: https://onlinelibrary.wiley.com/doi/abs/10.1002/adfm.202105111.

[148] J. Stohr and H. C. Siegmann, *Magnetism: From Fundamentals to Nanoscale Dynamics*. Springer Series in Solid-State Sciences, 2006.

[149] M. Baranava, D. Hvazdouski, V. Skachkova, V. Stempitsky, and A. Danilyuk, "Magnetic interactions in $Cr_2Ge_2Te_6$ and $Cr_2Si_2Te_6$ monolayers: Ab initio study," *Materials Today: Proceedings*, vol. 20, pp. 342–347, 2020, 11th International Conference on Advanced Nano Materials, ISSN: 2214-7853. DOI: https://doi.org/10.1016/j.matpr.2019.10.072. [Online]. Available: https://www.sciencedirect.com/science/article/pii/S2214785319335813.

[150] J. Kanamori, "Superexchange interaction and symmetry properties of electron orbitals," *Journal of Physics and Chemistry of Solids*, vol. 10, no. 2, pp. 87–98, 1959, ISSN: 0022-3697. DOI: https://doi.org/10.1016/0022-3697(59)90061-7. [Online]. Available: https://www.sciencedirect.com/science/article/pii/0022369759900617.

[151] P. W. Anderson, "Antiferromagnetism. theory of superexchange interaction," *Phys. Rev.*, vol. 79, pp. 350–356, 2 Jul. 1950. DOI: 10.1103/PhysRev.79.350. [Online]. Available: https://link.aps.org/doi/10.1103/PhysRev.79.350.

[152] J. B. Goodenough, "Theory of the role of covalence in the perovskite-type manganites [La, M(II)]MnO_3," *Phys. Rev.*, vol. 100, pp. 564–573, 2 Oct. 1955. DOI: 10.1103/PhysRev.100.564. [Online]. Available: https://link.aps.org/doi/10.1103/PhysRev.100.564.

[153] J. Kanamori, "Crystal distortion in magnetic compounds," *Journal of Applied Physics*, vol. 31, no. 5, S14–S23, 1960.

[154] P. W. Anderson, "New approach to the theory of superexchange interactions," *Physical Review*, vol. 115, no. 1, p. 2, 1959.

[155] D. G. Van Campen, R. J. Pouliot, and L. E. Klebanoff, "Spin-resolved x-ray-photoelectron-spectroscopy study of ferromagnetic iron," *Phys. Rev. B*, vol. 48, pp. 17 533–17 537, 23 Dec. 1993. DOI: 10.1103/PhysRevB.48.17533. [Online]. Available: https://link.aps.org/doi/10.1103/PhysRevB.48.17533.

[156] R. Jungblut, C. Roth, F. Hillebrecht, and E. Kisker, "Spin-polarized electron spectroscopy as a combined chemical and magnetic probe," *Surface Science*, vol. 269-270, pp. 615–621, 1992, ISSN: 0039-6028. DOI: https://doi.org/10.1016/0039-6028(92)91320-B. [Online]. Available: https://www.sciencedirect.com/science/article/pii/003960289291320B.

[157] A. Jain et al., "Commentary: The Materials Project: A materials genome approach to accelerating materials innovation," *APL Materials*, vol. 1, no. 1, p. 011 002, Jul. 2013, ISSN: 2166-532X. DOI: 10.1063/1.4812323. [Online]. Available: https://doi.org/10.1063/1.4812323.

[158] M. Gibertini, M. Koperski, A. F. Morpurgo, and K. S. Novoselov, "Magnetic 2d materials and heterostructures," *Nature Nanotechnology*, vol. 14, no. 5, pp. 408–419, May 2019, ISSN: 1748-3395. DOI: 10.1038/s41565-019-0438-6. [Online]. Available: http://dx.doi.org/10.1038/s41565-019-0438-6.

[159] B. Chen et al., "Magnetic properties of layered itinerant electron ferromagnet Fe_3GeTe_3," *Journal of the Physical Society of Japan*, vol. 82, p. 124 711, Dec. 2013. DOI: 10.7566/JPSJ.82.124711. [Online]. Available: https://doi.org/10.7566/JPSJ.82.124711.

[160] N. Leon-Brito, E. D. Bauer, F. Ronning, J. D. Thompson, and R. Movshovich, "Magnetic microstructure and magnetic properties of uniaxial itinerant ferromagnet Fe_3GeTe_3," *Journal of Applied Physics*, vol. 120, no. 8, p. 083 903, Aug. 2016, ISSN: 0021-8979. DOI: 10.1063/1.4961592. [Online]. Available: https://doi.org/10.1063/1.4961592.

[161] R. Roemer, C. Liu, and K. Zou, "Robust ferromagnetism in wafer-scale monolayer and multilayer Fe_3GeTe_3," *npj 2D Materials and Applications*, vol. 4, no. 33, pp. 2397–7132, 2020. DOI: 10.1038/s41699-020-00167-z. [Online]. Available: https://doi.org/10.1038/s41699-020-00167-z.

[162] Z. Fei et al., "Two-dimensional itinerant ferromagnetism in atomically thin Fe_3GeTe_3," *Nature Materials*, vol. 17, no. 778, pp. 1476–4660, 2018. DOI: 10.1038/s41563-018-0149-7. [Online]. Available: https://doi.org/10.1038/s41563-018-0149-7.

[163] K. Kim et al., "Large anomalous hall current induced by topological nodal lines in a ferromagnetic van der waals semimetal," *Nature Materials*, vol. 17, no. 794,

pp. 1476–4660, 2018. DOI: 10.1038/s41563-018-0132-3. [Online]. Available: https://doi.org/10.1038/s41563-018-0132-3.

[164] C. Tan et al., "Hard magnetic properties in nanoflake van der waals Fe_3GeTe_3," *Nature Communications*, vol. 9, no. 1554, pp. 2041–1723, 2018. DOI: 10.1038/s41467-018-04018-w. [Online]. Available: https://doi.org/10.1038/s41467-018-04018-w.

[165] S. Y. Park et al., "Controlling the magnetic anisotropy of the van der waals ferromagnet Fe_3GeTe_3 through hole doping," *Nano Letters*, vol. 20, no. 1, pp. 95–100, 2020, PMID: 31752490. DOI: 10.1021/acs.nanolett.9b03316. [Online]. Available: https://doi.org/10.1021/acs.nanolett.9b03316.

[166] K. Pei et al., "Anomalous spin behavior in Fe_3GeTe_3 driven by current pulses," *ACS Nano*, vol. 14, no. 8, pp. 9512–9520, 2020, PMID: 32538609. DOI: 10.1021/acsnano.0c03269. [Online]. Available: https://doi.org/10.1021/acsnano.0c03269.

[167] H. L. Zhuang, P. R. C. Kent, and R. G. Hennig, "Strong anisotropy and magnetostriction in the two-dimensional stoner ferromagnet Fe_3GeTe_3," *Phys. Rev. B*, vol. 93, p. 134 407, 13 Apr. 2016. DOI: 10.1103/PhysRevB.93.134407. [Online]. Available: https://link.aps.org/doi/10.1103/PhysRevB.93.134407.

[168] M.-C. Jiang and G.-Y. Guo, "Large magneto-optical effect and magnetic anisotropy energy in two-dimensional metallic ferromagnet Fe_3GeTe_3," *Phys. Rev. B*, vol. 105, p. 014 437, 1 Jan. 2022. DOI: 10.1103/PhysRevB.105.014437. [Online]. Available: https://link.aps.org/doi/10.1103/PhysRevB.105.014437.

[169] K. Zhang et al., "Gigantic current control of coercive field and magnetic memory based on nanometer-thin ferromagnetic van der waals Fe_3GeTe_3," *Advanced Materials*, vol. 33, no. 4, p. 2 004 110, 2021. DOI: 10.1002/adma.202004110. [Online]. Available: https://doi.org/10.1002/adma.202004110.

[170] X. Xu et al., *Spectroscopic signature for local-moment magnetism in van der waals ferromagnet* Fe_3GeTe_3, 2020. [Online]. Available: https://arxiv.org/abs/2004.10379.

[171] Y. Zhang et al., "Emergence of kondo lattice behavior in a van der waals itinerant ferromagnet, Fe_3GeTe_3," *Science Advances*, vol. 4, no. 1, eaao6791, 2018. DOI: 10.1126/sciadv.aao6791. [Online]. Available: https://www.science.org/doi/abs/10.1126/sciadv.aao6791.

[172] J.-X. Zhu et al., "Electronic correlation and magnetism in the ferromagnetic metal Fe_3GeTe_3," *Phys. Rev. B*, vol. 93, p. 144 404, 14 Apr. 2016. DOI: 10.1103/PhysRevB.93.144404. [Online]. Available: https://link.aps.org/doi/10.1103/PhysRevB.93.144404.

[173] Y. Li et al., "Field-dependent magnetic domain behavior in van der waals Fe_3GeTe_3," *JOM*, vol. 74, no. 2310, pp. 1543–1851, 2022. DOI: 10.1007/s11837-022-05299-9. [Online]. Available: https://doi.org/10.1007/s11837-022-05299-9.

[174] B. Ding et al., "Observation of magnetic skyrmion bubbles in a van der waals ferromagnet Fe_3GeTe_3," *Nano Letters*, vol. 20, no. 2, pp. 868–873, 2020, PMID: 31869236. DOI: 10.1021/acs.nanolett.9b03453. eprint: https://doi.org/10.1021/acs.nanolett.9b03453. [Online]. Available: https://doi.org/10.1021/acs.nanolett.9b03453.

[175] M. Yang et al., "Creation of skyrmions in van der waals ferromagnet fe3gete2on (co/pd)n superlattice," *Science Advances*, vol. 6, no. 36, eabb5157, 2020. DOI:

10.1126/sciadv.abb5157. eprint: https://www.science.org/doi/pdf/10.1126/sciadv.abb5157. [Online]. Available: https://www.science.org/doi/abs/10.1126/sciadv.abb5157.

[176] H.-J. Deiseroth, K. Aleksandrov, C. Reiner, L. Kienle, and R. K. Kremer, "Fe_3GeTe_3 and Ni_3GeTe_3 – two new layered transition-metal compounds: Crystal structures, hrtem investigations, and magnetic and electrical properties," *European Journal of Inorganic Chemistry*, vol. 2006, no. 8, pp. 1561–1567, 2006. DOI: https://doi.org/10.1002/ejic.200501020. eprint: https://chemistry-europe.onlinelibrary.wiley.com/doi/pdf/10.1002/ejic.200501020. [Online]. Available: https://chemistry-europe.onlinelibrary.wiley.com/doi/abs/10.1002/ejic.200501020.

[177] D. Xiao, G.-B. Liu, W. Feng, X. Xu, and W. Yao, "Coupled spin and valley physics in monolayers of MoS_2 and other group-vi dichalcogenides," *Physical review letters*, vol. 108, no. 19, p. 196 802, 2012.

[178] K. F. Mak, K. He, J. Shan, and T. F. Heinz, "Control of valley polarization in monolayer MoS_2 by optical helicity," *Nature nanotechnology*, vol. 7, no. 8, pp. 494–498, 2012.

[179] H. Zeng, J. Dai, W. Yao, D. Xiao, and X. Cui, "Valley polarization in MoS_2 monolayers by optical pumping," *Nature nanotechnology*, vol. 7, no. 8, pp. 490–493, 2012.

[180] M. A. McGuire, H. Dixit, V. R. Cooper, and B. C. Sales, "Coupling of crystal structure and magnetism in the layered, ferromagnetic insulator CrI_3," *Chemistry of Materials*, vol. 27, no. 2, Dec. 2014, ISSN: 0897-4756. DOI: 10.1021/cm504242t. [Online]. Available: https://www.osti.gov/biblio/1185798.

[181] X. Li and J. Yang, "$CrXTe_3$ (x = Si, Ge) nanosheets: Two dimensional intrinsic ferromagnetic semiconductors," *J. Mater. Chem. C*, vol. 2, pp. 7071–7076, 34 2014. DOI: 10.1039/C4TC01193G. [Online]. Available: http://dx.doi.org/10.1039/C4TC01193G.

[182] R. Cowan, *The Theory of Atomic Structure and Spectra* (Los Alamos Series in Basic and Applied Sciences). University of California Press, 1981, ISBN: 9780520038219. [Online]. Available: https://books.google.de/books?id=avgkDQAAQBAJ.

[183] N. F. Mott, "The basis of the electron theory of metals, with special reference to the transition metals," *Proceedings of the Physical Society. Section A*, vol. 62, no. 7, p. 416, Jul. 1949. DOI: 10.1088/0370-1298/62/7/303. [Online]. Available: https://dx.doi.org/10.1088/0370-1298/62/7/303.

[184] J. C. Slater, "The ferromagnetism of nickel," *Phys. Rev.*, vol. 49, pp. 537–545, 7 Apr. 1936. DOI: 10.1103/PhysRev.49.537. [Online]. Available: https://link.aps.org/doi/10.1103/PhysRev.49.537.

[185] J. C. Slater, "The ferromagnetism of nickel. ii. temperature effects," *Phys. Rev.*, vol. 49, pp. 931–937, 12 Jun. 1936. DOI: 10.1103/PhysRev.49.931. [Online]. Available: https://link.aps.org/doi/10.1103/PhysRev.49.931.

[186] E. C. Stoner and R. Whiddington, "Collective electron specific heat and spin paramagnetism in metals," *Proceedings of the Royal Society of London. Series A - Mathematical and Physical Sciences*, vol. 154, no. 883, pp. 656–678, 1936. DOI: 10.1098/rspa.1936.0075. eprint: https://royalsocietypublishing.org/doi/pdf/10.

1098/rspa.1936.0075. [Online]. Available: https://royalsocietypublishing.org/doi/abs/10.1098/rspa.1936.0075.

[187] E. C. Stoner, "Collective electron ferromagnetism," *Proceedings of the Royal Society of London. Series A. Mathematical and Physical Sciences*, vol. 165, no. 922, pp. 372–414, 1938. DOI: 10.1098/rspa.1938.0066. [Online]. Available: https://royalsocietypublishing.org/doi/abs/10.1098/rspa.1938.0066.

[188] V. Sunko et al., "Probing spin correlations using angle-resolved photoemission in a coupled metallic/mott insulator system," *Science Advances*, vol. 6, eaaz0611, Feb. 2020. DOI: 10.1126/sciadv.aaz0611.

[189] J. Moulder and J. Chastain, *Handbook of X-ray Photoelectron Spectroscopy: A Reference Book of Standard Spectra for Identification and Interpretation of XPS Data*. Physical Electronics Division, Perkin-Elmer Corporation, 1992, ISBN: 9780962702624. [Online]. Available: https://books.google.de/books?id=A_XGQgAACAAJ.

[190] A. Hubert and R. Schafer, *Magnetic Domains:The Analysis of Magnetic Microstructures*. Springer Berlin, Heidelberg, 1998.

[191] D. G. Hopkinson et al., "Nanometre imaging of Fe_3GeTe_2 ferromagnetic domain walls," *Nanotechnology*, vol. 32, no. 20, p. 205 703, Feb. 2021. DOI: 10.1088/1361-6528/abe32b. [Online]. Available: https://dx.doi.org/10.1088/1361-6528/abe32b.

[192] M. J. Meijer et al., "Chiral spin spirals at the surface of the van der waals ferromagnet Fe_3GeTe_2," *Nano Letters*, vol. 20, no. 12, pp. 8563–8568, 2020, PMID: 33238096. DOI: 10.1021/acs.nanolett.0c03111. eprint: https://doi.org/10.1021/acs.nanolett.0c03111. [Online]. Available: https://doi.org/10.1021/acs.nanolett.0c03111.

[193] A. Chakraborty et al., "Magnetic skyrmions in a thickness tunable 2d ferromagnet from a defect driven dzyaloshinskii–moriya interaction," *Advanced Materials*, vol. 34, no. 11, p. 2 108 637, 2022. DOI: https://doi.org/10.1002/adma.202108637. eprint: https://onlinelibrary.wiley.com/doi/pdf/10.1002/adma.202108637. [Online]. Available: https://onlinelibrary.wiley.com/doi/abs/10.1002/adma.202108637.

[194] H. Wang et al., "Characteristics and temperature-field-thickness evolutions of magnetic domain structures in van der waals magnet Fe_3GeTe_2 nanolayers," *Applied Physics Letters*, vol. 116, no. 19, p. 192 403, May 2020, Art. no. 192403. DOI: 10.1063/5.0009484.

[195] H.-H. Yang et al., "Magnetic domain walls of the van der waals material Fe_3GeTe_2," *2D Materials*, vol. 9, no. 2, p. 025 022, Mar. 2022. DOI: 10.1088/2053-1583/ac5d0e. [Online]. Available: https://dx.doi.org/10.1088/2053-1583/ac5d0e.

[196] W. Zhang et al., "Current-induced domain wall motion in a van der waals ferromagnet Fe_3GeTe_2," *Nature Communications*, vol. 15, no. 1, p. 4851, Jun. 2024. DOI: 10.1038/s41467-024-48893-y. [Online]. Available: https://doi.org/10.1038/s41467-024-48893-y.

[197] N. Tombros, C. Jozsa, M. Popinciuc, H. T. Jonkman, and B. J. Van Wees, "Electronic spin transport and spin precession in single graphene layers at room temperature," *nature*, vol. 448, no. 7153, pp. 571–574, 2007.

[198] A. Pal, K. Parto, K. Agashiwala, W. Cao, and K. Banerjee, "Computational study of spin injection in 2d materials," in *2019 IEEE International Electron Devices Meeting (IEDM)*, 2019, pp. 24.2.1–24.2.4. DOI: 10.1109/IEDM19573.2019.8993578.

[199] K. F. Mak, K. L. McGill, J. Park, and P. L. McEuen, "The valley hall effect in MoS_2 transistors," *Science*, vol. 344, no. 6191, pp. 1489–1492, 2014.

[200] J. R. Schaibley et al., "Valleytronics in 2d materials," *Nature Reviews Materials*, vol. 1, no. 11, pp. 1–15, 2016.

[201] C. Bigi, F. Mazzola, J. Fujii, I. Vobornik, G. Panaccione, and G. Rossi, "Measuring spin-polarized electronic states of quantum materials: $2H - NbSe_2$," *Phys. Rev. B*, vol. 103, p. 245 142, 24 Jun. 2021. DOI: 10.1103/PhysRevB.103.245142. [Online]. Available: https://link.aps.org/doi/10.1103/PhysRevB.103.245142.

[202] W. Jung et al., "Warping effects in the band and angular-momentum structures of the topological insulator Bi_2Se_3," *Phys. Rev. B*, vol. 84, p. 245 435, 24 Dec. 2011. DOI: 10.1103/PhysRevB.84.245435. [Online]. Available: https://link.aps.org/doi/10.1103/PhysRevB.84.245435.

[203] Y. Guo, Y. Zhang, S. Yuan, B. Wang, and J. Wang, "Chromium sulfide halide monolayers: Intrinsic ferromagnetic semiconductors with large spin polarization and high carrier mobility," *Nanoscale*, vol. 10, no. 37, pp. 18 036–18 042, 2018.

[204] T. Miyamae, S. Hasegawa, D. Yoshimura, H. Ishii, N. Ueno, and K. Seki, "Intramolecular energy-band dispersion in oriented thin films of n-cf3(cf2)22cf3 observed by angle-resolved photoemission with synchrotron radiation," *The Journal of Chemical Physics*, vol. 112, no. 7, pp. 3333–3338, Feb. 2000, ISSN: 0021-9606. DOI: 10.1063/1.480915. eprint: https://pubs.aip.org/aip/jcp/article-pdf/112/7/3333/19027683/3333_1_online.pdf. [Online]. Available: https://doi.org/10.1063/1.480915.

[205] D. Vollhardt, "Dynamical mean-field theory for correlated electrons," *Annalen der Physik*, vol. 524, no. 1, pp. 1–19, 2012. DOI: https://doi.org/10.1002/andp.201100250. eprint: https://onlinelibrary.wiley.com/doi/pdf/10.1002/andp.201100250. [Online]. Available: https://onlinelibrary.wiley.com/doi/abs/10.1002/andp.201100250.

[206] E. Gao, S.-Z. Lin, Z. Qin, M. J. Buehler, X.-Q. Feng, and Z. Xu, "Mechanical exfoliation of two-dimensional materials," *Journal of the Mechanics and Physics of Solids*, vol. 115, pp. 248–262, 2018, ISSN: 0022-5096. DOI: https://doi.org/10.1016/j.jmps.2018.03.014. [Online]. Available: https://www.sciencedirect.com/science/article/pii/S0022509618300280.

[207] N. M. R. Peres, "Colloquium: The transport properties of graphene: An introduction," *Rev. Mod. Phys.*, vol. 82, pp. 2673–2700, 3 Sep. 2010. DOI: 10.1103/RevModPhys.82.2673. [Online]. Available: https://link.aps.org/doi/10.1103/RevModPhys.82.2673.